Structural and Physical Properties of Low-Dimensional Chalcogenides

by

Jack Corps

A thesis submitted for the degree of Doctor of Philosophy

Heriot-Watt University

Institute of Chemical Sciences

December 2013

Abstract

This thesis describes work on three families of low-dimensional chalcogenides. The Jamesonite-Benavidesite series has been investigated to observe the effects of chemical substitution as iron is replaced by manganese. A series of materials with the general formula $Fe_{1-x}Mn_xPb_4Sb_6S_{14}$ ($0 \leq x \leq 1$) has been synthesised for analysis. Structural investigations of the highly anisotropic structure using powder neutron diffraction have been performed at temperatures from 2 K up to room temperature. The magnetism has been studied with low temperature powder neutron diffraction and SQUID magnetometry. Benavidesite ($x = 1$) has been shown to have antiferromagnetic order at 2 K with moments of 2.58(9) μ_B. The electrical transport properties indicate materials are p-type semiconductors with activation energies in the range 177.2 meV to 626 meV.

Work on a cobalt Shandite series, $Co_3Sn_{2-x}In_xS_2$ ($0 \leq x \leq 2$), enables tuning of the Fermi level within narrow Co d-states. This results in a compositionally induced double metal-to-semiconductor-to-metal transition and manipulation of the electronic and thermal transport properties. A narrow semiconducting region exists between compositions of $1 \leq x \leq 1.05$. There are two main group sites in the structure: one in an intra-layer trigonal antiprismatic site and one in a kagome layer. Powder neutron diffraction has been used to investigate ordering of indium and tin across the two main-group sites. X-ray Photoelectron Spectroscopy and ^{119}Sn Mössbauer spectroscopy have been used to determine the oxidation states of the elements in the material. Results suggest that cobalt, tin, indium and sulphur are all in the 0 oxidation state. The thermoelectric properties have been measured and the figure of merit for $Co_3Sn_{1.2}In_{0.8}S_2$ and $Co_3Sn_{1.15}In_{0.85}S_2$ ($ZT = 0.28$) are the highest reported for a sulphide at 425 K.

The sulphide $In_2Sn_3S_7$ has been prepared as a bulk polycrystalline phase for the first time. Powder neutron diffraction has been undertaken to study partial ordering of tin and indium over the MS_6 (M = Sn, In) octahedral sites within the structure. Sites were observed to contain approximately two-thirds indium and one-third tin. The structural analogue $Cr_2Sn_3Se_7$ has also been synthesised. The electrical resistivity, Seebeck coefficient and thermal conductivity have been measured for both samples. The previously unreported $Cr_2Sn_3S_7$ phase (Space Group: $P2_1/m$, $a = 11.2945(6)$ Å, $b = 3.6456(2)$ Å, $c = 12.2473(7)$ Å, $\beta = 105.352(2)$ °) has been synthesised as well as a new ternary chromium tin selenide with the approximate stoichiometry $Cr_2Sn_5Se_{11}$.

Acknowledgements

There are many people, groups and institutions who have helped and assisted me during the course of my Ph. D. and I would like to take this opportunity to thank them for all their efforts.

First and foremost, I would like to thank my supervisors Professor Anthony V. Powell and Dr Paz Vaqueiro. Without their support, guidance and expertise, I would not have been able to start, let alone complete the work that I am going to present in the thesis.

Thanks are also extended to:

Alan Barton, whose expert opinion was very much appreciated every time an instrument failed and required repair.

Paul Allan for the countless silica tubes prepared for me and the timely fashion in which repairs to glassware were completed.

Dr Ron Smith, Dr Winfried Kockelmann and Dr Kevin Knight for their assistance before, during and after neutron diffraction experiments at ISIS.

Professor Jean-Claude Jumas for performing ^{119}Sn Mössbauer Spectroscopy measurements and analysis for samples of cobalt Shandite.

Dr Anders Barlow at the National EPSRC XPS Users Service (NEXUS) for performing X-ray Photoelectron Spectroscopy on samples of cobalt Shandite.

Dr Marek Jura and William Jamieson for performing SQUID measurements on samples in the Jamesonite-Benavidesite series at ISIS.

Dr Anna Kusmartseva for assistance with SQUID measurements at CSEC.

Barbara Corps for proofreading my thesis.

ACADEMIC REGISTRY
Research Thesis Submission

Name*:*	Jack Corps		
School/PGI:	School of Engineering and Physical Sciences / Institute of Chemical Science		
Version:	Final	Degree Sought (Award **and** Subject area)	Doctor of Philosophy (Chemistry)

Declaration

In accordance with the appropriate regulations I hereby submit my thesis and I declare that:

1) the thesis embodies the results of my own work and has been composed by myself
2) where appropriate, I have made acknowledgement of the work of others and have made reference to work carried out in collaboration with other persons
3) the thesis is the correct version of the thesis for submission and is the same version as any electronic versions submitted*.
4) my thesis for the award referred to, deposited in the Heriot-Watt University Library, should be made available for loan or photocopying and be available via the Institutional Repository, subject to such conditions as the Librarian may require
5) I understand that as a student of the University I am required to abide by the Regulations of the University and to conform to its discipline.

* *Please note that it is the responsibility of the candidate to ensure that the correct version of the thesis is submitted.*

Signature of Candidate*:*		Date:	

Submission

Submitted By *(name in capitals):*	
Signature of Individual Submitting:	
Date Submitted:	

For Completion in the Student Service Centre (SSC)

Received in the SSC by *(name in capitals):*			
Method of Submission *(Handed in to SSC; posted through internal/external mail):*			
E-thesis Submitted **(mandatory for final theses)**			
Signature:		Date:	

Table of Contents

Chapter 1 – Introduction

The structure of a solid is dependent on the forces between atoms within the material. These can be covalent, ionic or metallic bonds, or van der Waals' interactions. From a geometrical perspective, crystal structures can be constructed from polyhedra of anions formed around cations. Not only does this determine the structure of the solid, it affects the physical properties of the material. Understanding the relationship between the structural and the physical properties of a material is highly desirable. It could lead to the targeting of new materials that incorporate specific structural characteristics, so the properties are ideal for usage in the required application.

Chalcogenides are materials that contain a group sixteen element (sulphur, selenium or tellurium), along with other main-group or transition-metal elements. In general, the band structures of oxide materials have large band gaps, which results in the material having insulating properties. Materials containing other group sixteen elements generally have smaller band gaps, resulting in semiconducting behaviour. This makes these materials more suited for applications where semiconducting properties are required.

This thesis presents work on several low-dimensional chalcogenide systems: the Jamesonite-Benavidesite, cobalt Shandite and $In_2Sn_3S_7$-$Cr_2Sn_3Se_7$ series. Polycrystalline samples have been synthesised and the effects of structure and chemical substitution investigated. Structural investigations have been performed using powder X-ray and neutron diffraction. Physical properties such as magnetic susceptibility, electrical resistivity, Seebeck coefficient and thermal conductivity have been investigated for these materials.

1.1 Low-Dimensionality

Low-dimensional materials have been shown to possess several unique and useful combinations of properties. They have been exploited for use in applications including electronics, energy storage and conversion, catalysis,[1] photodetectors and lasers.[2]

1.1.1 Low-Dimensional Structures

Low-dimensional materials are solids in which there is anisotropy in the chemical bonding of the structure. There are a wide variety of solid structures known for oxides,

however, low-dimensionality, while not unheard of, is not commonly observed. On the other hand, in sulphide, selenide and telluride chemistry, low-dimensional structures are more widely reported. There are several reasons for the observed differences in behaviour between oxide and sulphide materials. Sulphur is less electronegative when compared to oxygen. This leads to lower repulsion effects between adjacent sulphur atoms. The small size of the oxygen limits the number of atoms that can bond with an atom at one time. The increase in ionic radii of sulphur, selenium and tellurium allows for more atoms to surround the atom and the range of geometries and possible structures increases. In practice, a one-dimensional system can be a chain or thin ribbon and a two-dimensional system can be a layered solid. Structures can also be constructed from several different low-dimensional motifs as will be described in section 1.6.

1.1.1.1 One-Dimensional Chains

An example of a structure constructed from one-dimensional chains is SiS_2 (Figure 1.1). Infinite chains of edge linked SiS_4 tetrahedra run parallel to the *c* axis and are held together by van der Waals' interactions. One-dimensional chains are also observed as structural motifs within larger crystal structures.

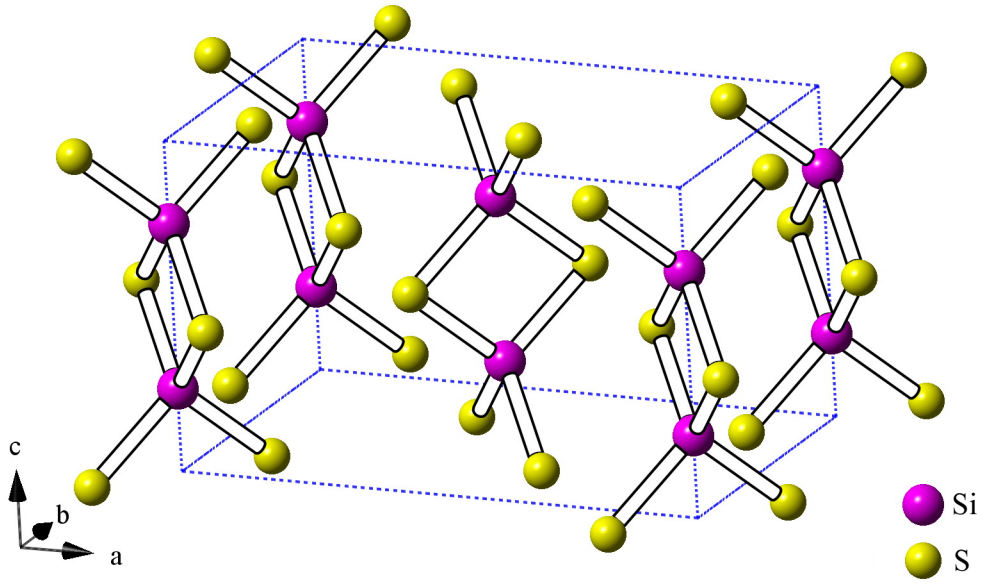

Figure 1.1: One-dimensional chains in the structure of SiS_2.

1.1.1.2 Two-Dimensional Layers

There are a wide variety of layered materials in the literature. The construction of the layers and their stacking arrangement add to the number of potential structures. An

ABC notation can be used to describe the stacking sequence of each slab within the layered structure. The first slab in the sequence is labelled A, the next B and so on. Layers in the stack that superimpose on a previously labelled slab are given the same label. This can lead to stacking sequences of slabs such as A, AB, ABC and ABABC.

TiS_2 is an example of a layered disulphide (Space group: $P\bar{3}m$) consisting of infinite layers of edge-sharing TiS_6 octahedra (Figure 1.2).[3] In the layers, TiS_6 octahedra are combined with each other tightly through strong covalent bonds, while the layers, which are superimposed on each other, are held together by van der Waals' interactions. TiS_2 would be classified as having an A stacking sequence.

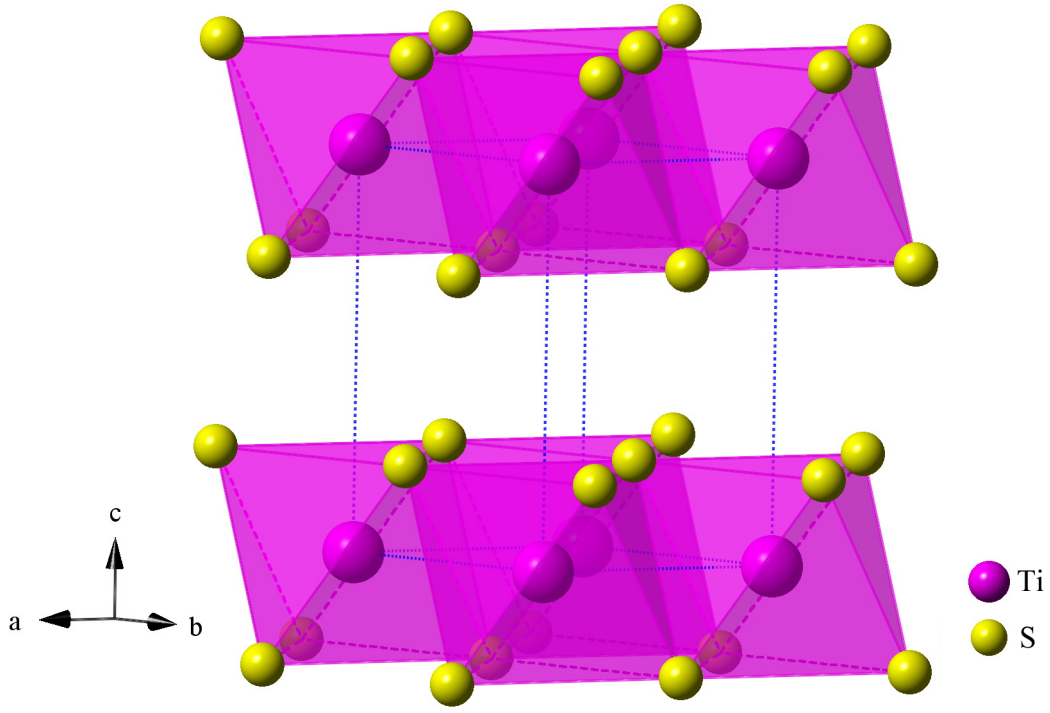

Figure 1.2: Layered structure of TiS_2.

An example of a layered sulphide where slabs are stacked AB is SnS, where corrugated layers are formed from corner-sharing SnS_3 pyramids (Figure 1.3).[4]

Materials containing two layers, each with different structures are also known. The ternary sulphide pavonite, $AgBi_3S_5$, is one such material (Figure 1.4). Layer type 1 is constructed from an AgS_6 octahedron and two edge-sharing BiS_5 square based pyramids. Layer type 2 is built from one AgS_6 and four BiS_6 edge-sharing octahedra.[5] The layers are linked through corner sharing of the octahedra in adjacent layers.

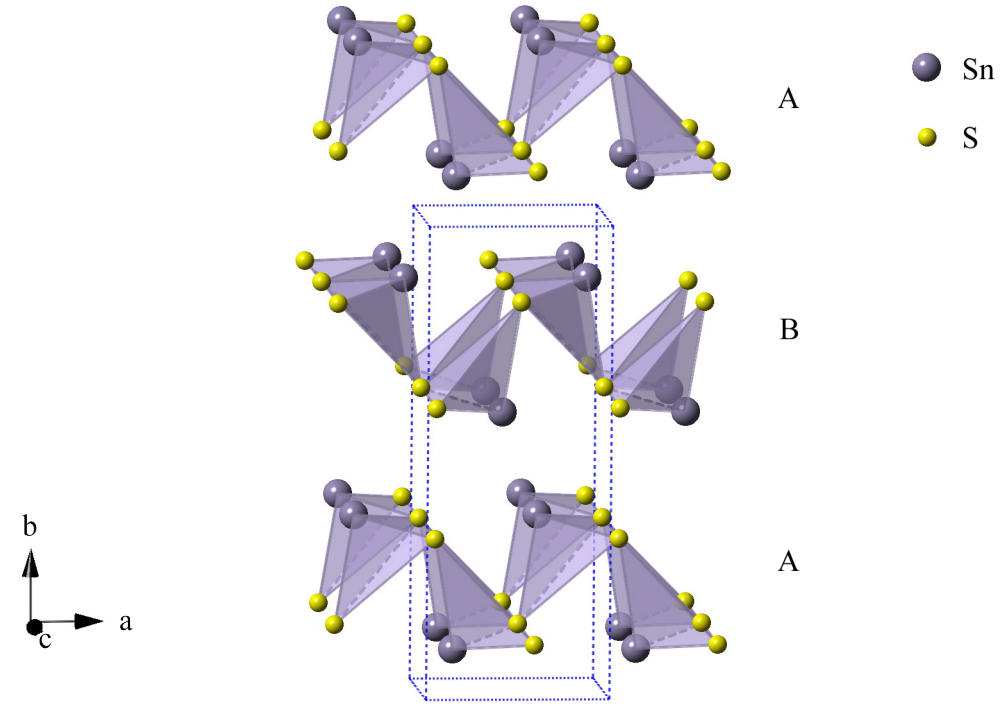

Figure 1.3: Corrugated layered structure of SnS showing AB stacking sequence.

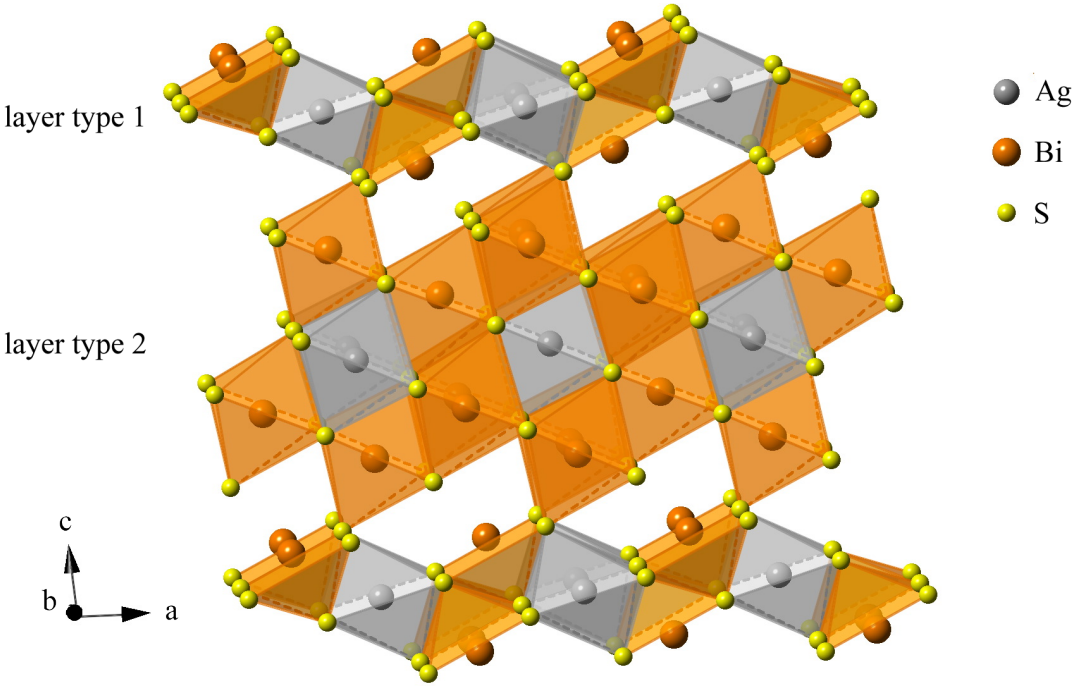

Figure 1.4: Structure of pavonite showing the two types of layer.

1.2 Magnetism

Other than in cases where diamagnetism is observed, magnetism occurs in materials that contain atoms with unpaired electrons. Because electrons have spin angular momentum and moving charges generate a magnetic field, electrons have a magnetic moment.[6] The

magnetic properties of a material can be determined by measuring the magnetisation (M). The magnetic susceptibility (χ) is the quantitative measure of the response of a material to an applied magnetic field (H) (1.1).

$$\chi = \frac{M}{H} \tag{1.1}$$

1.2.1 Diamagnetism

Diamagnetic materials have no inherent magnetic dipole, however a moment can be induced by a magnetic field. An applied magnetic field causes a circulating current and therefore a moment antiparallel to the original field. The magnetic susceptibility of a diamagnetic material is small and negative. In general, it becomes more negative as the valence electron count increases.

1.2.2 Paramagnetism

Paramagnetism occurs in materials that have magnetic moments. However, interactions between adjacent moments are weak and they point in random directions. The alignment of moments is not observed without an applied field. When a field is applied, it tries to align moments parallel to it. Positive magnetic susceptibilities are observed for paramagnetic materials. The temperature dependence of the molar magnetic susceptibility (χ_{mol}) of an ideal paramagnet follows the Curie Law (1.2). This results in a linear dependence of the inverse of the molar susceptibility against temperature, which passes through the origin.

$$\chi_{mol} = \frac{C}{T} \tag{1.2}$$

However, there can be a divergence from the ideal paramagnetic behaviour. A modification to the Curie law is the Curie-Weiss law (1.3) and this is used to describe the deviation caused by interactions between moments. This results in a linear dependence of the inverse of the molar susceptibility against temperature, which does not pass through the origin. The offset is quantified by the Weiss constant (θ). Positive and negative values of the Weiss constant indicate ferromagnetic and antiferromagnetic interactions respectively.

$$\chi_{mol} = \frac{C}{T - \theta} \tag{1.3}$$

Another type of paramagnetism is Pauli paramagnetism. When a magnetic field is applied, the conduction band splits into bands for spin up and spin down electrons. Due to differences in the magnetic potential energy between spin up and down electrons, one band moves up and one moves down in energy. The Fermi level has to be the same in both bands, meaning the lower band contains additional electrons of the spin type that occupies the lower band. Pauli paramagnetism arises from this surplus of electrons.

1.2.3 Cooperative Magnetism

Magnetic moments within a solid can order in several different arrangements (Figure 1.5). Ferromagnetic ordering describes a situation where each magnetic moment aligns in the same direction. Antiferromagnetic order describes moments being orientated in a head to tail configuration. Ferrimagnetic ordering is a type of antiferromagnetic ordering and describes a structure containing two different magnetic ions where the moments from each are different. Canting describes antiferromagnetic ordering where the alignments of the head to head and tail to tail magnetic moments are not parallel to each other.

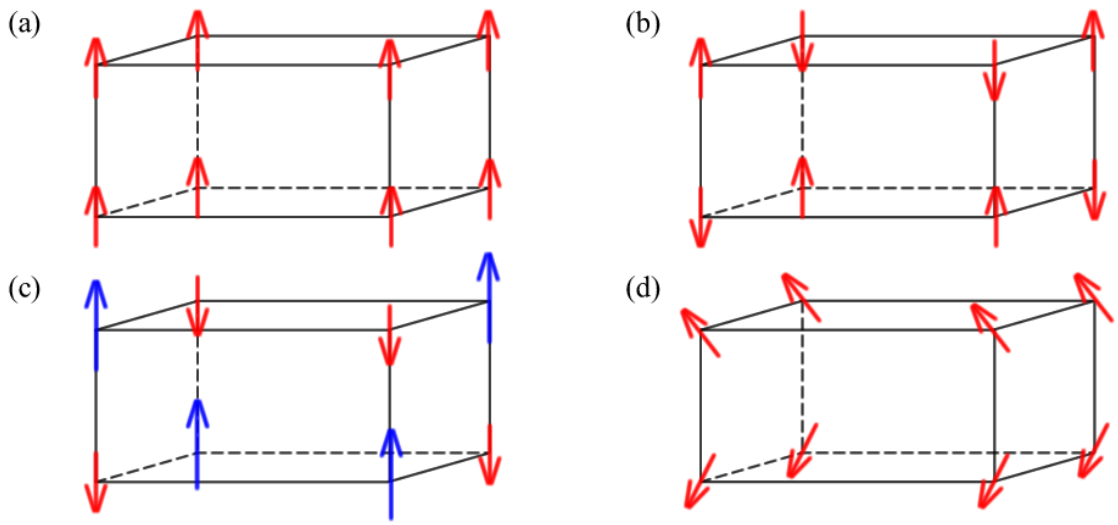

Figure 1.5: Arrangement of magnetic moments in (a) ferromagnetic, (b) antiferromagnetic and (c) ferrimagnetic ordering. (d) An example of canted antiferromagnetic moments.

Measuring the magnetic susceptibility of a material against temperature can be used to determine the magnetic ordering temperature, if any, of the material. It can also indicate the type of order within the system. Typical inverse magnetic susceptibility curves are shown in Figure 1.6. An ideal paramagnet is linear and goes through the origin. At high temperatures, both antiferromagnets and ferromagnets can show linear paramagnetic behaviour.

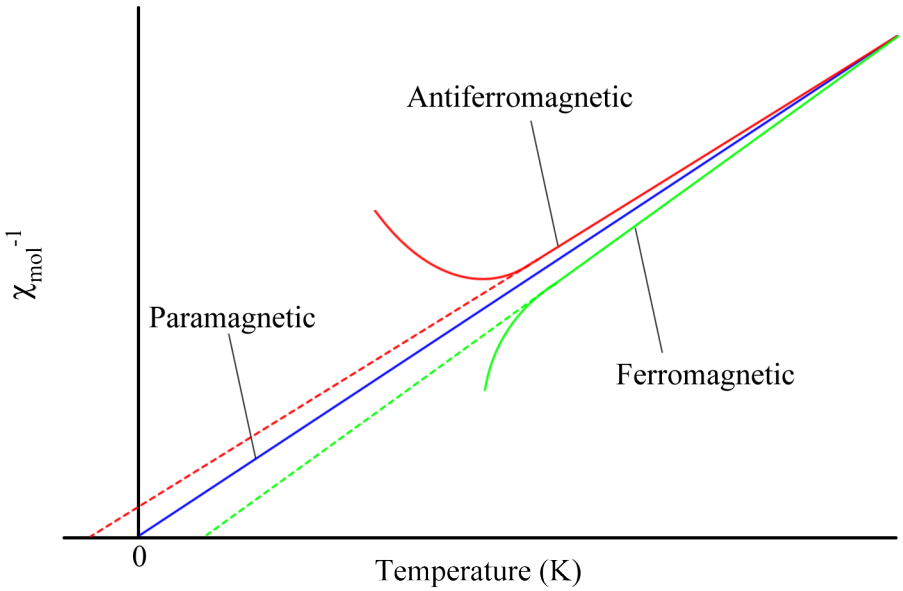

Figure 1.6: Typical plots of inverse molar magnetic susceptibility (χ_{mol}) as a function of temperature for paramagnetic, ferromagnetic and antiferromagnetic materials. Dashed lines show the divergence from the paramagnetic behaviour observed at lower temperatures.

1.3 Electronic Properties

It is important to understand the electronic properties of a material in order to explain observed experimental results. The ability to explain the electronic behaviour of a material is highly desirable.

1.3.1 Band Theory and Density of States

When compared with atoms and molecules, the number of molecular orbitals that exist in a solid is larger. This lowers the energy gap between each orbital and eventually, the gap in energy is so small, that it can be thought of as a continuous band of energy levels (Figure 1.7). Regions where energy levels are not located correspond to gaps between the bands. This leads to the concept of the density of states, N(E). The density of states

is defined as the number of allowed energy levels per unit volume of the solid in the energy range E to E + ΔE.[7]

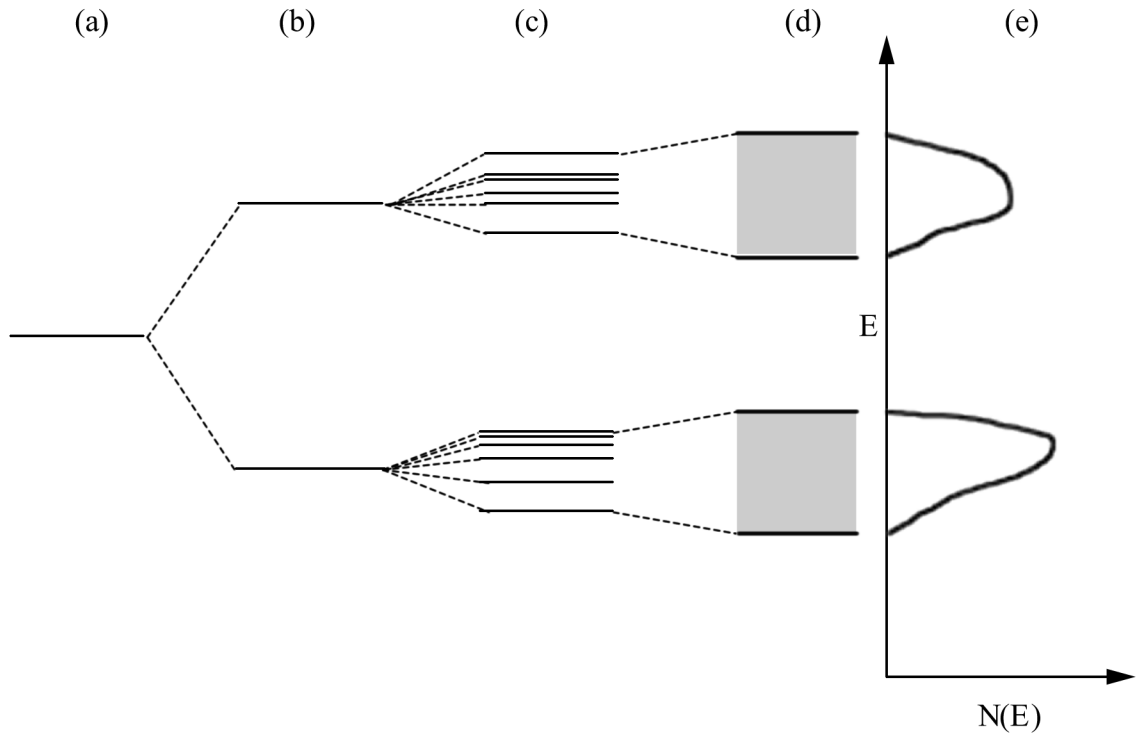

Figure 1.7: Orbital energies of (a) an atom, (b) a small molecule, (c) a large molecule and (d) a solid. (e) The density of states corresponding to (d).

The Fermi level (E_F) describes the energy level where there is a 50% probability that it is occupied. In semiconductors and insulators, the Fermi level lies in the band gap (E_g) between the valence and conduction bands. The size of the gap determines if the material is semiconducting or insulating. If electrons can be thermally excited across the band gap it is semiconducting. A schematic of conduction and valence bands of insulators, semiconductors and metals is shown in Figure 1.8. The position of the Fermi level within the density of states is an important factor in the properties exhibited by the material.

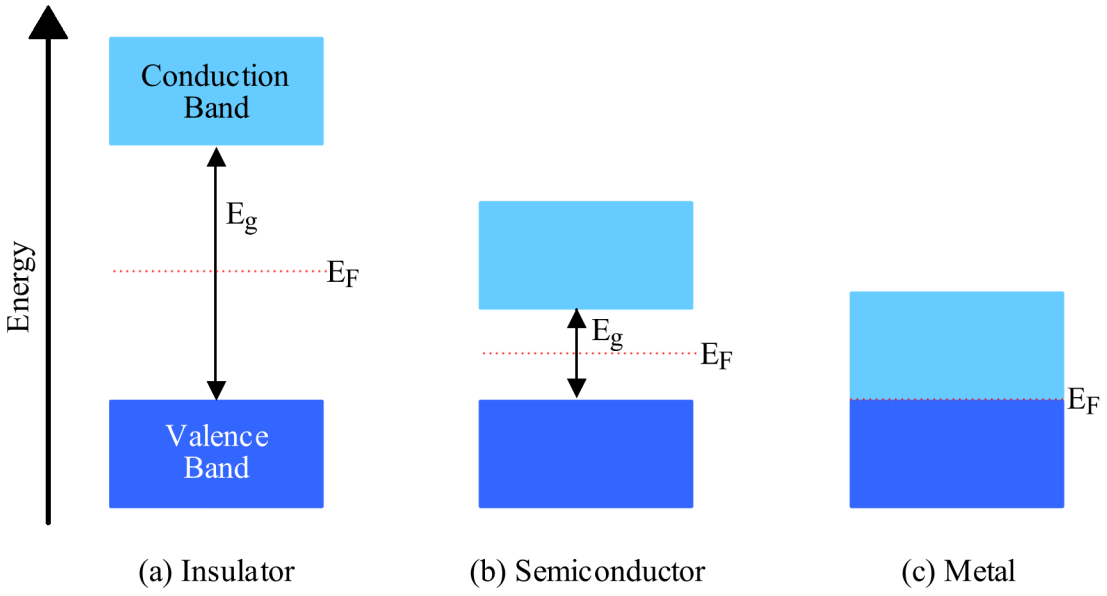

Figure 1.8: Schematic of conduction and valence bands in (a) insulators, (b) semiconductors and (c) metals.

1.3.2 Conduction Mechanisms

The electronic properties of a material are important for a wide range of applications including semiconductors and thermoelectrics. There are several possible conduction mechanisms and the method charge carriers use to move through a material has an effect on its electronic properties. It is therefore important to understand the conduction mechanism, so that new materials for specific applications can be targeted. There are two main categories of conductors: electronic and ionic. Electronic conductors describe metals, semiconductors and insulators where charge carriers are electrons and holes. Ionic conductors describe materials where the charge carriers are ions moving to neighbouring defects within the crystal structure.[8] Materials can be described as intrinsic or extrinsic conductors. Intrinsic conductors are materials where the only charge carriers are those that can be thermally (or optically) promoted across a band gap. In extrinsic conducting materials, the number of charge carriers is determined by the levels of doping.

The electrical resistivity (ρ) of many materials follows the Arrhenius law (1.4), where K_B is the Boltzmann constant. Conduction is thermally activated and charge carriers flow to the nearest available site within the structure. Materials following this type of behaviour are observed to have a linear dependence of the ln ρ when plotted against 1/T.

$$\rho = \rho_0 e^{\frac{E_g}{2K_B T}} \tag{1.4}$$

Variable range hopping is a conduction model that describes a situation where the charge carrier does not necessarily conduct to the nearest available site. Instead of only considering the distance to the site, the energy difference is also accounted for. The characteristic temperature dependence of the electrical resistivity (1.5) is dependent on the number of dimensions (d) available for conduction. Materials following this type of behaviour are observed to have a linear dependence of ln ρ when plotted against $1/T^3$ or $1/T^4$ depending on the number of dimensions.

$$\rho = \rho_0 e^{(T_0/T)^{1/(d+1)}} \tag{1.5}$$

Polarons are quasiparticles of conduction electrons (or holes) and phonons resulting from vibrations in an ionic or highly polar structure.[9] Distortion of the lattice is caused by the passage of polarons through the material. Polarons with a radius less than the unit cell of the crystal structure are termed as 'small' and polarons are 'large' if the radius is bigger than the unit cell dimensions. Polaronic conduction is different for each polaron size. Large polarons tend to behave like band conductors, whereas with small polarons, the charge carriers tend to be localised.

1.3.3 Metal to Non-Metal Transitions

The transitions observed in some materials between metallic conduction and non-metallic conduction is an interesting phenomenon. There are several possible types of transition, which can be induced by pressure and temperature changes as well as chemical substitution.

Metal to non-metal transitions can be induced by altering the population of electrons in bands within the density of states. This changes the location of the Fermi level. Substitution of atoms within a structure for an electron deficient one depopulates bands and lowers the Fermi level, while the reverse is true if substitution is with a more electron rich element. If the material's band structure contains band gaps, the depopulation or population of the band could result in the emptying of bands above or filling of bands below the gap. This would push the Fermi level into the band gap and

the material would become non-metallic. Temperature-induced transitions are also possible in materials where band gaps are situated close to the Fermi level. Thermal excitations of electrons allow for previously unpopulated bands to be filled. Again this changes the position of the Fermi level and can induce a metal to non-metal transition if it moves to within the band gap.

The interaction between electrons and holes within a material plays a role in the electrical conductivity of a solid. In certain cases band theory breaks down and materials that should be conductive become insulating. Mott insulator-metal transitions occur in materials with narrow bands in the vicinity of the Fermi level.[8] An insulating state can be obtained when the kinetic energy is lower than the potential energy due to repulsion of electrons in a partially filled band. Coulombic interactions between free electrons and free holes draw them together preventing either from conducting. When the number of charge carriers (n_c) in the system is large, electrons and holes interact through screened Coulomb interactions. If these interactions are weak, a transition from a material with no free charge carriers to one with a large number available can be observed. The Mott criterion describes the onset of metallic behaviour for this type of material. It relates the number of charge carriers (n_c) to the to the Bohr radius (a_H) as shown in (1.6). Below this criteria solids are non-metallic in the Mott formulation.

$$n_c^{1/3} a_H \simeq 0.25 \tag{1.6}$$

Electron-electron repulsion and the localisation of electrons within a structure have an effect on the electronic properties of a solid. The Hubbard model assumes that the important repulsive effects are between two electrons on the same atom.[7] The effect of repulsion can make a half-filled band insulating. Mott-Hubbard splitting is observed in materials with poor orbital overlap, which has the effect of localising electrons on each atom. The Hubbard U describes the energy difference between two sub bands created by localisation of electrons. Hubbard U is calculated from the ionisation energy (I) minus the electron affinity (A). The ionisation energy describes the energy required for an electron to move from orbitals on one atom to another. The addition of an electron into an occupied site releases energy through the electron affinity. As orbital overlap improves, the bandwidth (W) increases and at W = U no gap exists. The Hubbard

criterion for metallic behaviour is therefore W > U. Orbital overlap can be improved by increasing the pressure or substitution of elements within the framework.

The Herzfeld criterion is used to predict metal-insulator transitions in wide band gap semiconductors and insulators.[10] It states a material is metallic when $R/V \geq 1$ where R is the molar refractivity of the atomic species in the gaseous state and V is the molar volume in the condensed state.

1.3.4 Half-Metals

A half-metal is a magnetically ordered solid where the spins of electrons are required to be fully polarised at the Fermi level. For electrons of one spin orientation, the material is metallic, but for the opposite spin, it is semiconducting or insulating. Depending on the conduction behaviour of each spin polarised state, half-metals can be placed into one of ten categories[11] (Table 1.1).

Table 1.1: Summary of the classification of half-metals.[11]

Type	*DOS*	*Conductivity*	$\uparrow e^-$ *at* E_F	$\downarrow e^-$ *at* E_F
I_A	half-metal	metallic	itinerant	none
I_B	half-metal	metallic	none	itinerant
II_A	half-metal	non-metallic	localised	none
II_B	half-metal	non-metallic	none	localised
III_A	metal	metallic	itinerant	localised
III_B	metal	metallic	localised	itinerant
IV_A	semimetal	metallic	itinerant	localised
IV_B	semimetal	metallic	localised	itinerant
V_A	semiconductor	semiconducting	few, itinerant	none
V_B	semiconductor	semiconducting	none	few, itinerant

1.4 Thermoelectricity

The area of thermoelectricity is currently undergoing a period of renewed interest. This is due to a range of new semiconducting materials being discovered and the potential use of thermoelectricity in power generation, waste heat recovery systems and

refrigeration. The performances of the thermoelectric properties of materials are quantified by the dimensionless thermoelectric figure of merit (ZT). The Seebeck coefficient (S), the electrical resistivity (ρ) and the thermal conductivity (κ) are used to calculate ZT at a given temperature (1.7).

$$ZT = \frac{S^2 T}{\rho \kappa} \tag{1.7}$$

The Seebeck coefficient defines the voltage produced by placing a temperature gradient across a sample. Positive and negative values indicate that the dominant charge carriers are holes and electrons respectively. The electrical resistivity describes how effectively charge carriers travel through a material. The thermal conductivity describes the material's ability to transfer heat through it. There are two components to the thermal conductivity: the electronic (κ_e) and lattice contributions (κ_L). The electronic and lattice contributions describe the transport of thermal energy by electrons and phonons respectively. The lattice contribution is not affected by the numbers of charge carriers, but by the phonon scattering ability of the material. A phonon can be described as a quantum of lattice vibration, where the lattice oscillates at a regular frequency. The disruption of this regularity is called phonon scattering. There are three main types of phonon scattering. Alloy scattering occurs when a vibration through a material is affected by an irregularity in the material. A phonon travelling along a one-dimensional chain will oscillate uniformly. If the vibration encounters an irregularity, such as a different mass, the uniformity of the oscillation is disrupted, causing the phonon to be scattered. Rattling occurs in materials with cage like structures in their framework. These cages can trap ions or molecules inside them. When a phonon encounters a trapped ion, energy is given to it to rattle around in the cage and the phonon is diffused. Interface scattering occurs when a vibration meets interfaces inside materials. These interfaces can exist between individual particles or inside the structure of a material. Dense pellets are required to minimise the effects of scattering due to particle interfaces. Umklapp scattering is a phonon-phonon scattering process where the phonon momentum is not conserved. This type of phonon scattering is one of the limiting factors in high temperature thermal diffusivity.

For a material to have a high thermoelectric figure of merit, it requires a high Seebeck coefficient, a low electrical resistivity and a low thermal conductivity. However, high Seebeck coefficient and low thermal conductivity are typically found in insulators, while low electrical resistivity is found in metals, which leads to a conflict between the desired properties. As a compromise, efforts have been focused on investigating heavily doped semiconductors as potential thermoelectric materials. The dependence of three key properties for a thermoelectric material and the number of charge carriers is shown in Figure 1.9.

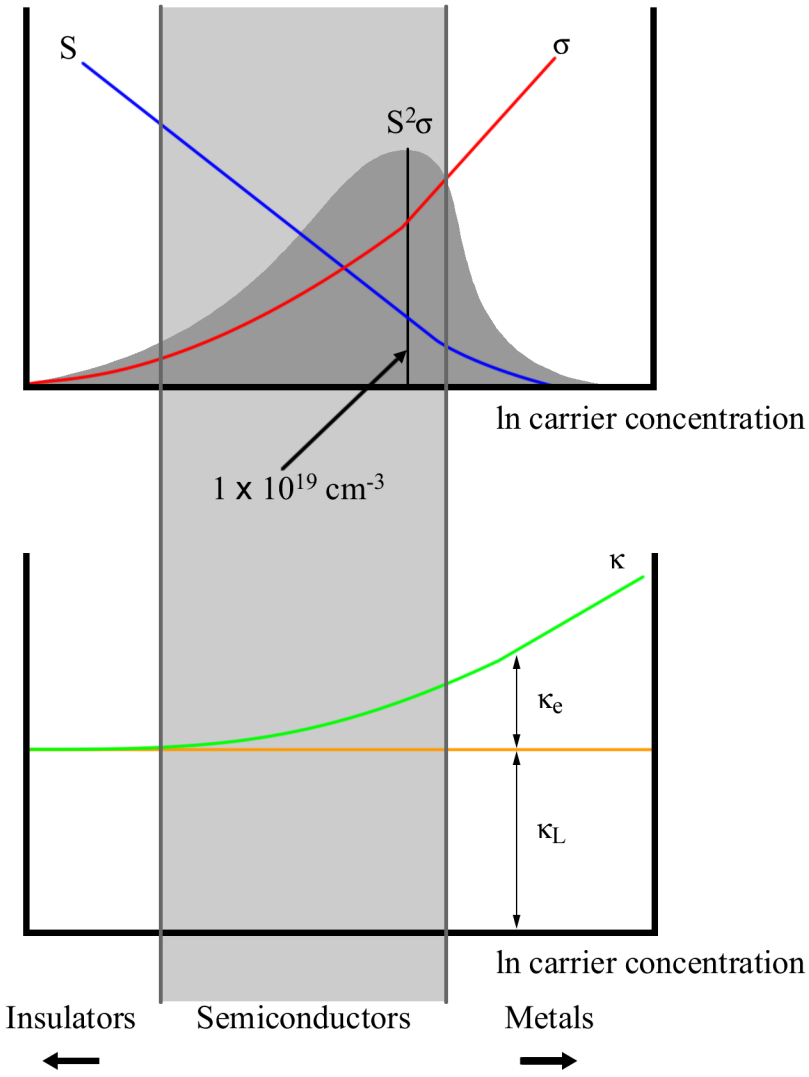

Figure 1.9: The effect of the number of charge carriers in a solid in relation to the Seebeck Coefficient (S), the electrical conductivity (σ) and the electronic (κ_e) and lattice (κ_L) contributions to the thermal conductivity (κ).

There are several strategies that are being used in thermoelectrics that could lead to the discovery of materials with an improved ZT and increase the optimal operating temperature range. Key strategies are outlined below. Chemical tuning of the band structure and the Fermi level has been investigated to maximise the Seebeck coefficient and minimise the electrical resistivity. Substitution of elements within the structure to create defects, which increases phonon scattering, has been investigated as a method to reduce the lattice thermal conductivity. Clathrates (A_8E_{46}, with A = Na, K, Ba; E = Al, Ga, In, Si, Ge, Sn) have cage like structures, which contain ions trapped inside them. These and similar materials have been studied in an attempt to reduce the lattice thermal conductivity, where the vibrations or 'rattling' of the ions inside the cage scatters phonons. Utilising low-dimensionality in thermoelectricity has had two main approaches.[12] The first is the preparation of solids with nanoscale units. This introduces quantum confinement effects into the system and hopefully improves the power factor, $S^2\sigma$. The second, is the insertion of low-dimensional motifs into bulk materials in an attempt to reduce the lattice contribution of the thermal conductivity.[13]

1.4.1 Thermoelectric Materials

The thermoelectric properties of a wide range of semiconducting materials have been investigated. Known thermoelectric materials are only effective over a narrow range of temperatures (Figure 1.10). Therefore, different materials are needed depending on the required operating temperature. Materials with working temperatures up to and around 400K, such as bismuth telluride and its alloys, are grouped together.[14] An intermediate range of 500K - 900K contains lead telluride alloys[14] and TAGS[15]. In the highest temperature range, 1000K to 1300K, Si-Ge alloys[16] are currently used.

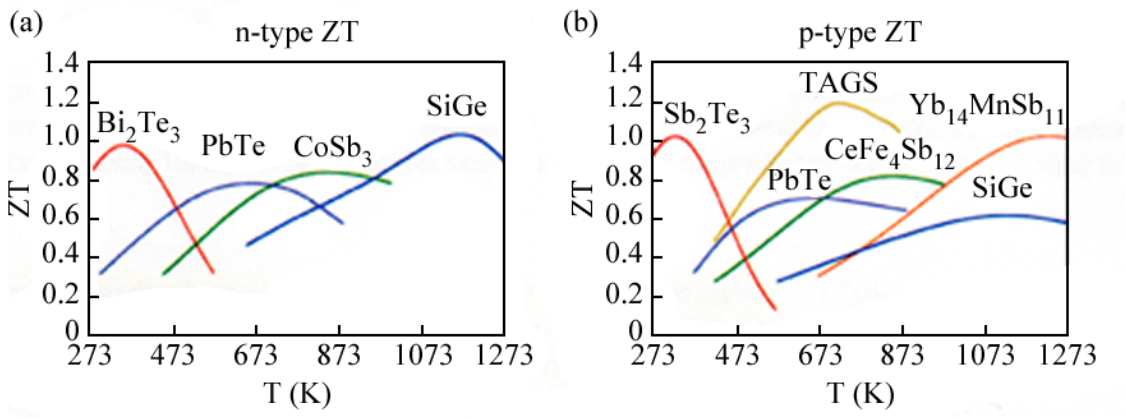

Figure 1.10: ZT as a function of temperature for (a) n-type and (b) p-type thermoelectric materials.[14]

The development of new thermoelectric materials, which are more effective, cheaper and less toxic than those currently in commercial use is highly desirable. Table 1.2 shows some thermoelectric materials along with the figure of merit and optimum operating temperature range.

Table 1.2: Bulk thermoelectric materials, their maximum ZT, dominant charge carrier and optimal temperature range.

Compound	*ZT*	*Type of Semiconductor*	*Optimal Temperature*
Bi_2S_3[17]	~0.05	n-type	200 K – 300 K
$(Sb_{0.8}Bi_{0.2})_2Te_3$[14]	~1.0	p-type	300 K – 400 K
$Bi_2(Te_{0.8}Se_{0.2})_3$[14]	~1.0	n-type	300 K – 400 K
$Bi_2Te_{3-x}Se_x$[18]	~1.2	n-type	300 K – 400 K
$Bi_{2-y}Sb_yTe_3$[18]	~1.2	p-type	300 K – 400 K
TiS_2[19]	~0.23	n-type	425 K
β-Zn_4Sb_3[20]	~1.3	p-type	670 K
PbTe[14]	~0.8	n-type	~700 K
TAGS*[15]	~1.2	p-type	~700 K
Bi_2S_3-0.5%$BiCl_3$[21]	0.6	n-type	760K
LAST-m*[22]	2.1	n-type	800 K
$Sr_8Ga_{15.5}In_{0.5}Ge_{30}$[23]	0.72	n-type	800 K
$CoSb_3$[14]	~0.8	n-type	~850 K
$NdGd_{1.02}S_3$[24]	0.51	n-type	950 K
$Cu_4Mo_6S_8$[25]	0.4	p-type	950 K
Na_xCoO_2[26]	0.5	p-type	973 K
$Si_{0.7}Ge_{0.3}$[16]	~ 0.6	p-type	~1100 K
$Yb_{14}MnSb_{11}$[27]	~ 1.0	p-type	~1200 K
$Zn_{0.98}Al_{0.02}O$[28]	0.3	n-type	1273 K

* TAGS = $(GeTe)_{0.85}(AgSbTe_2)_{0.15}$; Last-m = $AgPb_{18}SbTe_{20}$.

1.4.1.1 Bismuth Telluride

The most widely used commercial thermoelectric materials are alloys of Bi_2Te_3 and Sb_2Te_3.[14] They were originally investigated as thermoelectric materials in the 1950s, and at the time were the highest efficiency thermoelectric materials at near room

temperatures. Over fifty years later, these materials still posses a high ZT, even when compared with modern materials. The structure of Bi_2Te_3 (Space group $R\bar{3}m$) consists of layers of edge-sharing $BiTe_6$ octahedra, which lie perpendicular to the *c* axis (Figure 1.11).[29] Slabs of double layers of octahedra are stacked in an ABC sequence.

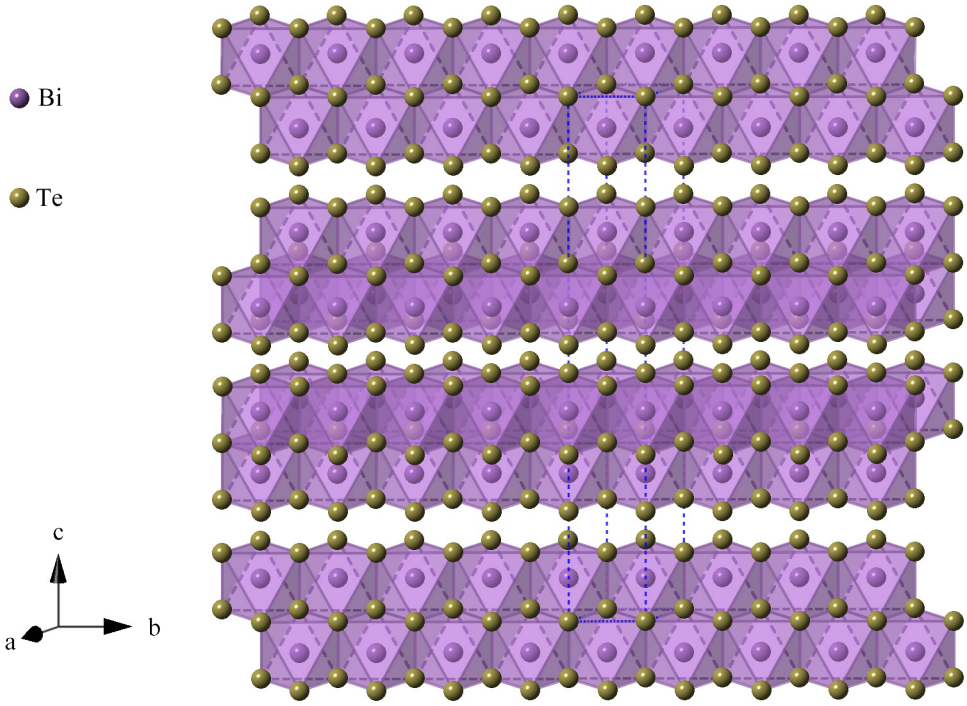

Figure 1.11: Layered structure of Bi_2Te_3.

Several bismuth telluride based compounds have now been prepared and evaluated. Analogues where bismuth has been substituted by antimony[29] and iron,[30] and tellurium for selenium[31] have also been investigated. Recent innovations include films, 0.1 mm thick, made from $Bi_{2-y}Sb_yTe_3$ and $Bi_2Te_{3-x}Se_x$ alloys[18] and one-dimensional Bi_2Te_3 nanotubes[32]. P-type Bi_2Te_3/Sb_2Te_3 exhibits the highest ZT value of any material to date: at 300K the ZT is observed to be ~2.4.[33]

1.4.2 Sulphide Thermoelectric Materials

Sulphides have been investigated as possible thermoelectric materials. Sulphur has the benefit of being cheaper and less toxic than tellurium and selenium, which is desirable in both economic and environmental terms. However, sulphides have been observed to produce the best thermoelectric performance at higher temperatures. Finding sulphides with good thermoelectric properties at ambient temperatures is therefore desirable.

1.4.2.1 Bi_2S_3

The sulphide analogue of the commercial thermoelectric Bi_2Te_3 has been investigated for its thermoelectric potential. Although its stoichiometry is identical to the tellurium analogue, their structures are different (Figure 1.12).[34] The structure is constructed from one-dimensional ribbons of Bi_2S_3. These ribbons are built from two edge-sharing BiS_5 square based pyramids and two corner-sharing BiS_3 pyramids, which extend infinitely along the *c* axis.

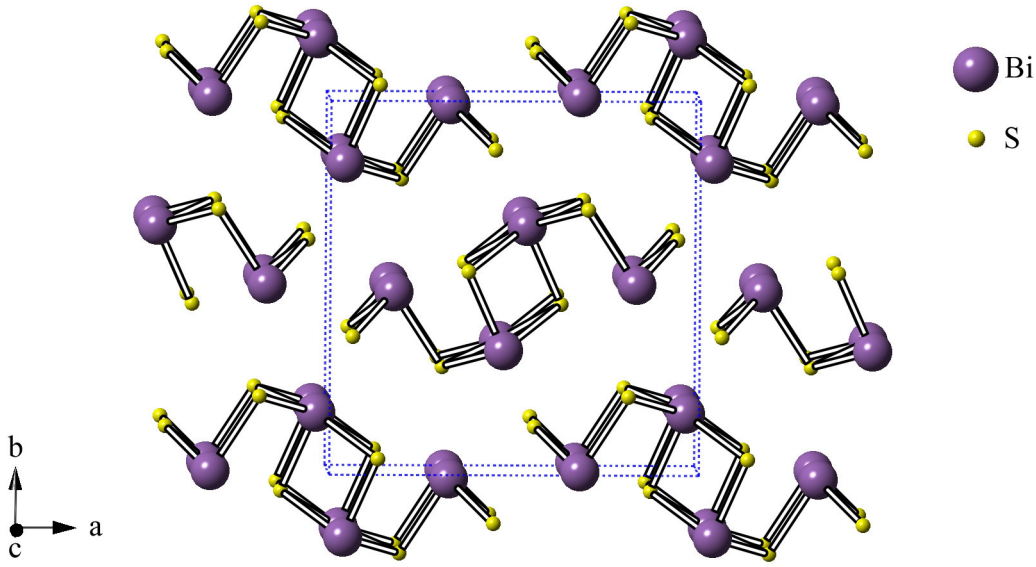

Figure 1.12: Structure of Bi_2S_3.

Undoped Bi_2S_3 is a wide gap semiconductor (1.3 eV), with a large negative Seebeck coefficient around -325 μV K^{-1} at 300 K.[17] The electrical resistivity has been shown to be dependent on the stoichiometry of sulphur in the material.[35] Sulphur vacancies in sulphur deficient samples assist with conduction. As these vacancies are filled, the electrical resistivity increases. When compared to the commercial thermoelectric Bi_2Te_3, the thermal conductivity is observed to be 25 % lower for the sulphide analogue.[17] Despite the promising values of Seebeck coefficient and thermal conductivity, the overall value of ZT around 0.05 is rather small.

Several methods of doping Bi_2S_3 have been investigated in an attempt to improve ZT. Doping with $BiCl_3$ at a 0.5% by mole level saw an improvement in ZT over the entire measured temperature range with a maximum ZT around 0.6 observed at 760 K.[21]

1.4.2.2 PbS

The commercial usage of PbTe has led to the thermoelectric properties of the sulphide PbS to be studied. PbS is an n-type semiconductor with a ZT of 0.31 at 723 K.[36] Doping with small levels of sodium (1-4 %) has shown that the material becomes more conductive and p-type Seebeck coefficients are observed. While the values of the Seebeck coefficient are lower than the parent compound, a ZT = 0.54 has been reported for the phase $Pb_{0.975}Na_{0.025}S$. Further nanostructuring of this doped phase with CaS and SrS has also been investigated. Values of ZT = 0.73 and 0.72 were observed at 723 K with the addition of 3% SrS and CaS respectively. These were shown to increase to ZT = 1.22 and 1.15 at 923K

1.4.2.3 Titanium Disulphide

Solids based on TiS_2, the structure of which is described in section 1.1.1.2, have been investigated for thermoelectric applications. A ZT ≈ 0.23 for TiS_2 at 425 K has been reported.[19] Intercalation of copper between the TiS_2 layers in the series Cu_yTiS_2 ($y \leq 0.1$), offered a reduction in the electrical resistivity and the lattice thermal conductivity, but also in the Seebeck coefficient. Overall, an improvement in the thermoelectric figure of merit above 650 K was observed, with a maximum ZT = 0.45 at 800 K for y = 0.1. Substitution of sulphur for selenium has also been investigated.[37] With the exception of x = 0.5, the replacement of sulphur in the solid solution $TiS_{2-x}Se_x$ ($0 \leq x \leq 2$) provided materials with lower ZT than the TiS_2 end member. The ZT for x = 0.5 was higher at all temperatures with values of 0.24 and 0.40 at 425 K and 700 K respectively. This result was achieved by an approximately 25% reduction of the thermal conductivity from 2.09 W m^{-1} K^{-1} for the TiS_2 end member to 1.46 W m^{-1} K^{-1} for x = 0.5. Further substitution reduced the electrical resistivity but the Seebeck coefficient was reduced significantly which led to low values of ZT.

Preparation of misfit layered sulphides of $(TiS_2)_2(MS)_{1.2}$ (M = Bi, Sn) have been investigated as a method of reducing the thermal conductivity of the material.[38] A ZT of 0.37 was observed for *M* = Sn at 700 K. Further substitution of the titanium and *M* sites (*M* = Bi) has been studied in an attempt to lower the charge carrier concentration.[39] The substitutions studied did lower the charge carrier concentration, however ZT decreased primarily due to the reduction of the Seebeck coefficient. $(Ti_{0.95}Mg_{0.05}S_2)_2(BiS)_{1.2}$ was observed to have a ZT ≈ 0.15 and $(TiS_2)_2(Bi_{0.9}Ca_{0.1}S)_{1.2}$ a ZT ≈ 0.22 at 700 K.

1.4.2.4 Chevrel Materials

Sulphides with the Chevrel structure, $M_xMo_6S_8$ ($1 \leq x \leq 4$), have been investigated for use as high temperature thermoelectric materials. The Chevrel structure consists of Mo_6S_8 clusters, which form a network of three-dimensional channels through the material (Figure 1.13). The clusters are constructed from octahedra of molybdenum with each of the eight faces capped by a sulphur atom.

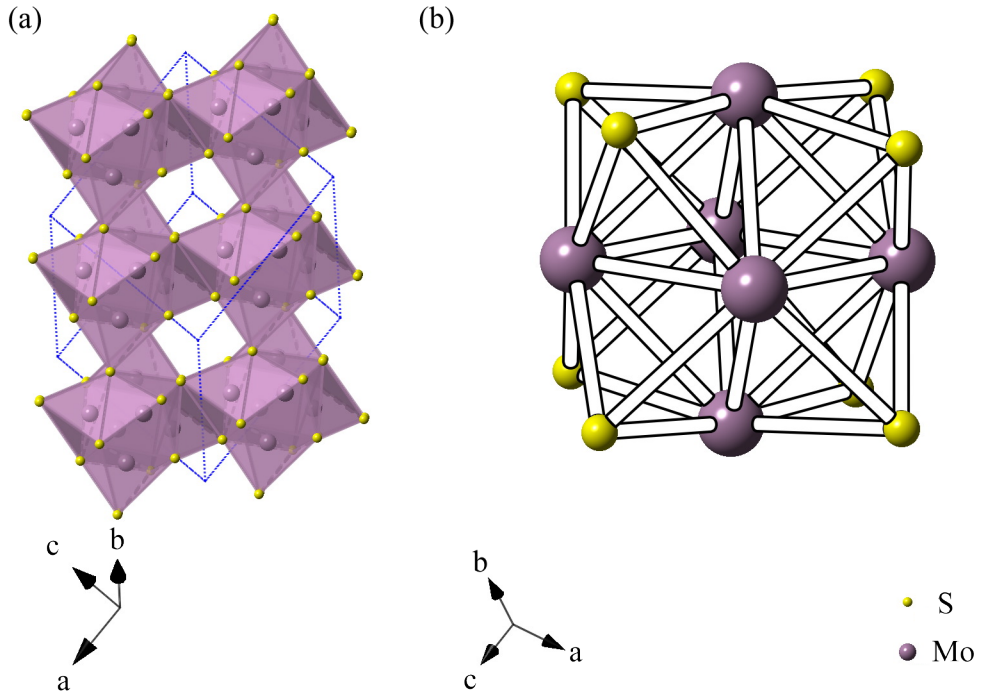

Figure 1.13: Structure of the Chevrel phase showing (a) the channels between the clusters and (b) a single cluster.

A wide variety of metals (*M*) have been shown to intercalate into these channels. The thermoelectric properties of $Cu_xMo_6S_8$ ($2 \leq x \leq 4$) have been investigated.[25] Increasing the quantity of copper in the channels, increased the Seebeck coefficient and electrical resistivity, but lowered the thermal conductivity, with the overall effect of a higher ZT. A maximum ZT = 0.4 at temperatures at 950 K was determined for sample with x = 4.

1.4.2.5 Rare Earth Sulphides

Rare Earth sulphides based on a defect Th_3P_4 structure have been shown to have good high temperature values of ZT. Materials of the general formula $LnGd_{1+x}S_3$ (*Ln* = Nd,[24] La and Sm[40]) have been investigated because of their self-doping abilities and low

thermal conductivities. Doping levels of x = 0.02 gave the best results with ZT of 0.51, 0.4 and 0.3 at 950 K for *Ln* = Nd, La and Sm respectively.

1.5 Structure – Property Relationships in Low-Dimensional Materials

The effect of low-dimensionality on the physical properties of a material is a topic of interest. The confinement of electrons and phonons is a key difference between low-dimensional and three-dimensional solids. In a three-dimensional solid, these have a free range of movement through the system. However, restrictions are enforced in low-dimensional systems where the number of degrees of freedom for electrons or phonons is restricted to less than three dimensions.[41] This anisotropic behaviour also means low-dimensional materials exhibit different physical properties along different axes of the structure. Several areas are discussed below.

Magnetic ordering in low-dimensional structures is a topic of interest. If magnetic atoms exist in a low-dimensional motif, the interactions between them will be relatively strong. However, interactions between neighbouring chains or layers will be relatively weak. This could lead to materials where localised correlations are initially observed before three-dimensional ordering is complete. One such material is the Ba_2CoS_3.[42] The structure is constructed from chains of vertex-sharing CoS_4 tetrahedra with Ba ions occupying trigonal prismatic inter-chain sites where one face is capped by a seventh sulphur atom. As the temperature is decreased, the $1/\chi^2$ dependence deviates away from Curie Weiss behaviour indicating the onset of localised intra-chain antiferromagnetic ordering. However at 46 K, there is a noticeable change in the temperature dependence. This corresponds to the onset of long-range inter-chain antiferromagnetic ordering.

Low-dimensionality in a structure also affects the density of states by introducing more structure (Figure 1.14). The curvature of the density of states is much sharper in low-dimensional materials. It goes from a typically parabolic curve for three-dimensional solids, to a stepped structure for two-dimensional structures and finally sharp peaks for one-dimensional materials. The distribution of the density of states is also affected. In a one-dimensional chain, the density of states is largest at the edge of the band. This differs from a three-dimensional system where the density of states is lowest nearest the edge of the band.

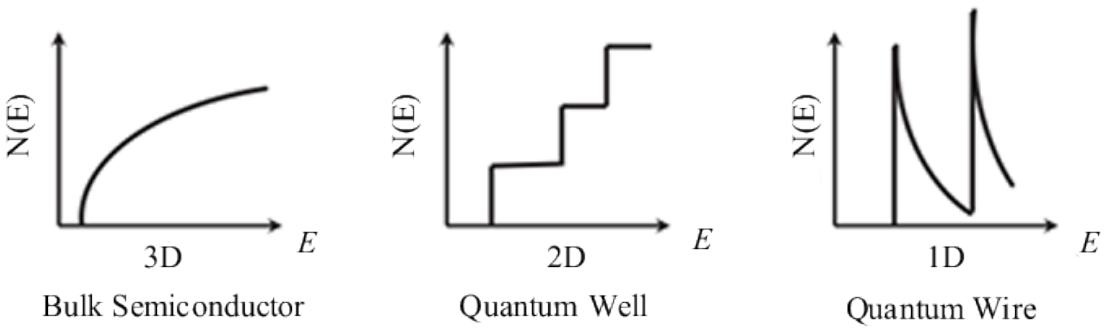

Figure 1.14: Density of States for bulk three-dimensional crystalline semiconductors, two-dimensional quantum wells and one-dimensional quantum wires.[12]

Band structures for one-dimensional SiS_2,[43] two-dimensional TiS_2[44] and three-dimensional MgS[45] are shown in Figure 1.15. This shows the increase in the structure of the bands as the dimensionality of the material is lowered. The sharpness of the bands is an important factor in determining the electronic properties. For example, the magnitude of the Seebeck coefficient increases with sharper bands. The sharp bands increase asymmetry of the hot and cold electron transport. This results in a large transport energy and a large number of charge carriers, therefore a larger Seebeck coefficient.[46]

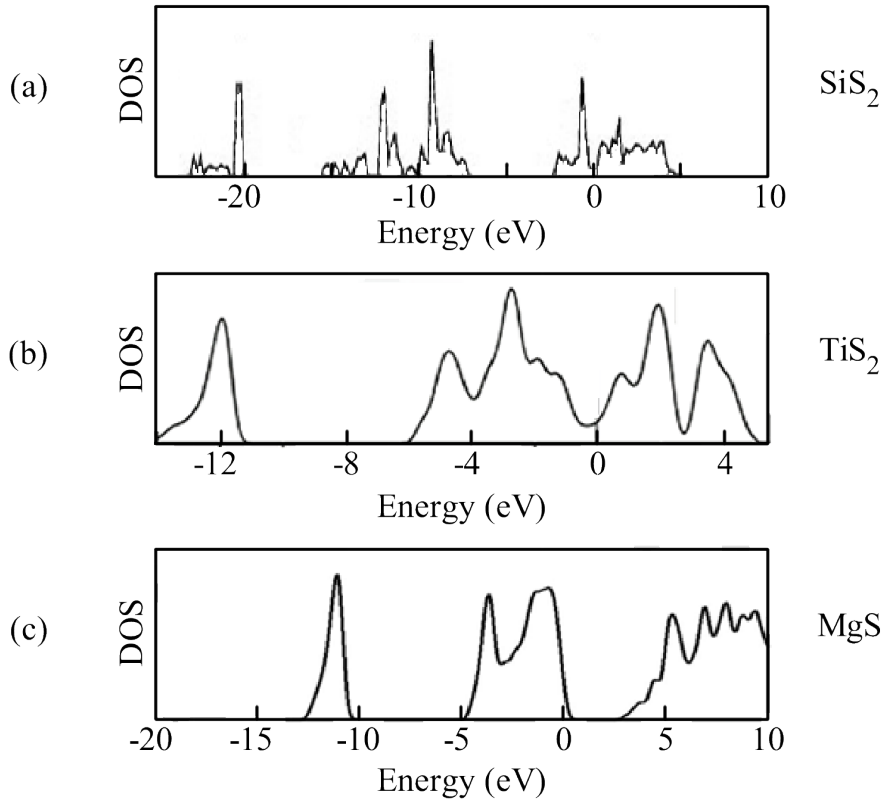

Figure 1.15: Reported Density of States for (a) one-dimensional SiS_2,[43] (b) two-dimensional TiS_2,[44] and (c) three-dimensional MgS.[45]

The conduction of charge carriers is affected by the confinement of electrons within low-dimensional structural motifs in a solid. For example, this could lead to metallic conduction within a layer and insulating properties between them. The thermal transport properties can also be affected by low-dimensionality. The structural features of the material can induce phonon scattering, which arises from scattering at interfaces between the low-dimensional structural motifs. This scattering reduces the lattice contribution of the thermal conductivity.

1.6 Materials Investigated in this Thesis

The sections below introduce the three families of materials that have been investigated during this work. The structures of the Jamesonite, Shandite and $In_2Sn_3S_7$ families of materials will be described. Previously reported physical property data will also be discussed.

1.6.1 Jamesonite and Benavidesite

Jamesonite is a naturally occurring mineral with the formula $FePb_4Sb_6S_{14}$. The structure (Figure 1.16) consists of rods of $(Pb_4Sb_6S_{14})_\infty$ and one-dimensional chains of FeS_6 edge-sharing octahedra. Both these structural motifs extend along the *c* axis and their arrangement leads to anisotropy within the structure due to van der Waals' gaps between adjacent rods. Synthetic Jamesonite differs from natural Jamesonite in that there can be small levels of substitution of iron for another transition-metal element such as cobalt, manganese or silver. Synthetic Jamesonite has none of these trace impurities. Benavidesite ($MnPb_4Sb_6S_{14}$) is a structural analogue of Jamesonite, where manganese replaces iron in the MS_6 octahedral chains. The existence of series of solid solutions using Jamesonite and Benavidesite as end members has been reported.[47] However, no physical property or magnetic measurements have been recorded for mixed transition-metal phases.

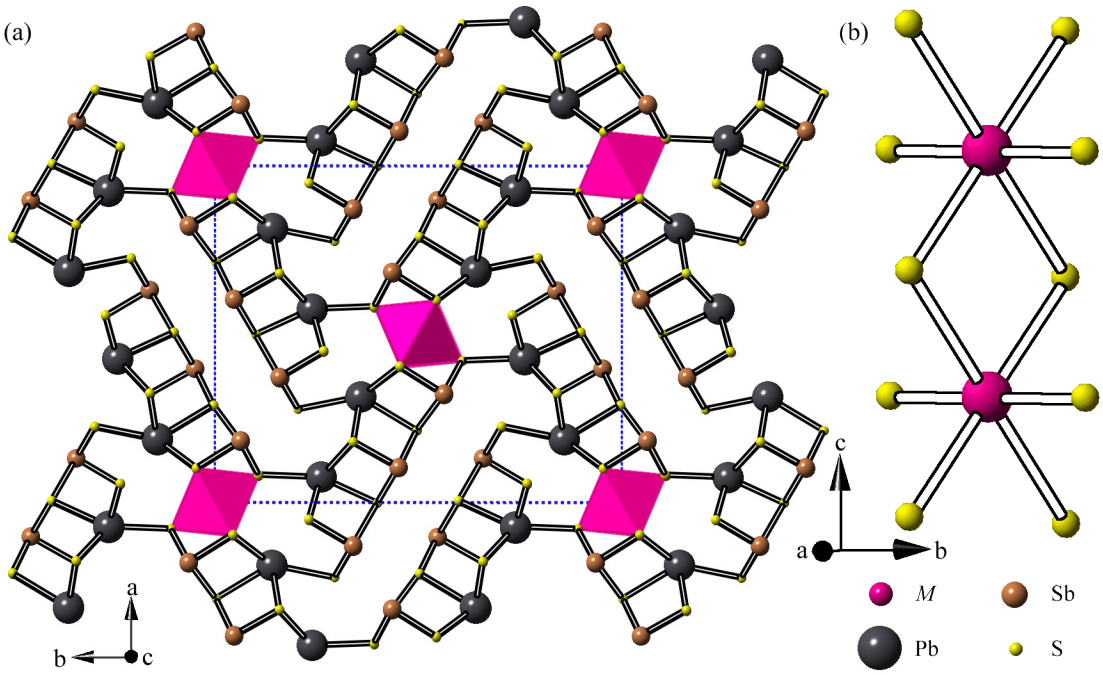

Figure 1.16: Structure of (a) MPb$_4$Sb$_6$S$_{14}$ (M = Fe, Mn) projected in the *ab* plane and (b) chains of edge-sharing MS$_6$ octahedra. Space group $P2_1/a$.

Band structure and density of state calculations of Jamesonite (Figure 1.17)[48] show that Fe(3d) states arising from two Fe atoms within the unit cell are partially filled with a small gap between the t_{2g} and e_g states. Unoccupied Sb(5p) states lie above the Fe d states, while below, bands from the Pb(5s), Sb(5s) and S(3p) states are fully occupied. As the Fe electrons are localised, Jamesonite can be described as a Mott insulator.

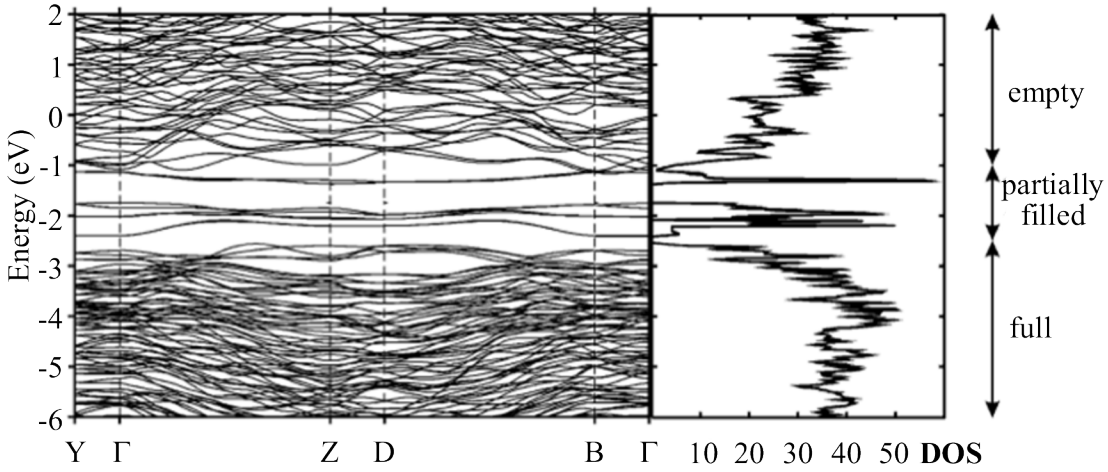

Figure 1.17: Band structure and Density of States of Jamesonite as determined by Derakhshan et al.[48]

A sample collected from an unknown deposit in Siberia has been used to investigate the magnetic structure of natural Jamesonite.[49] A canted antiferromagnetic structure was observed at 1.4 K with a magnetic moment of 3.3 μ_B. Benavidesite has been reported to order magnetically with a moment of 3.2 μ_B.[50] These are both lower than the spin-only values of 4 μ_B and 5 μ_B expected for Jamesonite and Benavidesite respectively. It has also been observed that Benavidesite has a different magnetic structure to that of Jamesonite. For the manganese analogue, the moments are aligned parallel to the *b* axis. Table 1.3 shows the magnetic structure and magnitude of the moments in the x, y and z directions for Jamesonite and Benavidesite.

Table 1.3: Magnetic structures of Jamesonite[49] and Benavidesite[50] (nuclear structure described in space group $P2_1/a$).

Atom[a]	*atomic coordinates*			*M = Fe*				*M = Mn*			
	x	*y*	*z*	M_x	M_y	M_z	M (μ_B)	M_x	M_y	M_z	M (μ_B)
M(1)	0	0	0	-0.5(2)	1.51(1)	2.8(1)	3.3(1)	0	3.2(1)	0	3.2(1)
M(2)	0.5	0.5	0	-0.5(2)	-1.51(1)	2.8(1)	3.3(1)	0	3.2(1)	0	3.2(1)
M(3)	0	0	0.5	0.5(2)	-1.51(1)	-2.8(1)	3.3(1)	0	-3.2(1)	0	3.2(1)
M(4)	0.5	0.5	0.5	0.5(2)	1.51(1)	-2.8(1)	3.3(1)	0	-3.2(1)	0	3.2(1)

[a] Positions derived from the 2(e) site taking into account the doubling of the c axis in the magnetic structure when compared to the nuclear structure.

The series $Fe_{1-x}Mn_xPb_4Sb_6S_{14}$ ($0 \leq x \leq 1$) has been prepared to investigate the effects of substitution on the physical and magnetic properties of the material. Work on the Jamesonite-Benavidesite series is described in Chapter 3.

1.6.2 Shandite ($A_3M_2X_2$)

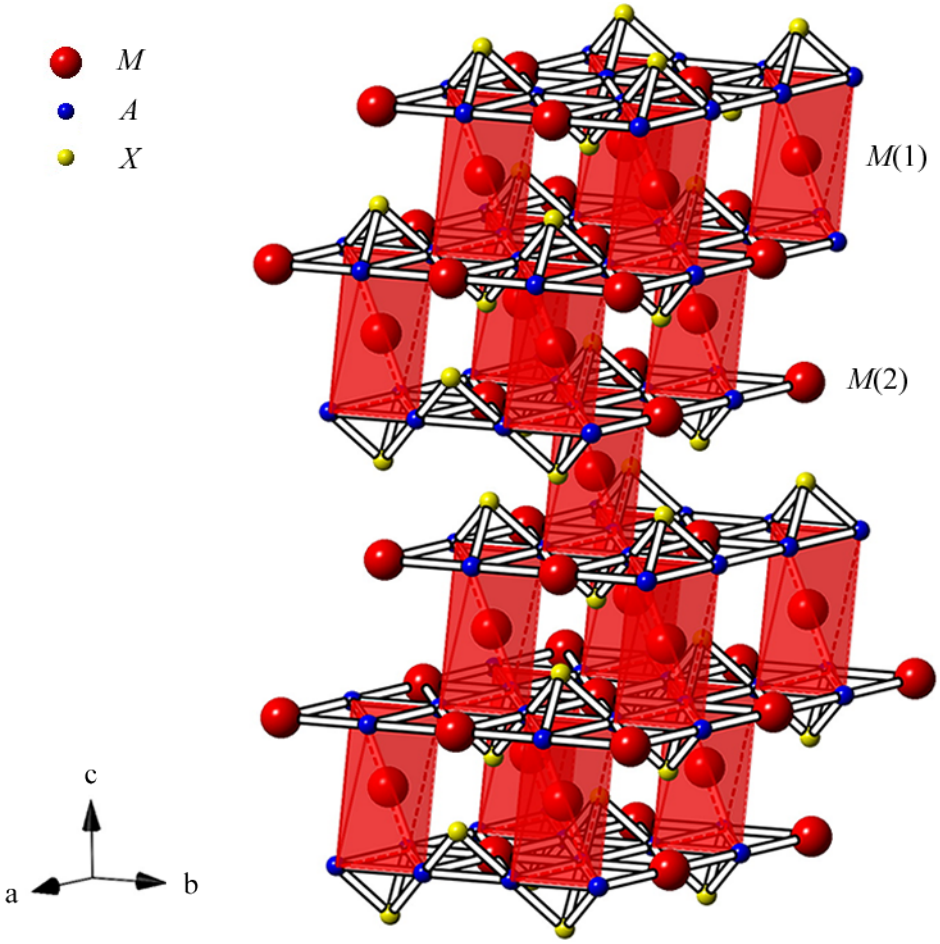

Figure 1.18: Shandite structure of $A_3M_2X_2$ showing $M(2)$ sites in the kagome layers and inter-layer $M(1)$ sites.

Shandites are a family of structurally-related materials of general formula $A_3M_2X_2$ (A = Ni, Co, Rh, Pd; M = Pb, In, Sn, Tl; X = S, Se).[51] The structure (Figure 1.18) (Space group $R\bar{3}m$) consists of a kagome lattice of corner-sharing A_3 triangles. The hexagonal sites generated in the kagome lattice are occupied by atoms of M. These layers are stacked in an ABC sequence. Triangular arrays of A atoms in adjacent layers generate trigonal antiprismatic inter-layer sites. Each of the A_3 triangles is capped above or below the kagome sheets by an X atom. M atoms are distributed over $M(2)$ sites in the kagome layers and $M(1)$ inter-layer sites. Lattice parameters and properties of known materials with the Shandite structure are shown in Table 1.4.

Table 1.4: Lattice parameters for known materials with the Shandite structure. Where available, values of the electrical resistivity and Seebeck coefficient at 300 K have been included.

$A_3M_2X_2$	*a* (Å)	*c* (Å)	ρ_{300K} (mΩ cm)	S_{300K} ($\mu V K^{-1}$)
$Ni_3Pb_2S_2$ [52]	5.60	13.62	0.13 [53]	-
$Ni_3In_2S_2$ [54]	5.37	13.56	0.16 [53]	-
$Ni_3Sn_2S_2$ [51]	5.46	13.19	0.05 [53]	-
$Ni_3Tl_2S_2$ [55]	5.47	13.85	-	-
$Ni_3In_2Se_2$ [56]	5.41	14.20	-	-
$Co_3Sn_2S_2$ [57]	5.37	13.19	0.45	-48
$Co_3In_2S_2$ [58]	5.32	13.64	0.44	-6.5
$Rh_3Pb_2S_2$ [58]	5.70	13.80	0.39	-4.3
$Rh_3In_2S_2$ [58]	5.60	13.61	0.19	+0.8
$Rh_3Sn_2S_2$ [56]	5.61	13.30	-	-
$Rh_3Tl_2S_2$ [56]	5.64	13.95	-	-
Rh_3PbInS_2 [58]	5.62	13.69	0.82	+16.0
$Rh_3Pb_2Se_2$ [58]	5.80	13.92	0.18	-13.2
$Pd_3Pb_2Se_2$ [58]	5.88	14.60	0.12	-9.0

1.6.2.1 $Co_3Sn_{2-x}In_xS_2$

Band structure calculations of $Co_3Sn_{2-x}In_xS_2$ (x = 0, 1, 2) reveal that states in the vicinity of the Fermi level are of predominantly Co (3d)-character, giving rise to sharp, narrow bands (Figure 1.19).[59] Electron populations indicate metallic behaviour for phases with x = 0 and 2. A pseudo gap is predicted in the $Co_3Sn_2S_2$ phase, whilst spin-polarised band structure calculations indicate a loss of spin degeneracy.[60] Majority and minority spin states respectively show metallic and semiconducting characteristics, leading to the description of $Co_3Sn_2S_2$ as a type I_A half-metal. Intriguingly, the calculations predict a transition to semiconducting behaviour in Co_3SnInS_2 (x = 1) when cation ordering is complete.

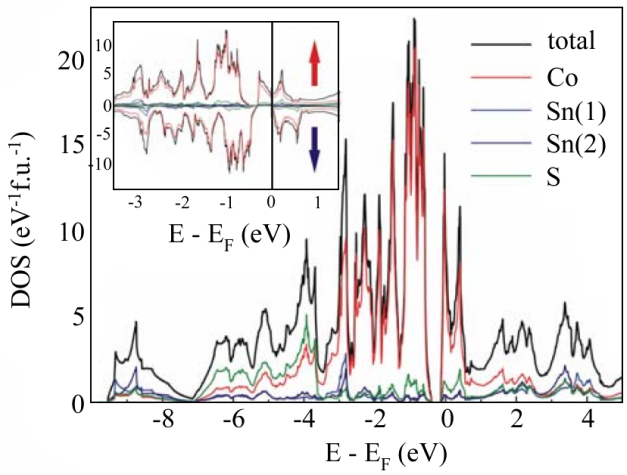

Figure 1.19: Density of States published by Dedkov et al[59] for $Co_3Sn_2S_2$ showing contributions from each of the elements in the material.

1.6.2.2 Parkerite - $A_3Bi_2S_2$

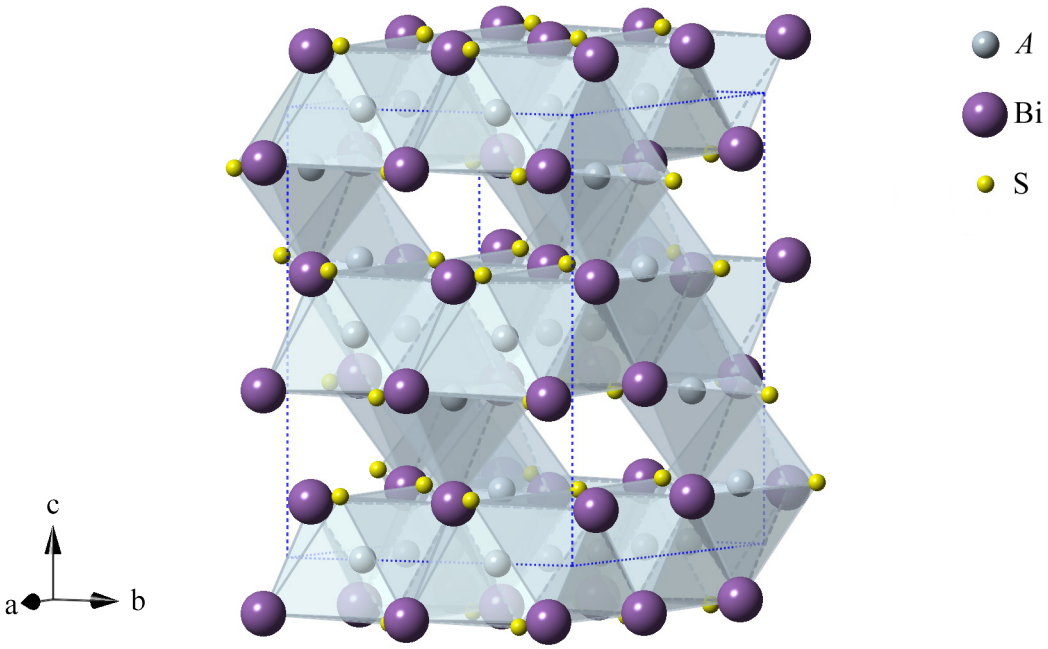

Figure 1.20: Structure of Parkerite.

Parkerites are sulphides with the same stoichiometry as Shandites, $A_3Bi_2S_2$ (A = Ni, Rh), however they crystallise with a structurally related, but different structure (Figure 1.20).[61] Layers of ABi_4S_2 edge-sharing octahedra stack in an AB sequence. The sulphur atoms are located in trans positions in the octahedra. An ABi_4S_2 octahedron shares a face with an octahedron in one layer and bridges to the adjacent layer through corner

sharing of a bismuth atom. These bridging octahedra edge share with a second bridging octahedron originating from the adjacent layer.

The ferromagnetic (T_C = 177 K) end-member phase, $Co_3Sn_2S_2$, despite its metallic properties, exhibits an unusually large Seebeck coefficient.[57] In this thesis, work to optimise the electron-transport properties through chemical substitution has been undertaken. This has been attempted through the preparation of the mixed main group series $Co_3Sn_{2-x}In_xS_2$ ($0 \leq x \leq 2$), which corresponds to a span of two in the electron count. Structural investigations to determine the ordering of the two available main group sites have been performed. The synthesis of previously unreported Shandite materials has also been explored. Work on the Shandite series of materials is described in Chapter 4.

1.6.3 $In_2Sn_3S_7$ and $Cr_2Sn_3Se_7$

The sulphide $In_2Sn_3S_7$ has previously been prepared and the structure determined from single crystal X-ray diffraction.[62] The monoclinic structure (Space group = $P2_1/m$, a = *11.643(2) Å*, b = *3.784(1) Å*, c = *12.628(2) Å*, β = *105.81(2)*°) is constructed from two different layers (Figure 1.21). The first is a single layer of edge-sharing InS_6 octahedra in the *bc* plane. The second is a layer consisting of two building blocks. Two SSn_5 square based pyramids, which are inverted with respect to each other, where the tin atom at the peak of one pyramid forms a corner of the base of the other. These are then linked through shared edges with additional square based pyraminds of the same inversion along the *b* axis. A region of two edge-sharing SnS_6 octahedra sit between the the square based pyraminds. They also form a bridge through corner sharing to octahedra on adjacent layers. Sn^{119} Mössbauer spectrometry has been used to investigate the oxidation state of tin.[63] The technique indicated that two Sn^{II} and two Sn^{IV} sites were present within the material. The two Sn^{II} are found in the SSn_5 squared based pyramid region and Sn^{IV} site at the centre of the SnS_6 octahedron. Observing two Sn^{IV} sites suggests that there is mixed occupany of the octahedral tin and indium sites across both layers. However, as X-ray diffraction cannot distinguish between indium and tin and the synthesis of a powdered bulk phase material for neutron diffraction has yet to be achieved, the site occupancy has not previously been determined from diffraction data.

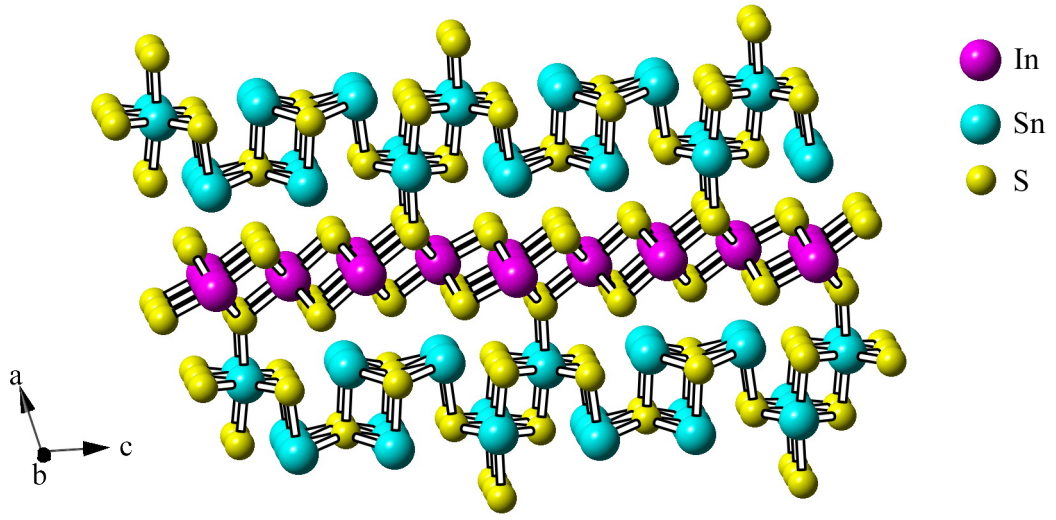

Figure 1.21: Structure of $In_2Sn_3S_7$ determined by single crystal X-ray diffraction.

The selenide $Cr_2Sn_3Se_7$ is a structural analogue of $In_2Sn_3S_7$ (Space group: *$P2_1/m$*, *a = 12.765(5) Å*, *b = 3.835(2) Å*, *c = 11.785(2) Å*, *β = 105.21(1)* °).[64] However, even though $In_2Sn_3S_7$ and $Cr_2Sn_3Se_7$ have identical space groups, the literature does not report the stacking of the layers along the same axis. $Cr_2Sn_3Se_7$ has been prepared as both a single crystal and an impure bulk powder phase. Measurements of the magnetic susceptibility suggest that ferromagnetic ordering is initially observed on cooling before the onset of antiferromagnetic ordering at T < 12 K.[64] Mixed occupancy of Cr^{III} and Sn^{IV} in the octaherdral sites has been identified as a reason for the observed magnetic behaviour. It has been suggested that disorder, created by tin, in the Cr^{III} sublattice, initially leads to localised ordering of chromium clusters.[65]

An orthorhombic phase of $Cr_2Sn_3Se_7$ has also been reported from single crystal X-ray diffraction (Space group: *Pnma*, *a = 23.097(1) Å*, *b = 3.8307(2) Å*, *c = 12.5414(6) Å*).[66] The structure (Figure 1.22) uses the same polyhedral building blocks as the monoclinic phase but in a different configuration. Ribbons, six MSe_6 edge-sharing octahedra wide, extend along the *b* axis. There are two orientations of the ribbon in the structure, which are linked with other ribbons through corner sharing. Ribbons of the same orientation are linked with the $SnSe_5$ square based pyramid structure found in the monoclinic phase. Antiferromagnetic ordering has been observed at T < 15 K.

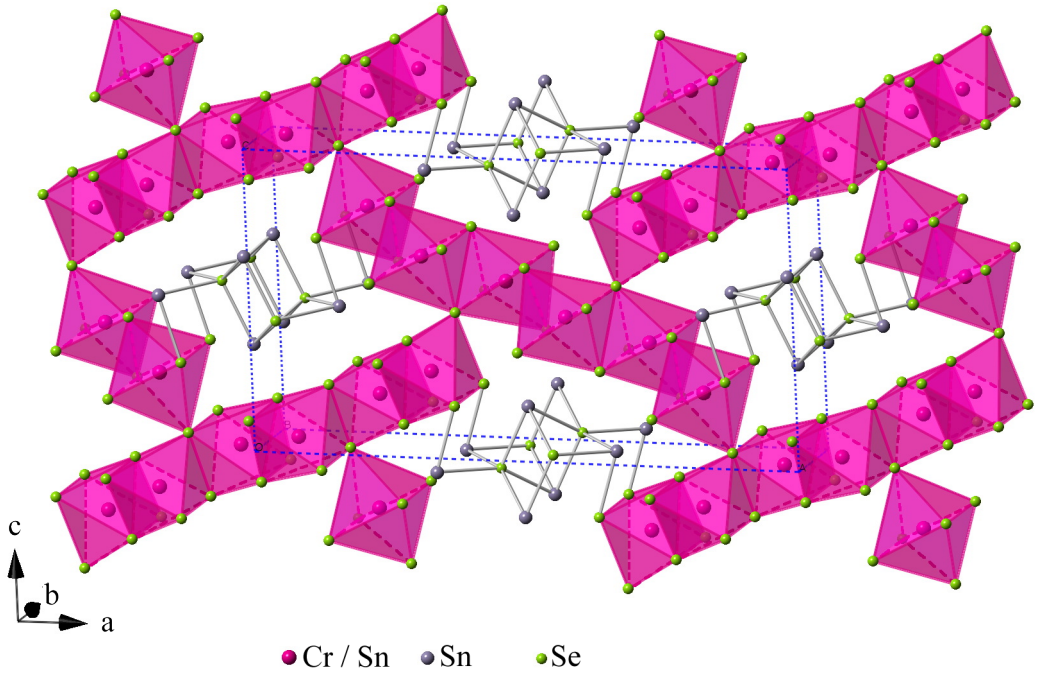

Figure 1.22: Structure of orthorhombic $Cr_2Sn_3Se_7$.

This thesis investigates the synthesis of both $In_2Sn_3S_7$ and $Cr_2Sn_3Se_7$ analogues and expansion of the range of known analogues through substitution. The site occupancy factors of the octahedral sites in $In_2Sn_3S_7$ have been investigated with powder neutron diffraction. Electrical and thermal transport properties for both previously reported analogues have been measured and the results discussed. Work on these materials is described in Chapter 5.

Chapter 2 – Experimental Techniques

2.1 Synthesis

Samples were synthesised using a sealed tube, solid-state reaction. This involves combining powdered elements and firing them at elevated temperatures inside a sealed and evacuated reaction vessel. This technique encourages the most thermodynamically favoured phase to be synthesised. Fused silica tubes were used as reaction vessels due to their relative inertness and their ability to maintain structural integrity at elevated temperatures in excess of 1000 °C. In instances where samples reacted with the silica, glassy carbon crucibles were sealed inside silica tubes and the reagents placed inside the crucible. Pyrex tubes were also used in the first firing of reactions that contained thallium. The lower softening temperature of pyrex, when compared with silica, significantly reduced the maximum possible reaction temperature. Evacuation of the reaction vessel is essential for two reasons. The removal of air prevents the formation of unwanted oxides and it reduces the risk of the vapour pressure inside from becoming too high, which could cause the tube to fail and explode. Grinding the sample into a homogeneous powdered mixture is important to minimise variations in stoichiometry across the sample. The diffusion rate of elements within the sample is the limiting factor of the reaction. Therefore, reaction times of days to several weeks are required.

Unless otherwise stated, starting elements were ground in an agate pestle and mortar in air before being sealed into evacuated ($<10^{-4}$ Torr) fused silica tubes. The rate of both heating and cooling of reactions were at the natural rate of the furnace. Intermediate regrinding was used to homogenise the samples between firings. The progress of each reaction was monitored by powder X-ray diffraction.

2.1.1 Jamesonite – Benevidesite Series: $Fe_{1-x}Mn_xPb_4Sb_6S_{14}$

Mixtures of elemental iron (-350 mesh, Alfa, 99.99 %), manganese (-350 mesh, Alfa, 99.99 %), lead (rod, Alfa, 99.999 %), antimony (-350 mesh, Alfa, 99.95 %) and sulphur (flakes, Aldrich, 99.99%), corresponding to stoichiometries $Fe_{1-x}Mn_xPb_4Sb_6S_{14}$ ($0 \leq x \leq 1$) were prepared. Samples were fired by increasing the temperature to 600 ºC and holding at this temperature for 120 hours, before cooling. This procedure was performed three times in total.

2.1.2 Shandite Series: $Co_3Sn_{2-x}In_xS_2$ ($0 \leq x \leq 2$)

Samples corresponding to stoichiometries $Co_3Sn_{2-x}In_xS_2$ ($0 \leq x \leq 2$) were prepared from mixtures of elemental cobalt (-350 mesh, Alfa, 99.95 %), tin (-350 mesh, Alfa, 99.8%), indium (-350 mesh, Alfa, 99.99 %) and sulphur (flakes, Aldrich, 99.99 %). The tin end-member phase (x = 0), was prepared according to the previously reported procedure[57] by heating the reaction mixture at 500 °C for 48 hours, followed by a second firing at 700 °C for 48 hours. The sample was ground between firings and cooled to room temperature at 0.5 °C min^{-1} after each firing. The indium end-member of this series (x = 2) was prepared by increasing the temperature to 800 ºC at 0.5 ºC min^{-1} and holding at this temperature for 96 hours, prior to cooling at the same rate. This procedure was performed three times in total with intermediate regrinding. All mixed main group metal compositions were prepared by heating samples for three periods of 48 hours at 900 ºC.

2.1.3 Co_2TlS_2

Initial reaction mixtures of Co_2TlS_2 were prepared inside a glove box from elemental cobalt (-350 mesh, Alfa, 99.95 %), thallium (chunks, Alfa, 99.99 %) and sulphur (flakes, Aldrich, 99.99 %). Samples were sealed into an evacuated ($<10^{-4}$ Torr) pyrex tube. Samples were placed into a furnace and heated to 480 °C for 48 hours. For the second and third firings, samples reground inside the glove box and sealed into an evacuated ($<10^{-4}$ Torr) fused silica tube. The sample was heated to 600 °C for 96 hours.

2.1.4 $In_2Sn_3S_7$

Initial reaction mixtures of $In_2Sn_3S_7$ were prepared in a glove box from elemental indium (-350 mesh, Alfa, 99.99 %), tin (-350 mesh, Alfa, 99.8 %) and sulphur (flakes, Aldrich, 99.99 %) of the corresponding stoichiometry. Reaction mixtures were placed into a glassy carbon crucible and sealed into an evacuated ($<10^{-4}$ Torr) fused silica tube. Samples were inserted into a furnace at 750 °C and fired for 48 hours. Sample tubes were removed from the hot furnace and cooled to room temperature in air before they were opened.

2.1.5 $Cr_2Sn_3Se_7$ and $Cr_2Sn_5Se_{11}$

$Cr_2Sn_3Se_7$ and $Cr_2Sn_5Se_{11}$ reaction mixtures were prepared in a glove box from elemental chromium (-200 mesh, Aldrich, 99.95 %), tin (-350 mesh, Alfa, 99.8 %) and selenium (shot, Alfa, 99.99 %) of the corresponding stoichiometry. Reaction mixtures were placed in a glassy carbon crucible and sealed into evacuated ($<10^{-4}$ Torr) fused

silica tubes. Samples were fired by increasing the temperature to 800 ºC and holding at this temperature for 96 hours before cooling. This procedure was performed three times in total. Samples were cold pressed into pellets for use in the next firing.

2.1.6 $Cr_2Sn_3S_7$

A reaction mixture for $Cr_2Sn_3S_7$ was prepared from stoichiometric quantities of the required elements (chromium (-200 mesh, Aldrich, 99.95 %), tin (-350 mesh, Alfa, 99.8 %) and sulphur (flakes, Aldrich, 99.99 %)). The mixture was heated from room temperature at 10°C min^{-1} to 800°C. The temperature was held at 800°C for three days before it was allowed to cool at the natural cooling rate of the furnace. Three firing cycles were completed for the sample.

2.2 Powder X-ray Diffraction

The principal technique for analysis of crystalline powdered samples is X-ray diffraction. X-rays are an electromagnetic radiation with wavelengths of the order of 10^{-10} m. They are generated by bombarding a metal with high-energy electrons. The electrons decelerate as they move through the metal and generate radiation with a continuous range of wavelengths. A few high intensity sharp peaks, at certain wavelengths, are produced. These arise from electrons colliding with electrons in the inner shell of the metal. The expulsion of an electron from the inner shell, allows a higher energy electron to drop down into the vacant site. The excess energy is emitted as an X-ray photon.

The interaction of X-ray photons and the electrons in atoms can be used to investigate the structures of crystalline materials. Due to samples containing heavy elements, the technique of reflection X-ray diffraction was utilised. The scattering of X-rays (and neutrons) mostly leads to destructive interference. Constructive interference is observed when Bragg's law (2.1) is satisfied. In Figure 2.1, the X-ray 1 is reflected at D by the second lattice plane, whilst X-ray 2 travels to C in the third plane. Therefore, X-ray 2 travels an additional path length of AC+CB through the lattice when compared with X-ray 1. Constructive interference requires this to be an integer number of λ.

$$\begin{aligned} &AC = CB = d\sin\theta \\ &\therefore AC + CD = 2d\sin\theta \\ &\therefore n\lambda = 2d\sin\theta \end{aligned} \qquad (2.1)$$

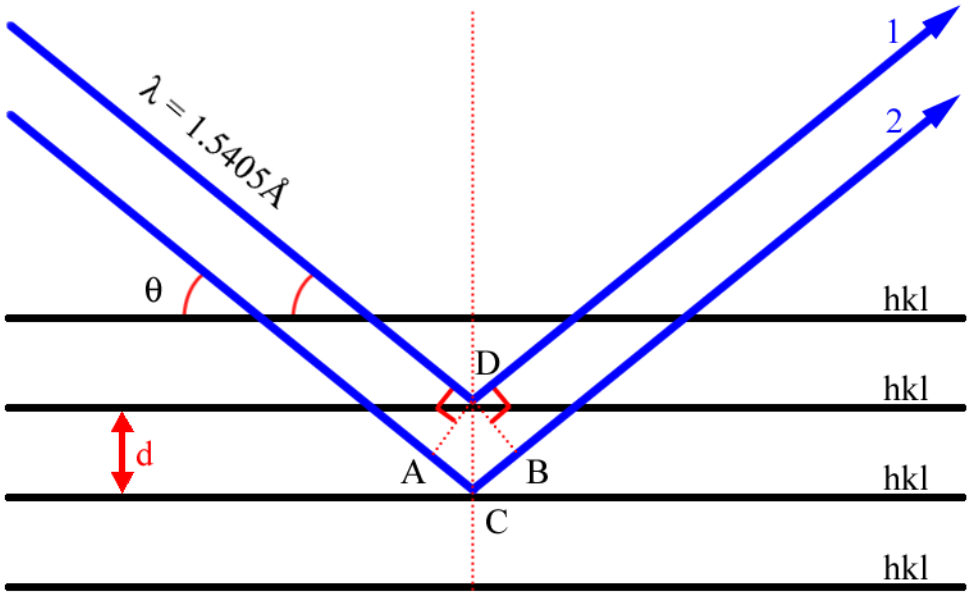

Figure 2.1: Diagram of parallel X-rays being reflected from adjacent planes in a crystal lattice.

The unit cells of solids are related to d-spacings in crystals. Diffraction patterns can therefore be predicted from known lattice parameters and in turn, lattice parameters can be determined from an experimental diffraction pattern. Different d-spacing geometry equations are used according to the symmetry of the crystal structure (Appendix A).

Samples were analysed on a Bruker D8 Advance powder X-ray diffractometer. This is a θ/2θ reflectance instrument with a monochromatic $CuK_{\alpha 1}$ radiation (λ = 1.5405Å) source and a LynxEye detector. Samples were ground into a fine powder with a mortar and pestle. The powder was loaded into a recessed polymethylmethacrylate sample holder with the excess scraped off the top leaving a flat surface. In instances where limited sample was available for measurements, samples were sprinkled onto a flat plate of single crystal silicon using a small quantity of vaseline to hold the sample in place. Collection times were typically doubled when using this method. Data to assess the purity of the sample were typically collected over the range $5 \leq 2\theta\ (°) \leq 85$ with a step size of 0.0092115171° and a counting time of 0.4s per step of detector position. The diffraction pattern was evaluated against the ICDD-PDF Data database using the EVA[67] software package. This allowed experimental data to be referenced against known materials in order to determine the phases present in the sample. Once single phase

materials had been obtained, patterns were recollected over the range $10 \leq 2\theta\ (^\circ) \leq 120$ with a step size of 0.027645513° and a counting time of 14.4s per step of the detector. The larger step size was to allow a longer data collection time at each position. The increase in counting time per step improves the signal to noise ratio, improving the statistical quality of the collected data. Patterns were analysed using the Topas3[68] and GSAS[69] software packages.

2.3 Powder Neutron Diffraction

The diffraction of neutrons differs from X-rays in two main respects. X-rays are scattered by the electrons, however the scattering of neutrons is a nuclear phenomenon. As a result, the intensity with which the neutrons are scattered is independent of the number of electrons and neighbouring elements may have markedly different scattering factors. This allows both to give complementary information. A second difference is that neutrons, due to their spin, possess a magnetic moment. This magnetic moment can couple to the magnetic fields of ions or atoms in a crystal and provide additional structural detail in the diffraction pattern. A consequence of this is that neutron diffraction is well suited to the investigation of magnetically ordered lattices, where neighbouring atoms may be of the same element but have different orientations of their electronic spin. Neutrons are also more penetrating than X-rays, allowing data collection in more complex sample environments to be studied.

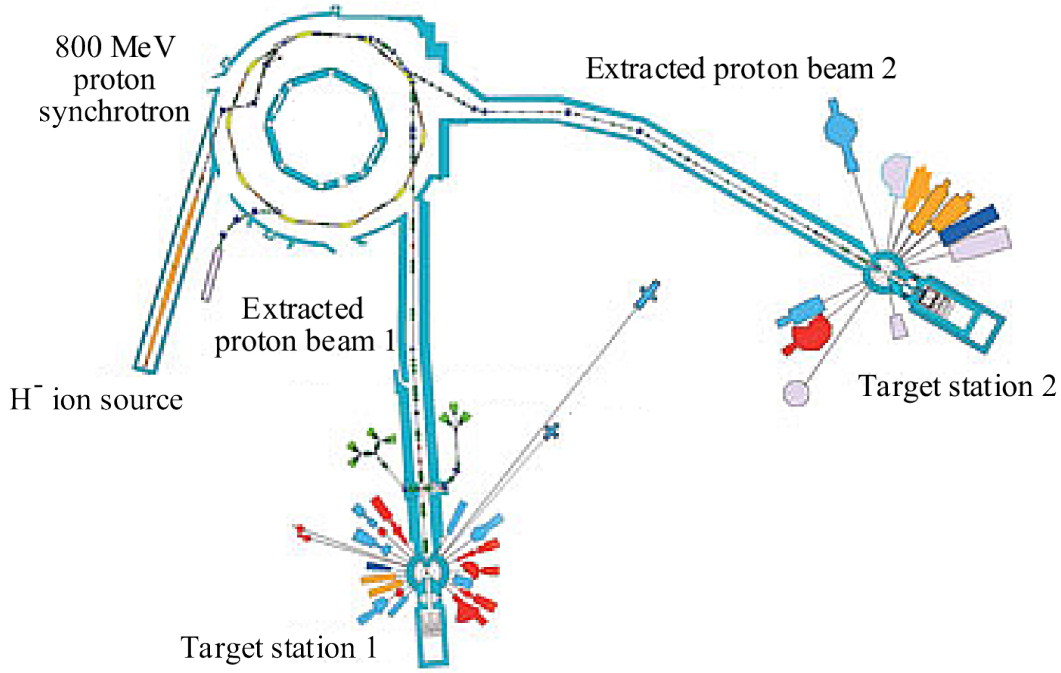

Figure 2.2: Schematic of synchrotron and target stations at the ISIS facility.

Powder neutron diffraction experiments were performed using several instruments at the ISIS facility, Rutherford Appleton Laboratory, Didcot, Oxfordshire. ISIS is a pulsed neutron source, which is used to collect time of flight neutron diffraction data. Neutrons are generated in a several stage spallation process at ISIS (Figure 2.2). An electrical discharge is used to create H^- ions. These are accelerated and separated into bunches by a Radio Frequency Quadrupole accelerator. These bunches are then accelerated to 37% of the speed of light in a 10 m long linear accelerator. Electrons are removed by passing the beam through an alumina window to leave a beam of protons, which is directed into a synchrotron. The protons are then accelerated by radio frequency electric fields around the 163 m long ring. This focuses the beam and increases the speed to 84% of the speed of light. The proton beam is then directed at a tungsten target. The high energy pulsed proton beam strikes the target, causing neutrons from the target to be ejected. These neutrons are then directed to various instruments surrounding the target to be used in sample analysis. All diffraction instruments used have a series of fixed detector banks covering a range of d-spacings and resolutions. Higher angle banks have the highest resolution and the smallest d range, whereas the opposite is true for low angle banks. The detector elements within each bank are resolution focused. This gives each element within the bank approximately the same resolution.

Neutrons enter the instrument through a window that produces a beam of adjustable height and width. A chopper is used to block fast neutrons from one pulse overtaking slow neutrons from the previous one. Powdered samples are held in vanadium cans. However in the case of measurements at higher temperatures, samples were also contained within an evacuated sealed Suprasil tube. Samples are positioned in the path of the beam. Neutrons interact elastically with the sample and diffraction data are collected simultaneously by each detector bank in the array. Elastic scattering describes situations where no energy is lost by the neutrons in the interaction with the investigated material. When the desired number of μA have been collected, the shutter is closed and the sample is removed. Its radioactivity is measured and the sample is stored in a radioactive samples cupboard until the radioactivity has decayed sufficiently for safe handling. This allows for further measurements of the samples properties to be performed.

Unlike the X-ray diffraction experiments, powder neutron diffraction experiments undertaken during this research used transmission diffraction (Figure 2.3). Neutrons

pass through a powdered sample held in a cylindrical holder usually made of vanadium. Although vanadium scatters X-rays strongly, it is relatively weak at scattering neutrons. Therefore it does not greatly interfere with the pattern produced by the material being investigated. Table 2.1 shows the peaks due to scattering from vanadium.

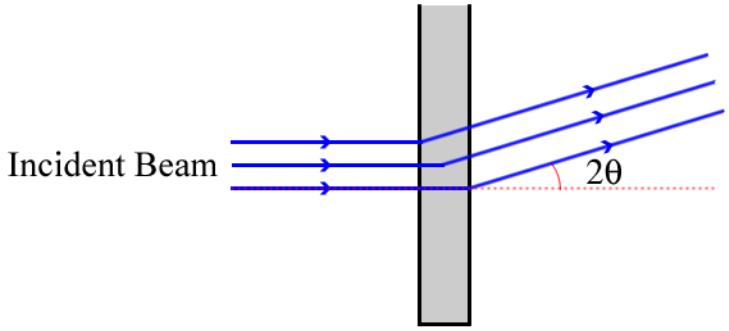

Figure 2.3: Diagram of parallel beams on neutrons used in transmission diffraction.

Table 2.1: Vanadium neutron diffraction scattering lengths.

hkl	*θ (°)*	*2θ (°)*	*d-spacing (Å)*	I_{rel}
110	21.09	42.18	2.1423	1000
200	30.59	61.18	1.5149	243
211	38.56	77.12	1.2369	388.46
220	46.03	92.06	1.0712	517.75
310	53.57	107.14	0.9581	647.44

Experiments performed on each neutron diffractometer described below are presented in Appendix B.

2.3.1 The Polaris Diffractometer

In the early days of the project, powder neutron diffraction experiments were conducted using the Polaris diffractometer. Polaris was a medium resolution diffractometer with a 12 m flight path to the sample. Four detector banks, arranged as shown in Figure 2.4, were utilised in data collection. Details of these are shown in Table 2.2. Polaris could be used for both ambient and extreme temperature measurements. Polaris was decommissioned during 2010, to be replaced by a new diffractometer of the same name.

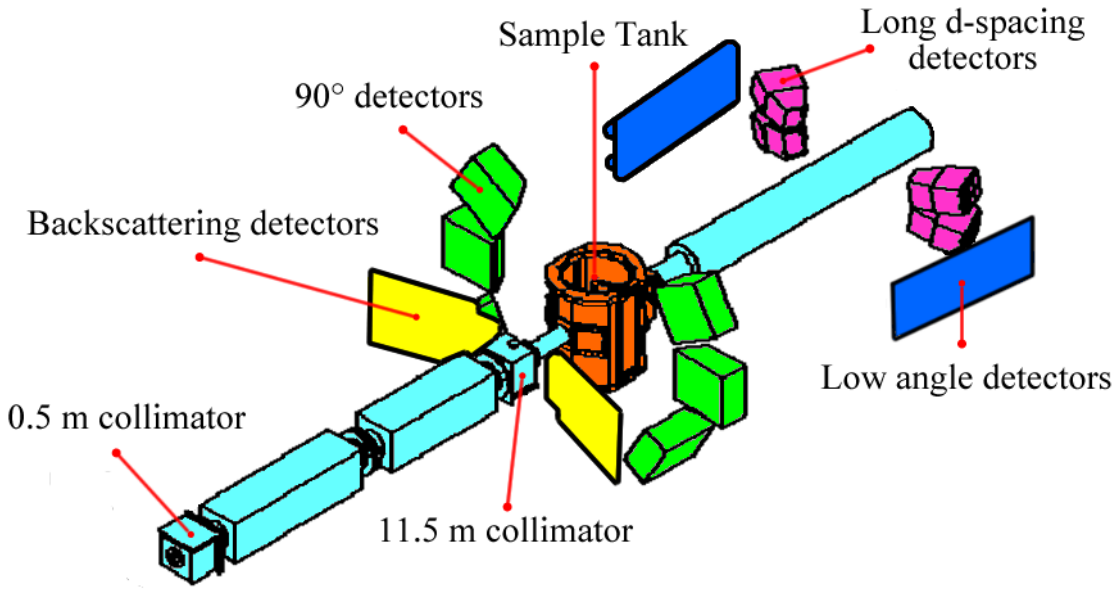

Figure 2.4: Schematic of the original Polaris diffractometer at ISIS. Adapted from Polaris User Guide.[70]

Table 2.2: Parameters of the original Polaris detector array.[70]

Position	*Long d-spacing*	*Low angle*	*90°*	*Backscattering*
Type	ZnS scintillator	^{3}He gas tubes	ZnS scintillator	^{3}He gas tubes
2θ range (°)	13 - 15	28 - 42	85 - 95	130 - 160
Δd/d (%)	3	1	0.7	0.5
d range (Å)	0.5 - 21.0	0.5 - 8.15	0.3 - 4.1	0.3 - 3.2

Powdered samples from the $Fe_{1-x}Mn_xPb_4Sb_6S_{14}$ series (x = 0.25, 0.75 and 1) were loaded into 8 mm diameter vanadium cans. Data were collected at room temperature and inside a cryostat at temperatures down to 2 K.

2.3.2 The GEM Diffractometer

The General Materials diffractometer is a high intensity, medium resolution diffractometer with a 17 m flight path. A schematic of GEM is shown in Figure 2.5. Details of the detector bank array are given in Table 2.3. Data from banks 5 and 5X, and from banks 6 and 7 were each combined to produce single data sets.

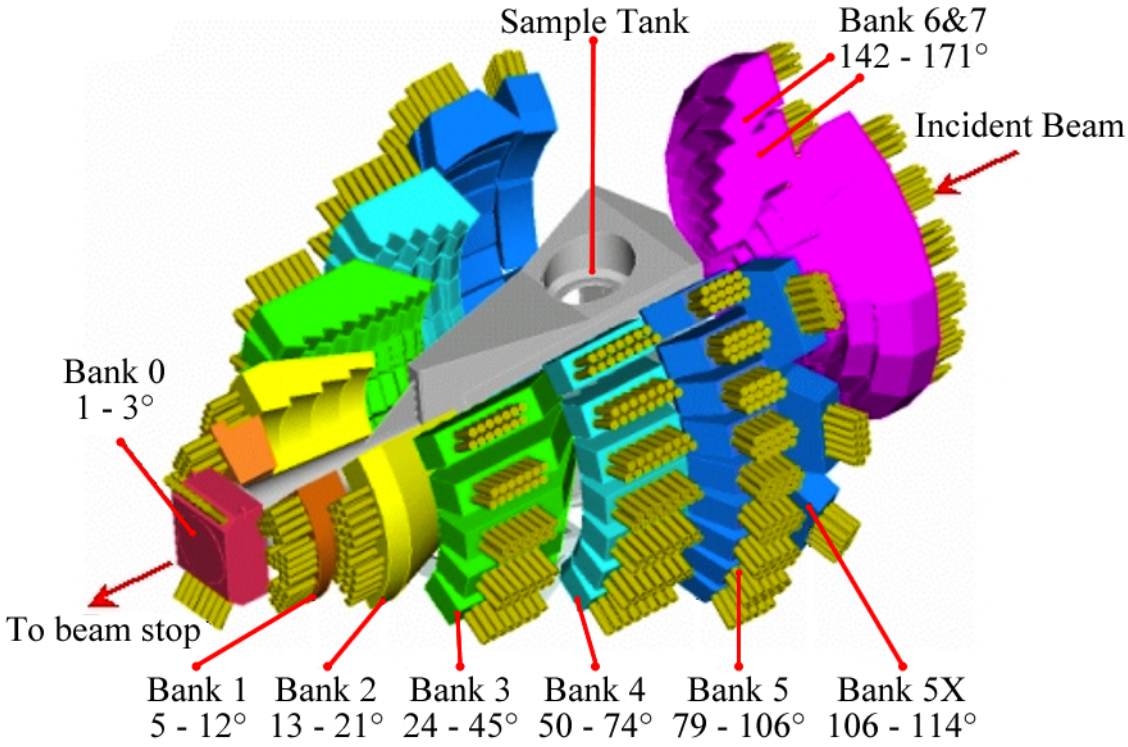

Figure 2.5: Schematic of the GEM diffractometer at ISIS.[71]

Table 2.3: Parameters of the GEM detector array.[72]

Bank	*1*	*2*	*3*	*4*	*5*	*5X*	*6*	*7*
2θ range (°)	5-12	13-21	24-45	50-74	79-104	105-113	142-149	149-169
Δd/d (%)	4.7	2.4	1.7	0.79	0.51	0.51	0.34	0.35
d range (Å)	2-30	1-14	0.8-7	0.7-4	0.5-2.5		0.3-1.7	

Powdered samples of $Co_3Sn_{2-x}In_xS_2$, from x = 0 to 2 in steps of 0.2, were loaded into 6mm diameter vanadium cans and the sample mass and height in the can measured. Data were collected at room temperature. Patterns for tin-rich samples were collected for 300 μA of beam current whilst indium-rich samples were collected for 400 μA. The increase in collection time was to offset the absorption of neutrons caused by the increased indium content.

Samples from the $Fe_{1-x}Mn_xPb_4Sb_6S_{14}$ series (x = 0 and 0.5) were loaded into 8 mm vanadium cans and data were collected at room temperature and at temperatures down to 2 K inside a cryostat.

2.3.3 The HRPD Diffractometer

The High Resolution Powder Diffractometer (HRPD) instrument at ISIS is a high intensity, high resolution neutron diffractometer with a flight path of 100 m. To prevent overlap of neutron pulses from the source, choppers at 6 and 9 m allow one out of every five pulses produced at ISIS to reach the instrument. A schematic of the instrument is shown in Figure 2.6 and details of the detector banks are given in Table 2.4.

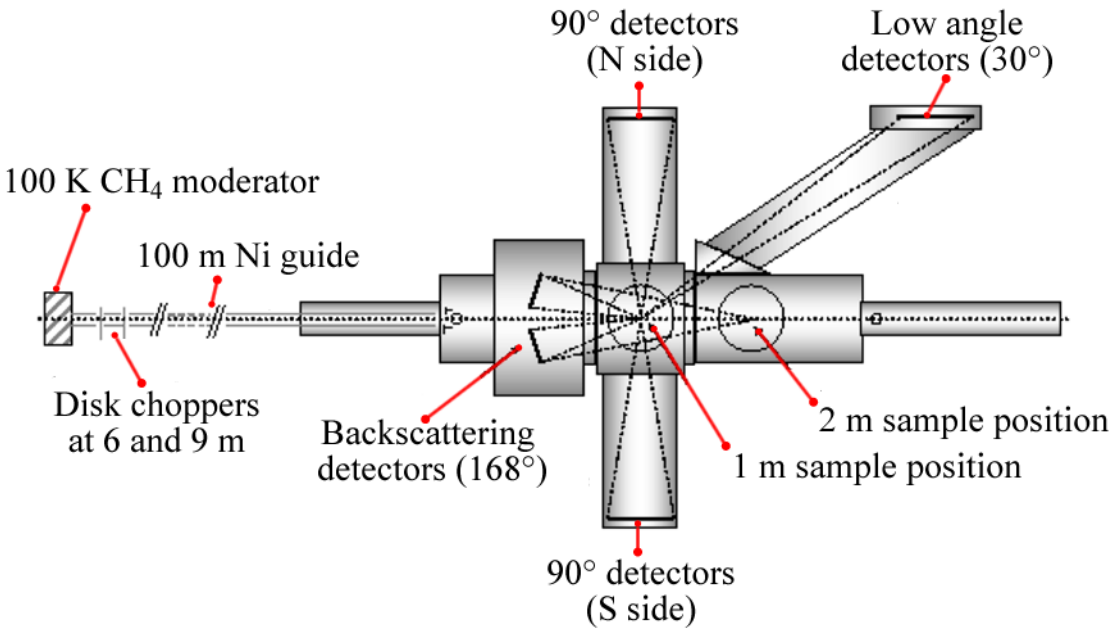

Figure 2.6: Schematic of the HRPD diffractometer at ISIS.[73]

Table 2.4: Parameters of the HRPD detector array.[73]

Position	*Low angle*	*90°*	*Backscattering*
Type	^{3}He gas tubes	ZnS scintillator	ZnS scintillator
2θ range (°)	28 - 32	87 - 93	160 - 176
Δd/d (%)	2	0.2	0.04-0.05
d range (Å)	2.2 – 16.5	0.9 – 6.6	0.6 – 4.6

Samples $In_2Sn_3S_7$ and $Cr_2Sn_3Se_7$ were analysed using the High Resolution Powder Diffractometer (HRPD) instrument. Powdered $In_2Sn_3S_7$ was sealed inside an evacuated Suprasil tube (8 mm internal diameter, 1 mm wall thickness). The tube was loaded into

a thin-walled vanadium can. Data were collected over the temperature range $20 \leq T$ (°C) ≤ 750 inside a furnace located on the beamline. $Cr_2Sn_3Se_7$ was loaded into a vanadium can and analysed at room temperature.

2.4 Structural Refinement Using Powder Diffraction Data

Diffraction data were analysed to obtain structural information of the material being investigated.

2.4.1 Unit Cell Refinement

Refined lattice parameters were obtained using the Topas3[68] software package. The software uses the raw data file obtained from X-ray diffraction experiments. The wavelength of the X-ray source used and the angle of the monochromator (LP Factor) were entered into the software. A model space group and lattice parameters were used to determine allowed peak positions and refine the lattice parameters against the experimental data. The resulting lattice parameters obtained from the refinement were used as part of the structural model in Rietveld refinements.

2.4.2 Rietveld Refinement

Powder X-ray and neutron diffraction data were analysed using the Rietveld method[74] with the General Structure Analysis System[69] (GSAS) software package. This allows the refinement of a structural model whereas Topas is only used to refine lattice parameters. The Rietveld method uses a least squares approach to refine a theoretical line profile against the collected experimental data. This method estimates the values of the adjustable parameters in a model that are used to predict observable quantities. The method attempts to minimise the difference between this predicted structural model and the experimental data.

To perform a Rietveld refinement, the collected diffraction pattern, an instrument parameter file and a structural model are required. It is important to have a good experimental data set and starting structural model or the refinement will fail or produce inaccurate results. The refinement of various parameters is used to obtain a good fit between the model and the experimental data. Structural parameters describe the lattice parameters, atomic coordinates, thermal parameters and site occupancy factors of the investigated sample. The refinement of instrument parameters must also be performed.

These describe the conditions of the experiment and the sample, and include the background, absorption correction, scale factors and peak shape profile coefficients.

After refining the model, the success of the refinement can be determined by examining the weighted profile R factor (R_{wp}) and the goodness of fit (χ^2). Equation (2.2) shows χ^2 is calculated from the total number of observations in all histograms (N_{obs}), the number of variables in the least squares refinement (N_{var}) and the minimisation function (M), which, as shown in equation (2.3), is obtained from the weighting factor (f_h) and the sum of each powder diffraction data component (M_h).[69] Each component occupies a separate histogram in the refinement. The weighting factor is used to balance contributions from all the histograms in the refinement. Refinements attempt to minimise the difference between the experimental data and the structural model across all histograms.

$$\chi^2 = \frac{M}{N_{obs} - N_{\text{var}}} \tag{2.2}$$

$$M = f_h \sum M_h \tag{2.3}$$

Values of χ^2 should be above, but as close to 1 as possible. Large values result from an inadequate model for the refinement. This can be improved by adding additional parameters to the refinement, adding additional phases or in some instances, changing the whole structural model. A value less than 1 usually indicates that the data quality is too poor for the number of parameters that are being refined. In this instance the only way to improve the fit is to improve the experimental method and collect a new data set.

The weighted profile R factor (R_{wp}), is the R factor that the Rietveld refinement is attempting to minimise.[74] It is calculated from the weights of the observed experimental data ($y_i(obs)$) and the calculated model ($y_i(calc)$) as shown in equation (2.4).

$$R_{wp} = \sqrt{\frac{\sum w_i \left(y_i(obs) - y_i(calc) \right)^2}{\sum w_i \left(y_i(obs) \right)^2}} \tag{2.4}$$

2.5 Hot Pressing

The technique of hot pressing was used to fabricate pellets of samples with high density. The density of a sample is an important factor with regards to property measurements. For example, grain boundaries between particles in a pellet impede the flow of electrons through the material. Pellets with densities that are significantly lower than the crystallographic value have a larger number of these boundaries than a denser pellet of the same material. Densification also reduces the porosity of the material. A more porous sample could lead to values of the electrical resistivity being orders of magnitudes higher than those recorded for dense samples.

Pellets for electrical and thermal transport property measurements were fabricated using a hot press constructed in-house, Figure 2.7. Approximately 1 g of sample was placed between two 13 mm diameter graphite anvils inside a graphite mould. Under an inert nitrogen atmosphere, samples were heated and put under pressure simultaneously. The pressure was released before the system was cooled to room temperature. In this way, pellets with >90% of the theoretical density were obtained. Table 2.5 shows the conditions used for each set of materials.

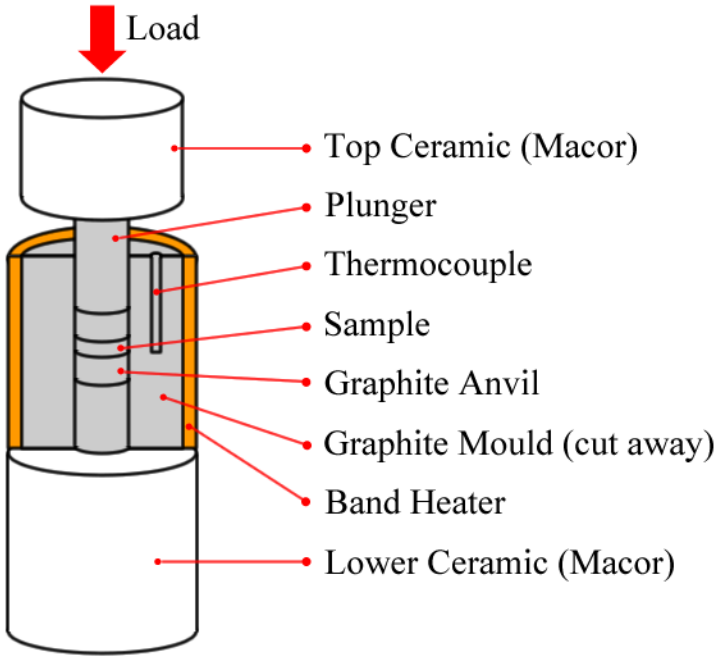

Figure 2.7: Schematic of in-house constructed hot press.

Table 2.5: Hot-pressing conditions for samples in this work.

Sample / Series	*Temperature (°C)*	*Hydraulic Pressure (bar)*	*Time (min)*
$Fe_{1-x}Mn_xPb_4Sb_6S_{14}$	450	50	30
$In_2Sn_3S_7$*	500	30	30
$Cr_2Sn_3Se_7$*	500	30	30
$Co_3Sn_{2-x}In_xS_2$	720	60	30
Co_2TlS_2	500	50	30

* Some impurities were formed during hot pressing.

2.6 Ingot Fabrication

Ingots for physical property measurements were cut from hot-pressed pellets using a rotating diamond tipped saw blade. Pellets were attached to a graphite block using molten wax, which hardened on cooling fixing the pellet to the graphite mount. The pellet was then lowered on to the diamond tipped saw, which was rotating at 90 rpm. Cuts were made to the circular pellet to form a square, from which three ingots were cut. Residual wax was removed from the ingot by scraping with a scalpel.

2.7 Electrical Resistivity

The electrical resistivity (ρ) is the reciprocal of the electrical conductivity (σ), which describes the ability of a material to conduct charge. This depends on the number of charge carriers (n), their charge (q) and their mobility (μ) as shown in equation (2.5).

$$\frac{1}{\rho} = \sigma = nq\mu \tag{2.5}$$

Measurements of the electrical resistivity were performed on two instruments, which measure over two complementary temperature ranges.

2.7.1 Low Temperature Measurements

Low temperature measurements of the electrical resistivity were performed using an instrument constructed in-house. Depending on the magnitude of the electrical resistivity, the instrument was used in one of two modes. Low electrically resistive samples ($\rho \leq 10$ meV) such as metals and small band gap semiconductors were

measured with the instrument setup in manual mode. More resistive semiconductors were measured using the instrument controlled by an automated LabView programme. The two methods are described below.

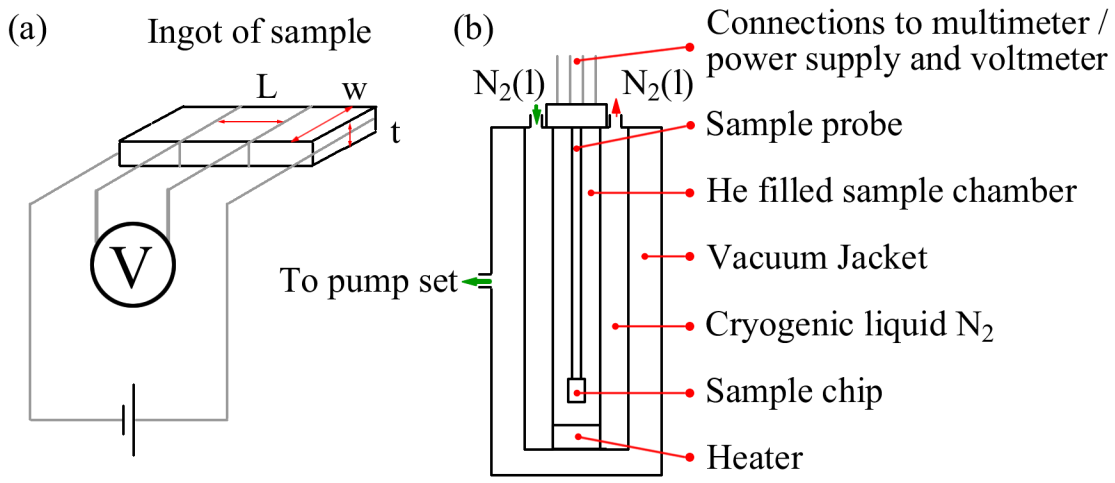

Figure 2.8: Schematic of (a) connections made to the ingot and (b) cryostat of in-house constructed electrical resistivity instrument.

2.7.1.1 Manual Measurements for Materials with Low Electrical Resistance

Electrical resistivity measurements over the temperature range $100 \leq T\ (K) \leq 350$ were made in 25 K steps, on ingots (*ca.* $8 \times 3 \times 1$ mm^3) cut, as described in section 2.6. As shown in Figure 2.8(a), four 50 μm silver wires were attached using colloidal silver paint and connections made to a TTi QL564P power supply and to a Keithley 2182 nanovoltmeter. The latter was used to measure the voltage drop when a 10 mA current was passed through the ingot. The resistance (R) was determined using Ohm's law and the electrical resistivity calculated from the resistance, the cross sectional area (A) and length between the two middle wires (L) using equation (2.6), The sample was mounted in a CF1200 cryostat connected to an Oxford Instruments ITC502 temperature controller, Figure 2.8(b).

$$\rho = \frac{RA}{L} \tag{2.6}$$

2.7.1.2 LabView Controlled Automatic Measurements

Electrical resistivity measurements over the temperature range $100 \leq T\ (K) \leq 350$ were made in 1 K steps, on ingots (*ca.* $8 \times 3 \times 1$ mm^3) cut as described in section 2.6. Four 50

μm silver wires were attached using colloidal silver paint and connections made to a HP34401A multimeter. The current used by the multimeter was automatically selected according to the magnitude of the resistance of the material to be measured. The voltage drop when the specified current was passed through the ingot was used to determine the resistance using Ohm's law. This in turn was used to calculate the resistivity using equation (2.6). The sample was again mounted in a CF1200 cryostat connected to an Oxford Instruments ITC502 temperature controller.

2.7.2 High Temperature Measurements

Measurements of the electrical resistivity were performed over the temperature range $303 \leq T\ (K) \leq 673$ in 10 K steps, using a commercial Linseis LSR3-800 on a hot-pressed ingot (ca. $8 \times 3 \times 1$ mm^3). An applied temperature gradient of 30 K and a current of 100 mA were used. Measurements were performed simultaneously with high temperature Seebeck coefficient measurements as described in section 2.8.2.

2.8 Seebeck Coefficient

The Seebeck coefficient (S) is a measure of an induced voltage when a temperature gradient is placed across a sample. Measurements can be used to indicate the nature of the dominant charge carrier. Negative and positive values indicate electron and hole carrier dominance respectively. The dependence of the Seebeck coefficient against temperature gives an indication of the metallic, semiconducting or insulating nature of the material.

2.8.1 Low Temperature Measurements

Measurements of Seebeck coefficient over the temperature range $100 \leq T\ (K) \leq 350$ were made on an ingot (*ca.* $8 \times 3 \times 1$ mm^3) cut as described in section 2.6, using an in-house constructed instrument, Figure 2.9. Ingots were mounted on a copper holder using silver adhesive. The holder incorporated a small heater (120 Ω strain gauge) located close to one end of the sample and was attached to the hot stage of a closed-cycle refrigerator (DE-202, Advanced Research Systems), controlled by a Lakeshore LS-331 temperature controller. Two 50 μm copper wires were attached to the ends of the sample using silver paint and connections made to a Keithley 2182A nanovoltmeter. Two Au: 0.07 % Fe *vs.* chromel thermocouples were placed close to the sample at the hot and cold ends, and connected to a second Lakeshore LS-331 temperature controller. The Seebeck coefficient was determined by applying a temperature gradient (ΔT) across

each sample and measuring the corresponding thermal voltage (ΔV). The slope of the line, ΔV/ΔT, was used to determine the Seebeck coefficient.

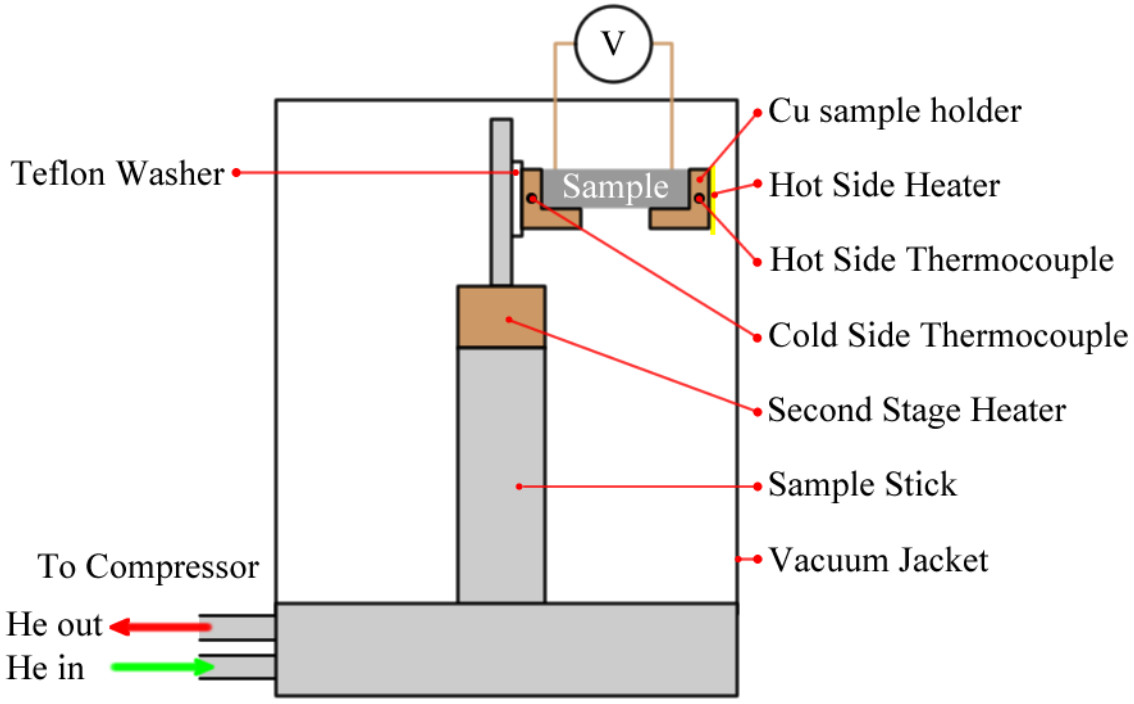

Figure 2.9: Schematic of sample probe on the in-house constructed Seebeck instrument.

2.8.2 High Temperature Measurements

Measurements of the Seebeck coefficient were performed on a hot-pressed ingot (ca. 8 × 3 × 1 mm^3) cut as described in section 2.6, over the temperature range 303 ≤ T (K) ≤ 673 in 10K steps, using a commercial Linseis LSR3-800. An applied temperature gradient of 30 K and a current of 100 mA were used. Measurements were performed simultaneously with high temperature electrical resistivity measurements described in section 2.7.2.

2.9 Thermal Conductivity

The thermal conductivity (κ) is a measure of a material's ability to transfer heat through its structure. There are two contributions to this, the electronic thermal conductivity (κ_e) and the lattice thermal conductivity (κ_L). The Wiedermann-Franz law, equation (2.7), can be used to determine the electron thermal conductivity from the temperature, Lorenz number (L) and the electrical resistivity. Therefore the number of charge carriers affects the electronic thermal conductivity. The value of L is often debated for different

cases. The value of L = 2.44 × 10^{-8} W Ω K^{-2} works well with small band gap semiconductors but poorly for low resistivity metals.

$$\kappa_e = \frac{LT}{\rho} \tag{2.7}$$

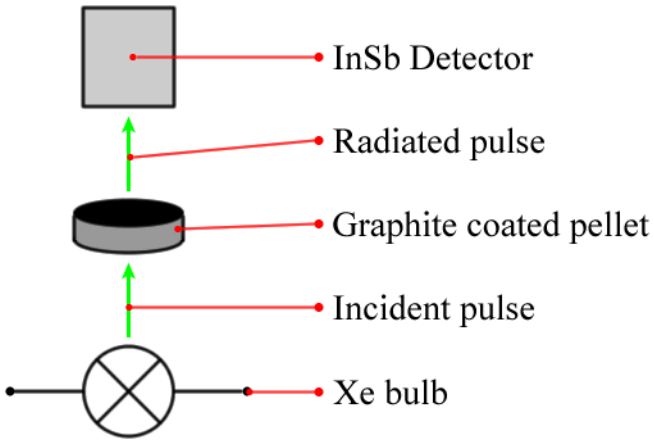

Figure 2.10: Schematic of a thermal conductivity measurement.

Thermal diffusivity measurements were carried out over the temperature range 373 ≤ T (K) ≤ 673 in steps of 50 K using an Anter Flashline 3000 instrument. The instrument uses the light flash technique. Measurements were made on 1 to 1.5 mm thick, 13 mm diameter hot-pressed pellets. The pellets' top and bottom surfaces were coated with a thin layer of graphite to aid black body absorption and radiance of the heat pulse. Pellets were loaded into a pyrophyllite sample holder and placed inside a sample chamber, which was evacuated and purged using nitrogen gas. One side of the pellet was subjected to a heating pulse and an InSb detector recorded the transmitted infrared radiation as a function of time. The thermal diffusivity (α (m^2 s^{-1})) was determined from the sample thickness (L (cm)), a dimensionless constant (K_x) and the percentage rise in the temperature (t_x) as shown in equation (2.8). The heat capacity (C_p) of the sample was determined from the radiant energy of the pulse (Q (cal cm^{-2})), the thickness of the sample (L (cm)) and the maximum temperature at the rear surface (T_M (K)) using equation (2.9). Equation (2.10) shows the thermal conductivity (κ (W K^{-1} m^{-1})) was calculated from the thermal diffusivity, heat capacity and the sample density (ρ (kg

m^{-3})). For the determination of the heat capacity, side-by-side testing of Pyroceram™ 9606, a reference material of known heat capacity, was carried out.

$$\alpha = \frac{K_x}{t_x} L^2 \tag{2.8}$$

$$C_p = \frac{Q / LT_M}{\rho} \tag{2.9}$$

$$\kappa = \alpha C_p \rho \tag{2.10}$$

2.10 SQUID

A Superconducting Quantum Interference Device (SQUID) was used to investigate the magnetic properties of the samples. The magnetisation (M) and magnetic susceptibility (χ) can be determined and used to investigate any ordering of unpaired electrons within a crystal structure.

Magnetic measurements were performed at the Centre for Science at Extreme Conditions (CSEC) based at the University of Edinburgh's King's Buildings Campus and at the ISIS facility at Rutherford Appleton Laboratories. In both instances, a Quantum Design XL SQUID susceptometer was used. Approximately 30 mg of powdered sample was loaded at room temperature into gelatine capsules. Susceptibility data were collected over the temperature range $2 \leq T\ (K) \leq 300$, both after cooling in a zero applied field (zfc) and in a measuring field (fc) of 1000 G. Data were corrected for the diamagnetism of the gelatine capsule and for intrinsic core diamagnetism. This was achieved by subtracting the capsule correction ($M^{capsule}$) from the measured value of M. The capsule correction was calculated from the weight of the capsule ($Mass_{capsule}$) in mg, the field strength in Gauss and a constant for gelatine as shown in (2.11). In addition, for selected samples, magnetisation data were collected as a function of field at 5 K, over the field range $0 \leq H\ (kG) \leq 10$.

$$M^{capsule} = -3.188 \times 10^{-10} \times Mass_{capsule} \times field \tag{2.11}$$

2.11 Thermogravimetric Analysis

The thermal stability of Co_3SnInS_2 was investigated by thermogravimetric analysis (TGA) using a DuPont Instruments 951 Thermal Analyser. Approximately 10 mg of powdered sample was placed in a silica crucible and hung using a platinum wire from a balance. The sample was heated from room temperature up to 1000 °C at a rate of 5 °C min^{-1}. Measurements under both oxygen and nitrogen flows of 60 mL min^{-1} were undertaken.

2.12 X-ray Photoelectron Spectroscopy

X-ray Photoelectron Spectroscopy (XPS) is an analytical technique used to investigate the surface of materials using soft X-rays.[75] X-rays produce a photoelectron emission according to equation (2.12), which shows the relationship between the kinetic energy (E_K) of the photoelectrons measured during the experiment, the energy of the X-ray source ($h\nu$) and the binding energy (E_B) of the electrons in the solid. Binding energies are dependent on what electron shell they are ejected from. Observed emissions for some elements are sufficiently different that they can be used to distinguish between the different oxidation states.

$$E_K = h\nu - E_B \tag{2.12}$$

XPS data were recorded for five samples in the $Co_3Sn_{2-x}In_xS_2$ ($0 \leq x \leq 2$) series at the Nexus facility, Newcastle University. Ingots from hot-pressed pellets of x = 0, 0.4, 1, 1.6 and 2 were cleaned by sputtering for 600 s with monoatomic Ar ions at 1 keV to remove as much surface impurity as possible. Measurements were performed in the presence of a flood gun, which is a charge neutralisation method that generates low energy electrons and Ar^+ ions near the vicinity of the surface. If the surface becomes positively charged it attracts the electrons and if negatively charged it attracts the Ar^+ ions.

2.13 ^{119}Sn Mössbauer Spectroscopy

Mössbauer spectroscopy is based on the recoilless emission and resonant absorption of gamma radiation by atomic nuclei.[76] A radioactive isotope of the element to be investigated is used to generate the γ-rays. Figure 2.11 shows a schematic of a

Mössbauer instrument. The source is driven forwards and back periodically. The γ-rays are collimated before being transmitted through the sample towards the detector.

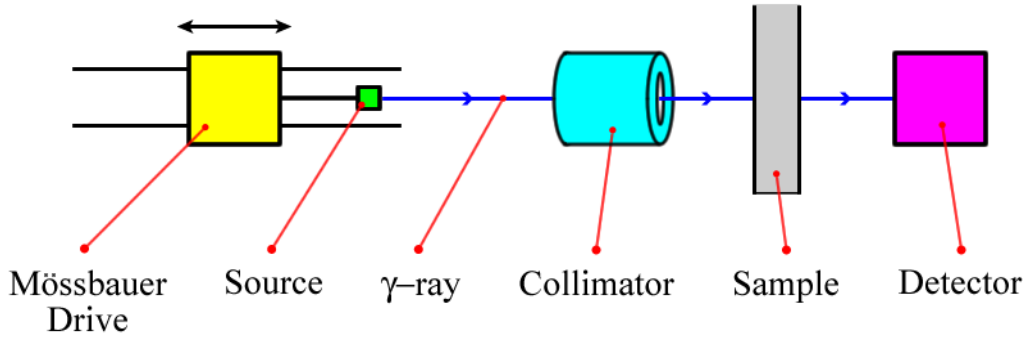

Figure 2.11: Schematic of Mössbauer instrument.

^{119}Sn Mössbauer spectroscopy was used to investigate the oxidation state of tin in $Co_3Sn_{2-x}In_xS_2$. Experiments were performed at the Laboratoire AIME, Universite Monpellier 2 by Prof. Jean-Claude Jumas. The ^{119}Sn Mössbauer spectra were recorded in transmission mode and in constant acceleration mode. The source used for the experiment was ^{119m}Sn embedded in a $CaSnO_3$ matrix. The velocity scale was calibrated with the magnetic sextet of a high-purity iron foil as the reference absorber and ^{57}Co (Rh) was used as the source. The spectra were fitted with Lorentzian profiles using the least-squares method and the errors regarding the hyperfine parameters were found to be smaller than 0.01 mm s^{-1} for the different $Co_3Sn_{2-x}In_xS_2$ compounds. The total error is estimated to be about 0.03 mm s^{-1}. The isomer shift values are given relative to the δ value of a $BaSnO_3$ spectrum recorded at room temperature. The absorbers containing 1–2 mg cm^{-2} of ^{119}Sn were prepared inside a glove box under an argon atmosphere. Powder samples were mixed with Apiezon vacuum grease and placed between two Kapton films. The sample holder was then sealed to prevent air contact.

Chapter 3 – Jamesonite - Benevidesite Series ($Fe_{1-x}Mn_xPb_4Sb_6S_{14}$)

3.1 Introduction

The high Seebeck coefficient observed in Jamesonite ($FePb_4Sb_6S_{14}$) is comparable to that of undoped Bi_2Te_3 at ambient temperatures. Therefore it has the potential to be a new structural category of thermoelectric material. Benavidesite ($MnPb_4Sb_6S_{14}$) is a known structural analogue, where manganese replaces iron. Both are found in nature and have synthetic equivalents. Previous studies have shown that both analogues order magnetically.[49,50] However, they have been observed to have different magnetic structures. Investigations of the magnetism in mixed iron and manganese analogues could show the effects of composition on the magnetic structure and the electrical properties.

In this chapter, the results obtained during the study of $Fe_{1-x}Mn_xPb_4Sb_6S_{14}$ ($0 \leq x \leq 1$) are outlined. A series of materials for which Jamesonite and Benavidesite are end members has been prepared. Samples of $Fe_{1-x}Mn_xPb_4Sb_6S_{14}$ discussed in this chapter were synthesised using high temperature solid-state reactions, as described in section 2.1.1. Structural investigations using powder X-ray and neutron diffraction were undertaken to observe the effects of substitution. The magnetic properties have been studied to investigate the competition between the two possible magnetic structures. The effect of composition on the electrical and thermal transport properties has also been determined.

3.2 Structural Investigations

3.2.1 Powder X-ray Diffraction

The purity of samples in the series $Fe_{1-x}Mn_xPb_4Sb_6S_{14}$ ($0 \leq x \leq 1$) was determined using powder X-ray diffraction (Figure 3.1). Lattice parameter refinements were performed on single phase samples using the powder X-ray diffraction data (Figure 3.2) and the Topas3[68] software package. Refinements were carried out using the space group $P2_1/a$. The substitution of the smaller Fe^{2+} by the larger Mn^{2+} ion (ionic radius: Fe = 92 pm, Mn = 97 pm)[77], led to an increase in all the lattice parameters. The refined lattice parameters were used as input to the initial structural model for full structural refinement using the powder neutron diffraction data.

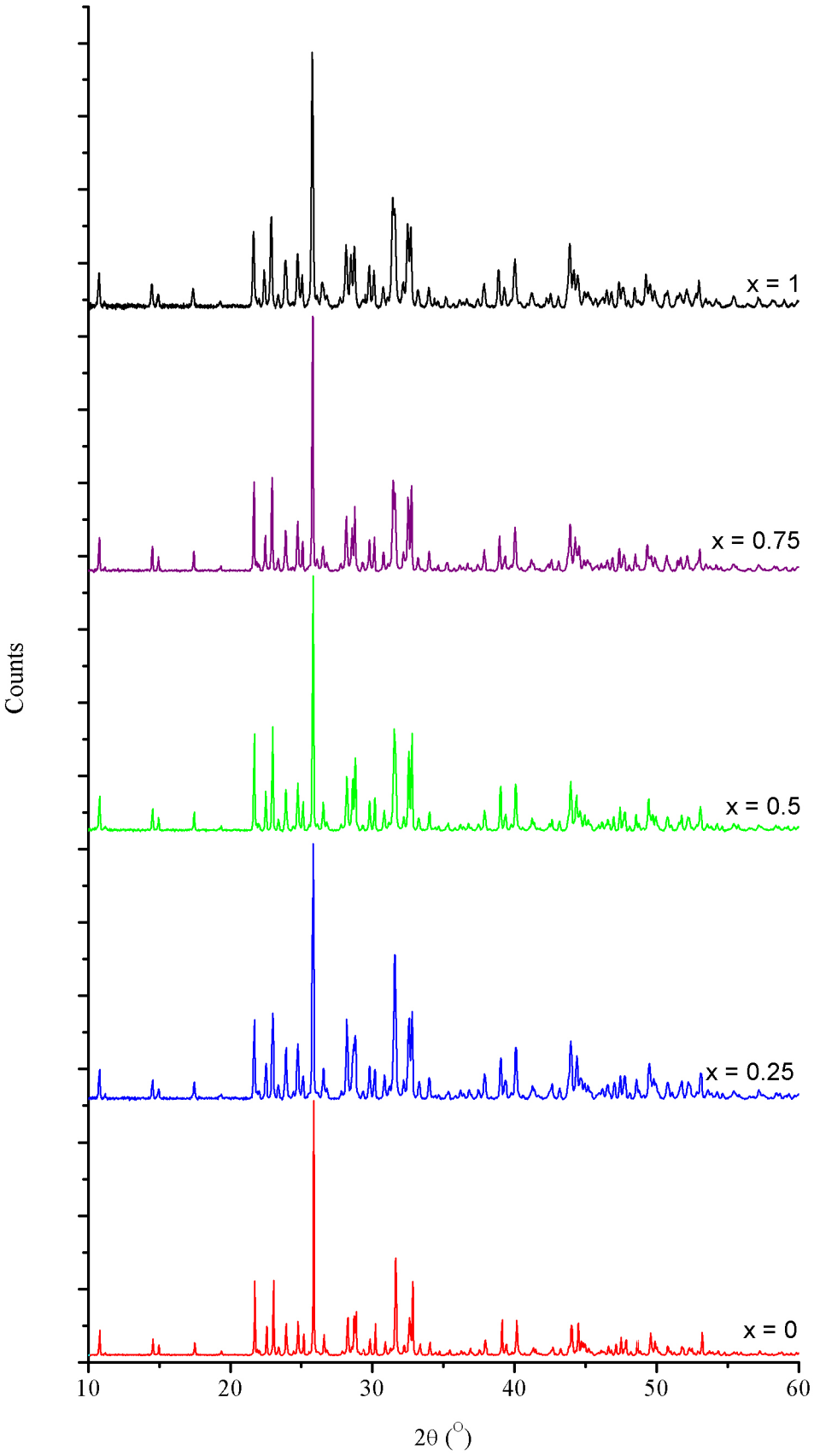

Figure 3.1: Powder X-ray diffraction patterns of $Fe_{1-x}Mn_xPb_4Sb_6S_{14}$ ($0 \leq x \leq 1$) in the range $10 \leq 2\theta\ (°) \leq 60$.

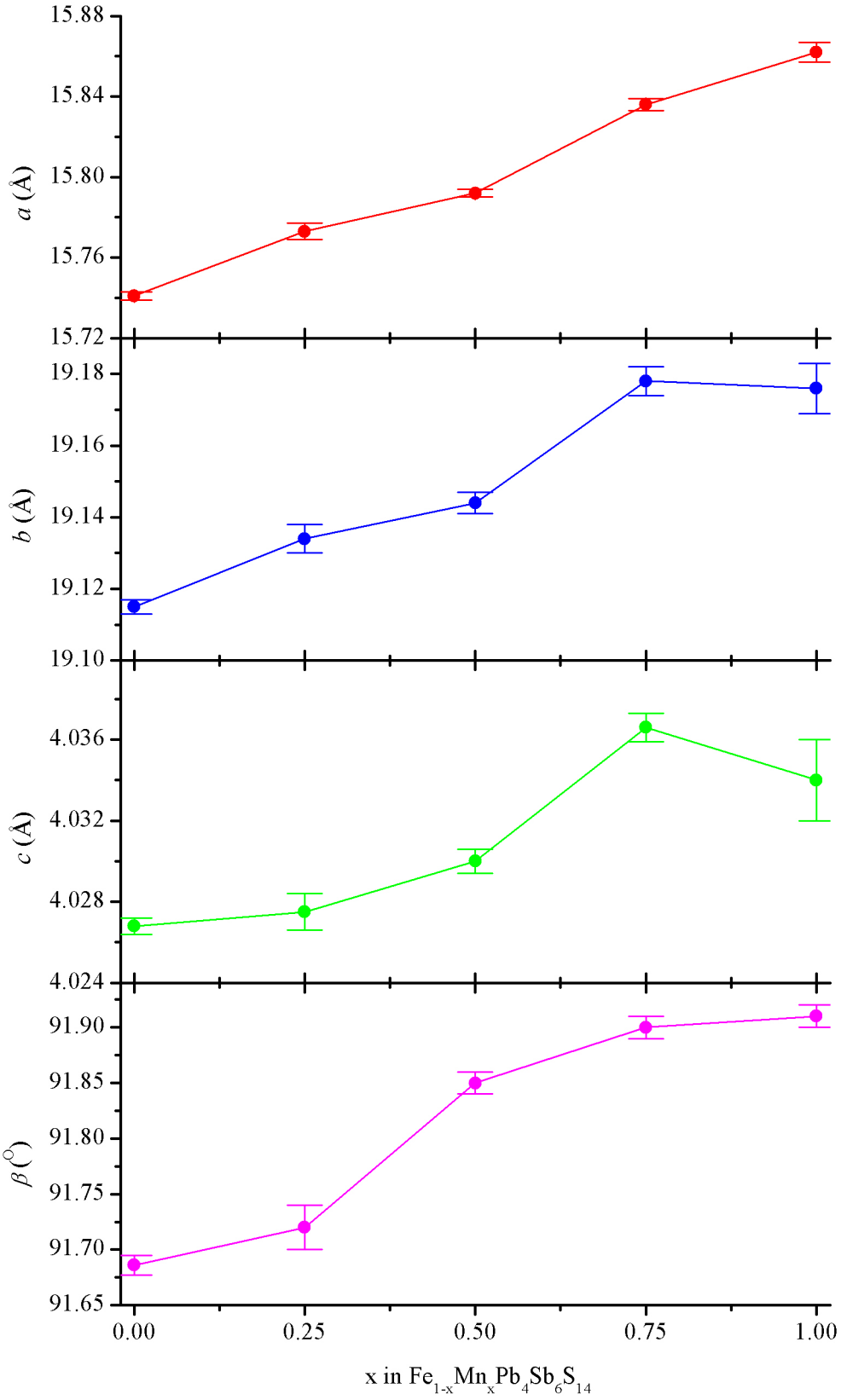

Figure 3.2: Lattice parameters of $Fe_{1-x}Mn_xPb_4Sb_6S_{14}$ ($0 \leq x \leq 1$) determined in the space group $P2_1/a$ from unit cell refinements using powder X-ray diffraction data.

3.2.2 Powder Neutron Diffraction

Powder neutron diffraction experiments were performed on both the original Polaris and GEM diffractometers as described in sections 2.3.1 and 2.3.2 respectively. Data were collected at room temperature and at 2 K for all samples. Additional temperature steps were collected for the two end-member phases x = 0 and x =1.

Structural refinements using the Rietveld method were performed with the GSAS[69] software package. Diffraction data from GEM's 154°, 91° and 35° detector banks were used in the structural refinements of phases corresponding to x = 0 (Figure 3.3 and Appendix C) and 0.5 (Appendix E). Diffraction data from the 145° and 35° banks on Polaris were utilised for samples with x = 0.25 (Figure 3.4 and Appendix D), 0.75 (Appendix F) and 1 (Appendix G). The parameters refined during Rietveld refinements were the background, histogram scale factor, absorption coefficient (Debye-Scherrer), lattice parameters, atomic coordinates, thermal parameters and profile coefficients (sig-1 and gam-1). The site occupancy factors of iron and manganese were fixed at values corresponding to the nominal stoichiometry of each sample. The Goodness of Fit indices, the lattice parameters, atomic coordinates and thermal parameters from the Rietveld refinement of $FePb_4Sb_6S_{14}$ using neutron diffraction data from the GEM diffractometer are shown in Table 3.1. Refined parameters corresponding to the sample with x = 0.5 are presented in Appendix H. The Goodness of Fit indices, the lattice parameters, atomic coordinates and thermal parameters from the Rietveld refinement of $Fe_{0.25}Mn_{0.75}Pb_4Sb_6S_{14}$ using neutron diffraction data from the Polaris diffractometer are presented in Table 3.2. Refined parameters corresponding to the samples with x = 0.75 and x = 0.25 are presented in Appendix H. Selected bond lengths and angles for all compositions are presented in Table 3.3.

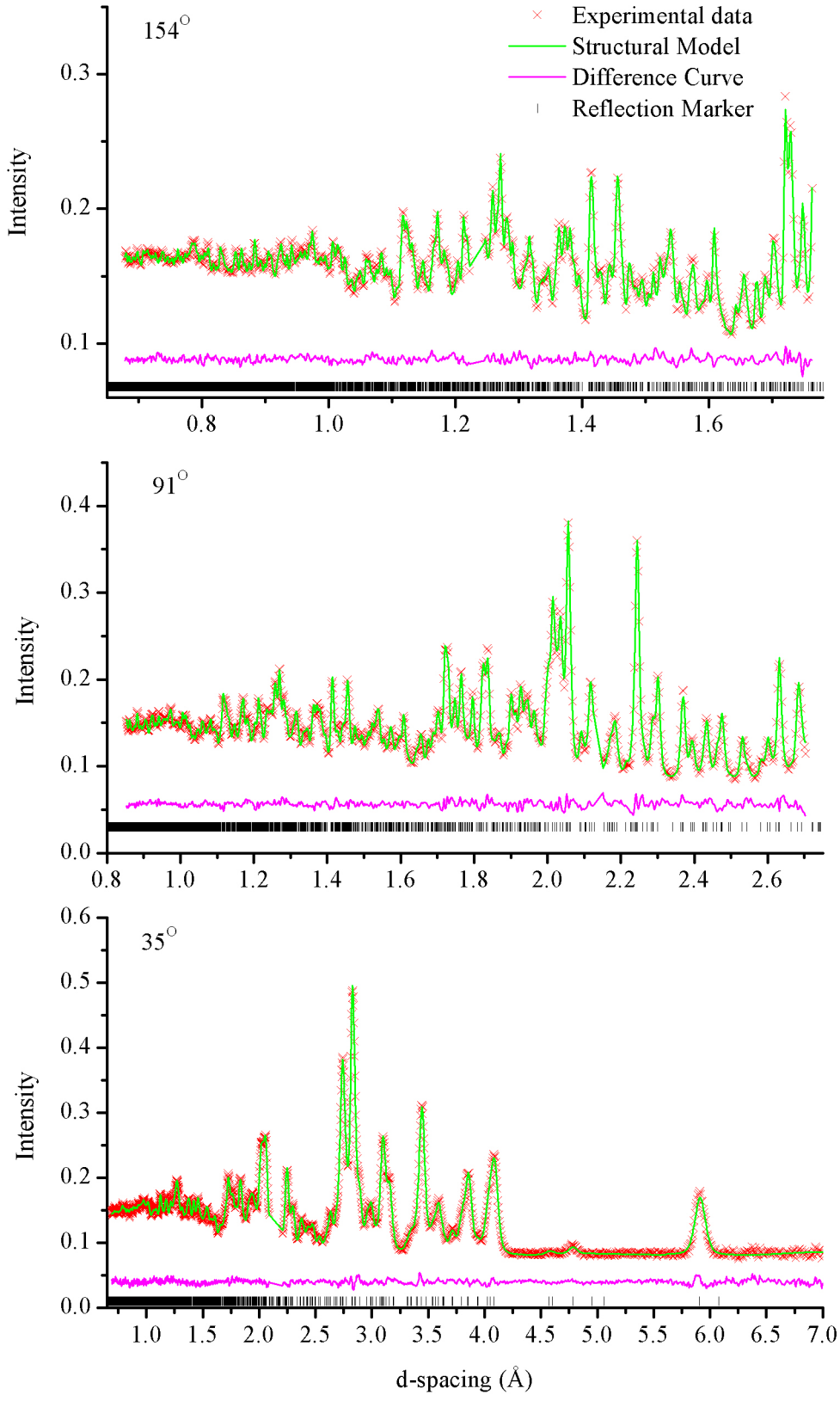

Figure 3.3: Powder neutron diffraction data from the 154°, 91° and 35° detector banks on the GEM diffractometer and the fit of the structural model for $FePb_4Sb_6S_{14}$ at 298 K.

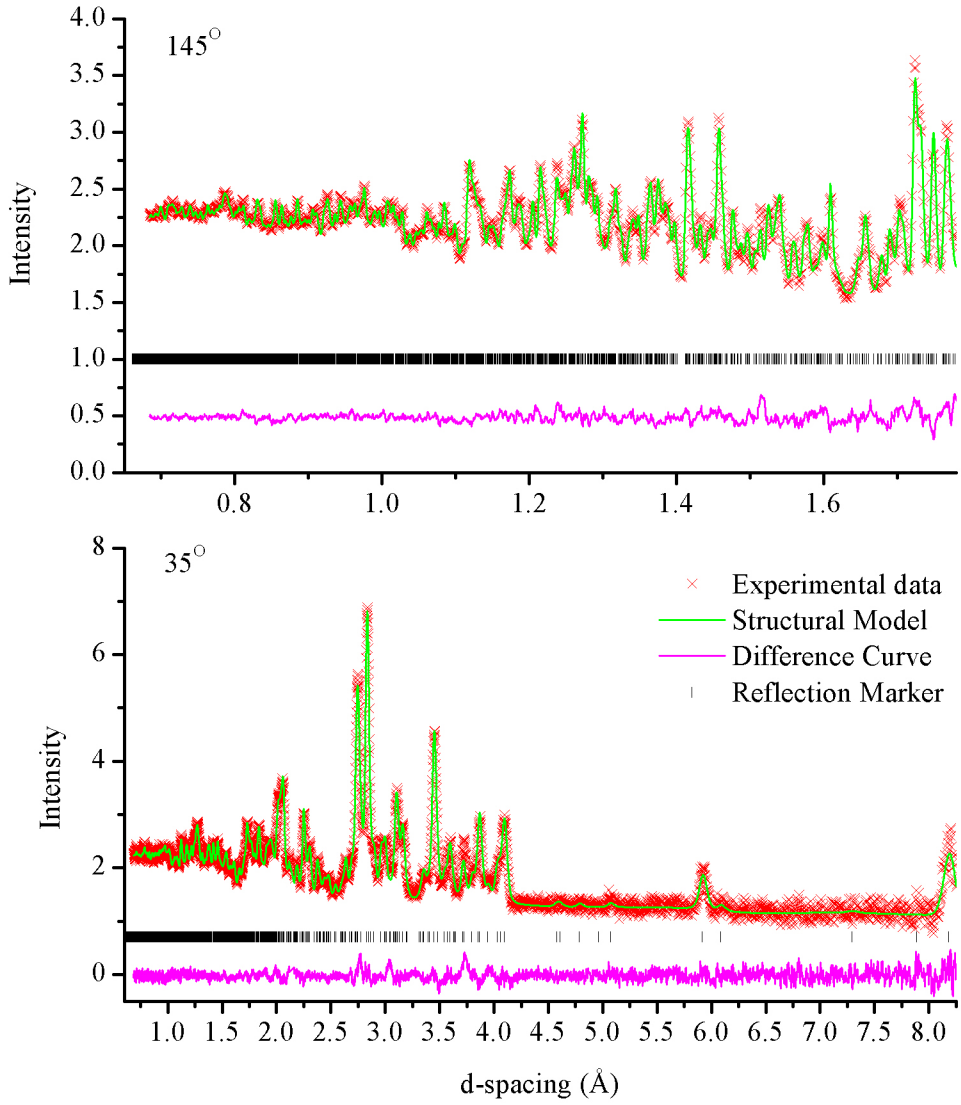

Figure 3.4: Powder neutron diffraction data from the 145° and 35° detector banks on the Polaris diffractometer and the fit of the structural model for $Fe_{0.75}Mn_{0.25}Pb_4Sb_6S_{14}$ at 298 K.

Table 3.1: Final refined parameters for $FePb_4Sb_6S_{14}$ obtained from Rietveld refinements using powder neutron diffraction data collected on the GEM diffractometer. Space Group: *$P2_1/a$.*

atom		*298 K*	*150 K*	*10 K*	*2 K*
Fe[a]	Uiso ($Å^2$)	0.019(1)	0.0059(9)	0.0025(9)	0.0042(7)
Pb(1)	x	-0.0744(1)	-0.0741(1)	-0.0729(1)	-0.0729(1)
	y	0.2613(1)	0.2619(1)	0.2625(1)	0.2626(1)
	z	0.0579(6)	0.0553(5)	0.0521(5)	0.0516(5)
Pb(2)	x	-0.3161(2)	-0.3149(2)	-0.3147(1)	-0.3144(1)
	y	0.3596(1)	0.3602(1)	0.3608(1)	0.3607(1)
	z	0.0352(6)	0.0310(5)	0.0288(5)	0.0296(5)
Pb	Uiso ($Å^2$)	0.0201(8)	0.0087(6)	0.0044(6)	0.0046(4)
Sb(1)	x	0.1313(2)	0.1321(2)	0.1325(2)	0.1324(2)
	y	0.3408(2)	0.3412(2)	0.3412(2)	0.3408(2)
	z	-0.3868(9)	-0.3899(9)	-0.3949(9)	-0.3958(9)
Sb(2)	x	-0.1035(3)	-0.1022(2)	-0.1026(2)	-0.1024(2)
	y	0.4520(2)	0.4536(2)	0.4541(2)	0.4544(2)
	z	-0.3862(9)	-0.3846(9)	-0.3892(9)	-0.3883(9)
Sb(3)	x	-0.1807(3)	-0.1801(3)	-0.1791(2)	-0.1791(2)
	y	0.0634(2)	0.0638(2)	0.0647(2)	0.0646(2)
	z	0.4070(9)	0.4123(9)	0.4158(8)	0.4153(8)
Sb	Uiso ($Å^2$)	0.0139(9)	0.0073(7)	0.0054(7)	0.0065(5)
S(1)	x	-0.2150(4)	-0.2145(4)	-0.2158(4)	-0.2157(4)
	y	0.4980(4)	0.4967(4)	0.4968(3)	0.4974(4)
	z	0.025(2)	0.023(2)	0.023(1)	0.022(2)
S(2)	x	-0.0766(5)	-0.0779(5)	-0.0777(4)	-0.0777(5)
	y	0.1039(4)	0.1046(3)	0.1053(3)	0.1052(3)
	z	-0.014(2)	-0.013(2)	-0.011(2)	-0.011(2)
S(3)	x	0.0935(5)	0.0926(4)	0.0924(4)	0.0926(4)
	y	0.0432(4)	0.0430(3)	0.0421(3)	0.0420(3)
	z	-0.475(2)	-0.478(2)	-0.481(2)	-0.481(2)
S(4)	x	0.0541(5)	0.0545(4)	0.0531(4)	0.0535(4)
	y	0.2306(4)	0.2313(3)	0.2310(4)	0.2310(3)

	z	-0.428(2)	-0.428(2)	-0.434(2)	-0.434(2)
S(5)	x	-0.1822(5)	-0.1815(4)	-0.1806(4)	-0.1811(4)
	y	0.3405(4)	0.3406(4)	0.3409(3)	0.3413(3)
	z	-0.449(2)	-0.457(2)	-0.456(2)	-0.457(2)
S(6)	x	-0.0004(5)	0.0005(5)	-0.0002(4)	-0.0001(4)
	y	0.3976(4)	0.3976(3)	0.3977(3)	0.3977(3)
	z	0.049(2)	0.052(2)	0.053(2)	0.052(2)
S(7)	x	-0.2752(5)	-0.2750(4)	-0.2741(4)	-0.2741(4)
	y	0.2027(4)	0.2038(4)	0.2039(3)	0.2043(3)
	z	0.075(2)	0.066(2)	0.064(2)	0.062(2)
S	Uiso ($Å^2$)	0.0149(9)	0.0054(7)	0.0063(8)	0.0071(6)
	a ($Å^2$)	15.7430(4)	15.7092(4)	15.7007(3)	15.7116(3)
	b ($Å^2$)	19.1195(4)	19.0784(4)	19.0486(4)	19.0607(4)
	c ($Å^2$)	4.02702(9)	4.01515(8)	4.00081(8)	4.00320(8)
	β (°)	91.700(3)	91.683(2)	91.655(2)	91.659(2)
	R_{wp} 35° (%)	2.1	1.5	1.5	1.5
	R_{wp} 91° (%)	2.1	2.2	2.3	2.4
	R_{wp} 154° (%)	1.4	1.1	1.1	1.1
	χ^2	1.5	2.0	2.5	2.6

Fe on 1(a) 0 0 0.

Table 3.2: Final refined parameters for $Fe_{0.25}Mn_{0.75}Pb_4Sb_6S_{14}$ obtained from Rietveld refinements using powder neutron diffraction data collected on the Polaris diffractometer. Space Group: $P2_1/a$.

atom		*298 K*	*2 K*
Fe / Mn[a]	Uiso (Å^2)	0.0145(5)	0.00550(4)
Pb(1)	x	-0.0737(1)	-0.0730(1)
	y	0.26093(8)	0.2615(1)
	z	0.0678(4)	0.0591(6)
Pb(2)	x	-0.3137(1)	-0.3127(2)
	y	0.35834(8)	0.3601(1)
	z	0.0419(4)	0.0335(6)
Pb	Uiso (Å^2)	0.0171(4)	0.00424(3)
Sb(1)	x	0.1300(1)	0.1315(2)
	y	0.3398(1)	0.3404(2)
	z	-0.3748(7)	-0.382(1)
Sb(2)	x	-0.1036(2)	-0.1032(2)
	y	0.4514(2)	0.4542(2)
	z	-0.3835(7)	-0.387(1)
Sb(3)	x	-0.1804(2)	-0.1792(3)
	y	0.0639(2)	0.0647(2)
	z	0.4027(7)	0.401(1)
Sb	Uiso (Å^2)	0.0129(5)	0.0062(6)
S(1)	x	-0.2124(4)	-0.2122(5)
	y	0.4976(3)	0.4969(3)
	z	0.039(1)	0.020(2)
S(2)	x	-0.0788(3)	-0.0815(5)
	y	0.1076(3)	0.1066(4)
	z	-0.006(1)	-0.001(2)
S(3)	x	0.0975(3)	0.0947(4)
	y	0.0434(3)	0.0440(4)
	z	-0.479(1)	-0.482(2)
S(4)	x	0.0542(3)	0.0515(4)
	y	0.2325(3)	0.2292(4)

	z	-0.411(1)	-0.433(2)
S(5)	x	-0.1817(3)	-0.1833(4)
	y	0.3404(3)	0.3441(4)
	z	-0.437(1)	-0.446(2)
S(6)	x	0.0017(3)	-0.0007(4)
	y	0.3987(3)	0.4007(4)
	z	0.063(1)	0.057(2)
S(7)	x	-0.2750(4)	-0.2714(4)
	y	0.2051(3)	0.2051(4)
	z	0.086(2)	0.060(2)
S	Uiso ($Å^2$)	0.0150(5)	0.0065(5)
	a ($Å^2$)	15.8361(3)	15.8037(4)
	b ($Å^2$)	19.1793(3)	19.1199(4)
	c ($Å^2$)	4.03629(6)	4.016396(6)
	β (°)	91.901(1)	91.825(2)
	R_{wp} 35° (%)	3.3	1.8
	R_{wp} 145° (%)	1.6	0.8
	χ^2	1.1	1.0

Fe / Mn site occupancy factor 0.25 / 0.75 on 1(a) 0 0 0.

The values of the Goodness of Fit indices suggest the structural model is correct and comparison of the structure as a function of composition is valid. The lattice parameters obtained from the structural refinements using room temperature neutron diffraction data are similar to those obtained using powder X-ray diffraction and similar compositional variation trends are observed. For each sample, the unit cell contracts as the temperature is reduced. The distortion of the bond lengths and bond angles of the MS_6 octahedral chain (Figure 3.5) are presented in Table 3.3. The *M*-S bonds forming the edge-sharing chain are lengthened and the ∠S-*M*-S decreases. This is mirrored in the increase in the *c* lattice parameter and the separation between the *M* ions within the chain. The separation between adjacent chains is always larger than 12.3 Å, however it increases with manganese content in the phase.

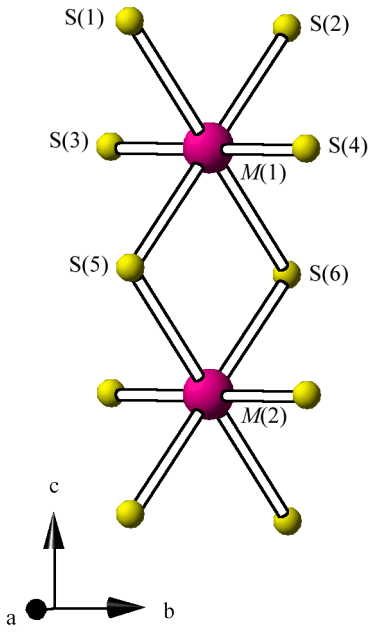

Figure 3.5: MS_6 octahedral chain found in $Fe_{1-x}Mn_xPb_4Sb_6S_{14}$ ($0 \leq x \leq 1$) showing the atom numbering scheme.

The same nuclear structure obtained from structural refinements using the room temperature data was fitted to the majority of patterns collected below ambient temperatures. However, additional Bragg reflections due to magnetic scattering were observed in the 2 K data set recorded for $MnPb_4Sb_6S_{14}$ (Figure 3.6). The magnetic structure has a propagation vector of k = (00½), which means there is a doubling of the unit cell along the *c* axis. The lattice parameters, atomic coordinates and thermal parameters from the nuclear structure were retained and an additional magnetic only phase was added to the refinement. The *P1* space group was selected for the magnetic phase and unit cell parameters *a*, *b*, *α*, *β* and *γ* were constrained to the values of the nuclear structure. The *c* parameter was constrained to be twice that of the nuclear structure. Four manganese sites were added to the magnetic structure based on the symmetry of the single crystallographic site in the nuclear structure. Magnetic moments pointing along the *b* axis were placed on these sites in an antiferromagnetic configuration. A refined value of 2.58(9) μ_B and antiferromagnetic alignment along the *b* axis was determined (Table 3.4). This ordered moment is smaller than the spin-only value of 5 μ_B expected for high spin Mn^{2+}:d^5. This suggests that the material is not fully ordered at this temperature. Other possibilities for this include the covalency of sulphur removing electron density from the manganese.

Table 3.3: Bond lengths, interatomic distances and bond angles of the MS_6 edge-sharing chain found in $Fe_{1-x}Mn_xPb_4Sb_6S_{14}$ ($0 \leq x \leq 1$) at 298 and 2 K.

x	*0*		*0.25*		*0.5*		*0.75*		*1*	
T (K)	*298*	*2*	*298*	*2*	*298*	*2*	*298*	*2*	*298*	*2*
M(1) – S(1/6) (Å) × 2	2.670(8)	2.628(7)	2.686(7)	2.629(1)	2.689(7)	2.69(4)	2.700(5)	2.660(7)	2.735(5)	2.683(7)
M(1) – S(2/5) (Å) × 2	2.583(7)	2.574(6)	2.618(7)	2.515(8)	2.602(6)	2.59(3)	2.647(5)	2.624(7)	2.648(5)	2.665(8)
M(1) – S(3/4) (Å) × 2	2.324(7)	2.346(7)	2.371(7)	2.441(8)	2.406(6)	2.33(3)	2.422(5)	2.410(7)	2.439(5)	2.429(7)
M(1) – *M*(2) (Å)	4.0270(1)	4.0032(1)	4.0280(1)	4.0107(1)	4.0299(1)	4.0182(5)	4.0363(1)	4.0164(1)	4.0323(1)	4.0170(1)
M(1) – *M*(1) (Å)	12.383(1)	12.351(1)	12.404(1)	12.373(1)	12.408(1)	12.386(1)	12.436(1)	12.403(1)	12.445(1)	12.413(1)
∠ S(1/5)-*M*(1)-S(2/6) (°) × 2	79.93(3)	79.35(3)	81.20(3)	85.40(3)	80.78(3)	81.02(3)	82.91(2)	81.05(2)	83.01(2)	82.64(3)
∠ S(1/2)-*M*(1)-S(5/6) (°) × 2	100.07(3)	100.65(3)	98.81(3)	94.59(3)	99.22(3)	98.98(3)	97.09(2)	98.96(2)	96.99(2)	97.36(3)
∠ S(1/6)-*M*(1)-S(3/4) (°) × 2	91.59(3)	91.73(3)	89.23(3)	82.09(3)	92.56(3)	92.29(3)	92.30(2)	91.17(2)	91.42(2)	89.92(3)
∠ S(2/5)-*M*(1)-S(4/3) (°) × 2	90.94(3)	91.47(3)	89.88(3)	81.06(3)	91.66(3)	91.36(3)	91.58(2)	92.60(2)	92.14(2)	91.82(3)
∠ *M*(1)-S(5/6)-*M*(2) (°) × 2	100.07(3)	100.65(3)	98.81(3)	94.59(3)	99.25(3)	98.98(3)	97.09(2)	98.96(2)	96.99(2)	97.36(3)

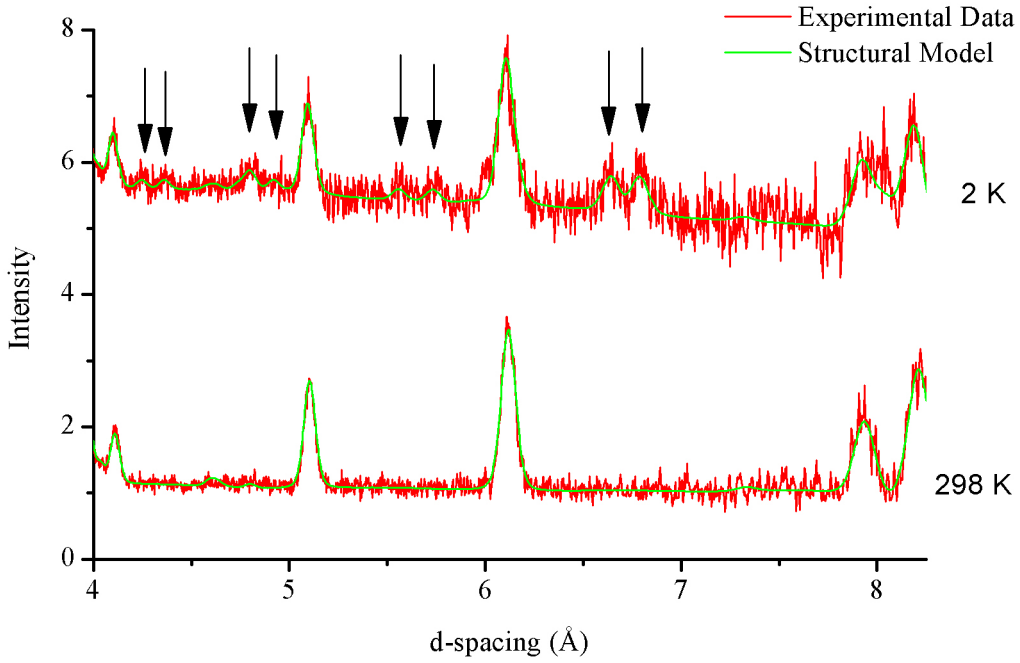

Figure 3.6: Comparison of diffraction patterns of $MnPb_4Sb_6S_{14}$ at 298 and 2 K. Arrows show peaks caused by magnetic scattering.

Table 3.4: Refined magnetic structure of the four manganese cations in the magnetic unit cell, generated from one crystallographic site, using the $MnPb_4Sb_6S_{14}$ powder neutron diffraction data collected at 2 K on the GEM diffractometer.

atom	*x*	*y*	*z*	*Mx*	*My*	*Mz*	M
Mn(1)	0	0	0	0	2.58(9)	0	2.58(9)
Mn(2)	0.5	0.5	0	0	2.58(9)	0	2.58(9)
Mn(3)	0	0	0.5	0	-2.58(9)	0	2.58(9)
Mn(4)	0.5	0.5	0.5	0	-2.58(9)	0	2.58(9)

Magnetic scattering was only observed in the neutron diffraction data set of $MnPb_4Sb_6S_{14}$ collected at 2 K. The magnetic moment determined during the refinement is lower than the spin-only value of 5 μ_B. This is likely due to incomplete long-range three-dimensional order at this temperature. One-dimensional order along individual chains exists, but full order between the chains does not. The separation between the chains of 12.413 Å is quite large for moments to interact and is a possible reason for the incomplete order between chains. As has previously been observed in the literature,[49]

magnetic scattering was expected for the iron-only phase. However the Jamesonite sample analysed in the previous literature study[49] was a natural sample rather than one with a definitive composition. This suggests that the natural sample has a slightly different composition to the pure synthetic sample prepared for these experiments. Patterns collected for the mixed transition-metal phases ($0.25 \leq x \leq 0.75$) suggest there is no long-range order in these samples down to 2 K.

3.3 Magnetic Properties

Previous studies indicated that the magnetic structures of Jamesonite and Benavidesite, while both being antiferromagnetic, differed from each other. Powder neutron diffraction experiments in the present work did not show any magnetic reflections in the pattern of $Fe_{1-x}Mn_xPb4Sb6S14$ ($0 \leq x \leq 0.75$) at 2 K. However the pattern collected for the fully manganese-substituted analogue did. Magnetic property measurements of all phases were performed in an attempt to determine the effects of composition on the magnetic behaviour.

3.3.1 Magnetic Susceptibility Measurements

Magnetic susceptibility measurements (Figure 3.7) were performed on samples as described in section 2.10. With the exception of the phase with $x = 0.25$, the magnetic susceptibility increases with increasing manganese content, consistent with the higher effective magnetic moment of manganese compared to iron. A broad maximum, which becomes more defined as manganese is added, beginning around 50 K with a maximum around 30 K is present in the $\chi_{mol}(T)$ data. This is induced by short-range correlations along the MS_6 chains. The susceptibility shows an increase again below 20 K, with the increase being larger for more iron-rich sample. There is a divergence at the maximum zero-field-cooled magnetic susceptibility (T_M) between the zero-field-cooled and field-cooled measurements for samples where $x \leq 0.5$ (Figure 3.8). As manganese is added, T_M decreases. For samples with $x \geq 0.75$, no divergence between the zero-field-cooled and field-cooled magnetic susceptibility measurements is observed. Structural refinements indicate that the separation between the chains is increased through the addition of manganese. This can be linked to the increase across the series in both the extent in the local ordering and the decrease in T_M. The increased distance means that intra-chain interactions begin to dominate. The increase in definition of the broad maxima as a function of manganese content suggests intra-chain interactions are more dominant. It also means that inter-chain order occurs at lower T_M as manganese content

is increased. Overall, magnetic susceptibility data suggests that there is a gradual change in the nature of the magnetic interactions.

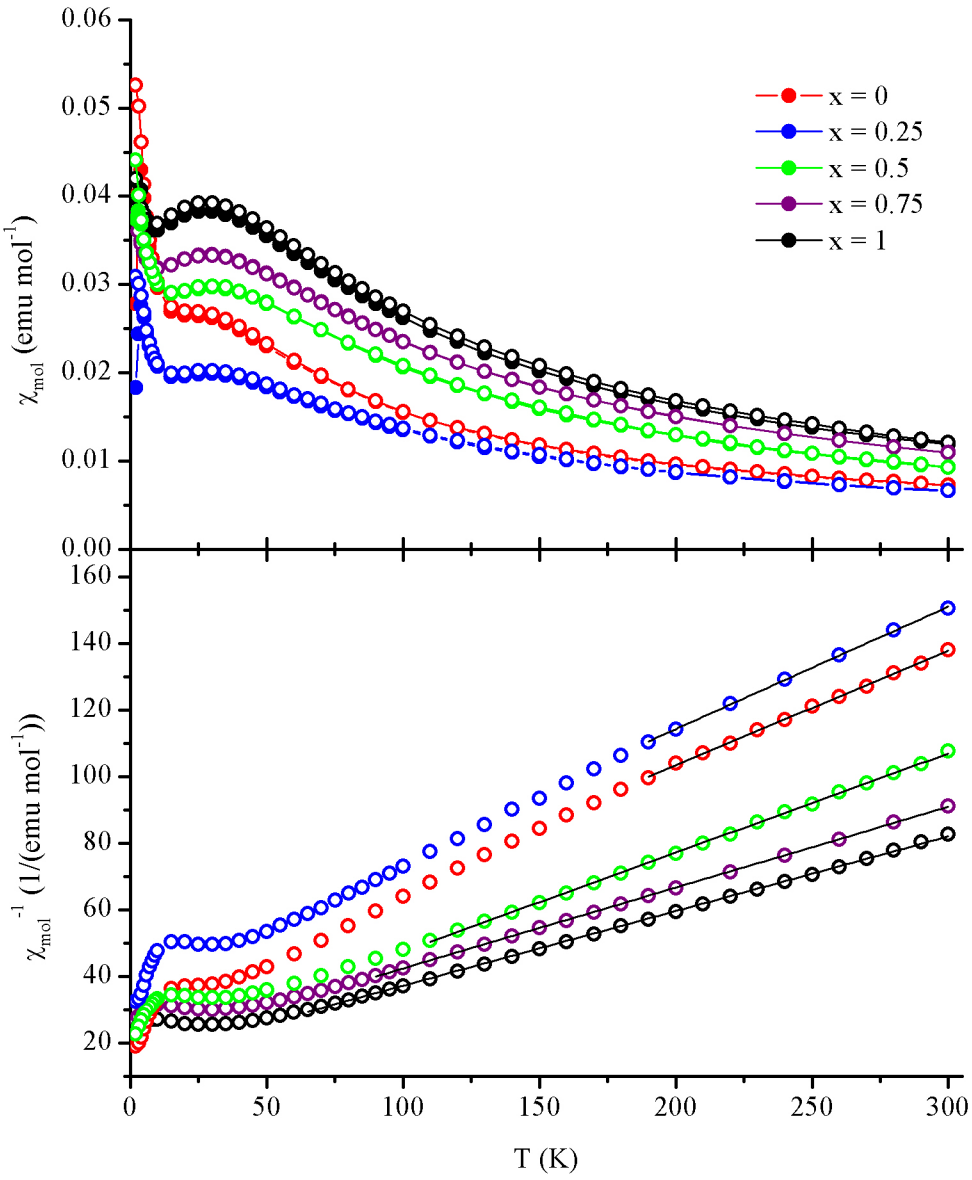

Figure 3.7: Temperature dependence of the zero-field-cooled (close circles) and field-cooled (open circles) molar magnetic susceptibility (top) and inverse of susceptibility (bottom) for $Fe_{1-x}Mn_xPb_4Sb_6S_{14}$ ($0 \leq x \leq 1$) between 2 and 300 K. The solid lines in the lower plot are the fits to the Curie-Weiss expression.

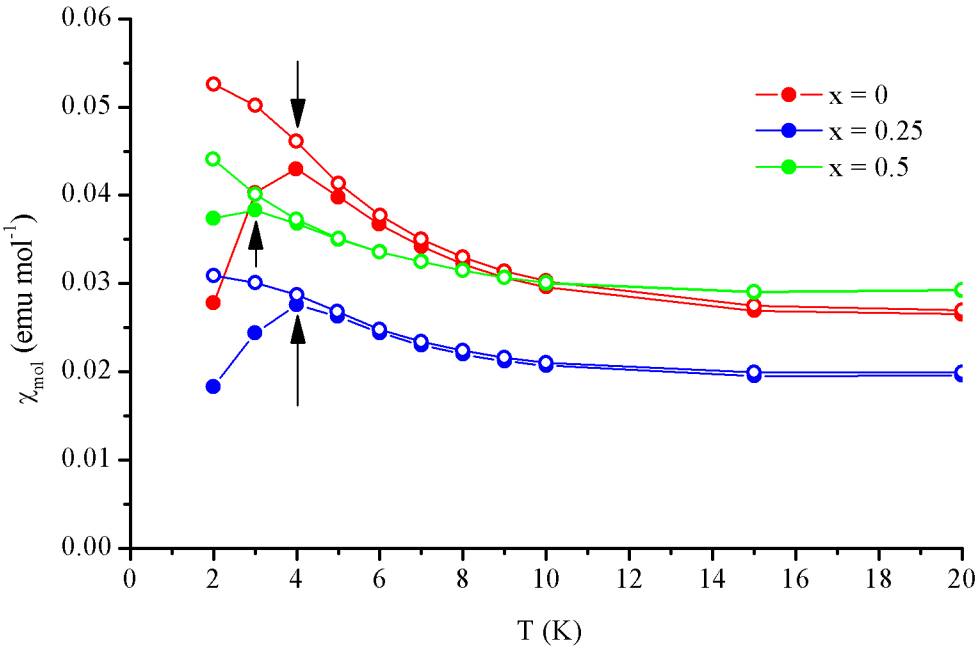

Figure 3.8: Divergence between the zero-field-cooled (closed circles) and field-cooled (open circles) susceptibilities data at T_M (marked with arrow) for $Fe_{1-x}Mn_xPb_4Sb_6S_{14}$ ($x \leq 0.5$).

Curie-Weiss paramagnetic behaviour is observed for all samples at higher temperatures. The range over which Curie-Weiss behaviour is observed extends to lower temperatures with the addition of manganese. The Curie constant (C) was calculated from the slope of the linear section of the plot of $1/\chi_{mol}$ against temperature. The Curie constant was then used to determine the Weiss constant and effective magnetic moment (μ_{eff}) (Table 3.5). The good agreement between the spin-only values calculated for the nominal composition and the experimental values of the Curie constant and the effective magnetic moment indicate that the moments are localised. The effective magnetic moments determined from the magnetic data indicate manganese and iron are high spin d^5 and d^6 respectively. The negative value of the Weiss constant indicates antiferromagnetic exchange interactions are dominant.

Table 3.5: Theoretical and experimental Curie constants, effective magnetic moments and Weiss constants for $Fe_{1-x}Mn_xPb_4Sb_6S_{14}$ ($0 \leq x \leq 1$).

x	*C-W Range (K)**	C_{TH}	*C*	$\mu_{eff(TH)}$	μ_{eff}	θ *(K)*
0	190 - 300	3	2.92(3)	4.90	4.83(4)	-102(3)
0.25	190 - 300	3.34	3.65(6)	5.17	5.40(5)	-148(4)
0.5	110 – 300	3.69	3.36(2)	5.43	5.18(1)	-59(2)
0.75	90 – 300	4.03	4.12(1)	5.68	5.74(1)	-75(1)
1	65 – 300	4.38	4.45(1)	5.92	5.97(1)	-66(1)

* Temperature ranges over which Curie-Weiss behaviour was observed.

3.4 Electrical and Thermal Transport Properties

3.4.1 Electrical Resistivity

Measurements of the electrical resistivity (Figure 3.9) were performed on hot-pressed ingots of samples (density ≥ 95% of crystallographic density) over the range $100 \leq T$ (K) ≤ 350 as described in section 2.7.1.2. Measurements of the electrical resistivity of $FePb_4Sb_6S_{14}$ increased as the temperature was reduced, which is typical of semiconducting behaviour. The same trend was observed for all compositions in the series. Plots of electrical resistivity are presented in Figure 3.9. The electrical resistivity increased as a function of manganese content. The resistance of $MnPb_4Sb_6S_{14}$ below 130 K was too large to be measured with our equipment. The substitution of Fe^{2+}:d^6 by Mn^{2+}:d^5 reduced the valence electron count of the material from 272 valence electrons per unit cell for the iron analogue, to 270 valence electrons by substituting iron by manganese. Density of State calculations[48] indicated that the highest filled bands for Jamesonite are the Fe(3d) orbitals and a small gap exists between the e_g and the t_{2g} states. In Jamesonite two iron atoms per unit cell generate six t_{2g}-related bands, which are filled with eight electrons, and four e_g-related bands filled with four electrons. It is likely Benavidesite has a similar band structure and while the e_g bands would have the same filling, the six t_{2g}-related states would be half filled with six electrons.

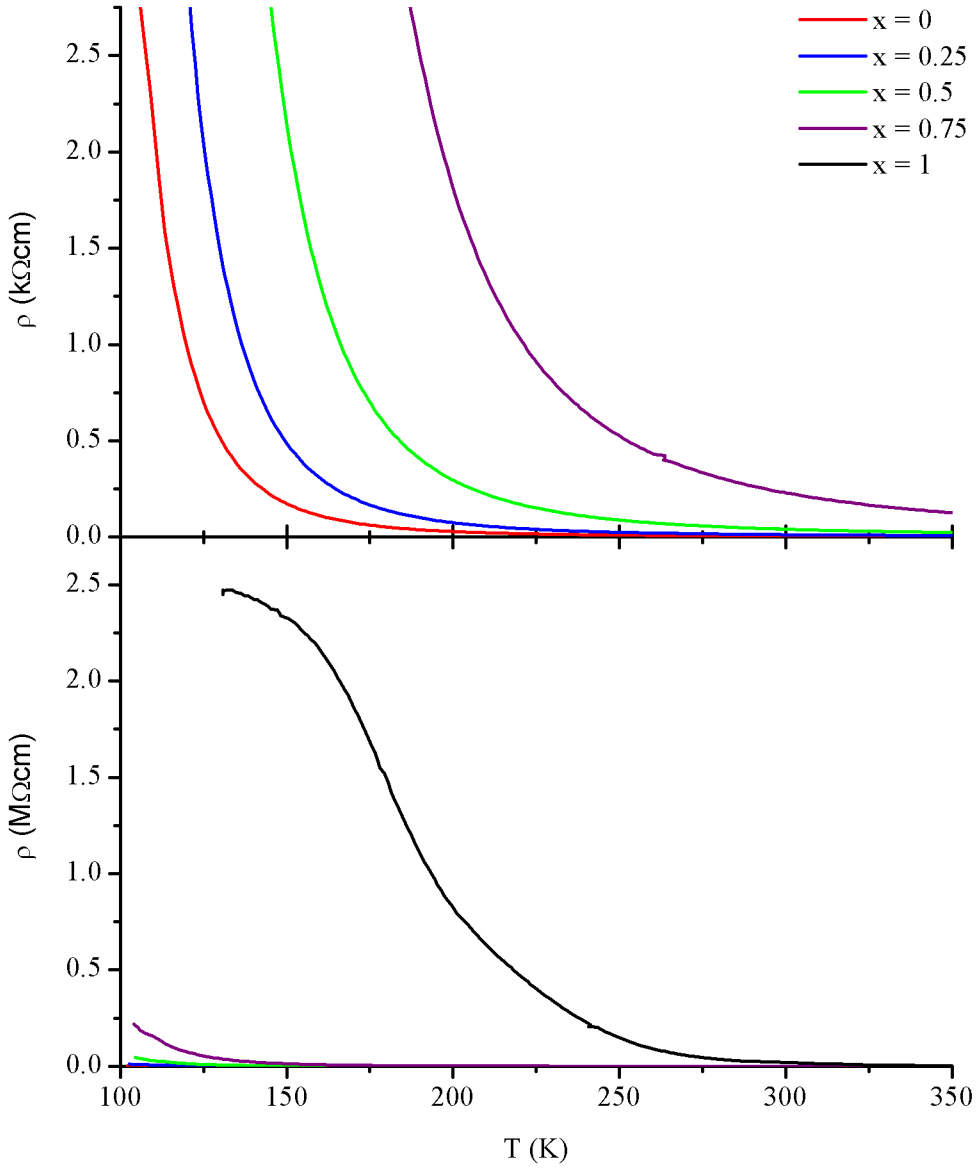

Figure 3.9: Electrical resistivity as a function of temperature for $Fe_{1-x}Mn_xPb_4Sb_6S_{14}$ ($0 \leq x \leq 1$) in the temperature range $100 \leq T\ (K) \leq 350$.

The room temperature electrical resistivity of Jamesonite (5 Ωcm) is lower than previously reported[48] (121 Ωcm). In previous studies pellets were prepared by cold-pressing and sintering, while pellets in this work were fabricated using a hot-press. The density of a pellet can affect the electrical resistivity, with less dense pellets giving a higher electrical resistivity because of an increase in grain boundary interactions and porosity. Repeating the cold-pressing technique from the literature, pellets with 85 % of the crystallographic density were prepared. However by hot-pressing, pellets with ≥ 95

% density were fabricated. This improvement in the density is likely to be the principal factor in the reduction of the electrical resistivity.

Plots of the natural log of the electrical resistivity as a function of the inverse temperature (Figure 3.10) were constructed to determine if materials followed the Arrhenius law (3.1). The linear fits of samples show Arrhenius type conduction and they were used to determine the band gap of each material. Divergence from Arrhenius like conduction exists at lower temperatures and suggests a change in conduction mechanism. The variable range hopping models for 1D, 2D and 3D conduction were investigated, but none could explain the conduction of the fully manganese substituted phase. The calculated band gaps are shown in Table 3.6.

$$\rho = \rho_0 e^{\frac{E_g}{2K_B T}} \tag{3.1}$$

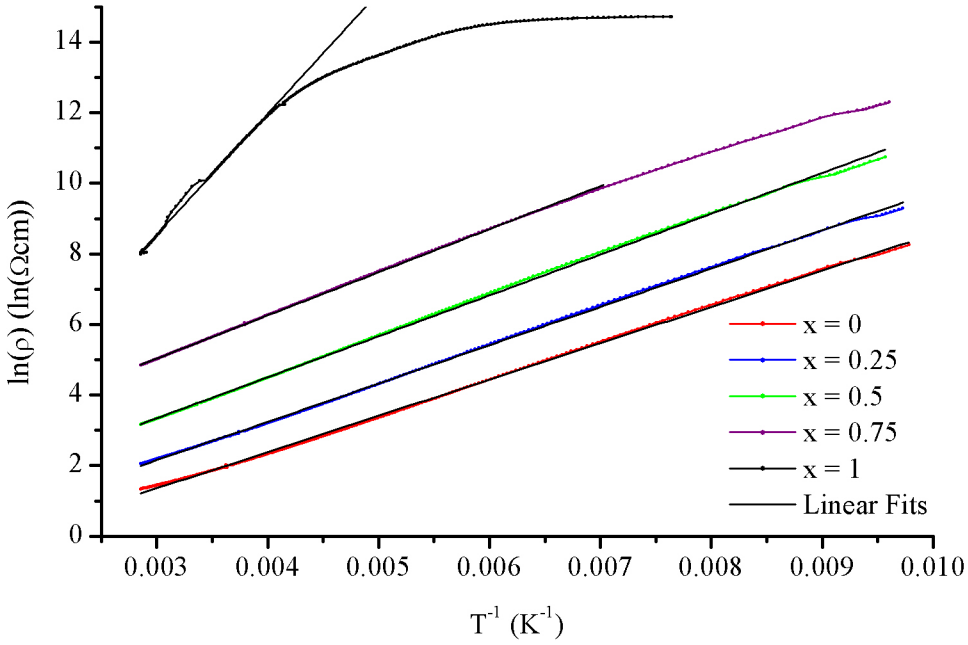

Figure 3.10: Log of electrical resistivity as a function of inverse temperature collected for $Fe_{1-x}Mn_xPb_4Sb_6S_{14}$ ($0 \leq x \leq 1$). Linear fits to the Arrhenius expression are shown.

Table 3.6: Band gaps of $Fe_{1-x}Mn_xPb_4Sb_6S_{14}$ calculated from Arrhenius plots of the electrical resistivity data.

x	*0*	*0.25*	*0.5*	*0.75*	*1*
E_g (meV)	177.2(4)	187.0(4)	199.6(4)	210.6(4)	626(18)

The band gap increases as a function of manganese content, which suggests the spin correlation splitting of the d sub-bands becomes larger. The band gaps of Marcasite, FeS_2, (340 meV)[78] and PbS (410 meV)[79] are smaller than that of Benavidesite but around twice as large as those of any iron containing phase.

3.4.2 Seebeck Coefficient

Measurements of the Seebeck coefficient (S) were performed on hot-pressed ingots of samples over the range $100 \leq T\ (K) \leq 350$ as described in section 2.8.1.

All samples other than that with x = 1 show a positive Seebeck coefficient at all temperatures (Figure 3.11). The iron end-member has a positive Seebeck coefficient indicating the dominant charge carriers are holes. The positive nature of the Seebeck coefficient is due to the half filled Fe e_g bands around the Fermi level. A maximum value of 252 $\mu V\ K^{-1}$ is observed at 112 K before the Seebeck coefficient gradually decreases at higher temperature. The Seebeck coefficient is proportional to the inverse temperature, which indicates semiconducting behaviour. This is consistent with the electrical resistivity as discussed above. Values around 300 K are similar to those previously reported.[48] The same S(T) dependence for samples with $x \leq 0.75$ was observed. Again this is consistent with the semiconducting behaviour observed for electrical resistivity measurements. However, the temperature of the maximum Seebeck coefficient increases, while the overall value of the Seebeck coefficient decreases as iron is replaced by manganese. The highest occupied orbitals in the band structure of Jamesonite are the Fe d states. These Fe d states are gradually replaced by Mn d states as the composition becomes more manganese rich until only Mn d states remain.

For the manganese end-member, the Seebeck coefficient is practically zero, with values measured being very small and negative at temperatures below 150 K. There is then a

rapid increase in the Seebeck coefficient between 200 and 300 K before it starts to level out reaching a maximum of 539 μV K^{-1} at 343 K, the highest measured temperature. The values of nearly zero for the Seebeck coefficient suggests the material is too resistive for the Seebeck to be measured below 150K. The over ranging of the multimeter set to record resistances in the 100 MΩ range also suggests the resistance is too large for measurements to be made. The high value of the Seebeck coefficient at temperatures above ambient indicates that the Fermi level is located on a sharp band in the density of states.

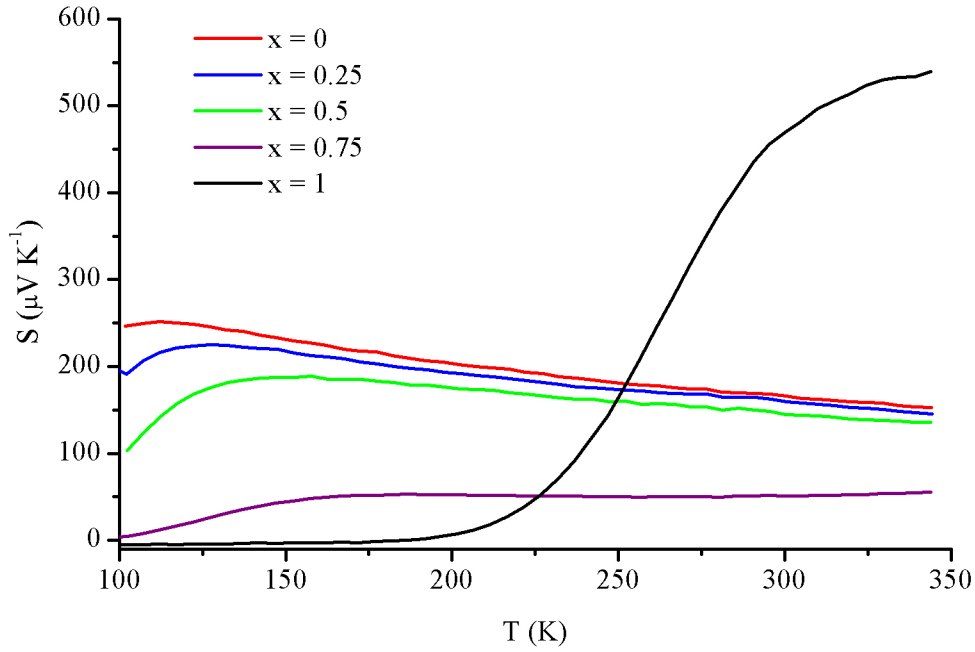

Figure 3.11: Seebeck Coefficient as a function of temperature for $Fe_{1-x}Mn_xPb_4Sb_6S_{14}$ ($0 \leq x \leq 1$) over the temperature range $100 \leq T\ (K) \leq 350$.

3.4.3 Thermal Conductivity

Measurements of the thermal conductivity (κ) were performed as described in section 2.9. In general there is a slight increase in thermal conductivity as the temperature is increased and the thermal conductivity changes only slightly between samples. The electronic contribution of the thermal conductivity (κ_e) could not be calculated due to the unavailability of high temperature resistivity measurements. The resistivity of the samples was too high to be measured with the available instrument. However, the electronic contribution is likely to be minimal due to the high resistivity of samples. The lattice contribution to the thermal conductivity is therefore likely to be the main

component of the thermal conductivity. The mass difference between iron and manganese is too small for alloy scattering of phonons to occur, so the lattice contribution is unlikely to be affected too greatly by substitution.

The Seebeck coefficient was comparable to the commercial thermoelectric material Bi_2Te_3 at 300K. However the thermal conductivity measured for samples of $Fe_{1-x}Mn_xPb_4Sb_6S_{14}$ ($0 \leq x \leq 1$) are significantly lower than that for bulk polycrystalline Bi_2Te_3[80] (2.44 W m^{-1} K^{-1} at 300 K). Values are also significantly lower than sulphide thermoelectric candidates PbS[81] (~2 W m^{-1} K^{-1} at 400 K) and TiS_2[19] (~3 W m^{-1} K^{-1} at 400 K). There are two factors that contribute to the low thermal conductivity of these phases. The high electrical resistivity reduces the electronic contribution. Low-dimensional motifs that are contained in the structure scatter phonons and reduce the lattice contribution.

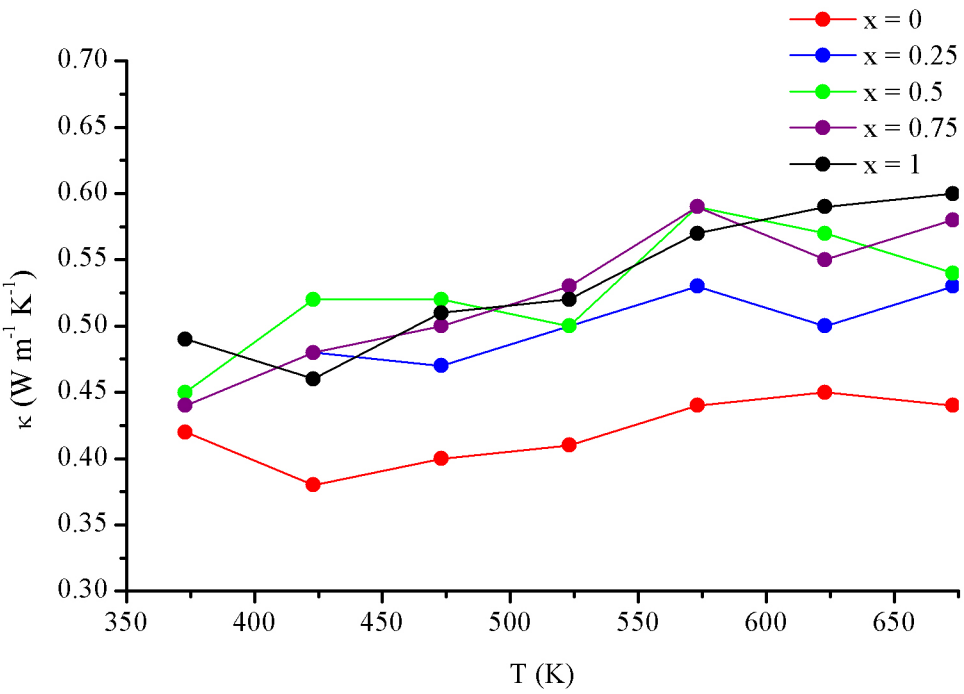

Figure 3.12: Thermal conductivity of $Fe_{1-x}Mn_xPb_4Sb_6S_{14}$ ($0 \leq x \leq 1$) over the range 373 $\leq$ T (K) $\leq$ 673.

3.5 Conclusions

In this chapter solid solution with the general formula $Fe_{1-x}Mn_xPb_4Sb_6S_{14}$ ($0 \leq x \leq 1$) have been prepared through high-temperature solid-state synthesis. For all samples,

magnetic susceptibility measurements show that localised magnetic correlations are observed along the MS_6 octahedral chains. The negative Weiss constant suggests these are antiferromagnetic in nature. However, as indicated by the non-zero magnetisation as a function of field these correlations are not collinear. Magnetic scattering was only observed in the neutron data for $MnPb_4Sb_6S_{14}$ at 2 K. Susceptibility measurements suggest that the nature of magnetic interactions changes gradually as a function of composition. Additional neutron diffraction measurements could be performed under the influence of a magnetic field to investigate the magnetic structure further.

Schematics of the density of states focusing on the partially occupied Fe/Mn(3d) bands around the Fermi level are presented in Figure 3.13. The increase in electrical resistivity and Seebeck coefficient as a function of manganese content can be explained by the depopulation of the down spin t_{2g} band. Depopulation of the down spin t_{2g} band reduces the number of electrons available for conduction and holes are the dominant charge carriers. Electrons are promoted on heating and the electron density in the t_{2g} band increases. This gives rise to an increasing number of electrons as charge carriers, which eventually reduces the positive Seebeck coefficient. Although promising values of Seebeck coefficient and thermal conductivity were recorded, the electrical resistivity observed was too large for use a viable thermoelectric materials. Maximum figure of merits of 5×10^{-4} for Jamesonite and 5×10^{-7} for Benavidesite at 340 K were calculated.

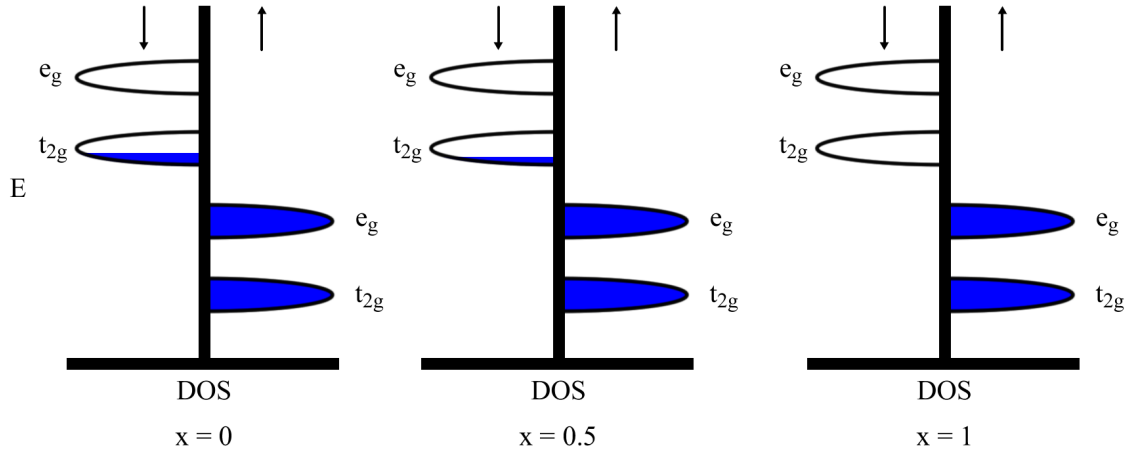

Figure 3.13: Schematic of transition metal up spin and down spin (3d) e_g and t_{2g} bands of $Fe_{1-x}Mn_xPb_4Sb_6S_{14}$ ($0 \leq x \leq 1$) showing decreasing concentration of t_{2g} (↓) electrons.

Chapter 4 – Cobalt Shandite ($Co_3Sn_{2-x}In_xS_2$)

4.1 Introduction

Materials in the cobalt Shandite family of materials ($Co_3Sn_{2-x}In_xS_2$) are interesting for several reasons. The structure has low-dimensional characteristics, which could lead to an interesting combination of properties, such as having metallic-like resistivity and insulating-like thermal conductivity. The tin end member has previously been reported to have a low electrical resistivity and high Seebeck coefficient.[57] These are two of the requirements for a thermoelectric material. Shandite materials are metal rich, containing five metal and two non-metal atoms. Progressive substitution of tin by indium across the series would lead to a reduction in the number of valence electrons. Tuning of the Fermi level through substitution would therefore be possible.

In this chapter the experimental results obtained during investigations of $Co_3Sn_{2-x}In_xS_2$ ($0 \leq x \leq 2$) are presented and discussed. Some results from this chapter have been published in the Journal of Materials Chemistry A (*J. Mater. Chem. A* **2013**, 1, 6553-6557), Powder X-ray and neutron diffraction experiments have been performed to investigate structural changes across the series and cation partitioning across the two main group sites. The relationships between the composition and the magnetism and transport properties have also been assessed and the thermoelectric properties have been determined. Samples of $Co_3Sn_{2-x}In_xS_2$ were synthesised according to the procedures described in section 2.1.2.

4.2 Structural Investigations

4.2.1 Powder X-ray Diffraction

Powder X-ray diffraction patterns (Figure 4.1) across the $Co_3Sn_{2-x}In_xS_2$ series show similarities, which gives an indication that a solid solution has been prepared. Lattice parameters for $Co_3Sn_2S_2$[57] described in the hexagonal space group $R\bar{3}m$ were used as starting values for unit cell refinements of the tin-substituted phase using Topas[68]. Refined lattice parameters were used for the next sample in the series through to the indium analogue. The change in the unit cell parameters across the series (Figure 4.2) shows that there is a contraction in the kagome lattice (*a* parameter) up to indium contents of x = 1, before levelling off. The change in the *c* parameter indicates the separation between the kagome layers increases with increasing indium contents.

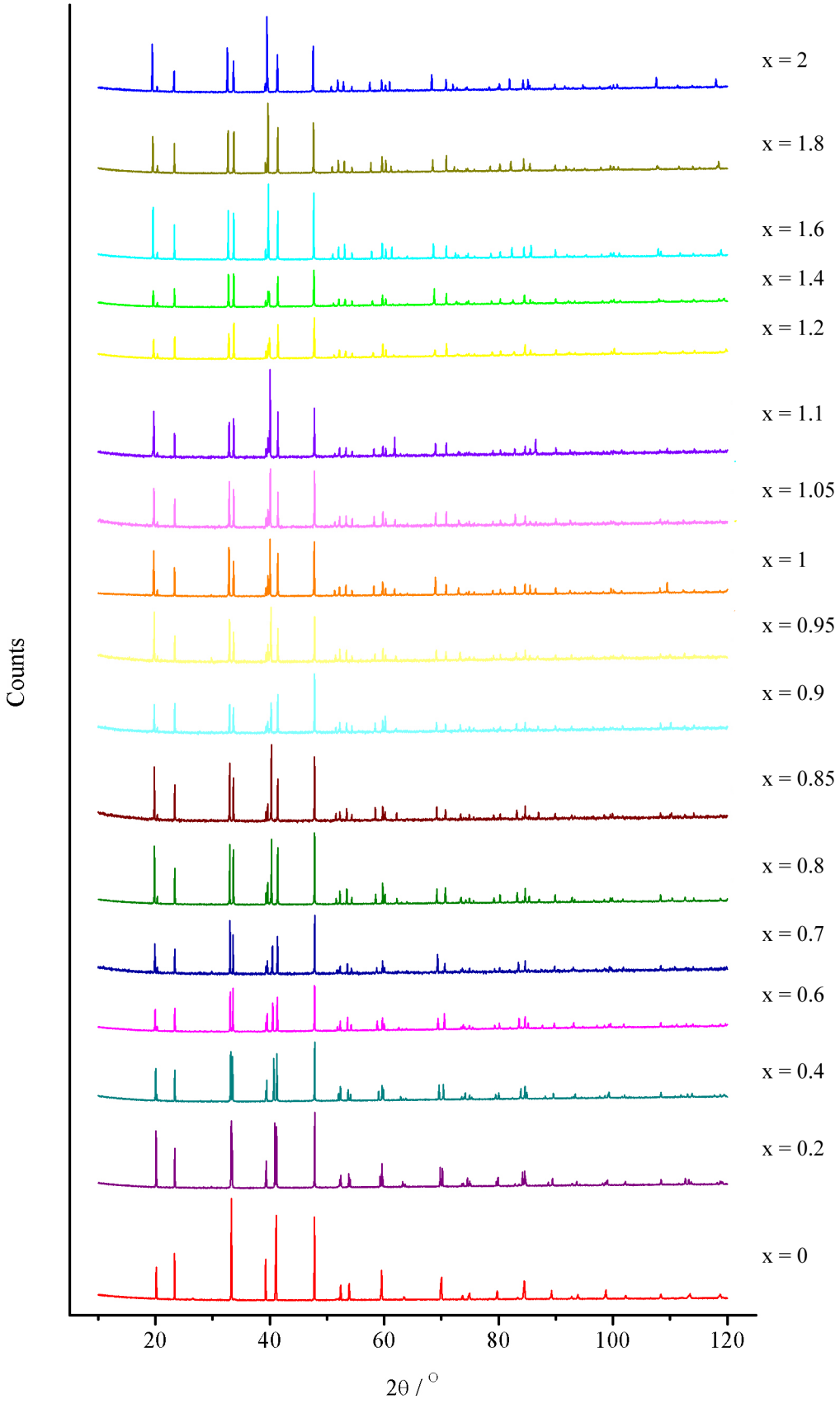

Figure 4.1: Powder X-ray diffraction data for $Co_3Sn_{2-x}In_xS_2$ ($0 \leq x \leq 2$).

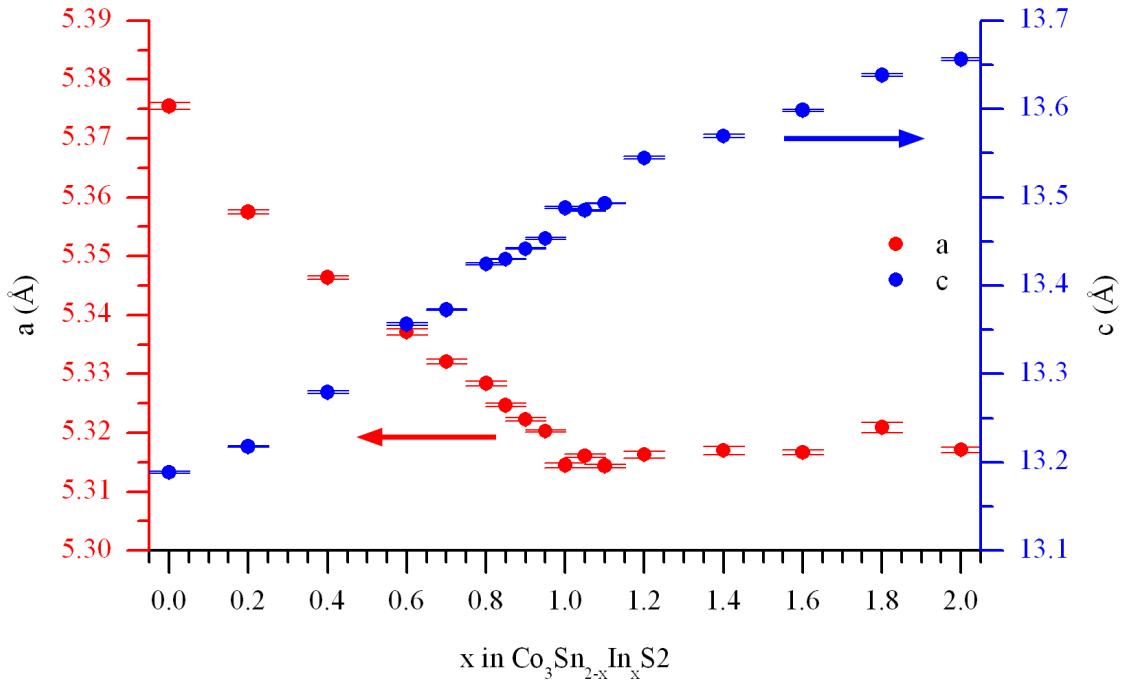

Figure 4.2: Compositional dependency of lattice parameters of $Co_3Sn_{2-x}In_xS_2$ lattice parameters obtained from refinements using powder X-ray diffraction data. Error bars are shown.

4.2.2 Powder Neutron Diffraction

Powder neutron diffraction data were collected on the GEM diffractometer at the ISIS facility as described in section 2.3.2. Data from banks 6, 5, 4 and 3 were used in a multibank Rietveld refinement using the GSAS[69] software package. Lattice parameters obtained from the refinements using Topas of the PXRD experiments and previously reported atom coordinates[57] were used for the initial structural model for Rietveld refinements. Lattice parameters were initially refined using bank 6 data. This is the highest resolution bank and provides the most accurate results. However, bank 6 has a short d-spacing range and data from additional banks were added to the refinement to extend it. In this way, the benefits of the high resolution of the backscattering bank and the larger d-spacing range of lower angle banks were used to provide complementary structural information. Structural refinements of the lattice parameters, atomic coordinates, thermal parameters and fractional occupancy of the main group site were performed. The experimental data collected from the 154°, 91°, 63° and 35° banks of the GEM diffractometer and the refinement of the x = 0.8 structural model are presented in Figure 4.3. Data and structural refinements of the remaining members of the series $Co_3Sn_{2-x}In_xS_2$ ($0 \leq x \leq 2$) are presented in Appendix I.

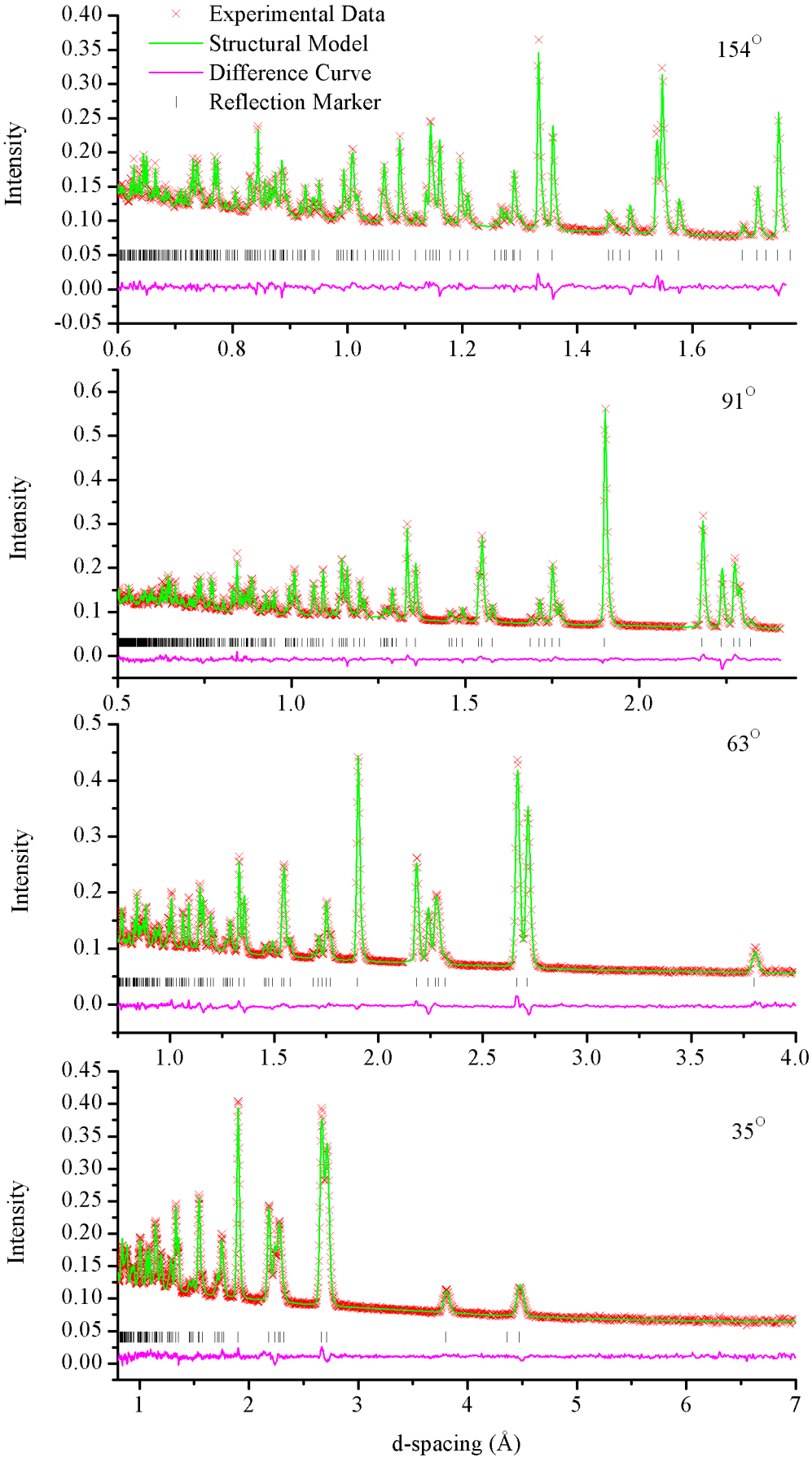

Figure 4.3: Powder neutron diffraction data collected from four banks of the GEM diffractometer and structural refinements of $Co_3Sn_{1.2}In_{0.8}S_2$.

The Goodness of Fit indices from the refinements are presented in Table 4.1. The low χ^2 and R_{wp} values indicate that the structural model and the $R\bar{3}m$ space group are correct. Therefore, it is appropriate to use the refined structural model to compare structural information across the series.

Table 4.1: Goodness of Fit indices from Rietveld refinements using Powder neutron diffraction data for $Co_3Sn_{2-x}In_xS_2$.

x	χ^2	R_{wp} *Bank 6 (154°)*	R_{wp} *Bank 5 (91°)*	R_{wp} *Bank 4 (63°)*	R_{wp} *Bank 3 (35°)*
0.0	4.2	2.05	2.94	3.17	3.13
0.2	1.9	1.86	1.95	2.10	2.54
0.4	1.9	1.93	1.96	1.95	1.78
0.6	2.2	1.96	2.26	2.24	2.76
0.8	2.1	2.33	2.27	2.33	2.39
1.0	3.1	2.38	2.41	2.53	2.72
1.2	2.7	2.56	2.61	2.37	2.52
1.4	1.9	2.12	2.19	2.17	2.42
1.6	1.6	2.28	2.15	2.00	2.33
1.8	1.5	1.92	2.00	2.06	2.42
2.0	2.2	2.20	2.43	2.64	2.88

There are four crystallographically independent atomic positions with the additional positions in the unit cell related through the $R\bar{3}m$ space group (Table 4.2). These positions along with the lattice parameters obtained from unit cell refinements made up the initial structural model. Refinements were performed by initially refining the background, histogram scale factor and absorption coefficient (Debye-Scherrer) with the initial structural model using the 154° bank data set. Once convergence was achieved, the next parameter was allowed to refine. The order in which the parameters were added to the refinement was as follows: lattice parameters, atomic coordinates, thermal parameters, site occupancy factors (where applicable), sig-1 profile coefficient and gam-1 profile coefficient. After convergence, these were then all set to not refine and the 91° bank data set was added as a second histogram. The background, histogram scale factor and absorbance were allowed to refine and converge. They were then

switched off and the diffractometer constants Diff-C, Diff-Z and Diff-A were refined individually for the newly added histogram until there was no significant change in their values on refinement. The initial histogram was then added to the refinement again and the parameters were switched on in the same order as before, this time for both histograms. This process was repeated for both the 63° and the 35° bank data sets. Two constraints were used on the *M*(1) and *M*(2) sites. The first was to keep the thermal parameters of both the same. The second was to allow the quantity of indium and tin in each site to be refined but to keep the overall site occupancy factor equal to 1. The refined lattice parameters, thermal parameters, atomic coordinates and site occupancy factors obtained from neutron diffraction experiments are shown in Table 4.3. Lattice parameters are consistent with those obtained from X-ray diffraction. The cobalt, both main group sites and the sulphur x and y coordinates are located on special positions. The sulphur z-coordinate is therefore the only variable atomic coordinate.

Table 4.2: Atomic coordinates of $Co_3Sn_{2-x}In_xS_2$.

Atom	*Wyckoff Site*	*x*	*y*	*z*
Co	9(d)	0.5	0	0.5
M(1)	3(a)	0	0	0
M(2)	3(b)	0	0	5
S	6(c)	0	0	(Table 4.3)

Refined inter-atomic distances and bond angles are shown in Table 4.4. Trends for Co-*M*(1), Co^a-*M*(1)-Co^a and Co^a-*M*(1)-Co^b echo those shown by the *c* lattice parameters. The angle between *M*(1) and two Co atoms in adjacent layers increases as indium is added while the angle between *M*(1) and two cobalt atoms in the same layer contract. This leads to a narrowing and elongation of the trigonal antiprismatic site as indium is added. The Co-*M*(2) and Co-Co bond distances in the kagome lattice follow the trend of the *a* lattice parameter. There is a contraction until around x = 1 before it levels out. These distances are slightly longer than those observed in the kagome lattice of CoSn (2.639 Å).[82] Co-S bond lengths and Co-S-Co bond angles only vary by small amounts across the series. These changes suggest that as indium is added, the contraction of the kagome lattice reaches a minimum where the lattice cannot contract further without causing unfavourable changes in the bond lengths and angles of the sulphur cap and the

Table 4.3: Refined lattice parameters, atomic coordinates, thermal parameters and site occupancy factors obtained from Rietveld refinements using powder neutron diffraction data for $Co_3Sn_{2-x}In_xS_2$ ($0 \leq x \leq 2$).

x	*a (Å)*	*c (Å)*	*Volume (Å^3)*	*S z-coordinate*	*Co Uiso (Å^2)*	*S Uiso (Å^2)*	*M Uiso (Å^2)*	*SOF In(1)**	*SOF In(2)#*
0.0	5.36994(5)	13.1934(3)	329.479(4)	0.28317(7)	0.0055(2)	0.0064(1)	0.0045(2)	0(-)	0(-)
0.2	5.36088(3)	13.2276(2)	329.217(4)	0.28323(5)	0.0062(1)	0.0056(1)	0.0050(2)	0.087(8)	0.113(8)
0.4	5.34994(3)	13.2925(2)	329.486(4)	0.28205(5)	0.0068(2)	0.0062(1)	0.0058(2)	0.260(6)	0.14(6)
0.6	5.33866(4)	13.3540(2)	329.615(4)	0.28174(6)	0.0067(2)	0.0063(2)	0.0061(2)	0.428(5)	0.172(5)
0.8	5.32480(4)	13.4167(2)	329.444(4)	0.28139(6)	0.0061(2)	0.0064(2)	0.0060(2)	0.604(4)	0.196(4)
1.0	5.31922(4)	13.4799(2)	330.303(5)	0.28108(7)	0.0059(2)	0.0062(2)	0.0054(3)	0.719(4)	0.281(4)
1.2	5.31173(5)	13.5261(2)	330.504(5)	0.28067(7)	0.0055(2)	0.0062(2)	0.0050(3)	0.825(4)	0.375(4)
1.4	5.31489(4)	13.5584(2)	331.686(5)	0.28037(6)	0.0050(2)	0.0069(2)	0.0048(2)	0.869(4)	0.531(4)
1.6	5.31495(4)	13.5909(2)	332.489(5)	0.28027(6)	0.0068(7)	0.00892(3)	0.0063(3)	0.902(4)	0.698(4)
1.8	5.31797(5)	13.6296(2)	333.702(7)	0.27969(8)	0.0065(2)	0.0106(3)	0.0061(3)	0.949(4)	0.851(4)
2.0	5.31811(6)	13.6646(3)	334.689(7)	0.27914(9)	0.0074(4)	0.0124(4)	0.0067(4)	1(-)	1(-)

* SOF In(1) + SOF Sn(1) = 1; ♯ SOF In(2) + SOF Sn(2) = 1

Table 4.4: Interatomic distances and selected bond angles in $Co_3Sn_{2-x}In_xS_2$ ($0 \leq x \leq 2$).

x	*Co-M(1) (Å)* × 6	*Co-M(2)/Co (Å)* × 6	*Co-S (Å)* × 3	*M(1)-S (Å)* × 6	*M(2)-S (Å)* × 2	*Co-S-Co (°)* × 3	*Co^a-M(1)-Co^a (°)* ×3	*Co^a-M(1)-Co^b (°)* ×3
0	2.69039(4)	2.68497(3)	2.1831(6)	3.1702(2)	2.8607(9)	75.90(3)	59.867(1)	120.133(1)
0.2	2.69354(2)	2.68044(1)	2.1752(4)	3.1681(2)	2.8806(6)	76.07(2)	59.678(1)	120.322(1)
0.4	2.70060(2)	2.67497(2)	2.1765(5)	3.1631(2)	2.8972(7)	75.83(2)	59.373(1)	120.622(1)
0.6	2.70716(2)	2.66933(2)	2,1764(5)	3.1583(2)	2.9146(7)	75.65(2)	59.077(1)	120.922(1)
0.8	2.71348(2)	2.66240(2)	2.1753(5)	3.1523(2)	2.9331(7)	75.46(21	58.758(1)	121.242(1)
1	2.72127(3)	2.65961(2)	2.1763(6)	3.1508(2)	2.9511(9)	75.323(3)	58.507(1)	121.493(1)
1.2	2.72641(3)	2.65587(2)	2.1746(7)	3.1484(2)	2.9667(9)	75.27(3)	58.295(1)	121.705(1)
1.4	2.73137(3)	2.65744(2)	2.1750(6)	3.1515(2)	2.9778(9)	75.31(3)	58.217(1)	121.783(1)
1.6	2.73587(3)	2.65747(2)	2.1767(6)	3.1522(2)	2.9863(9)	75.24(3)	58.133(1)	121.887(1)
1.8	2.74155(3)	2.65854(3)	2.1746(6)	3.1557(2)	3.0028(9)	75.36(3)	58.007(1)	121.993(1)
2	2.74655(4)	2.65905(3)	2.1723(9)	3.1584(3)	3.018(1)	75.47(4)	57.903(1)	122.097(1)

[a,b] differentiate between two adjacent kagome layers in the structure.

trigonal antiprismatic site. The orbitals surrounding the Fermi level are predominantly Co 3d in character. As electron density is removed from these orbitals with the replacement of tin for indium, there are fewer electrons available to bond within the kagome layer. This reduction in available electrons could also explain why the contraction in the *a* parameter stops. Anisotropy in the structure is created by the separation between the kagome layers. Density of States calculations and analysis of the orbital occupations[83] indicate that the main contributions to the Co-*M*(1) bonds are the *M*-5p_z orbitals and M-5$p_{x,y}$ for Co-*M*(2). The anisotropic nature of the bonding orbitals across the kagome layer and along the trigonal antiprism creates the van der Waals' gaps within the structure.

4.2.2.1 Main Group Atom Ordering

The ordering of the main group sites cannot be investigated using X-ray diffraction due to the similar scattering abilities of tin and indium. Neutron diffraction offers a contrast in scattering lengths between tin (4.065(20) fm)[84] and indium (6.225(2) fm)[84], which was exploited to investigate the ordering of the main group sites. There are two possible sites for the main group elements to occupy. *M*(2) located within the kagome layer and *M*(1), an intra-layer trigonal antiprismatic site. The refined site occupancy factors of indium in both sites are presented in Figure 4.4.

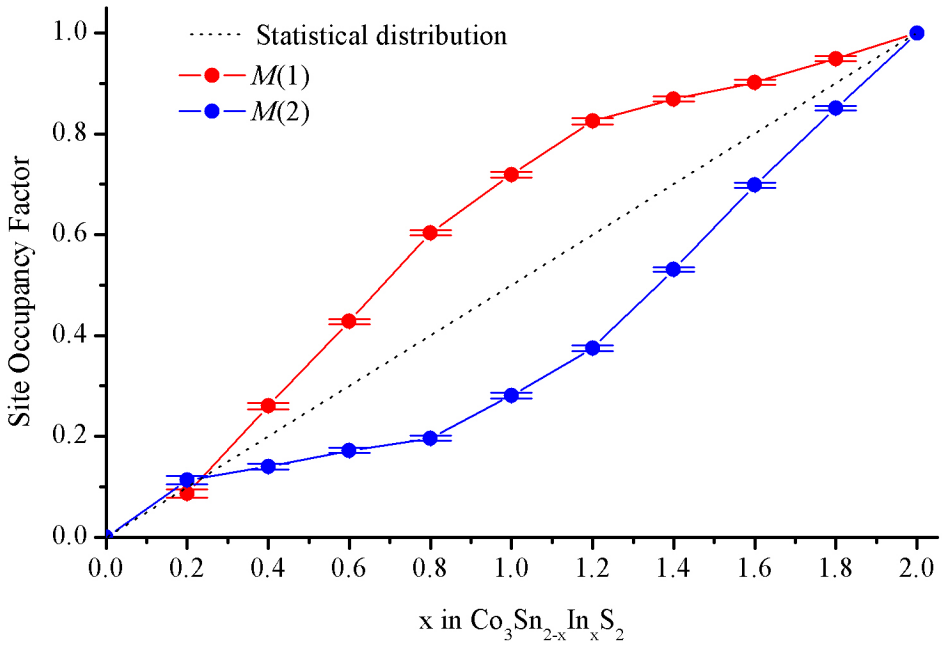

Figure 4.4: Indium site occupancy factor of *M*(1) and *M*(2) in $Co_3Sn_{2-x}In_xS_2$ ($0 \leq x \leq 2$) as a function of composition. Error bars are included.

The plot shows the statistical distribution was not followed and that indium partially orders into the *M*(1) site. The magnitude of this preference is shown in Figure 4.5. It is observed that a maximum of 75 % of available indium occupies the *M*(1) site when x = 0.8.

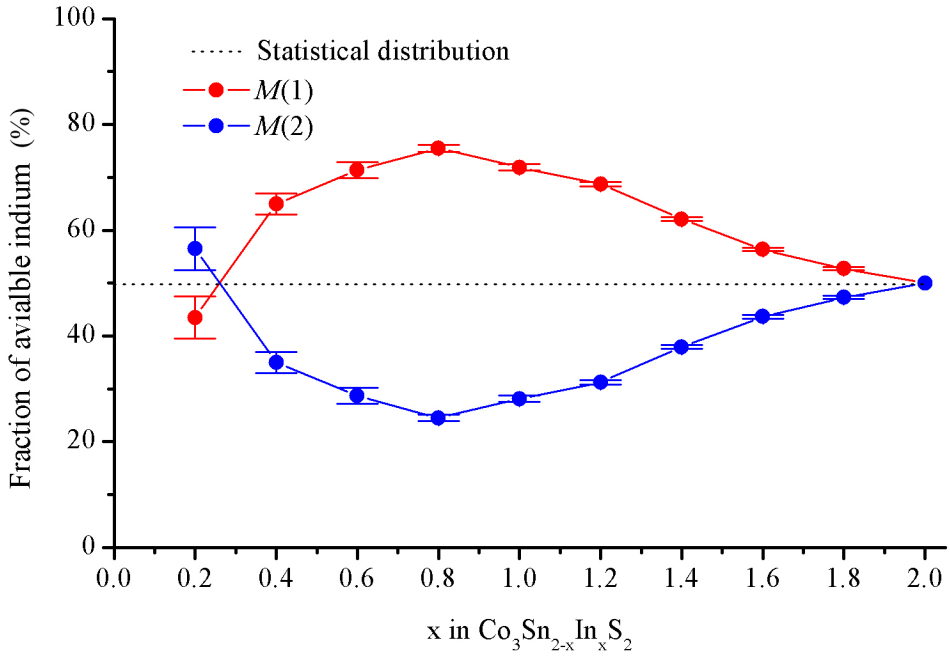

Figure 4.5: The percentage of the total available indium occupying *M*(1) and *M*(2) in $Co_3Sn_{2-x}In_xS_2$ ($0 \leq x \leq 2$) as a function of composition. Error bars are included.

4.3 Magnetic Properties

4.3.1 Magnetic Susceptibility Measurements

Samples were analysed using a Quantum Design MPMS SQUID magnetometer as described in section 2.10. Raw data were corrected for the contribution of the gelatine capsule and core diamagnetism, and converted to the molar susceptibility (χ_{mol}). Plots of molar susceptibility against temperature for both the zero–field-cooled (zfc) and field-cooled (fc) data for $Co_3Sn_2S_2$ (Figure 4.6) show magnetic ordering occurs below an ordering temperature (T_C) of 175 K. The large increase in susceptibility and divergence between the zero-field-cooled and field-cooled measurements suggests ferromagnetic ordering. The same is also true for samples x = 0.2 and 0.4, where T_C decreases to 170 K and 135 K respectively. However, at x = 0.6, magnetic ordering appears to be supressed. As indium is substituted into the system, the separation between the kagome

layers increases. The separation between cobalt atoms in adjacent layers increases from 4.692(1) Å (x = 0.4) to 4.711(1) Å (x = 0.6) becoming too large for long-range magnetic ordering to occur and there is a switch to low-dimensional magnetism. At a composition of x = 0.8 the magnetisation shows an increase below 50 K and indicates localised ordering of the magnetic moments (Figure 4.7 (a)). This increase is about a third of the magnitude when compared to the fully ordered materials. A much weaker increase in magnetisation is observed for the stoichiometric Co_3SnInS_2 phase. As materials become indium-rich ($1.2 \leq x \leq 1.6$), very small magnetisations (10^5 - 10^{-7}) that do not obey the Curie-Weiss law were recorded (Figure 4.7 (b)). This suggests that while electrons are being removed from what was a filled band for the stoichiometric phase, there are few unpaired electrons. The small positive magnetisation in these materials is likely to be due to Pauli paramagnetism. A further increase in indium composition (x = 1.8) shows a slight increase in magnetisation, however it also shows a slight change in the temperature dependence. As the temperature is reduced from 300 K, the magnetisation decreases. For the fully indium-substituted phase, there is a marked increase in magnetisation, indicating there is some localisation of electrons across the kagome lattice (Figure 4.7 (c)). For ordered materials, the Curie (C) and Weiss (θ) constants were determined from the gradient and intercept above T_C of plots of $1/\chi_{mol}$ against temperature (Figure 4.6 insets).

Measurements of magnetisation at 5 K as a function of field (Figure 4.8) were performed to determine the saturation magnetisation (M_S) of magnetically ordered materials. The magnetisation data were extrapolated to an infinite field to determine the saturation magentisation. The low saturation magnetisation values under 1 μ_B are consistent with type I_A half metallic behaviour.[85] This suggests like $Co_3Sn_2S_2$, samples with $x \leq 0.4$ are half metallic ferromagnets below T_C. As tin is replaced with indium, spin up electrons are removed from the Fermi level, therefore lowering the saturation magnetisation. There is a large decrease in magnetisation from the magnetically ordered to the non-magnetically ordered materials, which supports that samples $x \geq 0.6$ do not fully order. In general, magnetisation decreases as tin is replaced by indium between towards x = 1. There is a sharp drop between the ordered x = 0.4 phase and the non-ordered x = 0.6. Additional indium content above x = 1, increases the magnetisation. The magnetic properties of ordered materials, determined through magnetic measurements are summarised in Table 4.5.

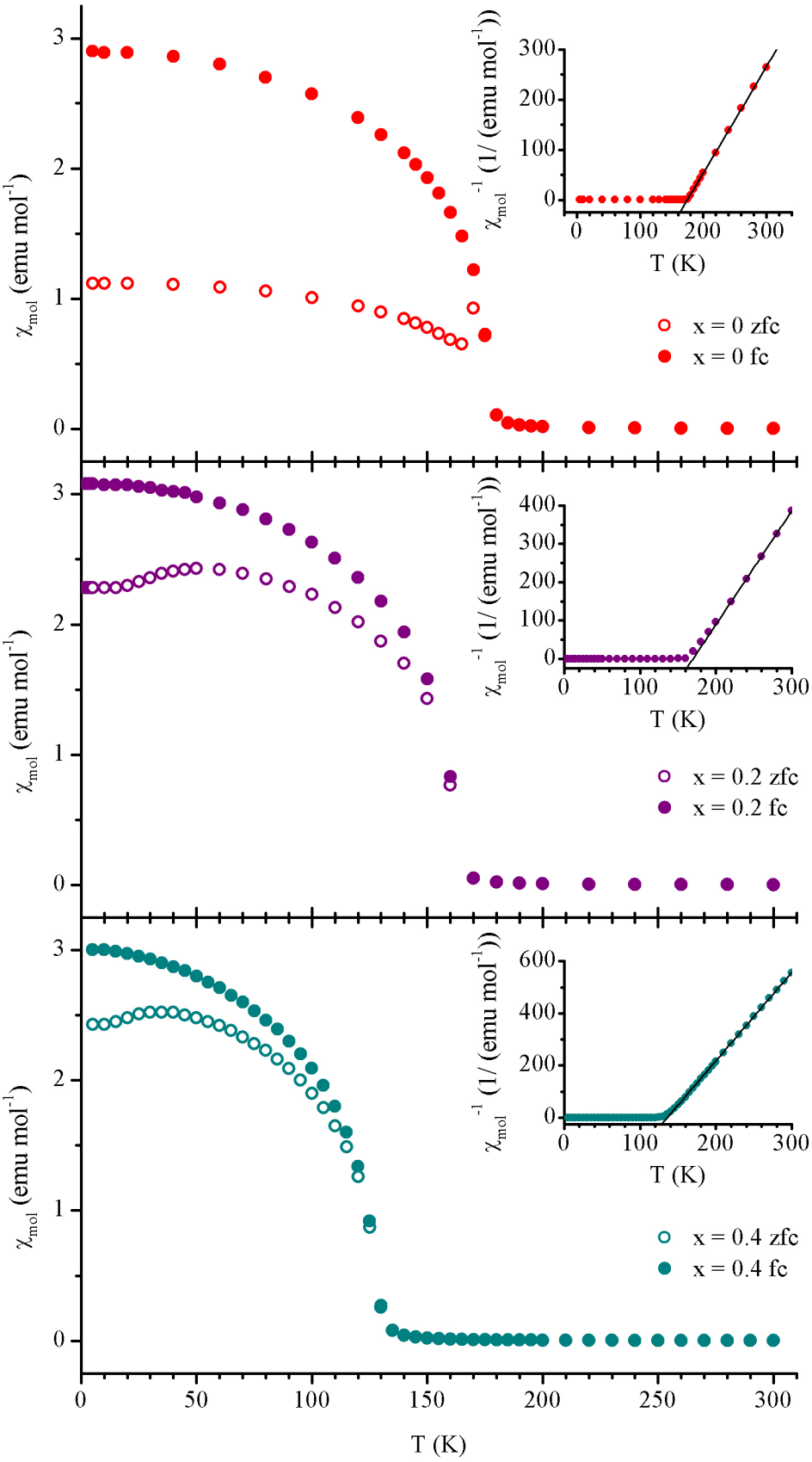

Figure 4.6: Zero-field-cooled (zfc) and field-cooled (fc) molar magnetic susceptibility of $Co_3Sn_2S_2$ (top), $Co_3Sn_{1.8}In_{0.2}S_2$ (middle) and $Co_3Sn_{1.6}In_{0.4}S_2$ (bottom). Insets show plots of $1/\chi_{mol}$ using fc data.

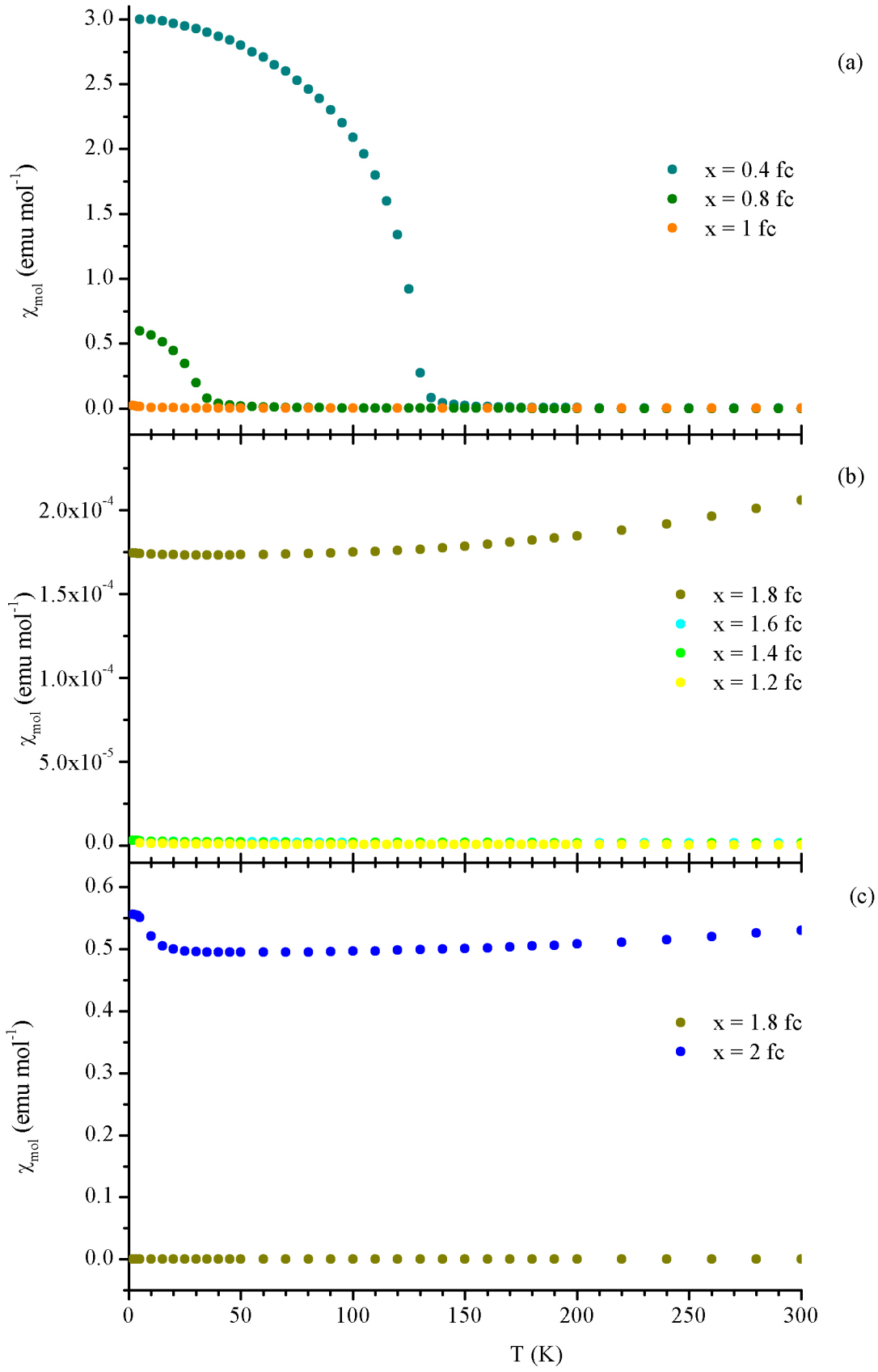

Figure 4.7: Field-cooled (fc) molar magnetic susceptibility of $Co_3Sn_{2-x}In_xS_2$ (a) ($0.4 \leq x \leq 1$) (b) ($1.2 \leq x \leq 1.8$) and (c) ($1.8 \leq x \leq 2$).

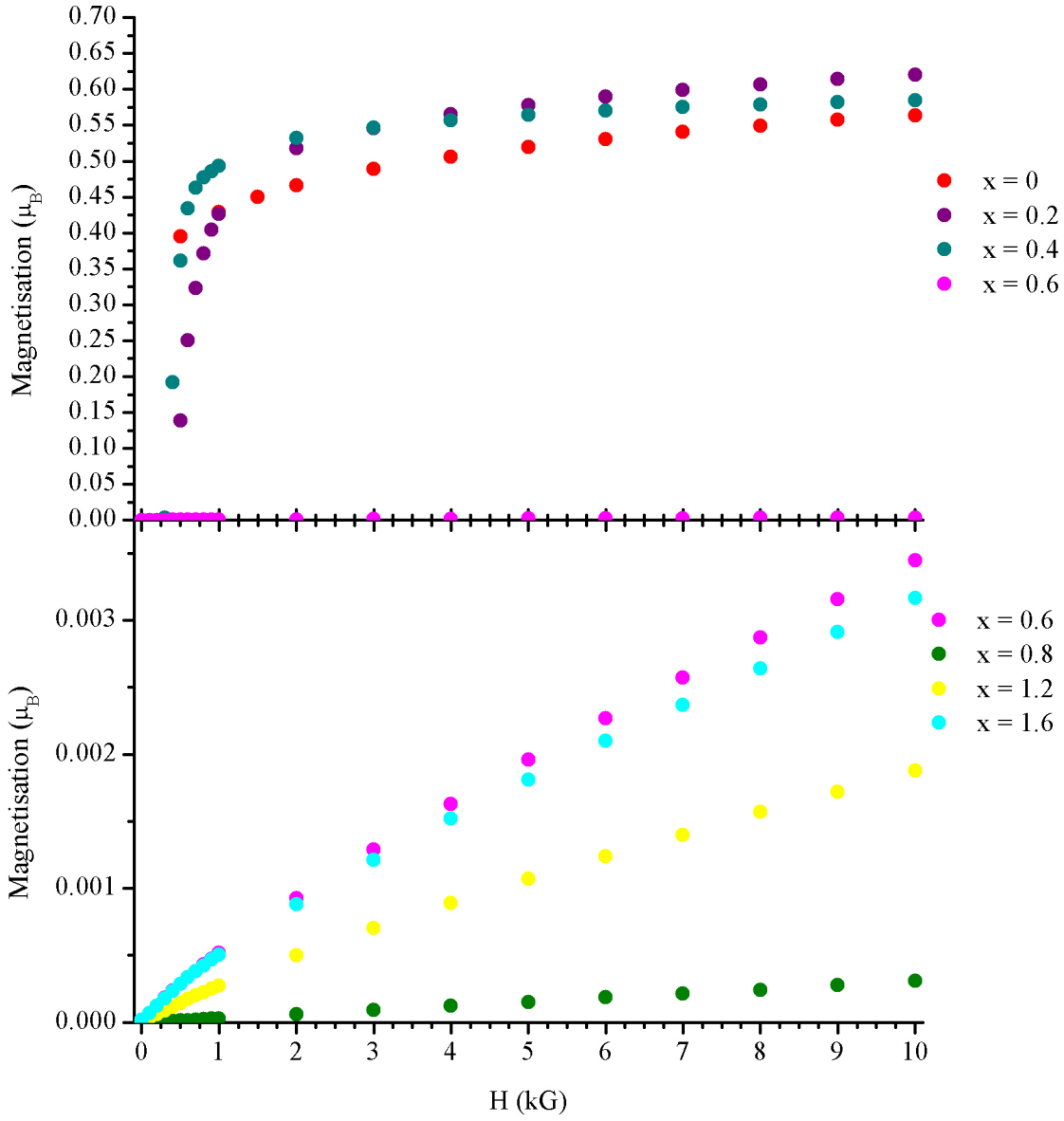

Figure 4.8: Field dependent magnetisation data of $Co_3Sn_{2-x}In_2S_2$ at 5 K. Magnetisation of ordered (top) and non-ordered samples (bottom) are presented.

Table 4.5: Determined magnetic parameters obtained from analysis of magnetic data.

x	*C* (cm^3 *K* mol^{-1})	*θ* (*K*)	μ_{eff} (μ_B)	T_C (*K*)	*Range of Fit* (*K*)	M_S (μ_B)
0.0	0.47(1)	175(5)	1.12(1)	175(5)	180 - 300	0.632(1)
0.2	0.34(2)	170(2)	0.95(2)	170(1)	220 - 300	0.672(1)
0.4	0.29(1)	135(3)	0.88(1)	135(4)	240 - 300	0.609(2)

4.3.2 Low Temperature Powder Neutron Diffraction

The magnetic susceptibility measurements discussed above confirm previous reports that $Co_3Sn_2S_2$ exhibits ferromagnetic ordering below 175 K.[57] Low temperature neutron diffraction experiments at 5 K and 190 K, above and below T_C, were performed (Figure 4.9). Refinements using the nuclear structural model obtained from the room temperature refinements showed a good fit to the below ambient temperature patterns with only a contraction in the unit cell (Table 4.6). Additional Bragg reflections or magnetic intensity due to magnetic scattering were not observed in patterns collected below T_C. This is likely to be due to measurements being performed under zero field and the low ordered moment observed in the susceptibility measurements.

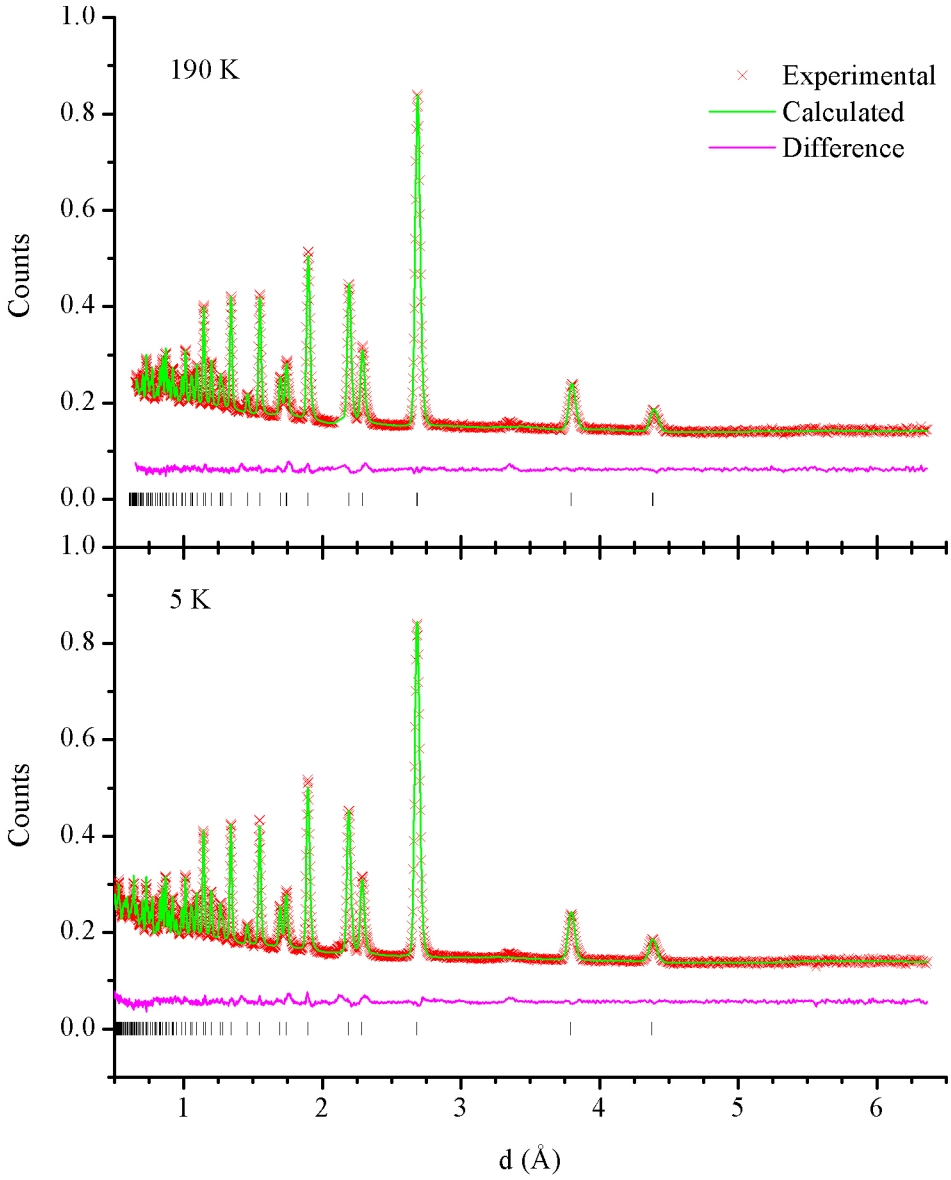

Figure 4.9: Refined structure of $Co_3Sn_2S_2$ using powder neutron diffraction data below (5 K) and above (195 K) T_C.

Table 4.6: Refined lattice parameters and Goodness of Fit indices for powder neutron diffraction of $Co_3Sn_2S_2$ at below ambient temperatures. The number in parenthesis after each R_{wp} shows the bank number.

T (K)	*a (Å)*	*c (Å)*	*Volume (Å^3)*	*R_{wp} (6)*	*R_{wp} (5)*	*R_{wp} (4)*	*R_{wp} (3)*	*χ^2*
RT	5.36994(5)	13.1934(3)	329.479(4)	2.05	2.94	3.17	3.13	4.2
190	5.36181(5)	13.1606(2)	327.665(3)	1.26	2.72	2.75	1.76	3.4
5	5.35803(6)	13.1287(3)	326.409(3)	1.52	3.25	3.75	2.12	4.9

4.4 Spectroscopic Techniques

The oxidation states of the cobalt, tin, indium and sulphur in the series have been investigated with X-ray photoelectron spectroscopy (XPS) and ^{119}Sn Mössbauer spectroscopy. The binding energies (K_B) observed in XPS spectra allow for the oxidation state of cobalt and sulphur to be investigated. The chemical isomer shift (δ) and the quadrupole splitting (Δ) obtained from Sn^{119} Mössbauer experiments were used to investigate the oxidation state and distribution across the main group sites of tin. Previous XPS measurements and Mössbauer measurements on the nickel tin sulphide analogue, $Ni_3Sn_2S_2$, indicated the oxidation states are Ni^0, Sn^{2+} and S^{2-}.[86]

4.4.1 X-ray Photoelectron Spectroscopy (XPS)

XPS was performed by the National EPSRC X-ray Photoelectron Spectroscopy Users Service (NEXUS) based at Newcastle University as described in section 2.12. Data were collected for the peaks corresponding to the C 1s peak, which arose from absorption of carbon from the air on to the surface. This peak was used to standardise the patterns by setting it to 284.8 eV. Spectra were collected in the regions associated for carbon, oxygen, sulphur, tin, indium and cobalt. Spectra collected for x = 1 are shown in Figure 4.10. Spectra collected for x = 0, 0.4, 1.6 and 2 are shown in Appendix J. Fitted peak positions and the standard residual errors of the fittings are shown in Table 4.7.

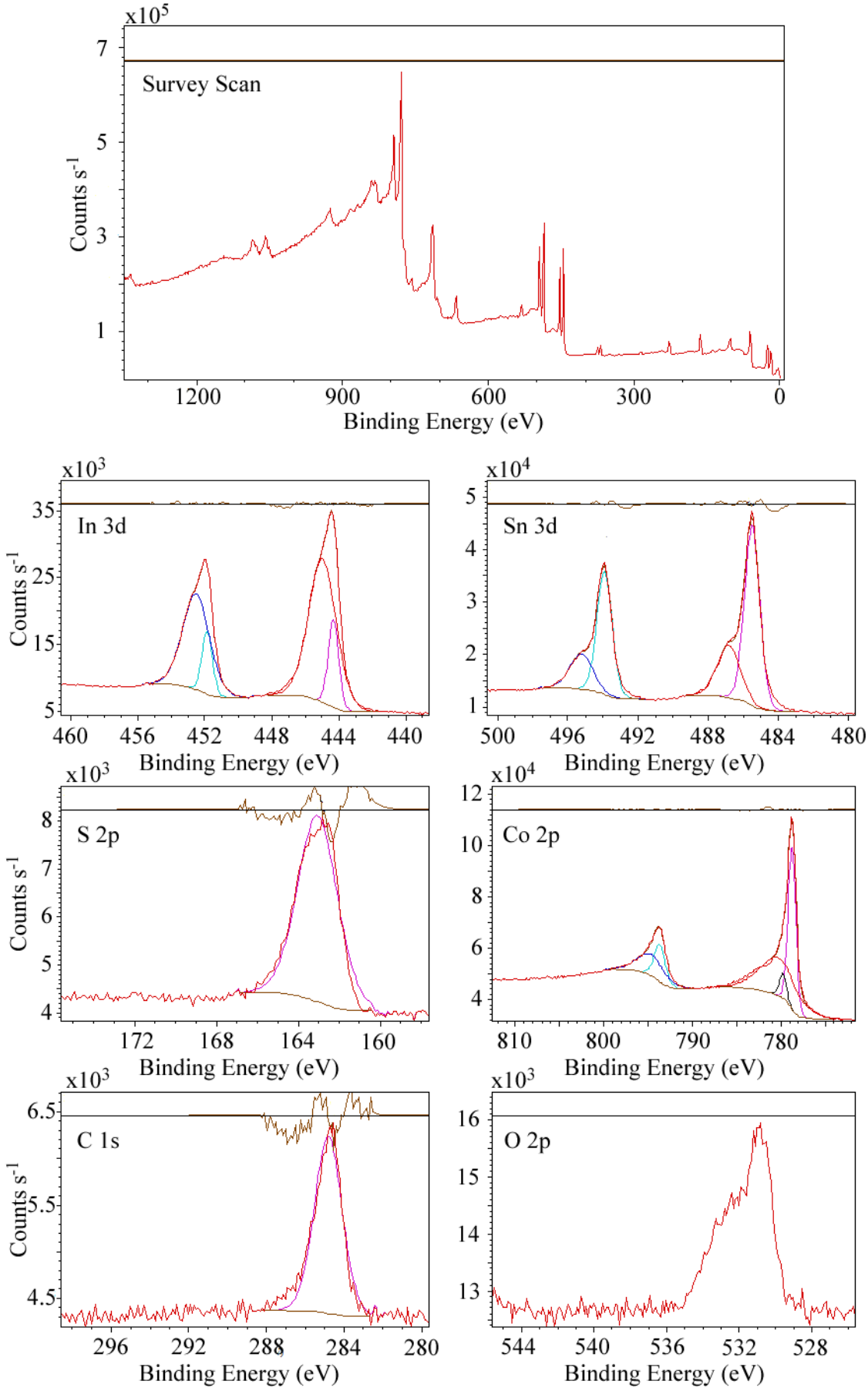

Figure 4.10: XPS spectra of Co_3SnInS_2 showing the survey scan and regions corresponding to In, Sn, S, Co, C and O. Peak fitting and difference curve are shown.

Table 4.7: Measured XPS peak positions of cobalt, tin, indium and sulphur with standard errors of fit of the peak fitting for samples $Co_3Sn_{2-x}In_xS_2$ ($0 \leq x \leq 2$). The C 1s line of adventitious carbon was set at 284.8 eV for all patterns.

	Peak Position (eV)			*Peak Position (eV)*			*Peak Position (eV)*			*Peak Position (eV)*	
x	*Co $2p_{3/2}$*	*Co $2p_{1/2}$*	*Fit Error*	*Sn $3d_{5/2}$*	*Sn $3d_{3/2}$*	*Fit Error*	*In $3d_{5/2}$*	*In $3d_{3/2}$*	*Fit Error*	*S 2p*	*Fit Error*
0	778.5	793.5	2.5	486.2	493.7	5.6	-	-	-	163.0	3.0
0.4	778.8	793.7	2.7	485.5	494.0	5.5	444.4	451.9	0.9	163.2	3.0
1	778.7	793.7	2.8	485.5	493.9	4.5	444.3	451.9	2,1	163.1	3.1
1.6	778.5	793.4	2.8	485.3	493.7	2.0	444.1	451.6	1.4	162.8	3.2
2	778.3	793.2	2.1	-	-	-	443.8	451.3	1.4	162.5	2.6

Measurements were performed in the presence of a flood gun, which is a charge neutralisation method that generates low energy electrons and Ar^+ ions near the vicinity of the surface. If the surface becomes positively charged it attracts the electrons and if negatively charged it attracts the Ar^+ ions. There were only small differences in the position of the C 1s peak, indicating that that the neutralisation was successful. The adventitious C 1s peak was standardised at 284.8 eV and all other peaks were shifted to account for this. The presence of surface oxides can be confirmed due to the structure observed for the O 2p peak. If it were just CO_2 or water adsorbed on the surface then a single peak would have been observed. However, this was not the case, and a peak with shoulders was measured. This gives a strong indication that some surface oxidation has occurred. Peaks obtained for cobalt, tin and indium show shoulders on the main peaks at higher binding energies. These shoulders correspond to the surface oxidation of the sample. The Sn $3d_{5/2}$ peak has binding energies of 486.0 eV and 487.1 eV for SnO and SnO_2 respectively.[87] Whereas the same peak for Sn and SnS are found at 484.7 eV and 485.7 eV.[87]

Assignment of the oxidation states can be achieved from observing the binding energy of the photoemission line associated with the element investigated. The Co $2p_{3/2}$ peaks for $Co_3Sn_{2-x}In_xS_2$ ($0 \leq x \leq 2$) were measured to have binding energies between 778.3 eV and 778.8 eV. The Co $2p_{1/2}$ lines were measured to have values between 793.2 eV and 793.7. These values are consistent with those of Co metal ($2p_{3/2}$ = 778.2 eV, $2p_{1/2}$ = 793.3 eV) and the intermetallic CoNi ($2p_{3/2}$ = 778.4 eV, $2p_{1/2}$ = 793.4 eV).[87] This suggests that the oxidation state of cobalt is Co^0 across the entire $Co_3Sn_{2-x}In_xS_2$ ($0 \leq x \leq 2$) series. This is consistent with the previously reported oxidation state of nickel in $Ni_3Sn_2S_2$.[86] The oxidation state of tin is less easily assigned. Reported values for tin in both Sn^0 ($3d_{5/2}$ = 484.9)[87] and $Sn^{II}S$ ($3d_{5/2}$ = 485.9 eV, $3d_{3/2}$ = 494.4 eV)[88] are consistent with those recorded for $Co_3Sn_{2-x}In_xS_2$ ($0 \leq x \leq 2$). Further assignment cannot be conclusive based on XPS measurements alone and ^{119}Sn Mössbauer spectroscopy was utilised as described in section 4.4.2. The binding energies recorded for the In $3d_{5/2}$ and $3d_{3/2}$ peaks are in the range $443.8 \leq E_B$ (eV) ≤ 444.4 and $451.3 \leq E_B$ (eV) ≤ 451.9 respectively. These compare favourably to indium metal ($3d_{5/2}$ = 444.0 eV, $3d_{3/2}$ = 451.4 eV) and In^0Sb ($3d_{5/2}$ = 444.4 eV). XPS measurements on In_2S_3 give values for In^{III} of 444.9 eV (In $3d_{5/2}$) and 452.9 eV (In $3d_{3/2}$).[89] Again the results are not definitive, however values are more like those observed for an oxidation state of In^0. The results obtained for sulphur put the binding energy of the S 2p peak in the range $162.5 \leq E_B$

(eV) ≤ 163.2. Comparing this to measurements of the S 2p peak in SnS (161.3 eV),[88] $In_2S^{2-}_3$ (161.8 eV)[89] and CoS^{2-} (161.9 eV),[90] the measured values for the S 2p peak in $Co_3Sn_{2-x}In_xS_2$ ($0 \leq x \leq 2$) series are higher. The reported value for the S 2p line in elemental S is 163.6 eV.[91] While this is slightly higher than those observed for $Co_3Sn_{2-x}In_xS_2$, the assignment of the oxidation state of sulphur in this series is more ambiguous than S^{2-} as originally reported for $Ni_3Sn_2S_2$.

4.4.2 ^{119}Sn Mössbauer Spectroscopy

Powdered samples in the $Co_3Sn_{2-x}In_xS_2$ ($0 \leq x \leq 2$) series were analysed by Professor Jean-Claude Jumas at Universite Montpellier 2, using ^{119}Sn Mössbauer spectroscopy. Measurements were undertaken as described in section 2.13.

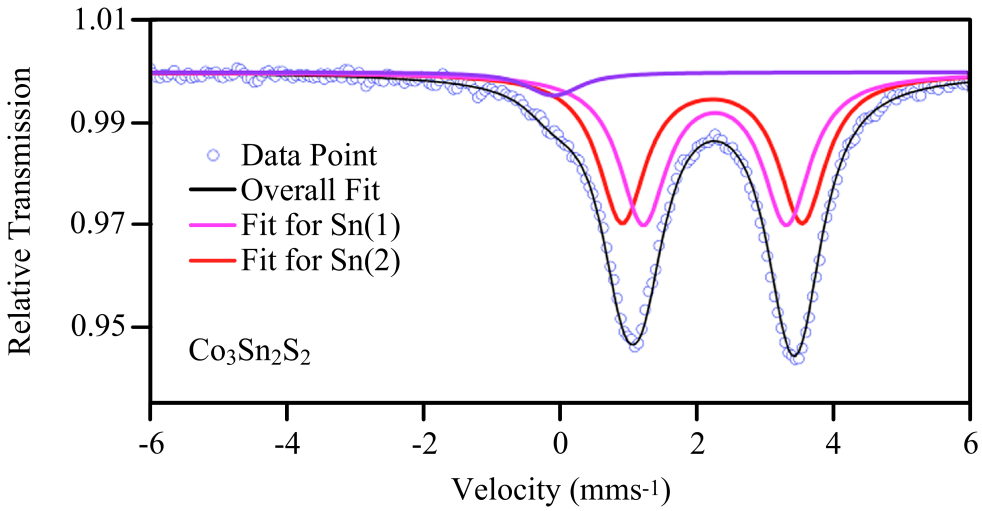

Figure 4.11: ^{119}Sn Mössbauer Spectra of $Co_3Sn_2S_2$ showing peak fitting, isomer shift and quadrupole splitting for tin in the Sn(1) and Sn(2) sites.

Measurements of the fully tin-substituted phase show peaks that can be attributed to both tin sites within the crystal (Figure 4.11). Peaks were fitted using a least squares Lorentzian peak fitting analysis. The assignment of the signal to each site is dependent on the quadrupole splitting (Δ). The fitted peak with the largest quadrupole splitting is assigned to the most distorted crystallographic site. In this case, Sn(2) within the kagome layer is the most distorted. Sn(1) in the trigonal antiprismatic site is assigned to the smaller quadrupole splitting. The contribution from each crystallographic site was in broad agreement with the data from the structural refinements using the powder neutron diffraction data (Table 4.8).

Table 4.8: The Isomer shifts relative to $BaSnO_3$ (δ), quadrupole splitting (Δ), line width (Γ), the contribution of each line to the spectra and the assignment of the signal to the crystallographic site for ^{119}Sn Mössbauer spectroscopy of $Co_3Sn_{2-x}In_xS_2$ ($0 \leq x \leq 2$).

x	*δ (mm s^{-1})*	*Δ (mm s^{-1})*	*Γ (mm s^{-1})*	*Contribution (%)*	*Assignment*
0	-0.19(8)	0.2(1)	0.84(5)	4	oxide
	2.14(1)	2.64(2)	0.84(5)	48	Sn(2)
	2.18(1)	2.10(2)	0.84(5)	48	Sn(1)
0.2	2.14(3)	2.68(7)	0.78(8)	47	Sn(2)
	2.16(3)	2.10(6)	0.78(8)	53	Sn(1)
0.4	2.13(2)	2.62(4)	0.83(8)	67	Sn(2)
	2.16(3)	2.01(6)	0.83(8)	33	Sn(1)
0.6	2.14(2)	2.81(7)	0.82(7)	40	Sn(2)
	2.15(3)	2.27(6)	0.82(7)	60	Sn(1)
0.8	2.14(2)	2.83(3)	0.80(6)	66	Sn(2)
	2.15(2)	2.32(3)	0.80(6)	34	Sn(1)
1	2.11(4)	2.92(8)	0.78(8)	41	Sn(2)
	2.16(3)	2.38(6)	0.78(8)	59	Sn(1)
1.2	2.14(3)	2.76(5)	0.8(1)	77	Sn(2)
	2.15(6)	2.31(9)	0.8(1)	23	Sn(1)
1.6	2.13(3)	2.79(6)	0.8(1)	77	Sn(2)
	2.20(9)	2.1(2)	0.8(1)	23	Sn(1)

The quadrupole splitting of the tin was used to determine the oxidation state. The quadrupole splitting of Sn^{II} (3.40(3) mm s^{-1}) and Sn^{IV} (1.46(3) mm s^{-1}) from the Mössbauer spectra of $Cr_3Sn_3Se_7$[65] do not match the quadrupole splitting of tin in $Co_3Sn_2S_2$. Quadrupole splitting for Sn^0 sit between those of Sn^{II} and Sn^{IV}. Literature values for Sn^0Mg_2 (1.8 mm s^{-1}), αSn^0 (2.1 mm s^{-1}), βSn^0 (2.6 mm s^{-1}) and Sn^0Sb (2.8 mm s^{-1})[92] are similar to quadrupole splitting of 2.10(2) and 2.64(2) measured for $Co_3Sn_2S_2$. This suggests that the oxidation state of tin in $Co_3Sn_2S_2$ is Sn^0. The peak with an isomer shift δ = -0.19(8) is caused by an oxide impurity. Measurements on additional samples across the series were performed (Appendix K). The quadrupole splitting ranges for Sn(1) ($2.01 \leq \Delta$ (mm s^{-1}) ≤ 2.38) and Sn(2) ($2.62 \leq \Delta$ (mm s^{-1}) ≤ 2.92)

indicating no significant differences as the tin content was changed. Therefore the Sn^0 oxidation state of tin remains constant across the full range of compositions

4.5 Thermogravimetric Analysis

The stability of Co_3SnInS_2 under oxygen and nitrogen was investigated using Thermogravimetric Analysis. Co_3SnInS_2 was selected as a representative of the series. Analysis of the thermal stability under a flow of O_2 indicated that there was < 1% increase in mass of the samples at temperatures up to 673 K. Above 673 K the mass increased suggesting that the sample started to oxidise. At 1070 K mass is lost as the sample started to vaporise. A small increase in weight was observed at 1150 K before falling again. Whereas under N_2, no weight change was observed up to 1050 K. The maximum temperature for physical property measurements was therefore set at 673 K.

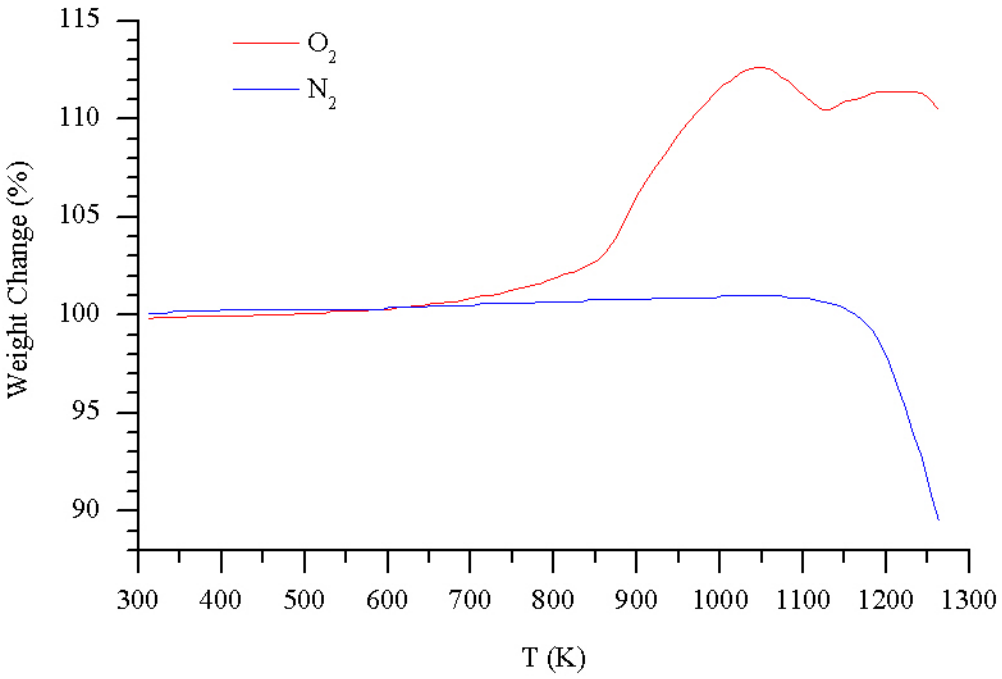

Figure 4.12: TGA data for Co_3SnInS_2 heated under a flow of oxygen (red line) and nitrogen (blue line).

4.6 Electrical Transport Properties

4.6.1 Electrical Resistivity

Measurements of the electrical resistivity (ρ) were performed on hot-pressed ingots of sample over two complementary temperature ranges as described in sections 2.7.1.1 and 2.7.2. Measurements below ambient temperature are shown in Figure 4.13.

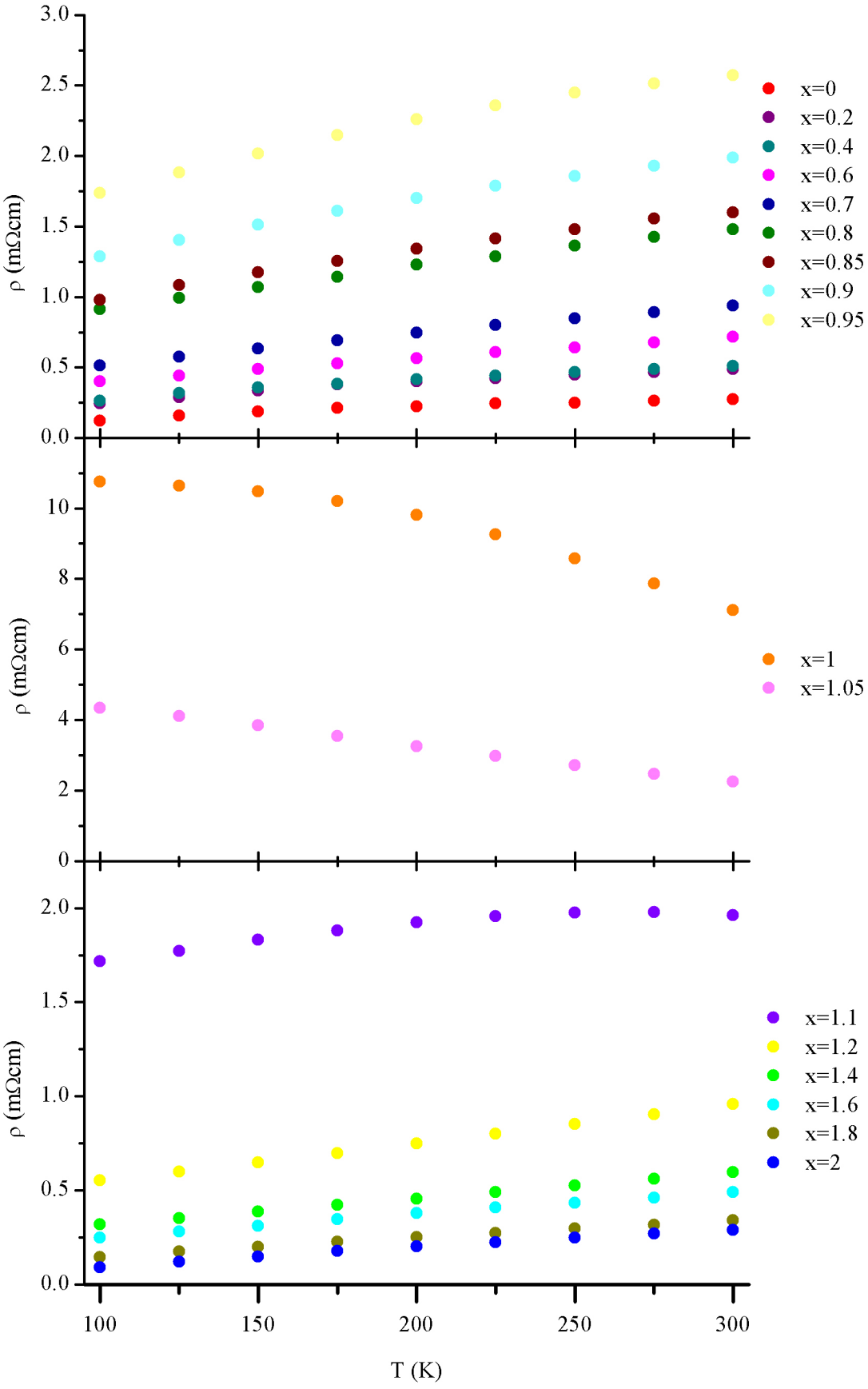

Figure 4.13: Electrical resistivity measurements as a function of temperature for $Co_3Sn_{2-x}In_xS_2$ ($0 \leq x \leq 2$) in the temperature range $100 \leq T\ (K) \leq 300$.

Measurements of the end-member phase $Co_3Sn_2S_2$ are consistent with metallic behaviour suggested by the high degree of delocalisation of electrons observed in magnetic susceptibility measurements. Metallic behaviour is retained to a composition corresponding to $x \leq 0.95$. At the point at which the stoichiometric phase Co_3SnInS_2 ($x = 1$) is reached, the absolute value of the resistivity increases markedly and a semiconducting temperature dependence is observed. Band structure calculations for the $x = 1$ composition reveal that the highest occupied state is a filled band (band 23),[60] accounting for the semiconducting nature of this material. Further substitution of tin by indium above the 50% level decreases the resistivity, although the semiconducting behaviour persists over a narrow range of composition extending to $x = 1.05$, before metallic behaviour is restored for $x \geq 1.1$. The variation in electrical properties and the double metal-to-semiconductor-to-metal transition is perhaps most clearly illustrated by examination of the resistivity at a given temperature as a function of composition (Figure 4.14).

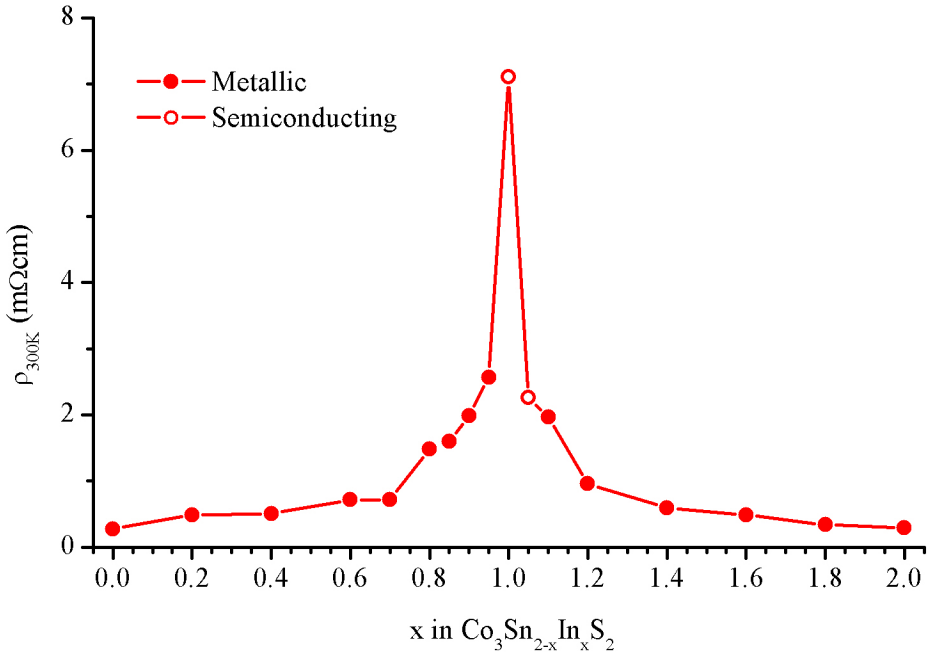

Figure 4.14: The electrical resistivity of $Co_3Sn_{2-x}In_2S_2$ at 300 K as a function of composition.

Extending the range of resistivity measurements to 673 K (Figure 4.15) shows that some samples show both metallic and semiconducting behaviour. While samples $x \leq 0.6$ and $x \geq 1.4$ continue to show a metallic-like $\rho(T)$ dependence, samples close to the

semiconducting region ($1 \leq x \leq 1.05$), as defined by low temperature measurements, show a change in $\rho(T)$ at higher temperatures. On heating, the slope, $d\rho/dT$, gradually changes from positive to negative values and semiconducting-like behaviour is observed. This is indicative of intrinsic semiconducting behaviour. The onset of this intrinsic semiconducting behaviour occurs at higher temperatures for compositions further from that of the stoichiometric Co_3SnInS_2 phase.

4.6.2 Seebeck Coefficient Measurements

Measurements of the Seebeck coefficient (S) of the end-member $Co_3Sn_2S_2$ phase below ambient temperature reveals that the Seebeck coefficient is negative and the dominant charge carriers are electrons. The linear S(T) dependence (Figure 4.16) is consistent with the metallic behaviour indicated by the resistivity measurements. With increasing indium content, the Seebeck coefficient increases significantly, attaining a value of -163 $\mu V\ K^{-1}$ at 265 K, for $x = 0.95$. A markedly different S(T) behaviour is observed on entering the semiconducting region ($1 \leq x \leq 1.05$) and the Seebeck coefficient decreases towards zero. At the start of the second metallic region the Seebeck coefficient is positive, and the material with a composition corresponding to $x = 1.1$ may be described as a p-type metal. At higher levels of indium incorporation, the Seebeck coefficient changes from positive to negative values on cooling, suggesting that these are mixed conductors, the overall sign of the Seebeck coefficient being determined by the conductivity-weighted sum of electron and hole conduction at a given temperature.

The compositional variation in the Seebeck coefficient at 300 K is illustrated in Figure 4.17. For the tin substituted phase a value of -53 $\mu V\ K^{-1}$ is observed. With gradual replacement of tin by indium, the Seebeck coefficient becomes more negative with a maximum of -155 $\mu V\ K^{-1}$ recorded for $x = 0.95$. On further substitution there is a sharp decrease in the Seebeck coefficient through $x = 1$ and $x = 1.05$. At $x = 1.1$ the value of the Seebeck coefficient is 73 $\mu V\ K^{-1}$. This positive Seebeck coefficient marks a change from the previously observed negative values. Continuing substitution to the fully indium-substituted phase ($x = 2$), a gradual decrease in the Seebeck coefficient is observed.

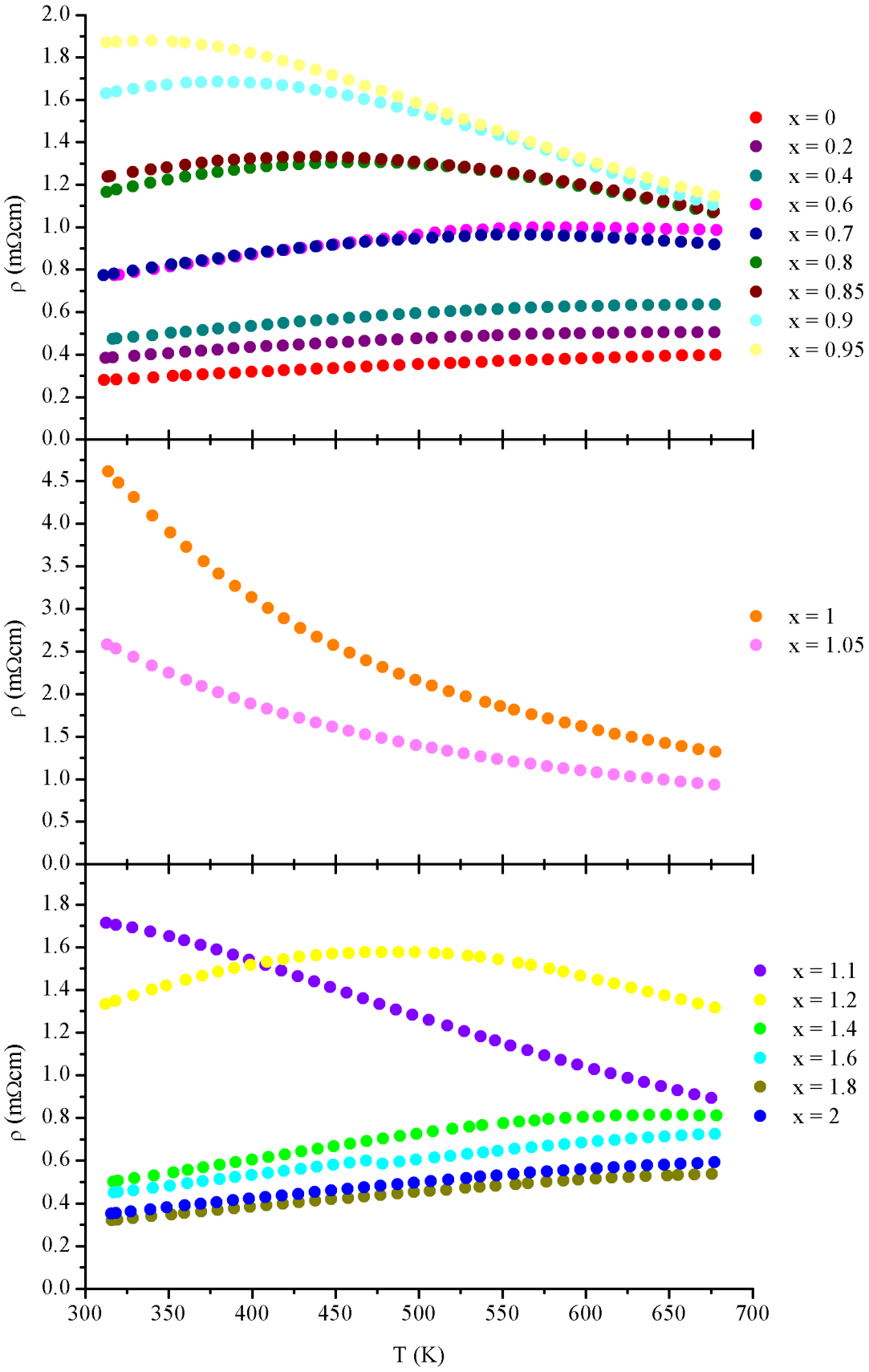

Figure 4.15: Electrical resistivity measurements as a function of temperature for $Co_3Sn_{2-x}In_xS_2$ ($0 \leq x \leq 2$) in the temperature range $300 \leq T\,(K) \leq 673$.

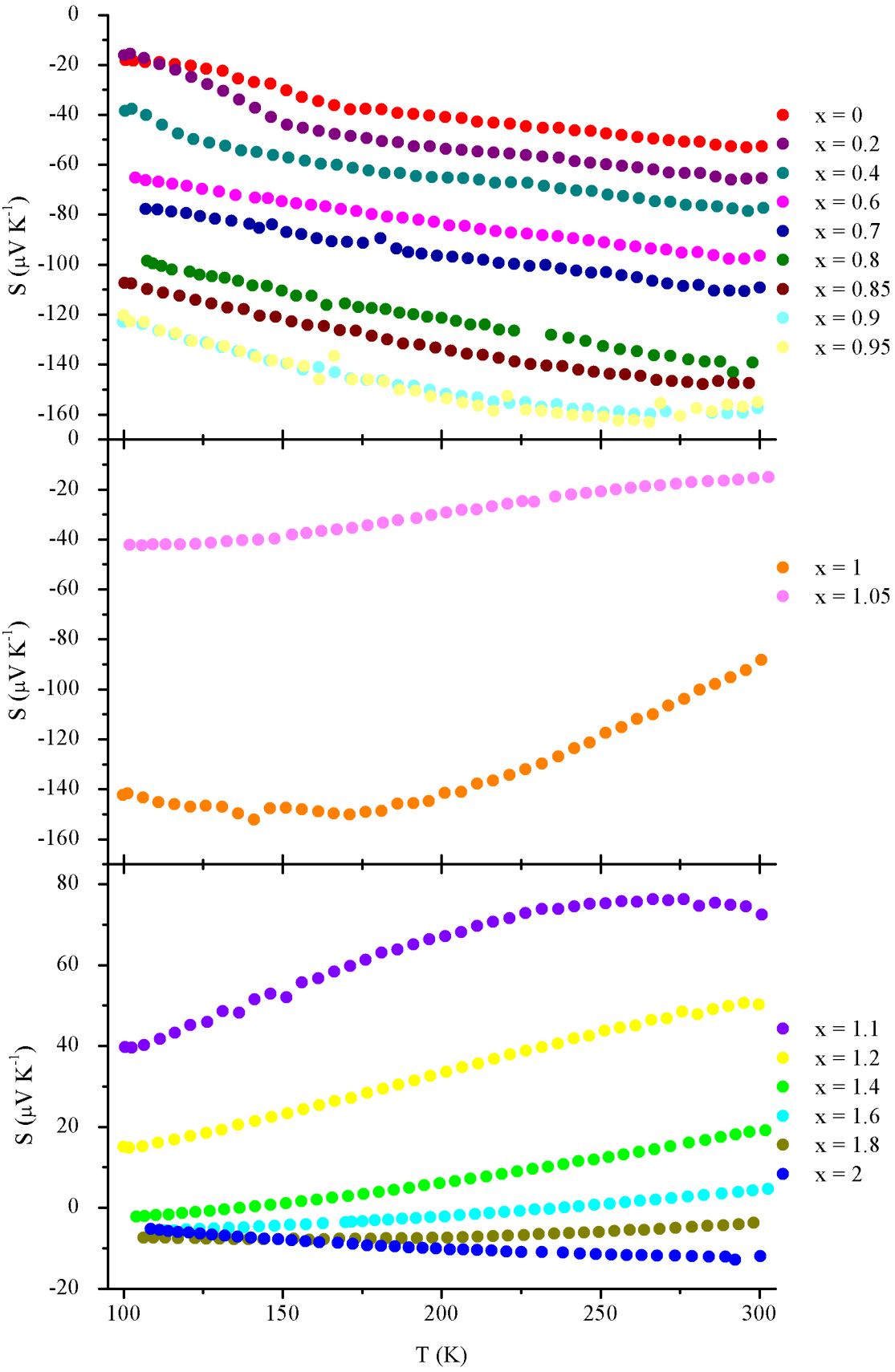

Figure 4.16: Seebeck coefficient of $Co_3Sn_{2-x}In_xS_2$ ($0 \leq x \leq 2$) determined at temperatures in the range $100 \leq T\ (K) \leq 300$.

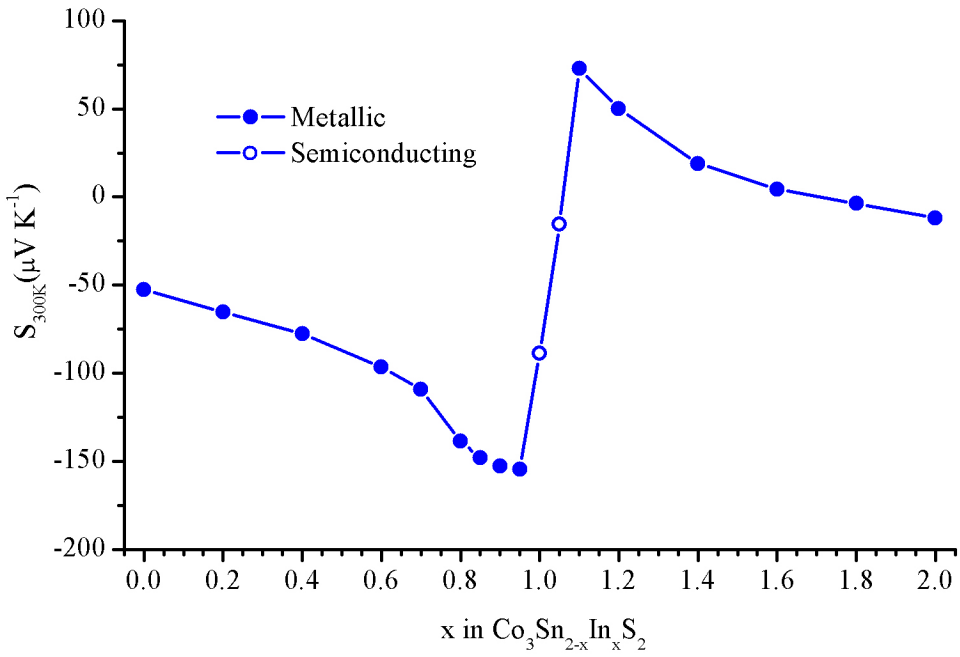

Figure 4.17: The variation of the Seebeck coefficient at 300 K across the series $Co_3Sn_{2-x}In_xS_2$ ($0 \leq x \leq 2$).

When compared with values obtained at 300 K for other known Shandite materials (Table 1.4), materials in the tin-rich region near to Co_3SnInS_2, show significantly larger negative values of the Seebeck coefficient than any of the previously measured ternary Shandites. Positive values of the Seebeck coefficient are far less commonly observed. Previously only rhenium Shandite containing indium and the quaternary Rh_3InPbS_2, have been shown to have positive values of the Seebeck coefficient. Values obtained for $Co_3Sn_{0.9}In_{1.1}S_2$ are over four times larger at 300 K than observed for Rh_3InPbS_2.

Extending measurements of the Seebeck coefficient to temperatures above ambient (Figure 4.18) indicates more complex behaviour than suggested by the low temperature data. Samples $x \leq 0.4$ continue to show a linear S(T) dependence. However, complementary to the change in ρ(T) dependency observed for samples $0.6 \leq x \leq 1.2$, there is also a change in the S(T) dependency. In general, decreases in the Seebeck coefficient are observed, indicating there is mixed conduction of both electrons and holes in these phases. The x = 1.8 phase which was shown as having a negative Seebeck coefficient in the low temperature data set, again has a negative Seebeck coefficient at low temperatures. However the absolute value of the Seebeck coefficient gradually decreases and at 359 K values become positive. This is similar to the trend observed in the low temperature data for x = 1.4 and x = 1.6.

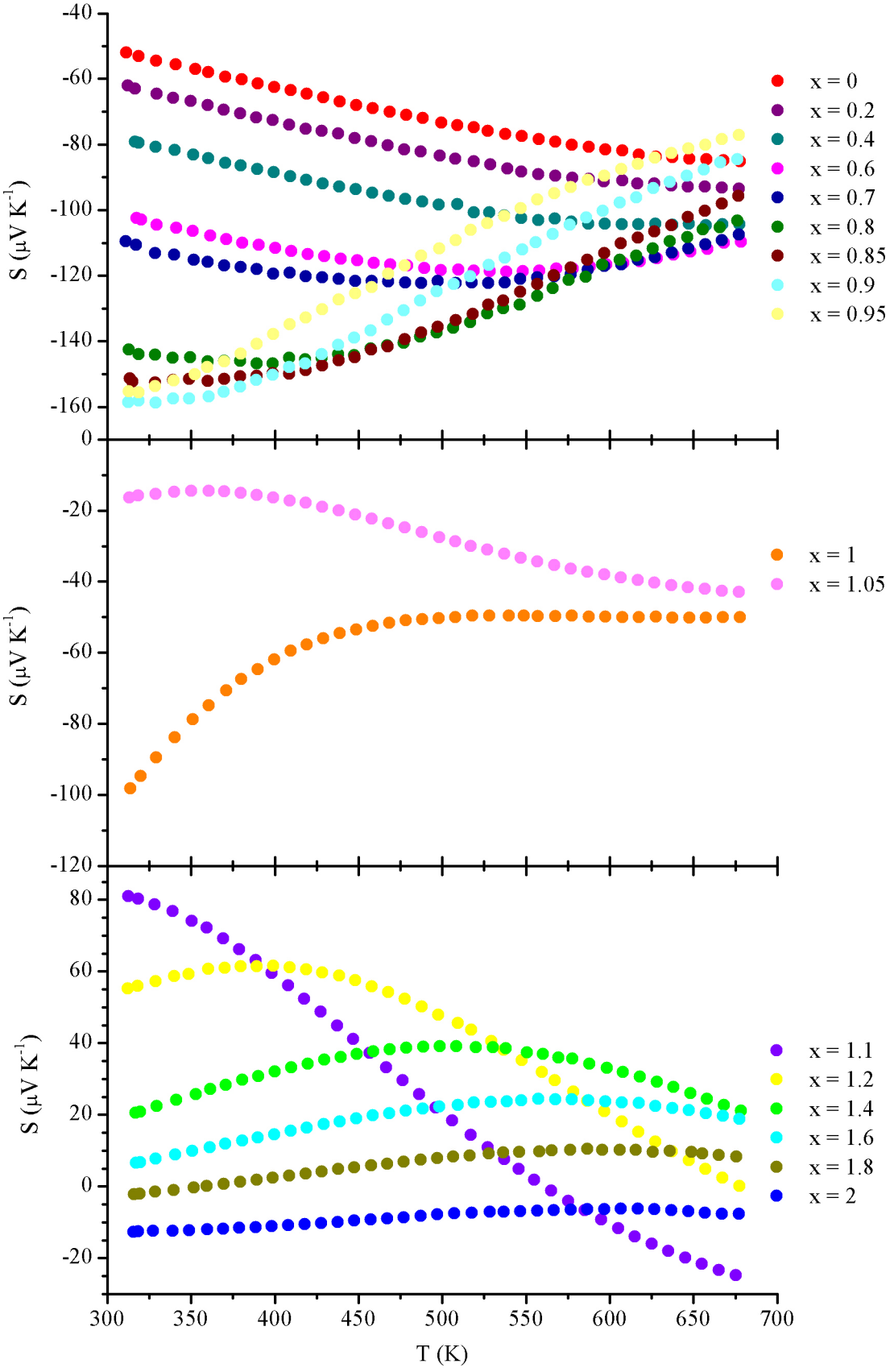

Figure 4.18: Seebeck coefficient data for samples of $Co_3Sn_{2-x}In_xS_2$ ($0 \leq x \leq 2$) at temperatures in the range $300 \leq T\ (K) \leq 673$.

The compositional variation in the electronic properties of the series $Co_3Sn_{2-x}In_xS_2$ may be understood in terms of the changing electron population induced by substitution. The end-member phase, $Co_3Sn_2S_2$, has 47 valence electrons. Band structure calculations (both spin-polarised and non-polarised)[60] locate the Fermi level in the 24th (of 31) valence bands, with the result that this narrow band of predominantly Co d-character is partially occupied. Replacement of tin by indium progressively removes valence electrons, decreasing by one electron for each unit increment in indium composition (Figure 4.19).

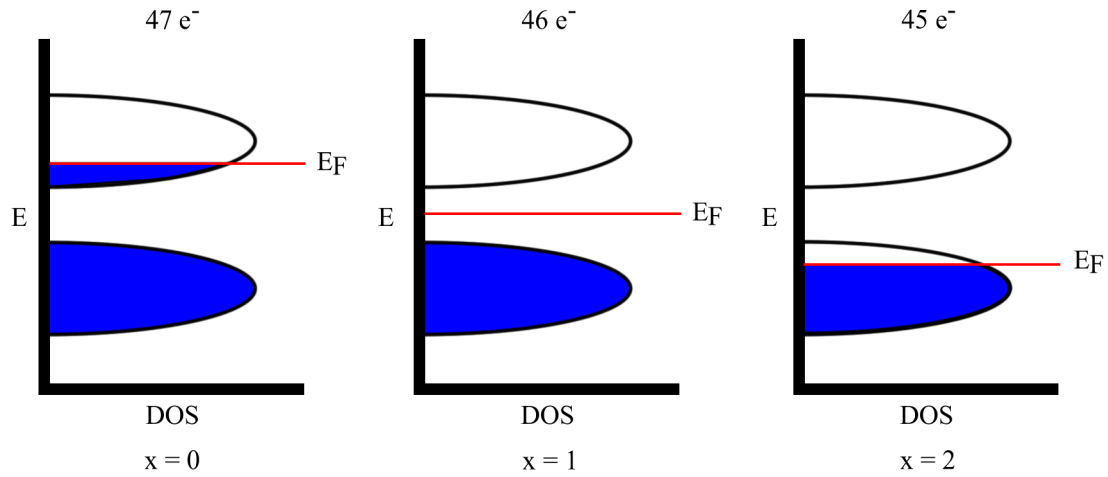

Figure 4.19: Schematic of the Density of States near the Fermi level (E_F) for $Co_3Sn_{2-x}In_xS_2$ ($0 \leq x \leq 2$).

Initially, this reduction in the electron count does not adversely affect the electrical resistivity which remains low and of metallic character. However, as the Fermi level is lowered through the lower band, the magnitude of the Seebeck coefficient increases markedly, suggesting that the Fermi level may be lowered to energies where the curvature in the density of states is more pronounced. At the mid-point in the series, Co_3SnInS_2 (x = 1), the valence electron count falls to 46 electrons. As this composition is approached, the resistivity increases and a semiconducting region is entered. Further indium substitution introduces holes into this band, which is consistent with the change to p-type behaviour indicated by the Seebeck coefficient measurements. Initially, it appears that the concentration of holes is insufficient to allow metallic behaviour and the material with a composition x = 1.05 retains the semiconducting properties of the stoichiometric mid-series phase. However, at higher levels of indium substitution,

metallic behaviour is restored as the valence electron count decreases progressively to 45 electrons in the end-member phase, $Co_3In_2S_2$.

The intrinsic semiconducting behaviour and drop in the Seebeck coefficient observed in the region of the semiconducting region suggests that as the temperature is increased, the thermal energy becomes high enough to promote electrons across the pseudo gap between bands 23 and 24. The addition of holes in the 23rd band in the tin-rich metallic region and the promoted electrons to the 24th band in the indium-rich metallic region make the material a mixed conductor, with both holes and electrons as charge carriers. This mixed conduction explains the reduction of the Seebeck coefficient observed at higher temperatures. It also explains the change from negative to positive values as more holes are created through excitation of electrons across the band gap.

4.7 Thermal Conductivity

Measurements of the thermal conductivity (κ) were performed as described in section 2.9. In general, the thermal conductivity is fairly flat with temperature and across the series, a broad minimum in the thermal conductivity is observed around the stoichiometric Co_3SnInS_2 phase (Figure 4.20). The Wiedemann-Franz law was used to calculate the electronic contribution to the thermal conductivity (κ_e) from the high temperature electrical resistivity data. The Lorentz constant used in these calculations was $L = 2.44\times10^{-8}$ W Ω K^{-2}. The electronic contribution to the thermal conductivity was subtracted from the measured thermal conductivity to obtain a value for the lattice contribution to the thermal conductivity (κ_L). In general the electronic contribution to the thermal conductivity increases with temperature, while the lattice contribution remains fairly constant with temperature. Figure 4.21 shows the observed change in the thermal conductivity across the series is due to changes in the electronic contribution. Although cation disorder is created through substitution across the main group sites, the mass difference between tin and indium is too small to affect the lattice contribution of the thermal conductivity through alloy scattering of phonons.

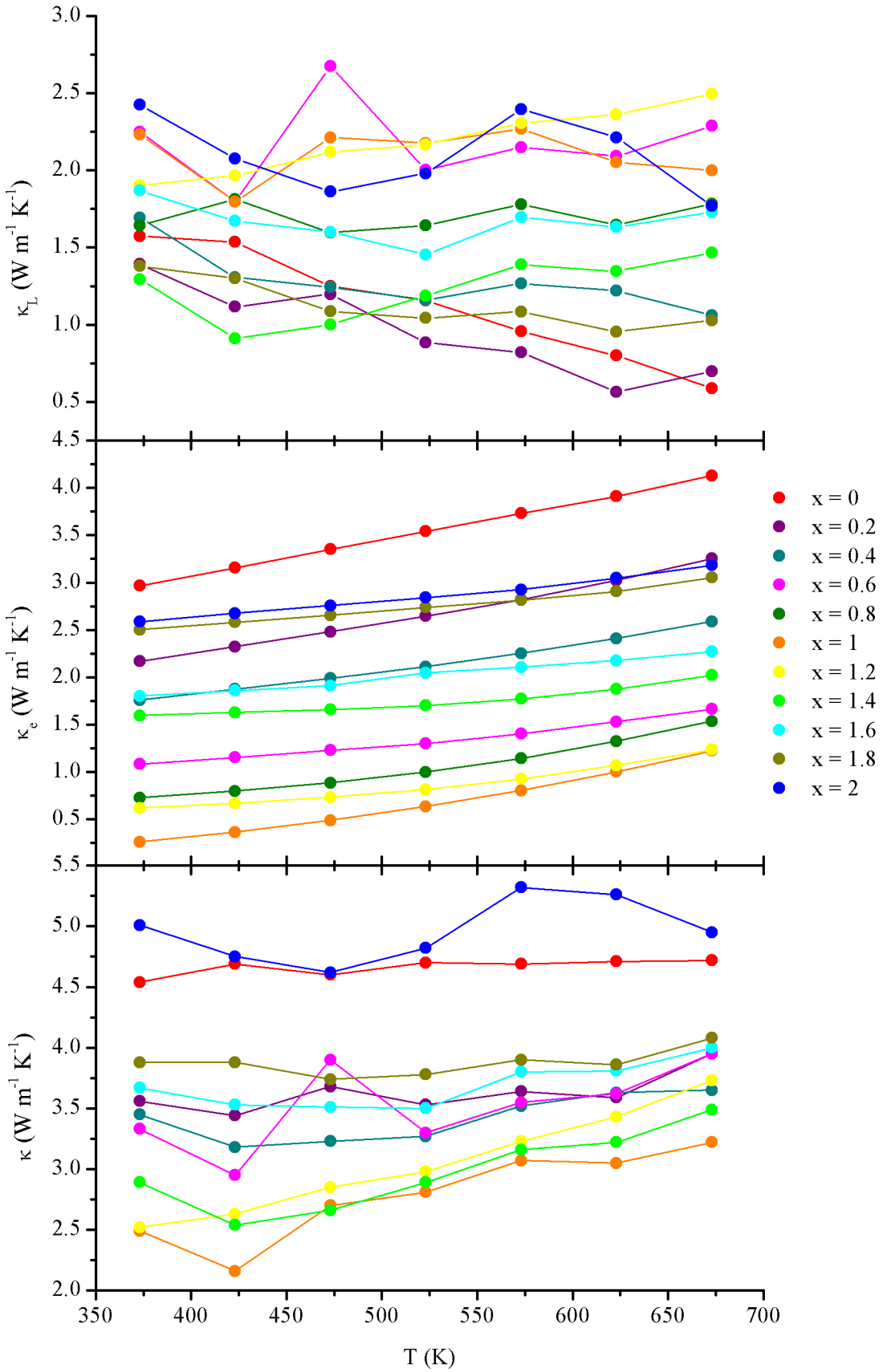

Figure 4.20: Temperature dependence of κ (bottom), κ_e (middle) and κ_L (top) for $Co_3Sn_{2-x}In_xS_2$ ($0 \leq x \leq 2$), where $\kappa = \kappa_e + \kappa_L$. κ_e was calculated using the Wiedemann-Franz law using high temperature measurements of the electrical resistivity.

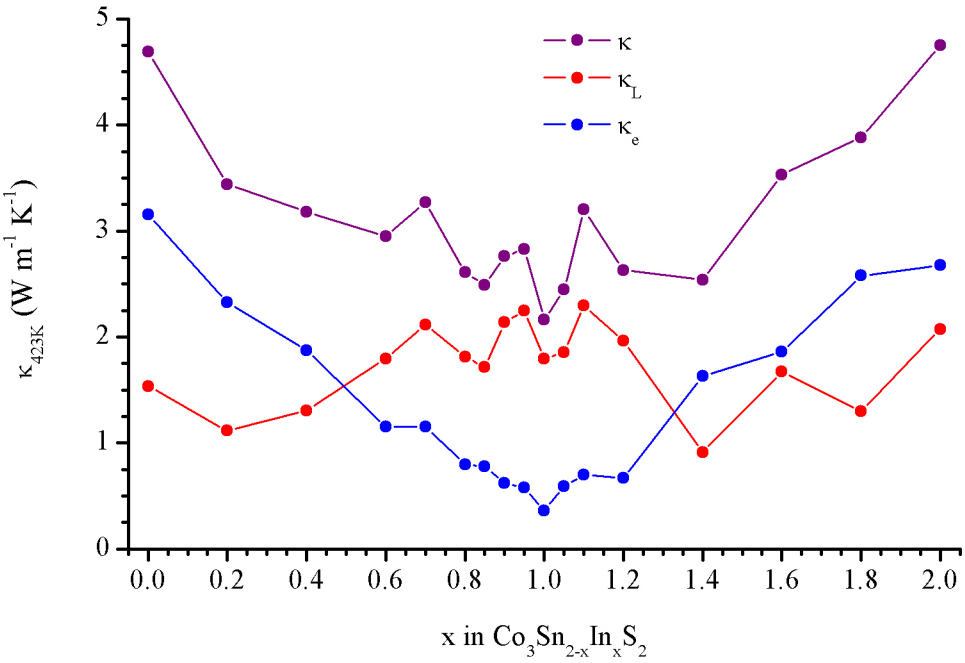

Figure 4.21: Changes in κ, κ_L and κ_e for the series $Co_3Sn_{2-x}In_xS_2$ ($0 \leq x \leq 2$) as a function of composition at 423 K.

4.8 Thermoelectric Properties

Electrical resistivity, Seebeck coefficient and thermal conductivity measurements were used to determine the thermoelectric power factor (S^2/ρ) and thermoelectric figure of merit (ZT) of the samples. The power factor was calculated for both temperature ranges over which measurements were performed, $100 \leq T\ (K) \leq 300$ (Figure 4.22) and $300 \leq T\ (K) \leq 673$ (Figure 4.23). The power factor reaches values of 12–19 μW cm^{-1} K^{-2} at temperatures in the region of ambient. These values compare favourably with those of commercial Bi_2Te_3-based materials (36 μW cm^{-1} K^{-2}).

The thermoelectric figure of merit was calculated over the higher temperature region only due to the unavailability of an instrument to measure the thermal conductivity at lower temperatures (Figure 4.24). Indium-rich members of the $Co_3Sn_{2-x}In_xS_2$ ($0 \leq x \leq 2$) series show low thermoelectric figures of merit, which is an effect of the low Seebeck coefficient. However, tin-rich members show more promising results. There have been a number of recent investigations on sulphide thermoelectrics motivated by the search for a tellurium-free replacement for Bi_2Te_3. Amongst conventional bulk materials, the Chevrel phase $Cu_4Mo_6S_8$,[25] $LaGd_{1.03}S_3$[40] and Cu_yTiS_2[19] have been reported to exhibit $ZT \geq 0.4$ at temperatures above the maximum investigated for $Co_3Sn_{2-x}In_xS_2$. The

maximum ZT of 0.32 occurs at 673 K for $Co_3Sn_{1.6}In_{0.4}S_2$. At the same temperature this is comparable with Cu_yTiS_2 and slightly higher than both $Cu_4Mo_6S_8$ and $LaGd_{1.03}S_3$. However, the ZT of 0.28 observed around 425 K for the cobalt Shandite phases corresponding to x = 0.8 and 0.85, are 50% higher than Cu_yTiS_2, double that of $Cu_4Mo_6S_8$ and nearly triple those reported for $LaGd_{1.03}S_3$ at the same temperature. From these results it can be concluded that the obtained ZT of 0.28 at 425 K for the cobalt Shandites $Co_3Sn_{1.2}In_{0.8}S_2$ and $Co_3Sn_{1.15}In_{0.85}S_2$, is the highest currently known for a sulphide thermoelectric material at this temperature.

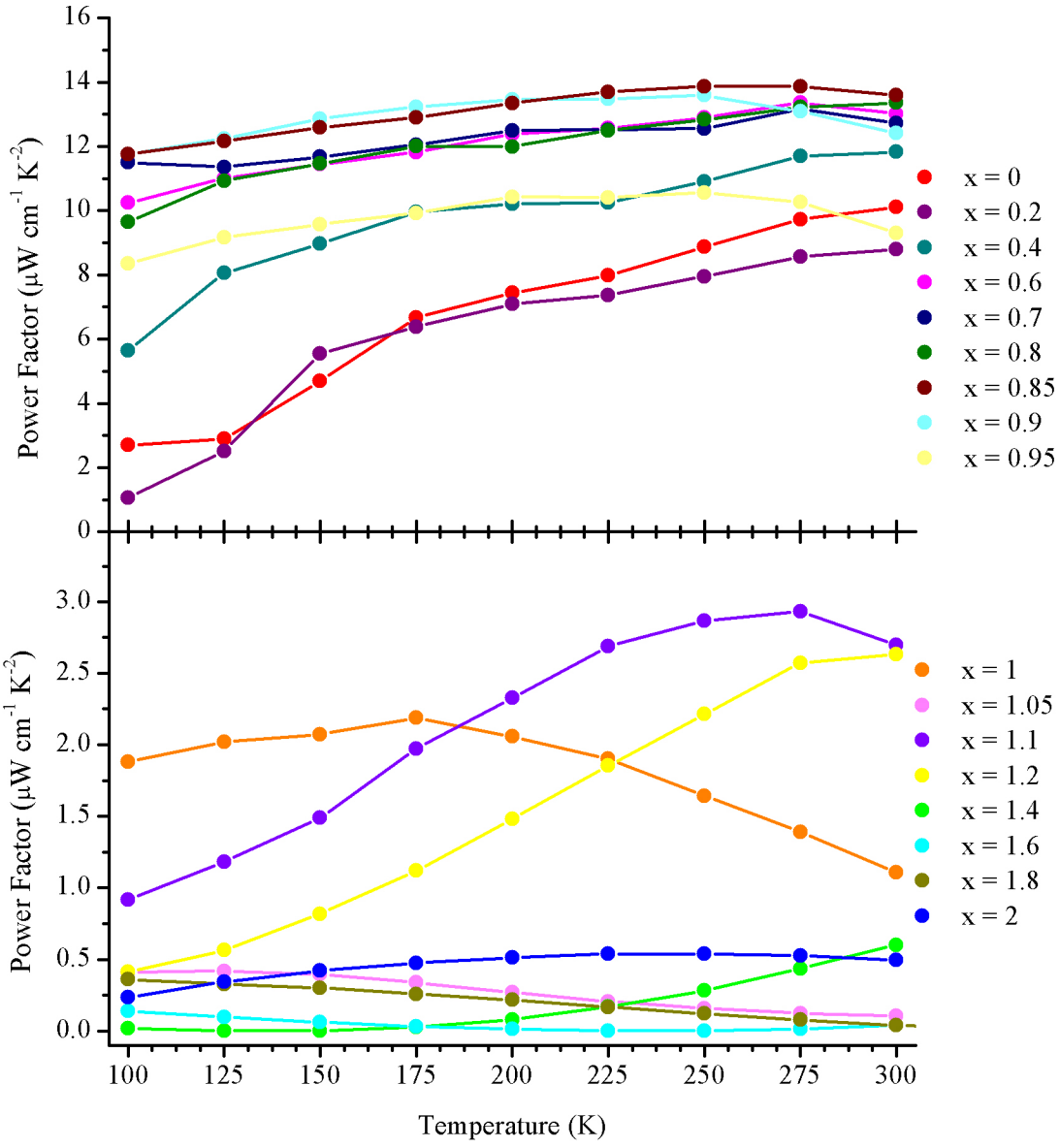

Figure 4.22: The Power factor as a function of temperature for samples of $Co_3Sn_{2-x}In_xS_2$ ($0 \leq x \leq 2$) between 100 and 300 K.

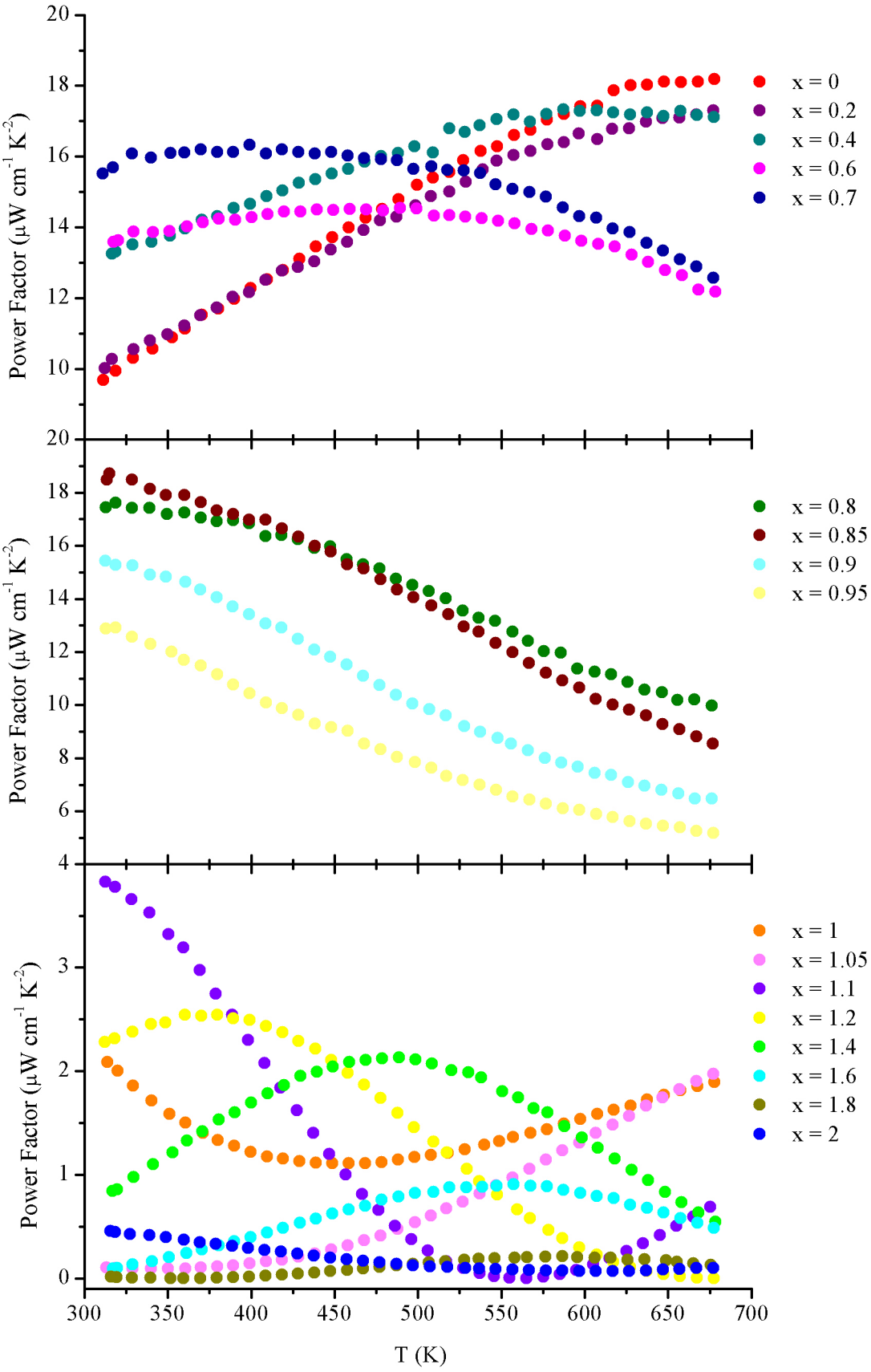

Figure 4.23: The Power factor of $Co_3Sn_{2-x}In_xS_2$ ($0 \leq x \leq 2$) in the temperature range $300 \leq T\ (K) \leq 673$.

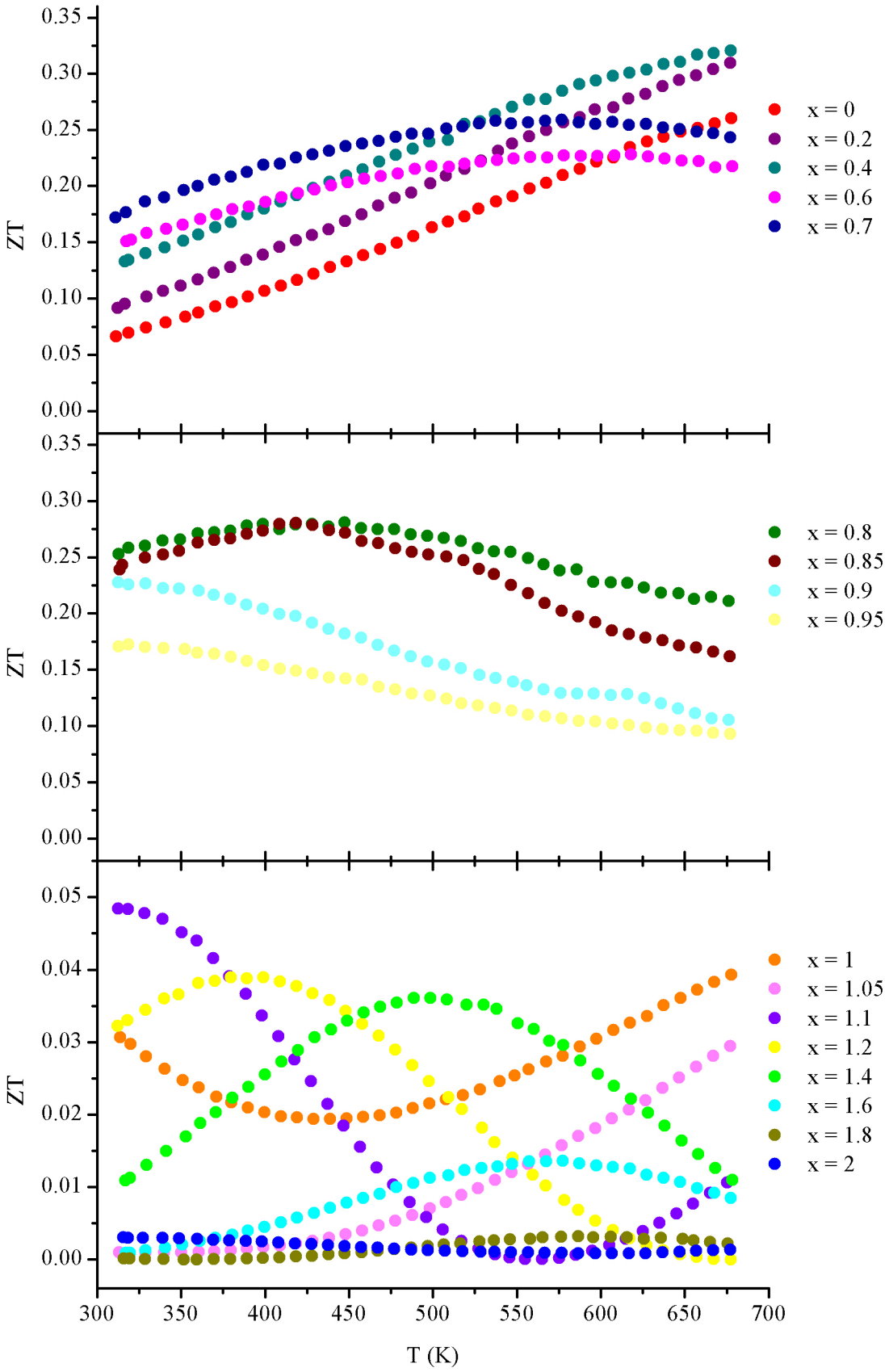

Figure 4.24: The thermoelectric figure of merit (ZT) for the series $Co_3Sn_{2-x}In_xS_2$ ($0 \leq x \leq 2$) in the temperature range $300 \leq T\ (K) \leq 673$.

4.9 Improving ZT

Samples in the cobalt Shandite series $Co_3Sn_{2-x}In_xS_2$ ($0 \leq x \leq 2$) have been shown to exhibit promising values of ZT. Efforts to improve the figure of merit through chemical substitution are described below.

4.9.1 Substitution at the transition-metal site

Substitution across the main-group site in $Co_3Sn_{2-x}In_xS_2$ has been shown to improve the thermoelectric properties of the material. Substitution at the transition-metal site of cobalt for nickel was investigated as a method of improving ZT. The substitution would increase the number of valence electrons available for conduction and reduce the electrical resistivity of the material. It was hoped that low levels of substitution would not affect the values observed for the Seebeck and thermal conductivity too greatly.

Substitution of cobalt within the kagome layer by nickel was investigated for samples of composition $Co_{3-y}Ni_ySn_{1.2}In_{0.8}S_2$ ($y = 0.05$ and 0.1). The tin and indium composition was chosen due to the high ZT of the fully cobalt-substituted phase. Samples were synthesised using the same procedure as the mixed main group samples described in section 2.1.2. X-ray diffraction patterns showed similarities with $Co_3Sn_{1.2}In_{0.8}S_2$ with slight shifting in Bragg reflections suggesting that a solid solution had resulted rather than a mixture of two distinct Shandite phases (Figure 4.25). Lattice parameters were obtained from a Topas refinement (Table 4.9). The lattice parameters are similar to the fully cobalt-substituted phase, with *a* increasing slightly and *c* decreasing slightly with substitution.

Table 4.9: Lattice parameters of $Co_{3-y}Ni_ySn_{1.2}In_{0.8}S_2$ ($0 \leq y \leq 0.1$) obtained from powder X-ray diffraction experiments.

y	*a (Å)*	*c (Å)*
0	5.32527(8)	13.4166(1)
0.05	5.32718(7)	13.4071(2)
0.1	5.32918(7)	13.4082(2)

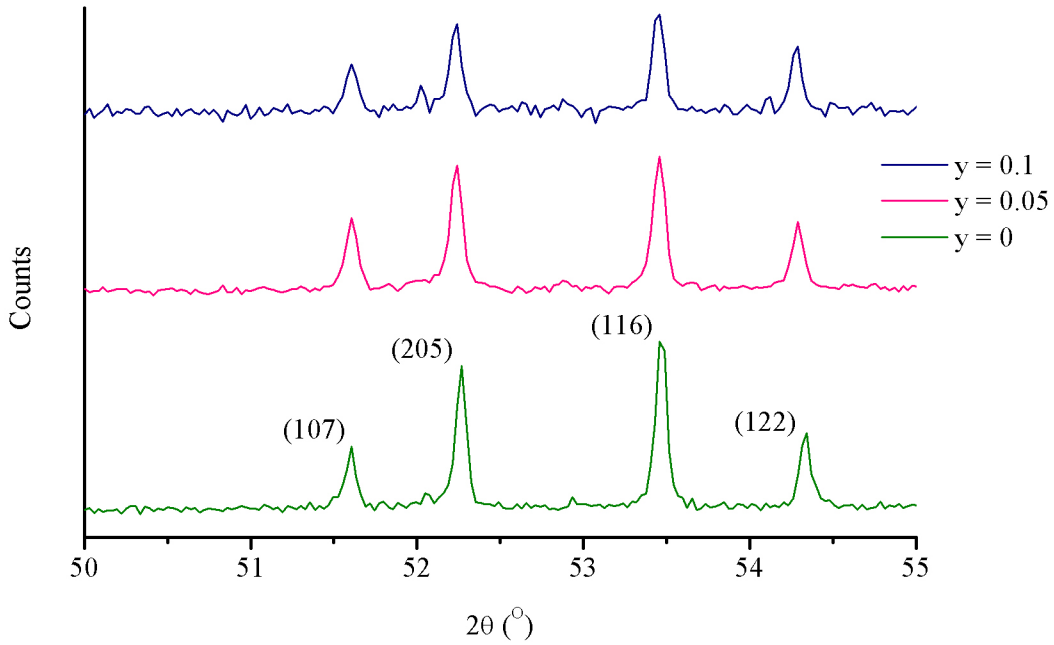

Figure 4.25: Changes in powder X-ray diffraction data for $Co_{3-y}Ni_ySn_{1.2}In_{0.8}S_2$ ($0 \leq y \leq 0.1$) as a function of nickel content. Numbers in parenthesis indicate the *hkl* value of the Bragg reflection.

Measurements of electrical resistivity, Seebeck coefficient (Figure 4.26)) and thermal conductivity (Figure 4.27) were performed for comparison with $Co_3Sn_{1.2}In_{0.8}S_2$. The addition of the more electron rich nickel reduces the electrical resistivity. A metallic ρ(T) dependence is observed at low temperature for all compositions. At higher temperatures a change to semiconducting behaviour is observed. The change in sign of dρ/dT was shifted to higher temperatures with increasing nickel content. There is a difference between the electrical resistivity values measured at the boundary between the low and high temperature ranges. Differences are in the region of 0.5 mΩcm and are exaggerated by the low resistivity of the materials. However, one explanation for the difference could come from the slight differences in the method used to collect the data. During low temperature measurements, the current is passed through the pellet in one direction. This could lead to a temperature gradient being created across the pellet. The joule heating induced temperature gradient could allow contributions from the Seebeck coefficient to counteract the conduction of charge carriers and increase the measured value of the electrical resistivity. The difference between the two data sets increases at higher temperatures where the Seebeck is higher, suggesting it a factor in the discrepancy. The high temperature instrument switches the current direction during the measurement, minimising any joule heating effects. The Seebeck coefficients of the

nickel-substituted phases show the same trend as a function of temperature as $Co_3Sn_{1.2}In_{0.8}S_2$. The Seebeck coefficient decreases on the addition of nickel. Nickel adds more electron density into the conduction band than cobalt. This increase changes the position of the Fermi level in the density of states and moves it to a less sharp region, therefore a lower Seebeck coefficient is observed. The thermal conductivity is observed to increase with the addition of nickel. This is caused by an increase in the electron thermal conductivity, as lattice thermal conductivity is unaffected by the substitution. The reduction in the electrical resistivity and the Seebeck coefficient and increase in the thermal conductivity leads to an overall decrease in ZT at lower temperatures. ZT drops off less quickly for y = 0.1 and at higher temperature is slightly larger than the nickel-free phase.

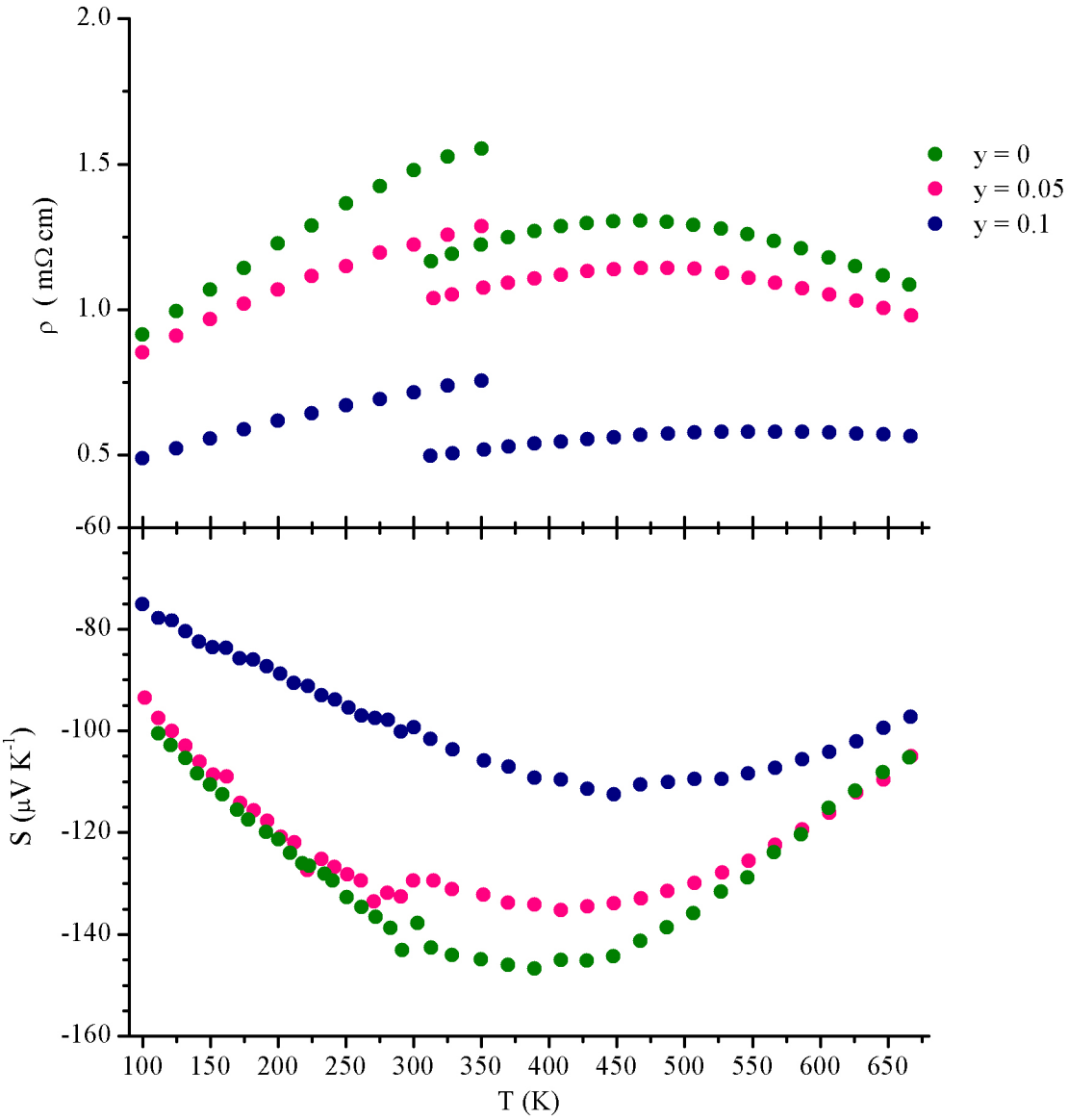

Figure 4.26: Electrical resistivity and Seebeck coefficient as a function of temperature for $Co_{3-y}Ni_ySn_{1.2}In_{0.8}S_2$ ($0 \leq y \leq 0.1$) in the temperature range $100 \leq T\ (K) \leq 673$.

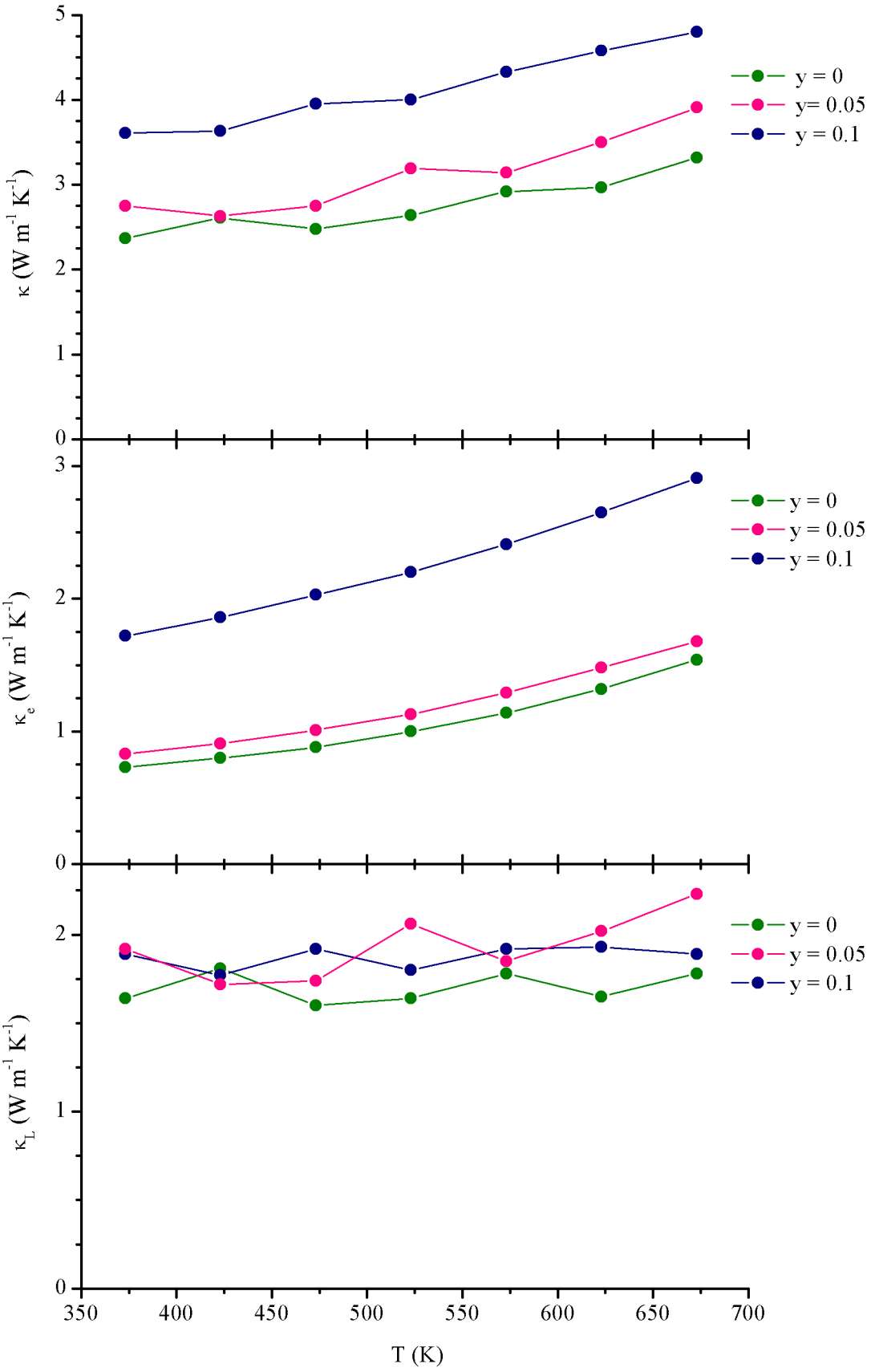

Figure 4.27: The thermal conductivity, κ (top), electronic contribution, κ_e (middle) and lattice contribution, κ_L (bottom) as a function of temperature for the series $Co_{3-y}Ni_ySn_{1.2}In_{0.8}S_2$ (y = 0, 0.05 and 0.1) in the temperature range $373 \leq T\ (K) \leq 673$.

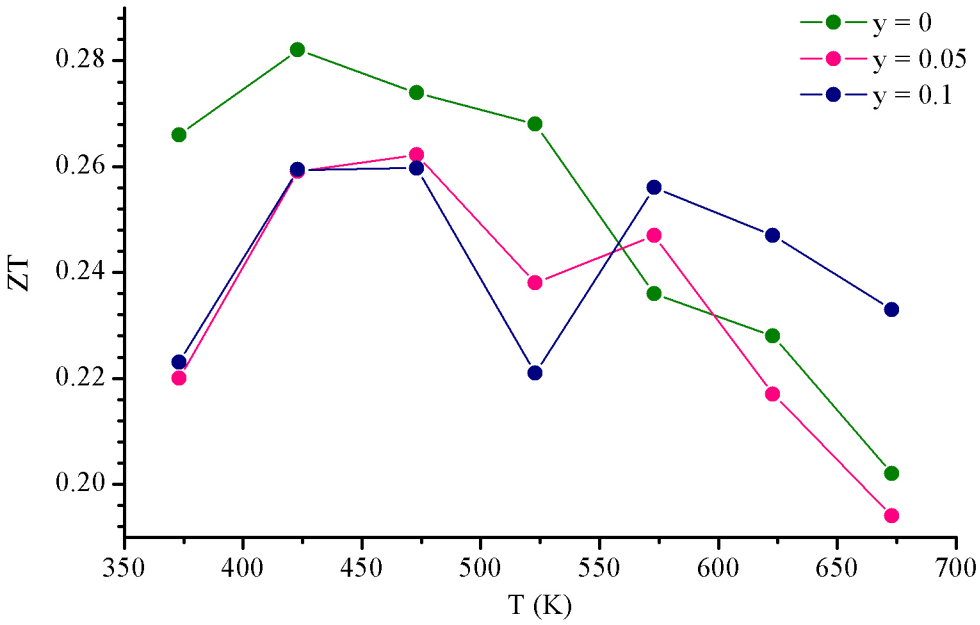

Figure 4.28: The thermoelectric figure of merit of $Co_{3-y}Ni_ySn_{1.2}In_{0.8}S_2$ ($0 \leq y \leq 0.1$) as a function of temperature in the temperature range $373 \leq T\ (K) \leq 673$.

With small quantities of nickel substitution (< 5 %), it can be assumed that the cobalt d-bands, which are located around the Fermi level, are not affected too greatly. The addition of nickel adds electrons into the conduction band and the increase in the number of available charge carriers for conduction, decreases the resistivity of the material. However, the Fermi level is also affected, moving higher into the conduction band. The Seebeck coefficient is reduced by moving the Fermi level away from the sharpest region of the density of states. Overall, this leads to a decrease in ZT. However, at 373 K, y = 0.1 has a similar electrical resistivity and thermal conductivity when compared to $Co_3Sn_{1.6}In_{0.4}S_2$. On the other hand, the Seebeck coefficient has increased from -85 to -107 $\mu V\ K^{-1}$ leading to a 37.5% increase in ZT at this temperature. This suggests that it may be possible to obtain a higher ZT with small levels of nickel substitution of more indium-rich members of the series. Through substitution of both the transition-metal and main-group sites, the optimum composition for high values of ZT could be investigated.

4.9.2 Reduction of thermal conductivity

4.9.2.1 Main-group substitution

Substitution to increase alloy scattering of phonons within the structure was investigated in an attempt to reduce the lattice contribution of the thermal conductivity of materials with the Shandite structure. As $Ni_3Tl_2S_2$ has previously been reported, it was believed that the preparation of the previously unreported cobalt analogue, $Co_3Tl_2S_2$, might be achievable. This could then lead to the preparation of a series where tin, indium and thallium could occupy the main group sites. When indium replaces tin, no alloy scattering is observed to lower the lattice thermal conductivity. However thallium is much heavier than indium and substitution would likely lead to a decrease in the lattice contribution.

Attempts to prepare $Co_3Tl_2S_2$ were unsuccessful. The previously reported phase Co_2TlS_2 resulted in all cases in conjunction with several additional impurity phases. The crystal structure of Co_2TlS_2 (Figure 4.29) is constructed from layers of edge-sharing SCo_4 square pyramids, where adjacent pyramids are inverted. Thallium occupies sites between these layers.

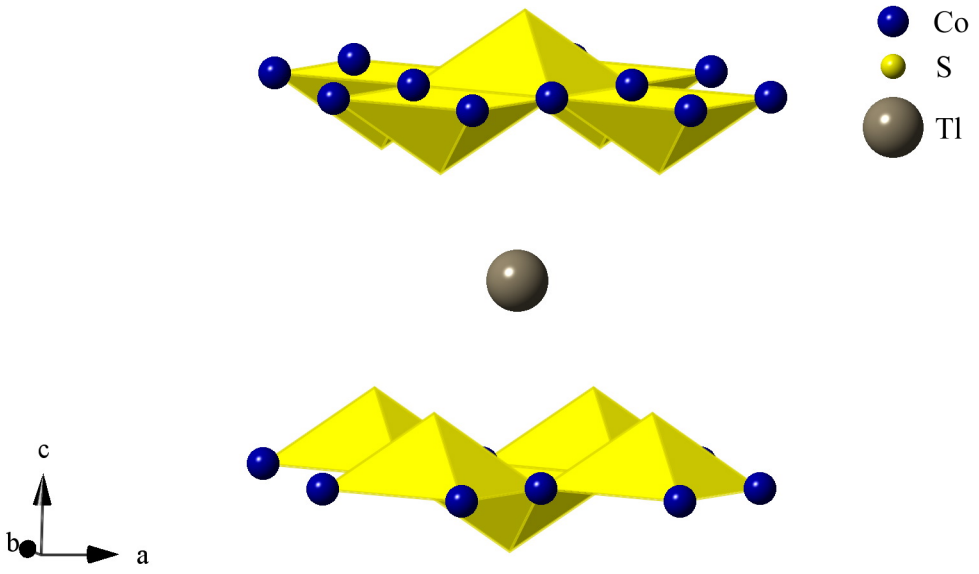

Figure 4.29: Structure of Co_2TlS_2.

Previous reports indicate that Co_2TlS_2 is metallic and magnetic susceptibility measurements show ferromagnetic ordering occurs below T_c = 152 K.[93] A single phase

sample of Co_2TlS_2 was synthesised as described in section 2.1.3 in order to investigate the electrical and thermal transport properties. Rietveld refinement of the structural model against powder X-ray diffraction data was performed. The Goodness of Fit indices (χ^2 = 1.4, R_{wp} = 2.4 %) suggest the structural model is correct (space group = *I4/mmm*, *a = 3.73991(7) Å*, *c = 12.9509(3) Å*).

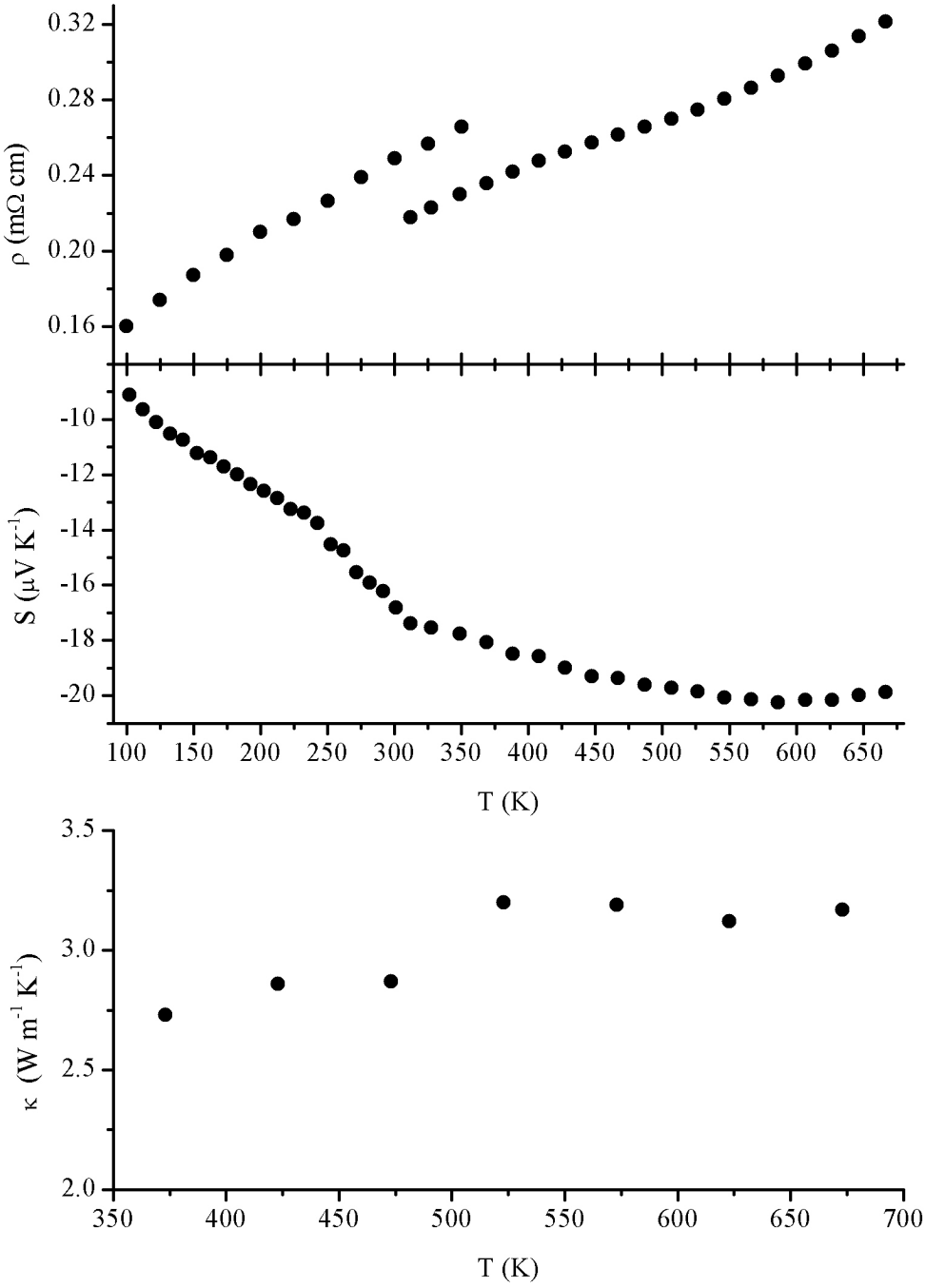

Figure 4.30: Temperature dependence of the electrical resistivity (top), Seebeck coefficient (middle) and thermal conductivity (bottom) for Co_2TlS_2.

Measurements of the electrical and thermal transport properties (Figure 4.30) on hot-pressed pellets of Co_2TlS_2 show metallic behaviour and negative values of the Seebeck coefficient across the measured temperature range. Despite values of electrical resistivity and thermal conductivity being acceptable for a thermoelectric material, low values of the Seebeck coefficient rule out any use of stoichiometric Co_2TlS_2 as a thermoelectric material. A maximum Power factor of 0.15126 mW m^{-1} K^{-2} at 489 K, and ZT of 0.026 at 673 K were recorded for this phase.

4.10 Conclusions

The effects of substitution of tin by indium across the $Co_3Sn_{2-x}In_xS_2$ ($0 \leq x \leq 2$) series have been studied. Retention of Shandite structure was confirmed for all members of the series. Powder neutron diffraction experiments to investigate the ordering of main-group atoms over the two available main-group sites show that there is partial order. Indium has a preference for the intra-layer *M*(1) site and tin for *M*(2), the site in the kagome layer.

The half metallic ferromagnetic behaviour of $Co_3Sn_2S_2$ has been shown to persist up to indium contents of x = 0.4 before the increased separation between the kagome layers appears to disrupt long-range order. Chemical control of the electron population produces an unusual double metal-to-semiconductor-to-metal electronic transition as the indium content is increased across the series. This is induced by the systematic and sequential depopulation of two bands that are separated by a band gap in the density of states. For the stoichiometric Co_3SnInS_2 phase, the conduction band is empty and the valence band is filled and the Fermi level sits in the band gap between them. It has been shown that samples either side of Co_3SnInS_2 that exhibit metallic behaviour at low temperatures, become intrinsic semiconductors upon heating. Changes in the Seebeck coefficient as a function of temperature in the same composition region indicate that the materials are mixed conductors of electrons and holes with the dominant charge carrier dependent on composition and temperature. In the case of x = 0, 0.2 and 0.4, where magnetic order is observed, measurements of the electrical resistivity and Seebeck coefficient both show slight changes in temperature dependence at the ferromagnetic ordering temperature. The magnetic, and electrical transport properties may be summarised in a phase diagram of the series (Figure 4.31). The thermal conductivity has been shown to have a minimum around Co_3SnInS_2, caused by changes in the electronic contribution. Substitution of tin by indium does not cause alloy scattering because of the

similarities in mass and the lattice contribution remains similar across the series. The oxidation states of the elements within the material were investigated using the complimentary techniques of X-ray Photoelectron Spectroscopy and ^{119}Sn Mössbauer spectroscopy. X-ray Photoelectron Spectroscopy indicated that cobalt has the oxidation state Co^0. It also supports the In^0 oxidation state, but was less definitive for tin and sulphur. ^{119}Sn Mössbauer Spectroscopy showed tin occupies two distinct sites, *M*(1) and *M*(2). The quadrupole splitting clearly indicates the oxidation state of tin as Sn^0. Using information from both X-ray Photoelectron Spectroscopy and ^{119}Sn Mössbauer spectroscopy, the oxidation states of the elements within the $Co_3Sn_{2-x}In_xS_2$ ($0 \leq x \leq 2$) have been determined to be Co^0, Sn^0, In^0 and S^0. This is in contrast with the reported oxidation states of $Ni^0{}_3Sn^{2+}{}_2S^{2-}{}_2$.[86]

The investigation of $Co_3S_{2-x}In_xS_2$, a low-dimensional material whose band structure contains sharp narrow bands in the vicinity of the Fermi level, has demonstrated it is possible to use chemical substitution to tune the electrical transport properties. This has lead to the thermoelectric power factor and figure of merit being maximised by exploiting the increase in the Seebeck coefficient, as the position of the Fermi level within the band is varied. This result is in accordance with the predictions of Hicks and Dresselhaus[94] and produces a 3-fold increase in the figure of merit over that of the ternary end-member material for x = 0.8 at 425 K. Key to the promising performance of these materials is a highly structured DOS, leading to narrow bands in the region of the Fermi level. The maximum ZT = 0.32 is observed for $Co_3Sn_{1.6}In_{0.4}S_2$ at high temperatures and ZT = 0.28 at 425 K for $Co_3Sn_{1.2}In_{0.8}S_2$ and $Co_3Sn_{1.15}In_{0.85}S_2$. Further optimisation through for example nanostructuring, may render such materials viable for applications in low-grade waste heat recovery.

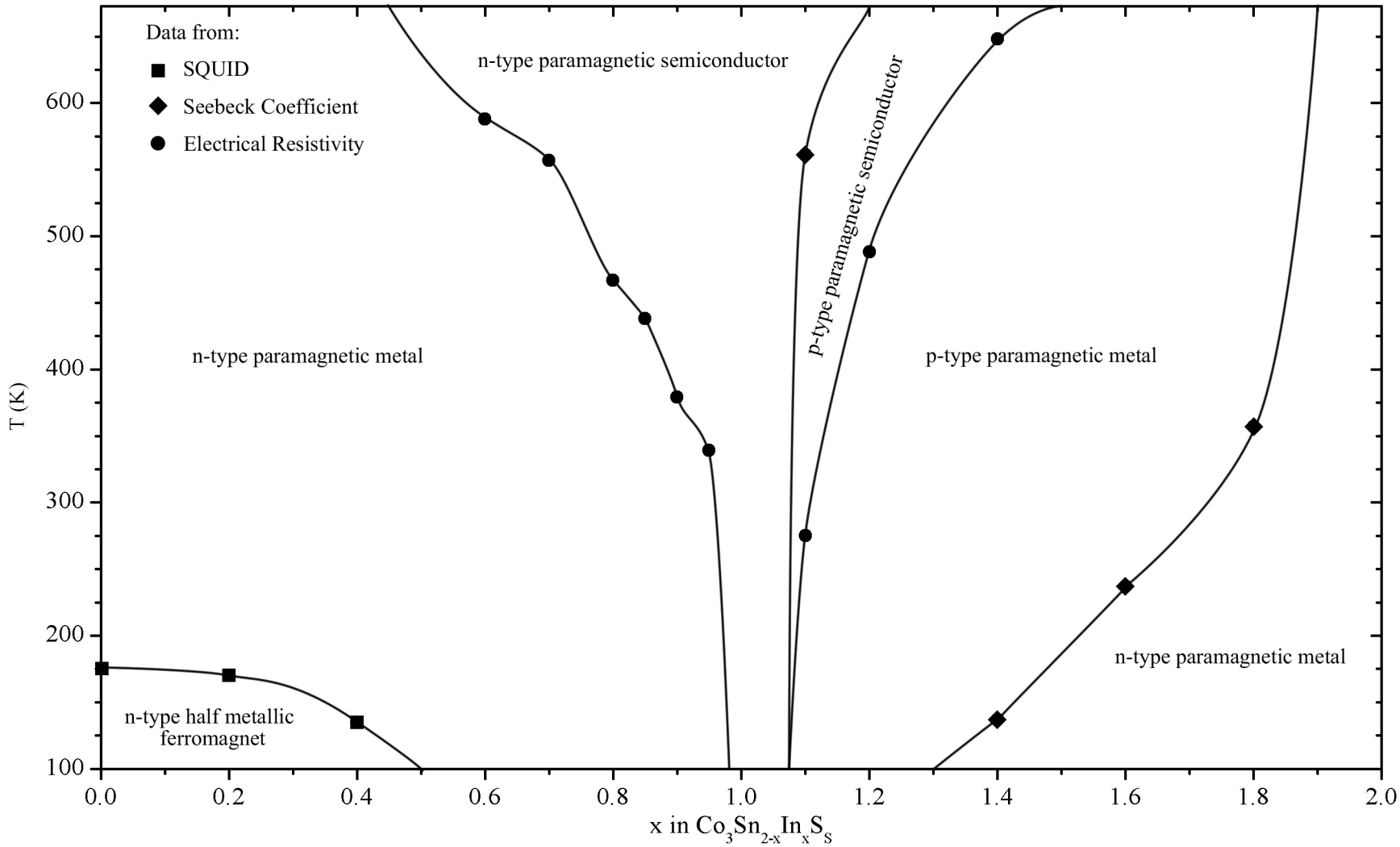

Figure 4.31: Phase diagram of magnetic and electrical transport properties of $Co_3Sn_{2-x}In_xS_2$ ($0 \leq x \leq 2$) between 100 and 673 K, established using data collected in this work.

Chapter 5 – $In_2Sn_3S_7$ and $Cr_2Sn_3Se_7$

5.1 Introduction

The sulphide $In_2Sn_3S_7$ and the selenide $Cr_2Sn_3Se_7$ have been shown to be structural analogues.[63-64] Both have previously been prepared as single crystals, however they have proved to be tricky to prepare as bulk polycrystalline materials. Samples in previous studies of $Cr_2Sn_3Se_7$ were found to contain the binary selenides of tin and chromium and preparation of bulk polycrystalline $In_2Sn_3S_7$ has not been reported. This work investigates the synthesis of these materials in an attempt to prepare good quality bulk samples for structural investigations and property measurements. The possibility of creating a series of materials with this structure through chemical substitution has also been investigated. As shown in section 1.6.3, the structure has three possible octahedral sites that indium, chromium and tin can occupy. Cation ordering across these sites has been investigated using powder neutron diffraction. Electrical and thermal transport property measurements have also been recorded.

Different synthesis strategies were attempted for the preparation of $In_2Sn_3S_7$. Reaction mixtures that were placed into cold furnaces and heated up to the reaction temperature at various rates produced impure samples, as did cooling the sample at rates between 1 and 10 °C min^{-1}. Extending and reducing the heating time also resulted in less pure samples. All this suggests that $In_2Sn_3S_7$ is not thermodynamically stable over a large range of synthetic conditions and more stable impurities are synthesised readily if the conditions are not optimal. Samples of $In_2Sn_3S_7$ were synthesised as described in section 2.1.4. The synthesis reported in the literature for $Cr_2Sn_3Se_7$ used a Cr:Sn:Se starting reaction mixture with a 2:4:9 molar ratio.[64] On investigation, it was found that this resulted in the formation of tin selenide as an impurity phase. Several methods were attempted to improve the purity of the final product, however a fully single-phase product could not be achieved. The synthesis of $Cr_2Sn_3Se_7$ is described in section 2.1.5.

5.2 Structural Investigations

5.2.1 Powder X-ray Diffraction

Powder X-ray diffraction was used to determine the purity and the lattice parameters of samples prepared. The diffraction data collected for the sample of $In_2Sn_3S_7$ (Figure 5.1) show very minor traces of In_2S_3 as an impurity. The space group $P2_1/m$ was used and

lattice parameters were determined as a = *11.6694(6) Å*, b = *3.78824(1) Å*, c = *12.7882(1) Å* and β = *105.816(3)* °, which are consistent with those obtained using single crystal X-ray diffraction, as reported in the literature.[63]

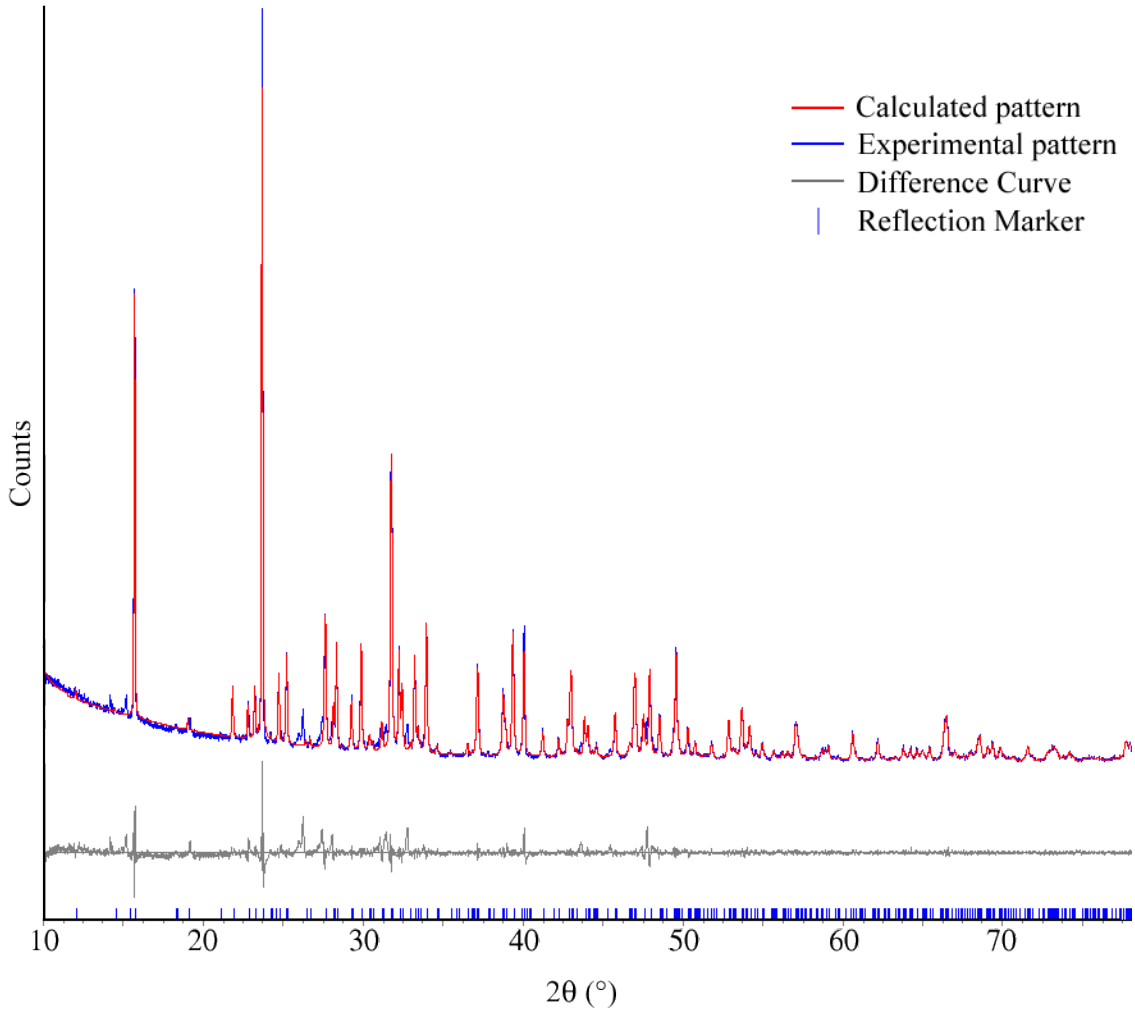

Figure 5.1: Powder X-ray diffraction pattern of $In_2Sn_3S_7$ showing the allowed reflection markers and calculated pattern from a refinement of lattice parameters.

The sample of $Cr_2Sn_3Se_7$ was shown to contain a few small peaks in the X-ray diffraction pattern due to an impurity phase (Figure 5.2). Matching peaks with the database and a subsequent lattice parameter refinement with the Topas3[68] package suggested the impurity peaks could be attributed to the orthorhombic phase of $Cr_2Sn_3Se_7$ (section 1.6.3). The same space group as the indium sulphide analogue ($P2_1/m$) was used for the monoclinic $Cr_2Sn_3Se_7$ phase and lattice parameters of a = *11.7701(4) Å*, b = *3.8187(1) Å*, c = *12.7468(4) Å* and β = *105.309(2)* ° were

determined. Lattice parameters for the orthorhombic phase (Space Group: *Pnma*) refined to *a = 22.919(5) Å*, *b = 3.826(1) Å* and *c = 12.574(1) Å*.

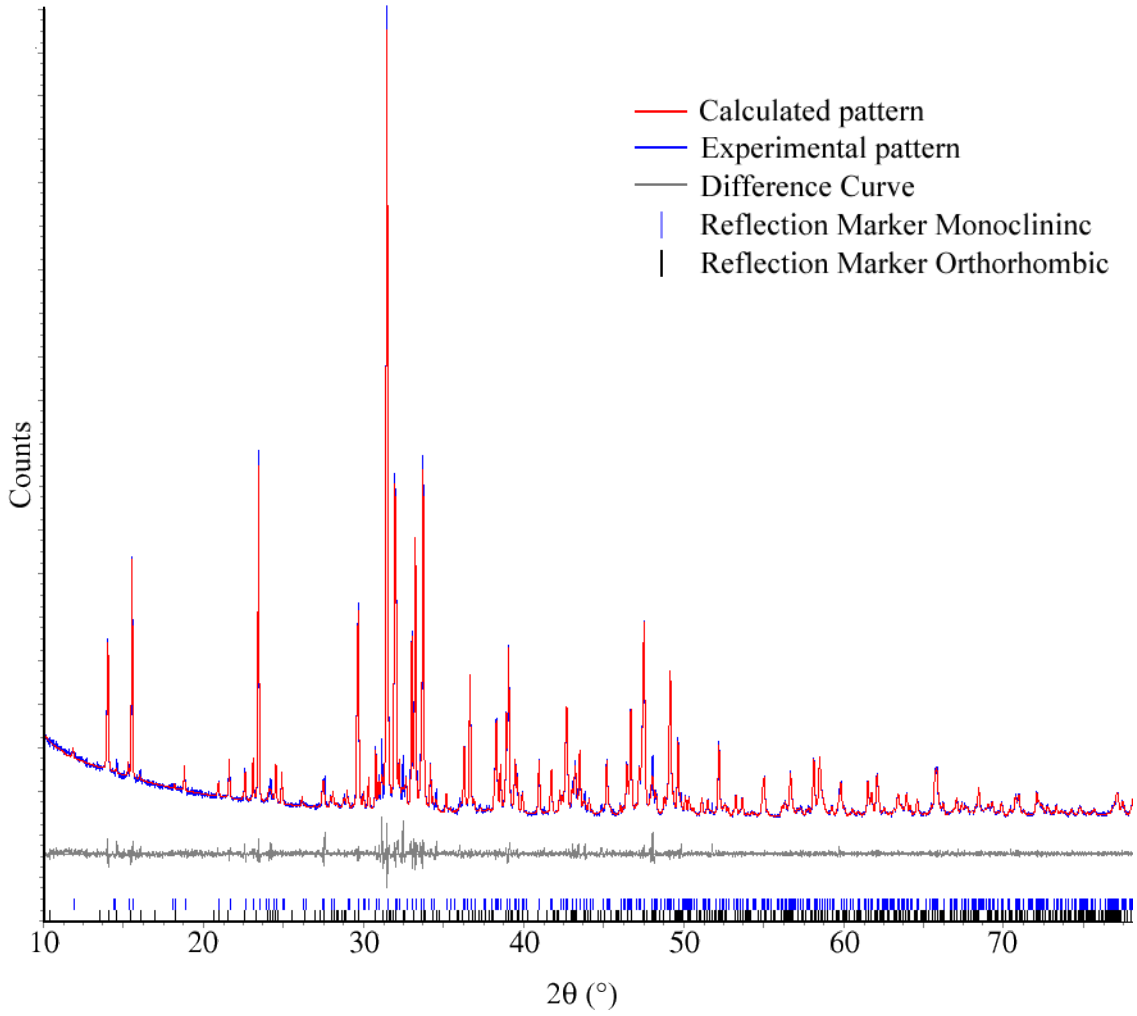

Figure 5.2: Powder X-ray diffraction pattern of $Cr_2Sn_3Se_7$ with allowed reflection markers for the primary monoclinic phase and the impurity orthorhombic phase, and the calculated pattern from a Le Bail lattice parameter refinement.

5.2.2 Powder Neutron Diffraction

Powder neutron diffraction experiments were performed on the HRPD diffractometer as described in section 2.3.3. Data were collected in a furnace for $In_2Sn_3S_7$ and at room temperature for $Cr_2Sn_3Se_7$. Structural refinements using the Rietveld method were performed with the GSAS software package.

5.2.2.1 $In_2Sn_3S_7$

Indium and tin are indistinguishable when using X-ray diffraction due to the similarities in electron count. Previously reported tin Mössbauer studies of $In_2Sn_3S_7$ suggested that indium and tin shared the occupancy of the three available octahedral sites.[63] Powder neutron diffraction was therefore used to investigate the site occupancy of the octahedral sites in both layers of the $In_2Sn_3S_7$ structure.

Indium is a neutron absorber, which led to a large background and small peak heights. The sample was contained within a Suprasil tube, which added structure to the background. The measurement also took place inside a furnace, which added peaks from the front and back vanadium windows. The diffraction pattern of the furnace and an empty tube was collected. However, this could not be subtracted from the experimental data because of the large mismatch in counting time between the two data sets. Due to error propagation from the background run, subtraction of the background gave significantly poorer data when compared to the original data set. As the background was not well defined by any of the available functions within GSAS, a manual fitting of the background was used. Refinements of the model resulted in values of χ^2 below 1 and gave no indication of the quality of the refinement. This can be caused by one of two things. Either poor counting statistics or there is a low peak size to background ratio.[74] In this case, χ^2 is below 1 because of the large background when compared with the intensities of the diffraction peaks. The manual fitting of the background used 100 points, which is the maximum allowed in the GSAS software package. During the structural refinements the lattice parameters, atomic coordinates, isotropic thermal parameters and the site occupancy factors of the octahedral sites were refined. The site occupancy factors of the three octahedral sites were constrained so that they each had the same indium and tin occupancies. Goodness of Fit data for the room temperature Rietveld refinement are presented in Table 5.1.

Table 5.1: Goodness of Fit parameters for the fit of the Rietveld refined model against room temperature neutron diffraction data for polycrystalline $In_2Sn_3S_7$.

χ^2	R_{wp} 168° (%)	R_{wp} 168° - B (%)	R_{wp} 90° (%)	R_{wp} 90° - B (%)
0.064	1.1	13	1.5	5

The R_{wp} for both data banks are around 1% which usually indicate a good fit. However the R_{wp} when the background is excluded, rises to 13% and 5% for the 168° and 90° banks respectively. The fitting of many of the background points is very good in the refinement, which lowers the overall R_{wp}. However when these points are excluded, the R_{wp} minus the background shows an increase. Visual inspection of both the sample and the background runs for the backscattering (Figure 5.3 and Figure 5.4) and the 90° bank (Figure 5.5 and Figure 5.6), shows areas where the pattern has the poorest fit are in regions where there are peaks and steps in the background. This suggests that although R_{wp} minus the background is larger than R_{wp}, the model fits the experimental data and structural information from the refinement is valid. Refined structural parameters are presented in Table 5.2. Support for the correctness of the refined structural model is provided by the lattice parameters and atomic coordinates, which are in agreement with the previously reported single crystal X-ray diffraction data.[63] This gives evidence that despite the low χ^2 and the large R_{wp} minus the background obtained, the Rietveld refinement of the structural model has yielded meaningful results. The refined site occupancy factors of the three octahedral sites show they are occupied by approximately two-thirds indium and one-third tin, giving the overall stoichiometry $In_{2.04(15)}Sn_{2.96(15)}S_7$. This is within error of the initial $In_2Sn_3S_7$ stoichiometry used during the synthesis of the sample.

Powder neutron diffraction experiments were performed over a range of elevated temperatures. It was hoped that some insight into the difficulties experienced during synthesis of the sample could be achieved. Data were collected from 400 °C up to 700 °C in 100 °C steps and at the synthesis temperature of 750 °C (Figure 5.7). As the temperature was raised to the synthesis temperature of 750 °C $In_2Sn_3S_7$ melts and a small impurity phase remained crystalline. The impurity phase peaks are consistent with strongest peaks of In_2Sn_3 but they were too weak to incorporate into a structural refinement.

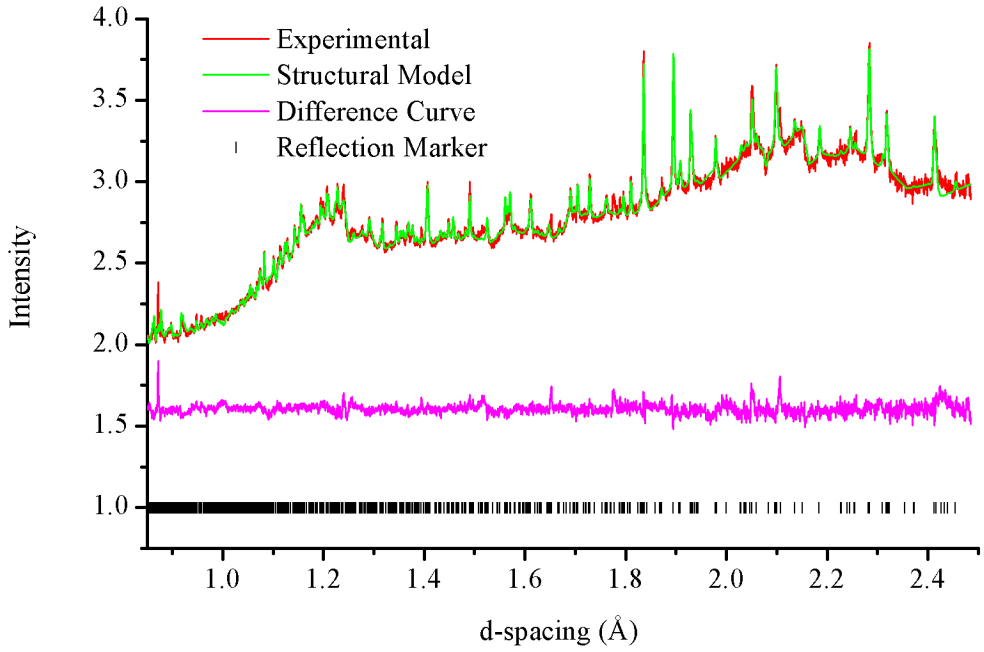

Figure 5.3: Powder neutron diffraction pattern of $In_2Sn_3S_7$ collected from the 168° bank on the HRPD diffractometer, the Rietveld refined structural model and the difference curve between the two.

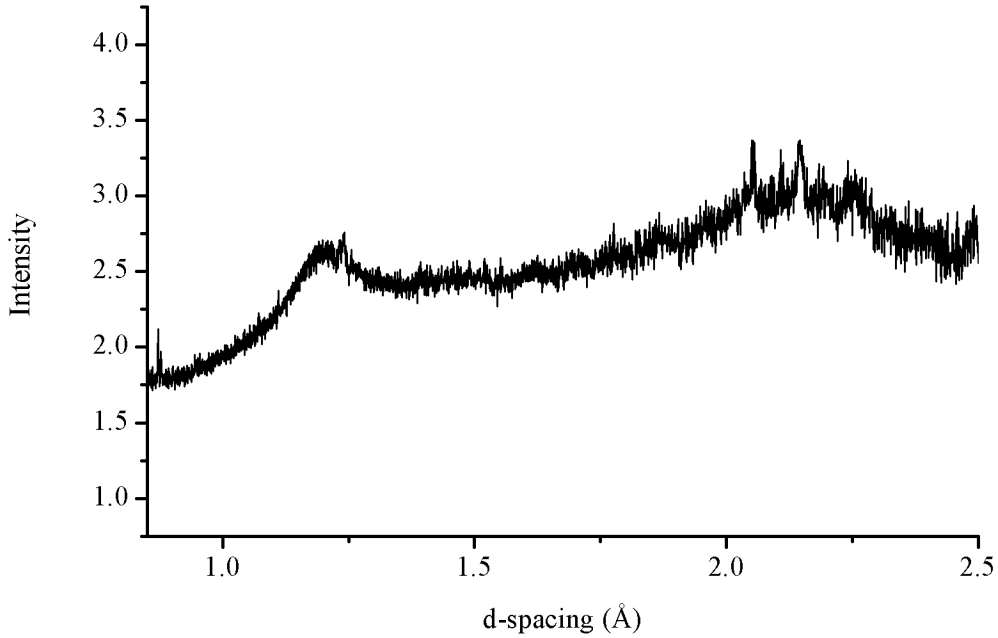

Figure 5.4: Background run of furnace, empty Suprasil tube and vanadium can for the 168° bank on the HRPD diffractometer.

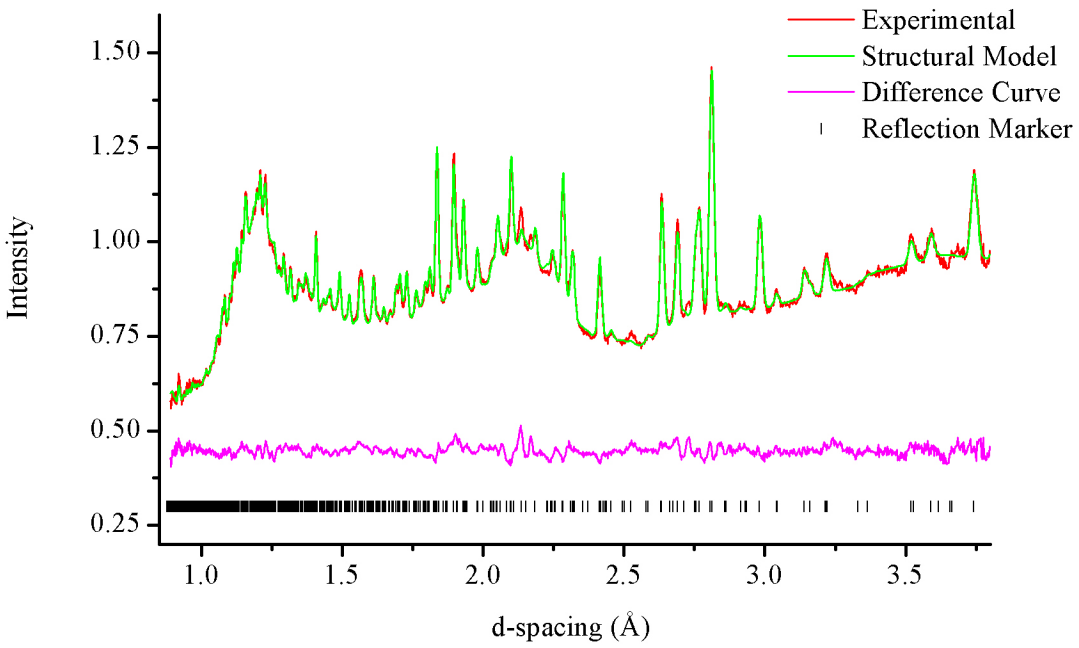

Figure 5.5: Powder neutron diffraction pattern of $In_2Sn_3S_7$ collected from the 90° bank on the HRPD diffractometer, the Rietveld refined structural model and the difference curve between the two.

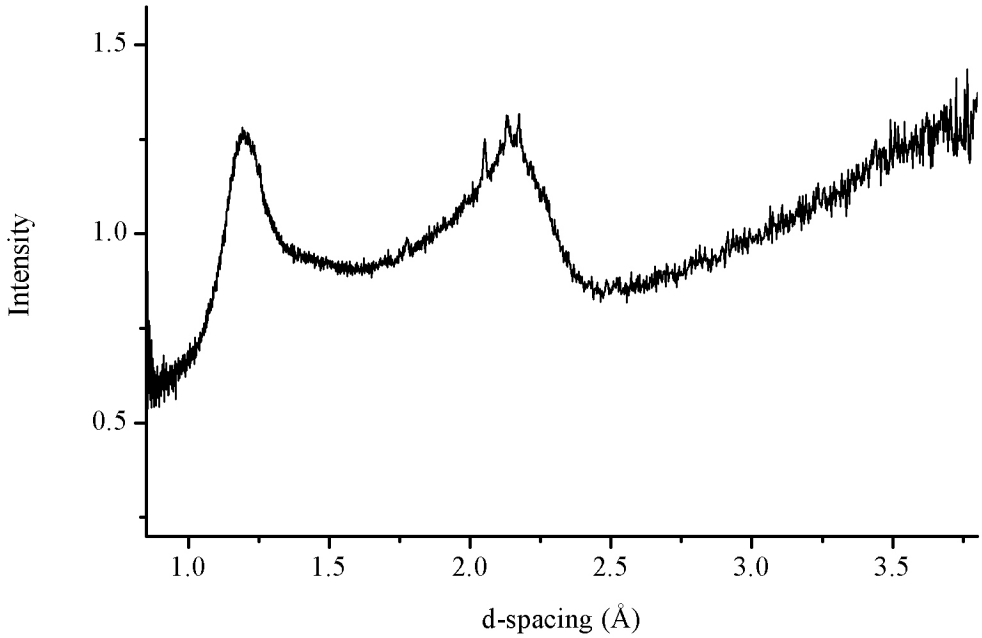

Figure 5.6: Background run of furnace, empty Suprasil tube and vanadium can for the 90° bank on the HRPD diffractometer.

Table 5.2: Atomic coordinates of $In_2Sn_3S_7$ obtained from Rietveld refinements of a structural model against powder neutron diffraction data collected on the HRPD diffractometer. Space Group: *$P2_1/m$*, *a = 11.6690(3) Å*, *b = 3.78854(6) Å*, *c = 12.6424(2) Å*, *β = 105.814(2) °*.

atom	*x*	*y*	*z*	*Uiso (Å^2)*	*SOF In*	*SOF Sn*
M(1)	0.5188(9)	0.25	0.380(1)	0.022(2)	0.68(5)	0.32(5)
M(2)	0.491(1)	0.25	0.878(1)	0.022(2)	0.68(5)	0.32(5)
M(3)	0.1098(9)	0.25	0.6081(9)	0.022(2)	0.68(5)	0.32(5)
Sn(4)	0.1528(9)	0.25	0.298(1)	0.068(3)	0(-)	1(-)
Sn(5)	0.1460(9)	0.25	0.966(1)	0.068(3)	0(-)	1(-)
S(1)	0.633(2)	0.25	0.073(2)	0.031(2)		
S(2)	0.383(2)	0.25	0.179(2)	0.031(2)		
S(3)	0.352(2)	0.25	0.679(2)	0.031(2)		
S(4)	0.619(2)	0.25	0.577(2)	0.031(2)		
S(5)	0.904(1)	0.25	0.241(1)	0.031(2)		
S(6)	0.882(1)	0.25	0.521(1)	0.031(2)		
S(7)	0.896(2)	0.25	0.879(2)	0.031(2)		

M = In, Sn.

Similar issues to those encountered in the room temperature refinement were present in the high temperature refinements. Table 5.3 shows the Goodness of Fit data for the refinements. The χ^2 are all smaller than 1, because of the high background. The R_{wp} are all less than or equal to 2 %, again because of the good fit to the background. The R_{wp} minus the background for both banks is a little larger. However, visually the fitting of the backscattering bank is good despite the Goodness of Fit statistics suggesting otherwise. There is a good fit to the 90° bank and the visual inspection of the data suggests the model is correct. The lattice parameters (Figure 5.8) and atomic coordinates (Appendix L) were determined during the Rietveld refinement of the $In_2Sn_3S_7$ structural model against the experimental powder neutron diffraction data. In general, as the temperature increases, the unit cell increase in all directions and the angle β decreases. Site occupancy factors of the octahedral sites were fixed at the value determined from refinements using the room temperature data.

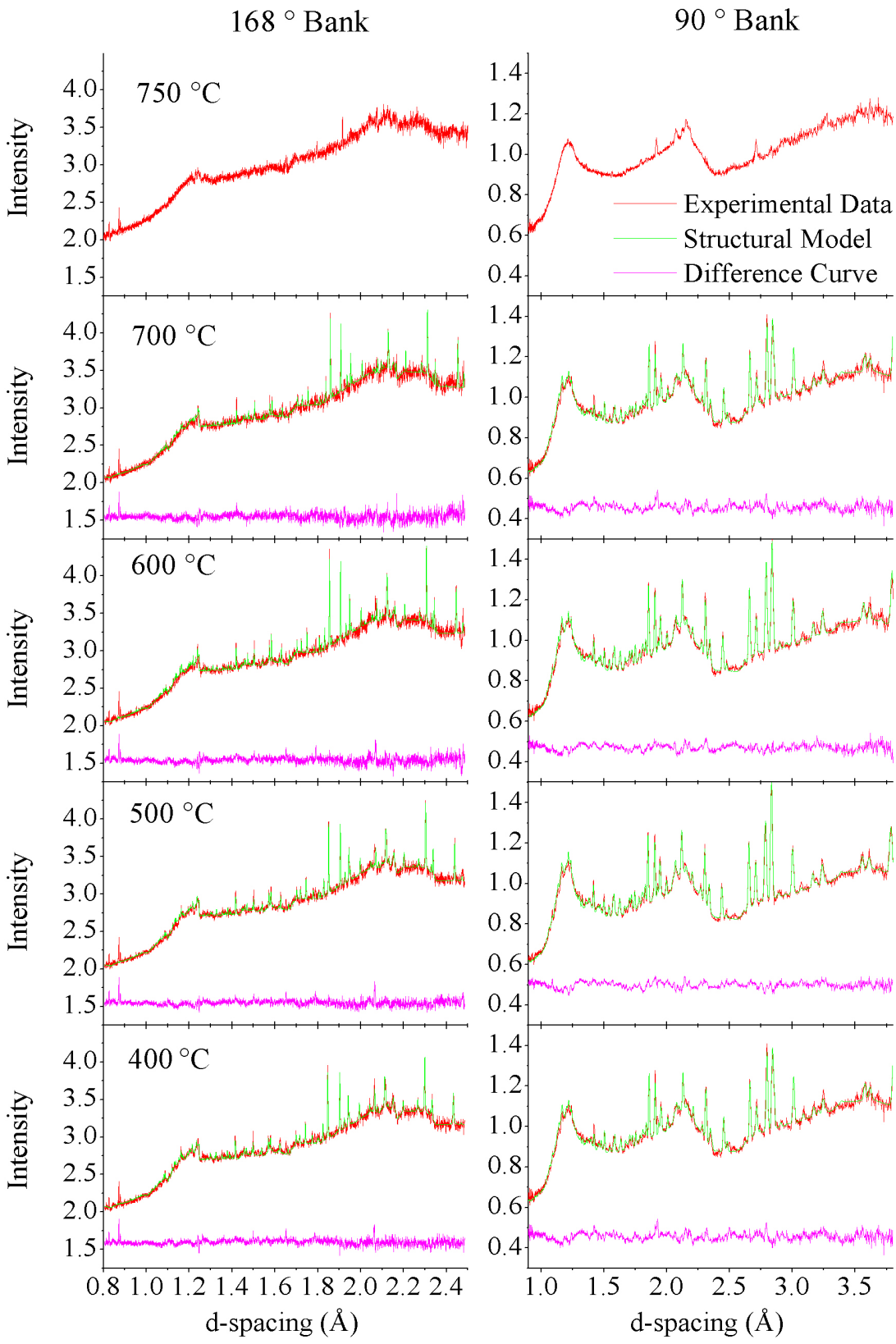

Figure 5.7: Refinements of the $In_2Sn_3S_7$ structural model against high temperature neutron diffraction data from the 168° and 90° banks on the HRPD diffractometer. The data collected at 750 °C correspond to the phase having melted.

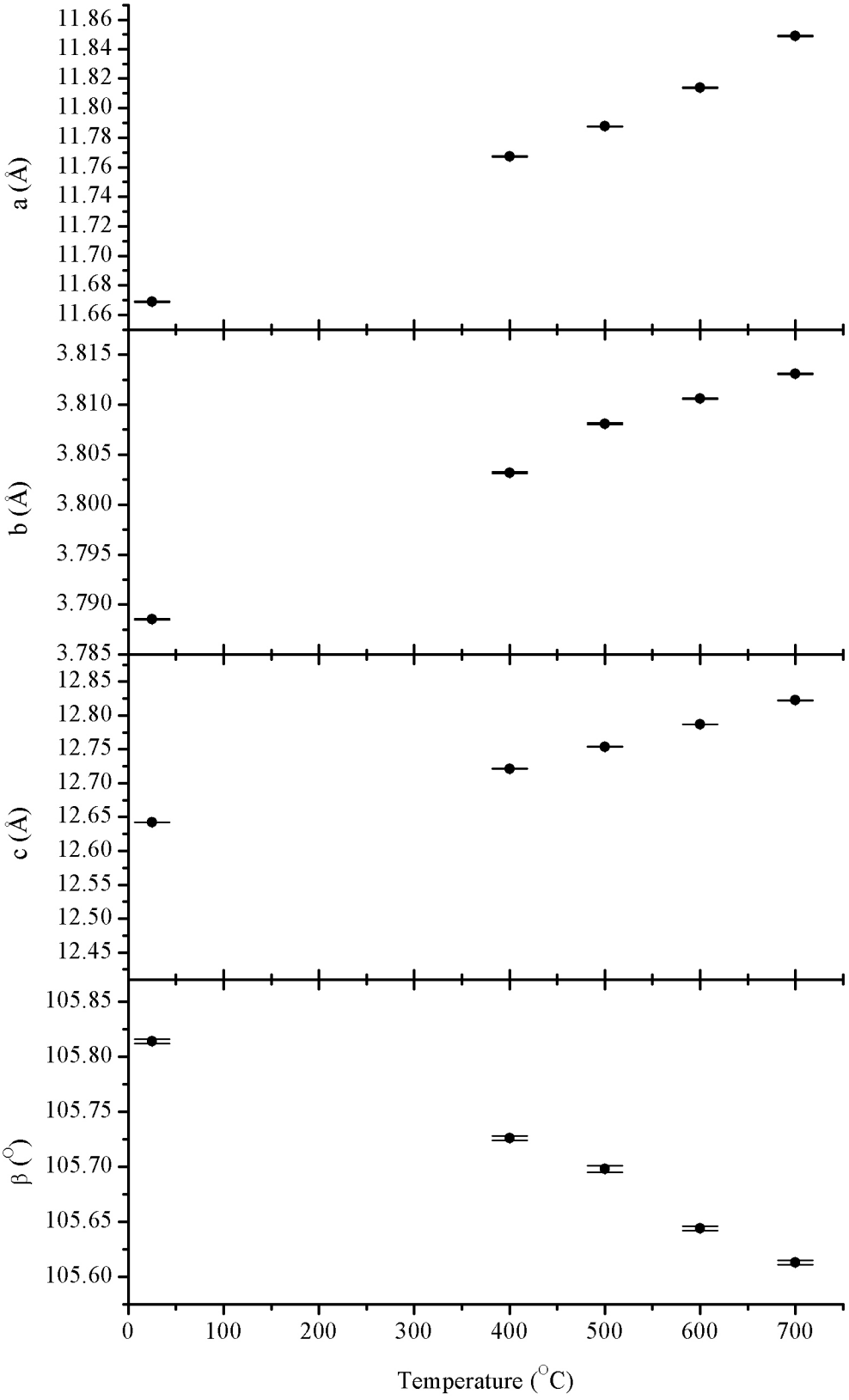

Figure 5.8: Lattice parameters *a*, *b*, *c* and *β* determined using powder neutron diffraction data for $In_2Sn_3S_7$ in the range 25 ≤ T (°C) ≤ 700.

Table 5.3: Goodness of Fit parameters for Rietveld refinements using high temperature neutron diffraction data.

T (K)	χ^2	R_{wp} 168° (%)	R_{wp} 168° - *B* (%)	R_{wp} 90° (%)	R_{wp} 90° - *B* (%)
400	0.079	1.2	9.1	1.7	4.7
500	0.085	1.3	8.3	1.7	4.4
600	0.11	1.5	10.0	1.8	4.2
700	0.065	1.5	9.7	2.0	5.8

The changes in final refined bond lengths and bond angles for $In_2Sn_3S_7$ at temperatures in the range $25 \leq T\ (°C) \leq 700$ are presented in Appendix M. The numbering system of atoms of the three octahedral and one square based pyramid site are presented in Figure 5.9. All three octahedral sites in $In_2Sn_3S_7$ are distorted. There are small fluctuations in the bond lengths and angles and the octahedra become more distorted at higher temperatures. The distortion around the *M*(3) site causes the separation between the layers to decrease from 2.72(2) Å at 25 °C to 2.47(4) Å at 700 °C. However the thickness of the layer containing the square based pyramid and *M*(3) increases as the *M*(3)-S(15) bond lengthens from 2.59(2) Å to 2.92(4) Å at 25 °C and 700 °C respectively.

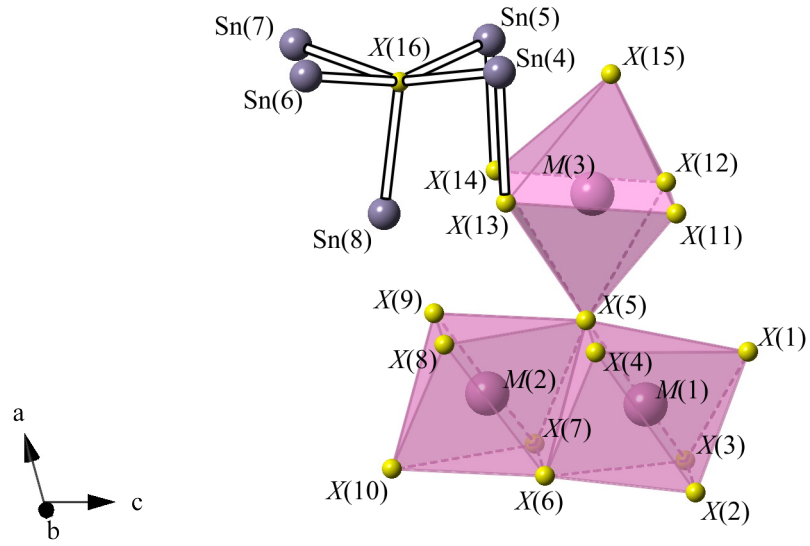

Figure 5.9: Atom labelling scheme for bond lengths and angles of $M_3Sn^{II}{}_2X_7$ (*M* = In, Sn^{IV}, Cr, *X* = S, Se).

5.2.2.2 $Cr_2Sn_3Se_7$

Data were collected for $Cr_2Sn_3Se_7$ at room temperature. Some problems were encountered during the refinement of the structural model. The impurity phase, which was thought to be the orthorhombic phase, could not be fitted to the data. Attempts to fit the second phase were made using both a full structural Rietveld fit and a Le Bail fitting in the GSAS software package. The impurity peaks did not fit any binary oxide of chromium or tin either. Fitting of the impurity against a previously unreported ternary chromium tin selenide (reported in section 5.4.2) was attempted. However, the data available for this potential new phase were not sufficient to fit the data with a Le Bail refinement of the lattice parameters. The impurity peaks were too close to or overlapping the peaks associated with $Cr_2Sn_3Se_7$ so they could not be excluded without losing structural information on $Cr_2Sn_3Se_7$. The refinement was therefore performed without inclusion of an impurity phase. This resulted in larger than desired Goodness of Fit parameters (Table 5.4).

Table 5.4: Goodness of Fit parameters for the fit of the Rietveld refined model against room temperature neutron diffraction data for polycrystalline $Cr_2Sn_3Se_7$

χ^2	R_{wp} 168° (%)	R_{wp} 168° - B (%)	R_{wp} 90° (%)	R_{wp} 90° - B (%)
46.5	9	13	11	13

Lattice parameters of $Cr_2Sn_3Se_7$ were determined during the Rietveld refinement and in general, they are in good agreement with the literature values. All values of the unit cell parameters are slightly shorter than that of the literature and β is slightly larger. Atomic coordinates and site occupancy factors obtained from the refinement are shown in Table 5.5.

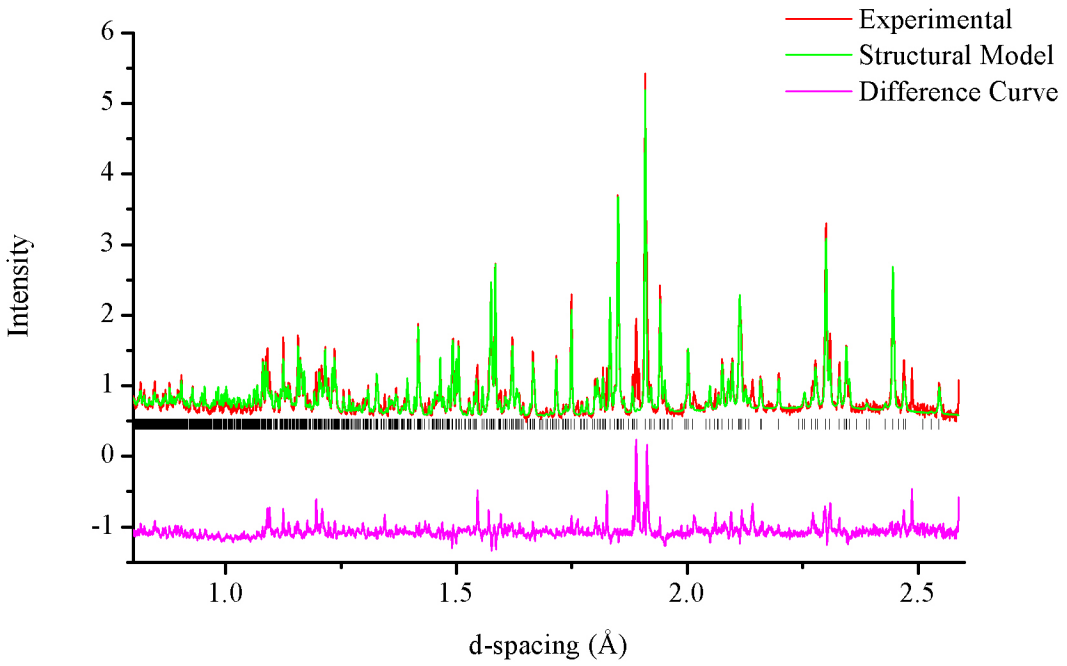

Figure 5.10: The final observed, calculated and difference profiles from Rietveld refinements of $Cr_2Sn_3Se_7$ against powder neutron diffraction data collected from the 168° bank on the HRPD diffractometer.

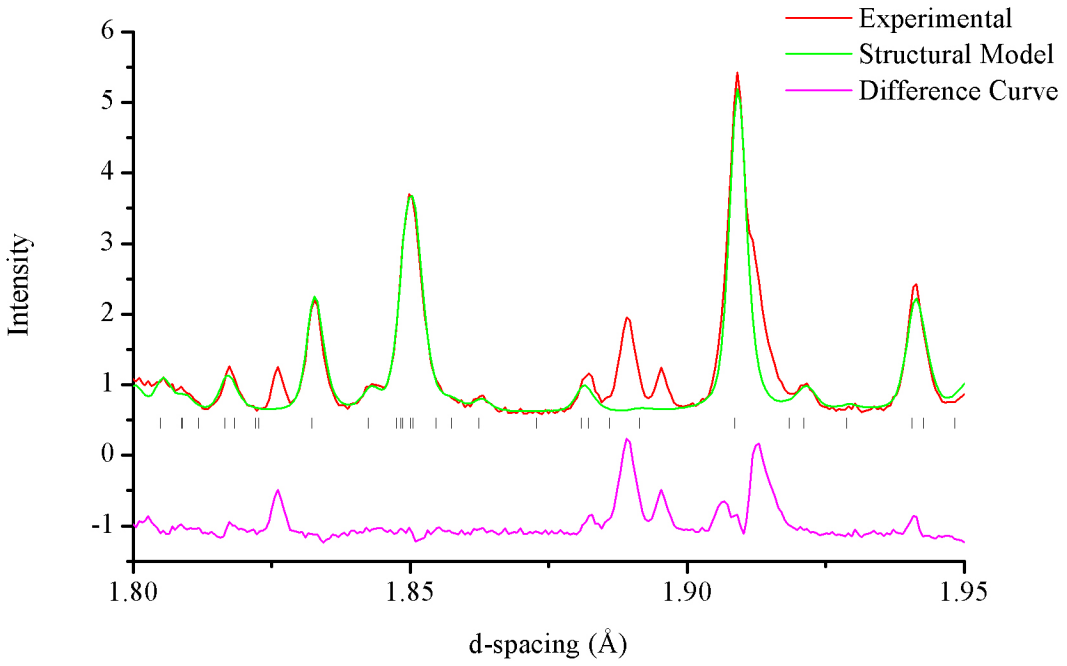

Figure 5.11: The final observed, calculated and difference profiles from Rietveld refinements of $Cr_2Sn_3Se_7$ against powder neutron diffraction data from the 168° bank on the HRPD diffractometer, showing impurity peaks between 1.8 Å and 1.95 Å

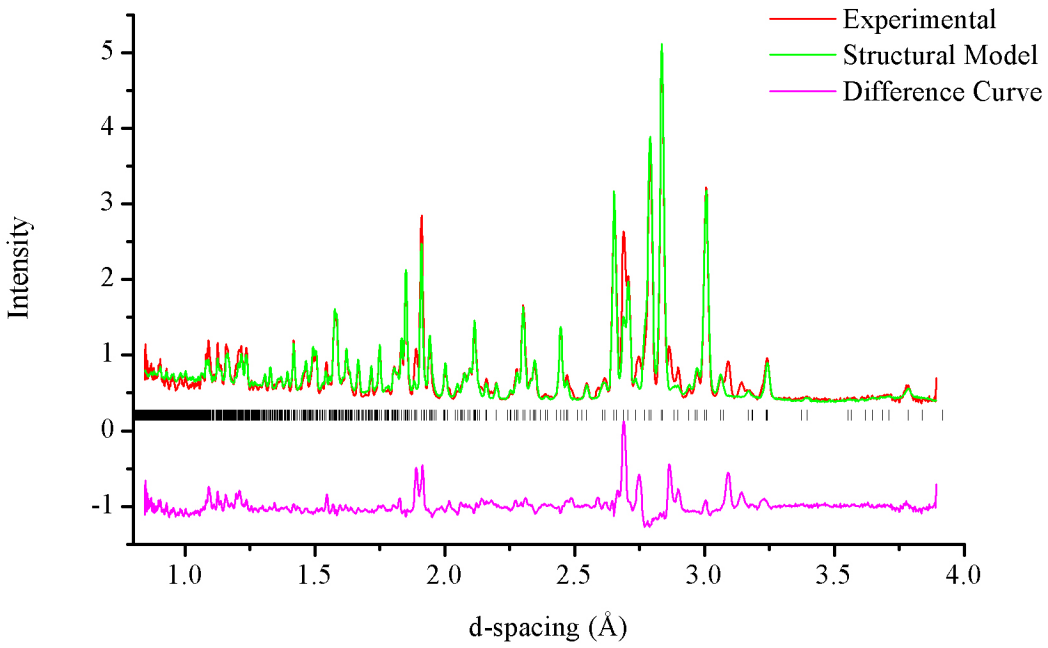

Figure 5.12: The final observed, calculated and difference profiles from Rietveld refinements of $Cr_2Sn_3Se_7$ against powder neutron diffraction data collected from the 90° bank on the HRPD diffractometer.

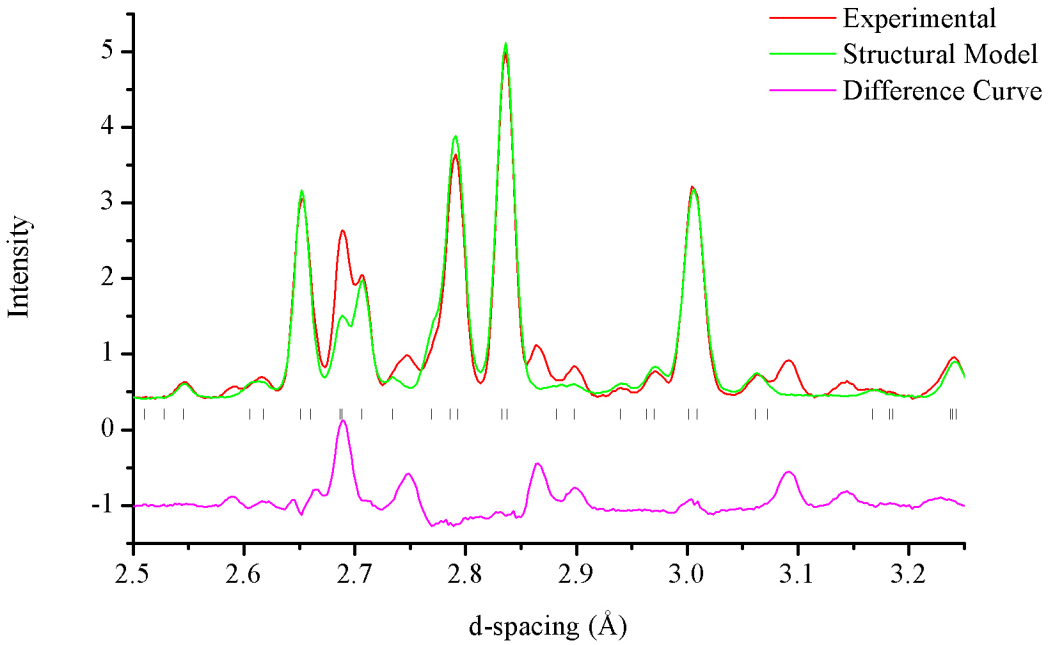

Figure 5.13: The final observed, calculated and difference profiles from Rietveld refinements of $Cr_2Sn_3Se_7$ against powder neutron diffraction data collected from the 90° bank on the HRPD diffractometer, showing impurity peaks between 2.5 Å and 3.25 Å.

Table 5.5: Atomic coordinates and thermal parameters of $Cr_2Sn_3Se_7$ obtained from Rietveld refinements of the literature structural model[64] against powder neutron diffraction data collected on the HRPD diffractometer. Space group: *$P2_1/m$*, *a = 11.7658(4) Å*, *b = 3.81708(9) Å*, *c = 12.7422(4) Å* and *β = 105.308(3)* °.

atom	*x*	*y*	*z*	*Uiso (Å^2)*	*SOF Cr*	*SOF Sn*
M(1)	0.102(1)	0.25	0.609(1)	0.042(2)	0.64(-)	0.36(-)
M(2)	0.483(1)	0.25	0.875(1)	0.042(2)	0.69(-)	0.31(-)
M(3)	0.526(1)	0.25	0.380(1)	0.042(2)	0.57(-)	0.43(-)
Sn(4)	0.1633(9)	0.25	0.2765(8)	0.042(2)	0(-)	1(-)
Sn(5)	0.1539(8)	0.25	0.9656(9)	0.042(2)	0(-)	1(-)
Se(1)	0.9038(6)	0.25	0.8894(7)	0.039(1)		
Se(2)	0.3895(7)	0.25	0.1840(7)	0.039(1)		
Se(3)	0.6129(8)	0.25	0.5849(7)	0.039(1)		
Se(4)	0.3506(6)	0.25	0.6744(7)	0.039(1)		
Se(5)	0.6229(7)	0.25	0.0608(7)	0.039(1)		
Se(6)	0.9082(6)	0.25	0.2530(6)	0.039(1)		
Se(7)	0.8919(6)	0.25	0.5299(6)	0.039(1)		

M = Cr, Sn.

Bond lengths and bond angles from the refined structure of $Cr_2Sn_3Se_7$ are presented in Appendix M. When compared to $In_2Sn_3S_7$ the octahedra in $Cr_2Sn_3Se_7$ are more distorted. The bond lengths become less uniform and the angles diverge further from 90°. Distortions of the *M*(3) octahedra cause layer separation to be smaller in $Cr_2Sn_3Se_7$ than in $In_2Sn_3S_7$. However, the layer containing the *M*(3) octahedra and the square based pyramids increases in thickness.

5.3 Electrical and Thermal Transport Properties

Pellets of both $In_2Sn_3S_7$ and $Cr_2Sn_3Se_7$ were prepared as described in section 2.5. Samples slightly decomposed to yield a small quantity of binary impurities during both hot and cold pressing, however cold-pressing followed by sintering resulted in pellets of lower density. For the $Cr_2Sn_3Se_7$ sample, peaks attributed to the unknown impurity were also observed to decrease, suggesting decomposition of the unknown impurity may be the possible source for the binary impurities. After considering both techniques, hot-pressing was chosen to fabricate pellets for physical property measurements. Powder X-ray diffraction data for $In_2Sn_3S_7$ and $Cr_2Sn_3Se_7$ after hot-pressing are presented in Figure 5.14 and Figure 5.15 respectively.

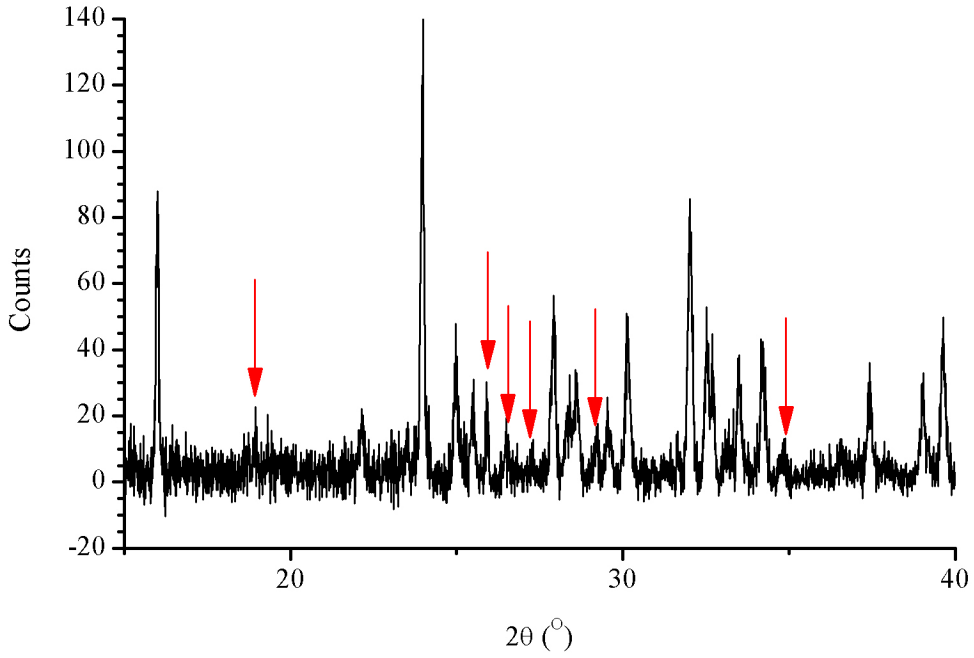

Figure 5.14: X-ray diffraction of hot-pressed pellet of $In_2Sn_3S_7$. Arrows mark the impurity peaks.

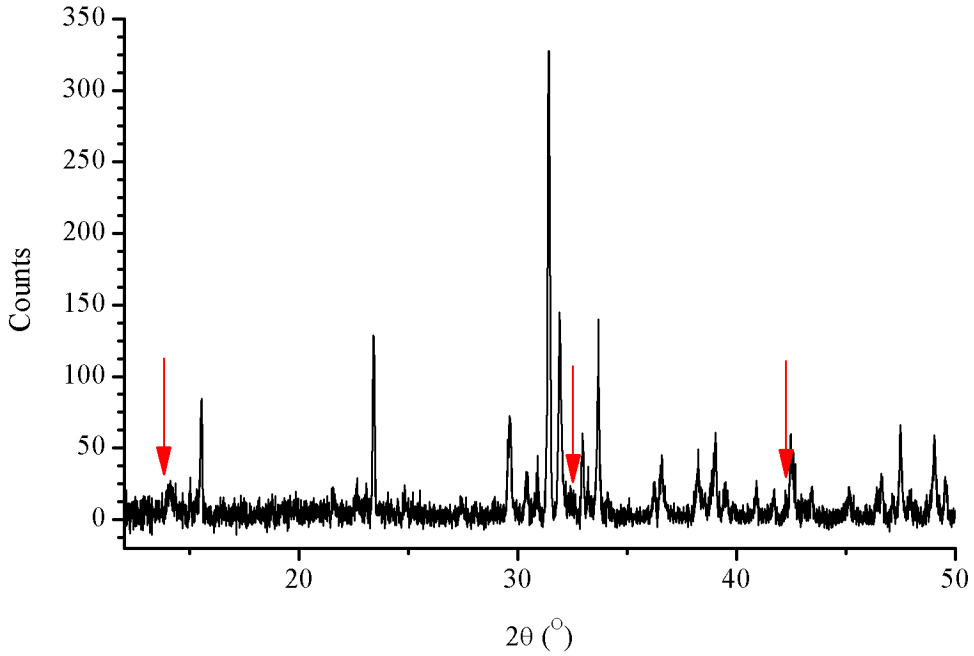

Figure 5.15: X-ray diffraction pattern of hot-pressed pellet of $Cr_2Sn_3Se_7$. Arrows mark the impurity peaks in the diffraction pattern.

5.3.1 Electronic Properties

The electrical resistivity (ρ) of hot-pressed ingots of $In_2Sn_3S_7$ and $Cr_2Sn_3Se_7$ were measured in the range $100 \leq T\ (K) \leq 350$ using a four-probe DC technique as described in section 2.7.1.2. Seebeck measurements were performed over the same temperature range, as described in section 2.8.1. High temperature Seebeck coefficient and electrical resistivity measurements on $Cr_2Sn_3Se_7$ were performed in the range $303 \leq T\ (K) \leq 673$, as described in sections 2.7.2 and 2.8.2. The electrical resistivity of $In_2Sn_3S_7$ could only be measured down to 180 K due to the resistance of the pellet being too high and the multimeter overloading below this temperature. Measurements could also only be made up to 350 K as the resistivity was too high to be measured on the available high temperature instrument.

Measurements of the electrical resistivity and the Seebeck coefficient of $In_2Sn_3S_7$ (Figure 5.16) indicate that the material is a p-type semiconductor above 197 K up to the top of the measured range of 350 K. The electrical resistivity is large with a value approximately 36 kΩcm at 300 K. The electrical resistivity follows an Arrhenius type dependency between 266 and 350 K (Figure 5.17) and a band gap of 734(2) meV was calculated. Below this temperature the resistivity follows a second Arrhenius

temperature dependence between 197 K and 231 K and a band gap of 429(2) meV was determined. The possibility of a variable range hopping conduction mechanism was also investigated. However, the electrical resistivity did not follow a variable range hopping dependence either. The Seebeck coefficient at 100K is small and negative and it remains that way up to 197 K where it becomes positive. This suggests that the electrical resistivity is too high below 197 K for the instrument to measure. This suggests that at temperatures below 197 K, charge carriers are localised within the structure and that conduction is thermally activated. As the temperature is raised, the Seebeck coefficient increases rapidly to a maximum of 510 μV K^{-1} at 335 K.

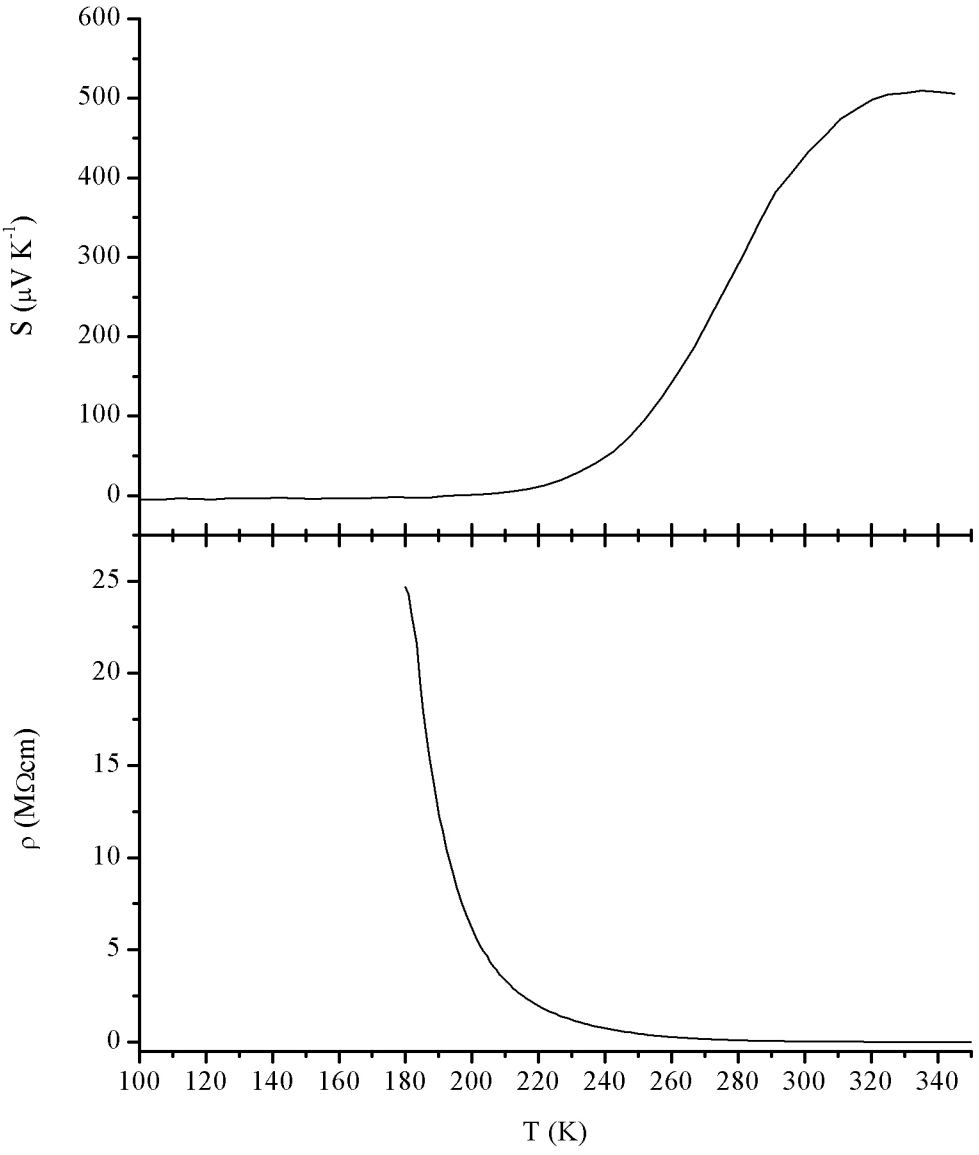

Figure 5.16: Measured Seebeck coefficient (top) and electrical resistivity (bottom) of $In_2Sn_3S_7$ in the temperature range $100 \leq T\ (K) \leq 350$.

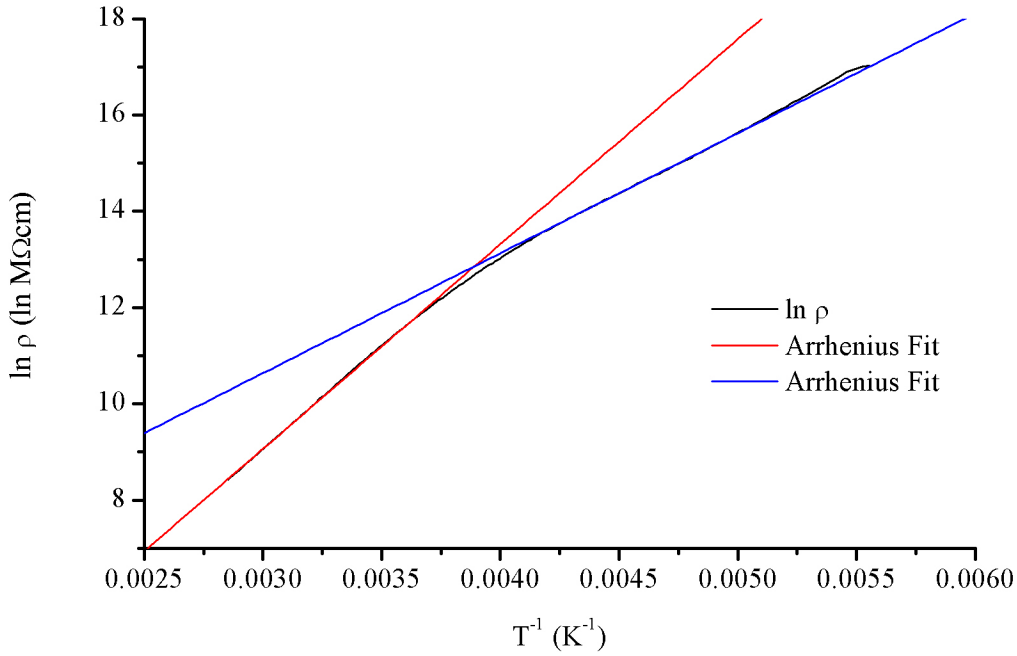

Figure 5.17: Arrhenius temperature dependence of the electrical resistivity measured for $In_2Sn_3S_7$

Compared to $In_2Sn_3S_7$, the electrical resistivity of $Cr_2Sn_3Se_7$ (Figure 5.18) is several orders of magnitude lower with a value of 0.33 Ωcm at 300 K. The electrical resistivity shows Arrhenius temperature dependence between 253 K and 350 K (Figure 5.19) with a calculated band gap of 108(2) meV. Above and below this temperature range another thermally activated conduction mechanism is observed. The Seebeck coefficient initially is negative at 100 K with a value of -18 μV K^{-1}. This decreases to a maximum negative value of -32 μV K^{-1} at 213 K, before the Seebeck coefficient heads to zero. At 415 K it becomes positive and increases to a maximum of 86 μV K^{-1} at 679 K. The Seebeck coefficient suggests that there is mixed conduction of holes and electrons in $Cr_2Sn_3Se_7$. Initially, electrons are promoted across the band gap. The Seebeck coefficient is negative, indicating that electrons are the dominant charge carriers. The depopulation of the valence band increases with temperature and the conduction of holes makes the Seebeck coefficient less negative. Holes eventually become the dominant charge carrier at 415 K and a positive Seebeck coefficient is observed.

There are several possible reasons why there are differences in the electrical transport property measurements between the two structural analogues. There will be a change in band structure caused by the substitution of sulphur for selenium, and indium for

chromium. It is likely that indium bands are low lying in the density of states. Replacing these with chromium bands, which are likely to be nearer the Fermi level, is the probable cause of the differences between the two materials. The position of the Fermi level within the density of states will also be affected by the substitutions. $In_2Sn_3S_7$ has 48 valence bands from the In-5s, In-5p, Sn-5s, Sn-5d, S-3s and S-3p atomic orbitals. These are filled to band 30 with 60 valence electrons. Electrical resistivity measurements suggest a band gap of 734(2) meV exists between bands 30 and 31. $Cr_2Sn_3Se_7$ has 50 valence bands from the Cr-3d, Sn-5s, Sn-5d, Se-4s and Se-4p atomic orbitals. These are filled with 66 valence electrons up to band 33 and a band gap of 108(2) meV exists between it and band 34.

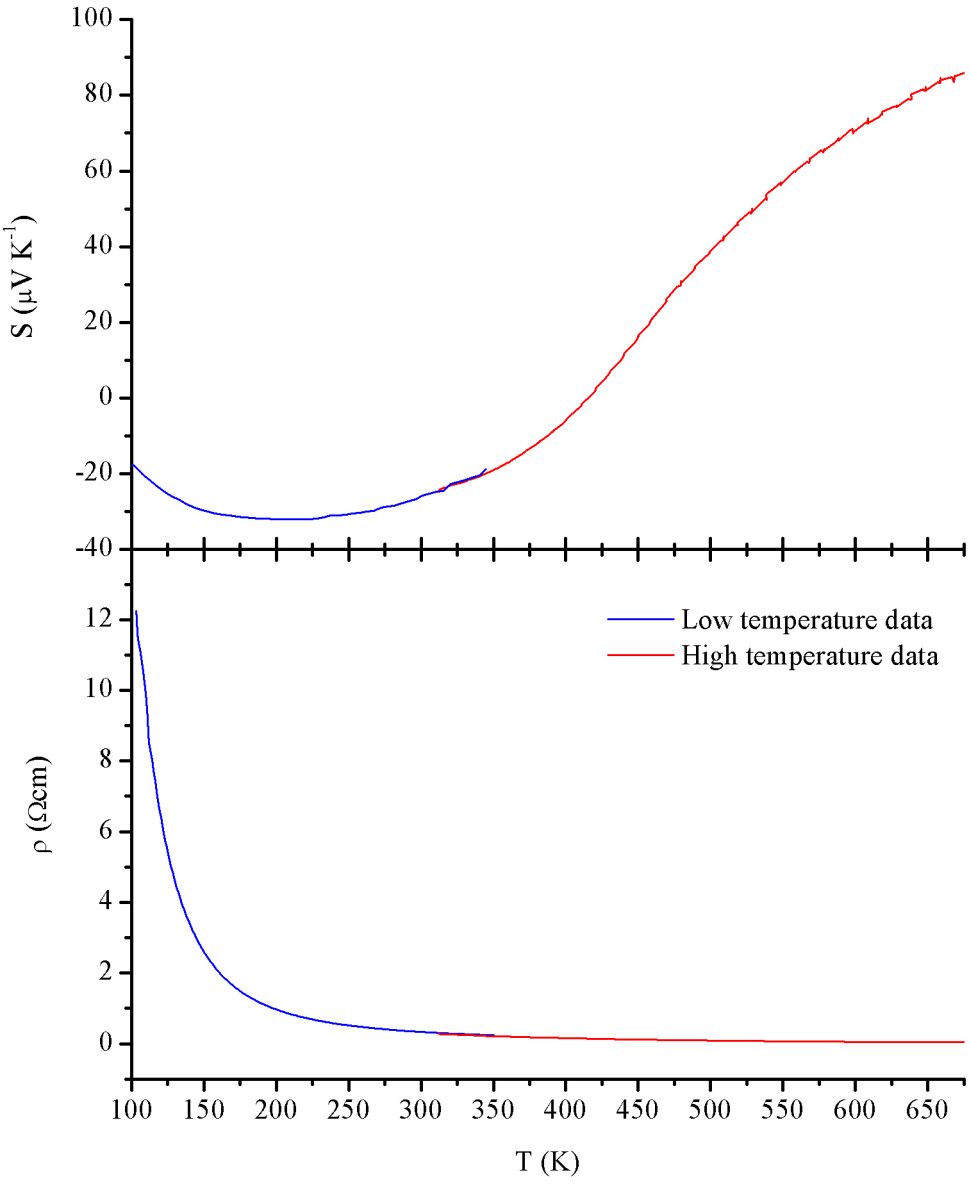

Figure 5.18: Measured Seebeck coefficient and electrical resistivity of $Cr_2Sn_3Se_7$ in the temperature range $100 \leq T\ (K) \leq 673$.

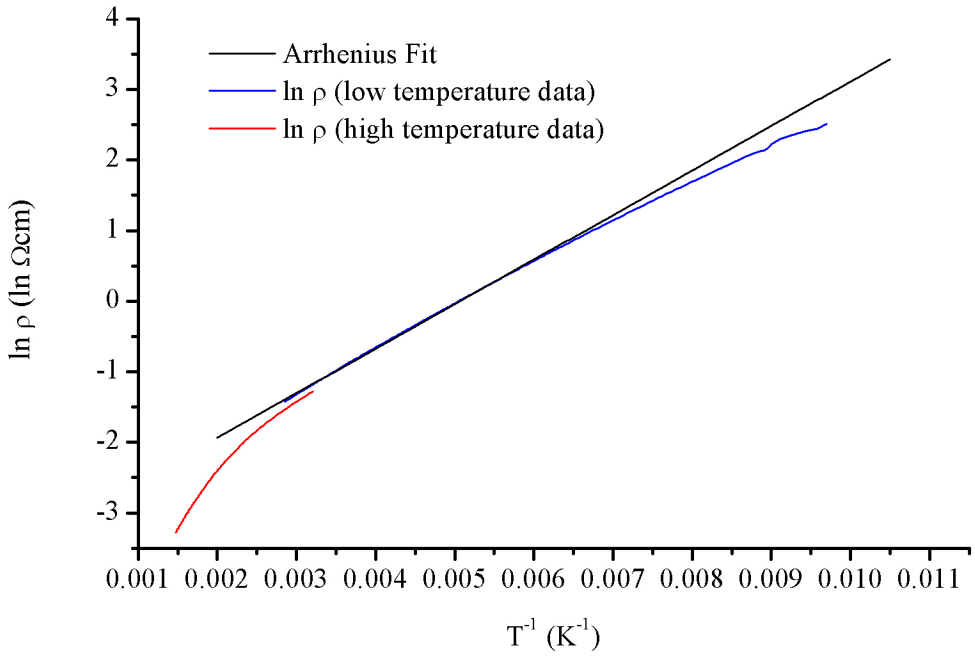

Figure 5.19: Arrhenius temperature dependence of electrical resistivity measured for $Cr_2Sn_3Se_7$

5.3.2 Thermal Conductivity

The thermal conductivity of $In_2Sn_3S_7$ and $Cr_2Sn_3Se_7$ was measured as described in section 2.9. The electronic contribution to the thermal conductivity was calculated for $Cr_2Sn_3Se_7$ from high temperature measurements of the electrical resistivity using the Wiedemann-Franz law. This allowed the lattice thermal conductivity to be calculated. The same could not be achieved for $In_2Sn_3S_7$ because the resistivity was too large to measure on the available instrument. However, the electronic thermal conductivity of $In_2Sn_3S_7$ would be much smaller than that determined for $Cr_2Sn_3Se_7$ and therefore it is likely that it makes a negligible contribution towards the total thermal conductivity. The thermal conductivity of $In_2Sn_3S_7$ and $Cr_2Sn_3Se_7$ show a slight upward trend as temperature increases and both have similar values in the region of 0.4 to 0.6 W m^{-1} K^{-1}. These values are very small.

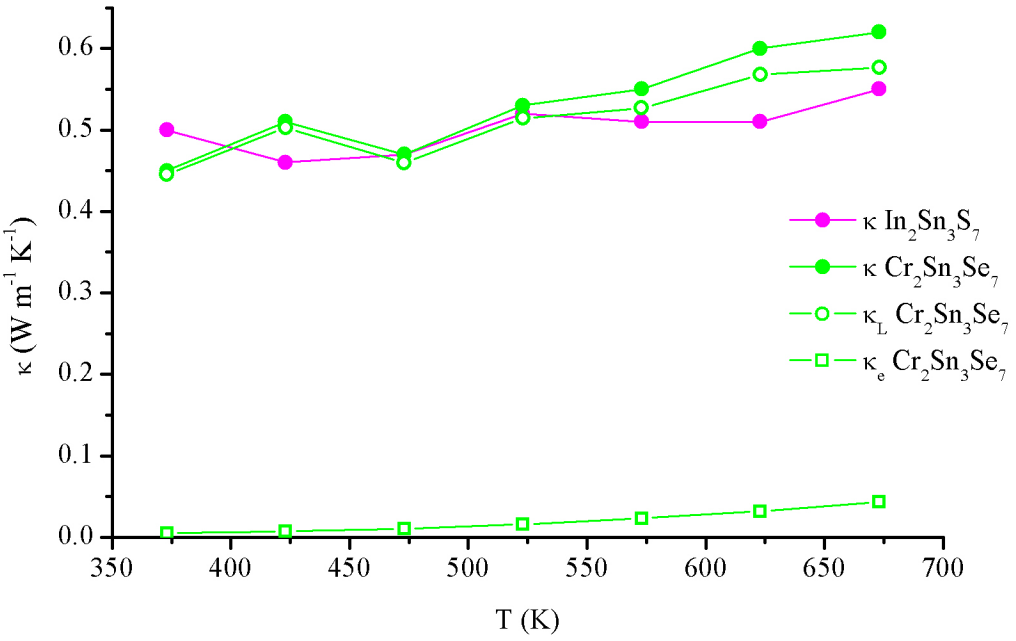

Figure 5.20: Thermal conductivity (κ) of $In_2Sn_3S_7$ and the thermal conductivity, lattice thermal conductivity (κ_L) and electronic thermal conductivity (κ_e) of $Cr_2Sn_3Se_7$.

5.4 Expansion of the Series and Related Phases

5.4.1 $Cr_2Sn_3S_7$ and $In_2Sn_3Se_7$

The analogous structures of $In_2Sn_3S_7$ and $Cr_2Sn_3Se_7$ led to investigations with the aim of expanding the series through chemical substitution. This was attempted by synthesising the previously unreported $In_2Sn_3Se_7$ and $Cr_2Sn_3S_7$. The synthesis methods used for both the known analogues were attempted along with several others. The synthesis described in section 2.1.6 yielded a powdered sample of $Cr_2Sn_3S_7$, which contained a small quantity of SnS_2 and elemental chromium impurities. The powder X-ray diffraction pattern collected for the sample was analysed using the Topas3[68] software package to determine the allowed peaks and the lattice parameters (Figure 5.21). The same space group ($P2_1/m$) as the two known structural analogues was used and lattice parameters (*a = 11.2945(6), b = 3.6456(2), c = 12.2473(7), β = 105.352(2)*) were determined. When compared with the known analogues, the unit cell lengths are smaller for $Cr_2Sn_3S_7$. The β angle is smaller than the indium analogue, but slightly larger than the selenide analogue. Despite various attempts, the $In_2Sn_3Se_7$ analogue was not prepared during this research.

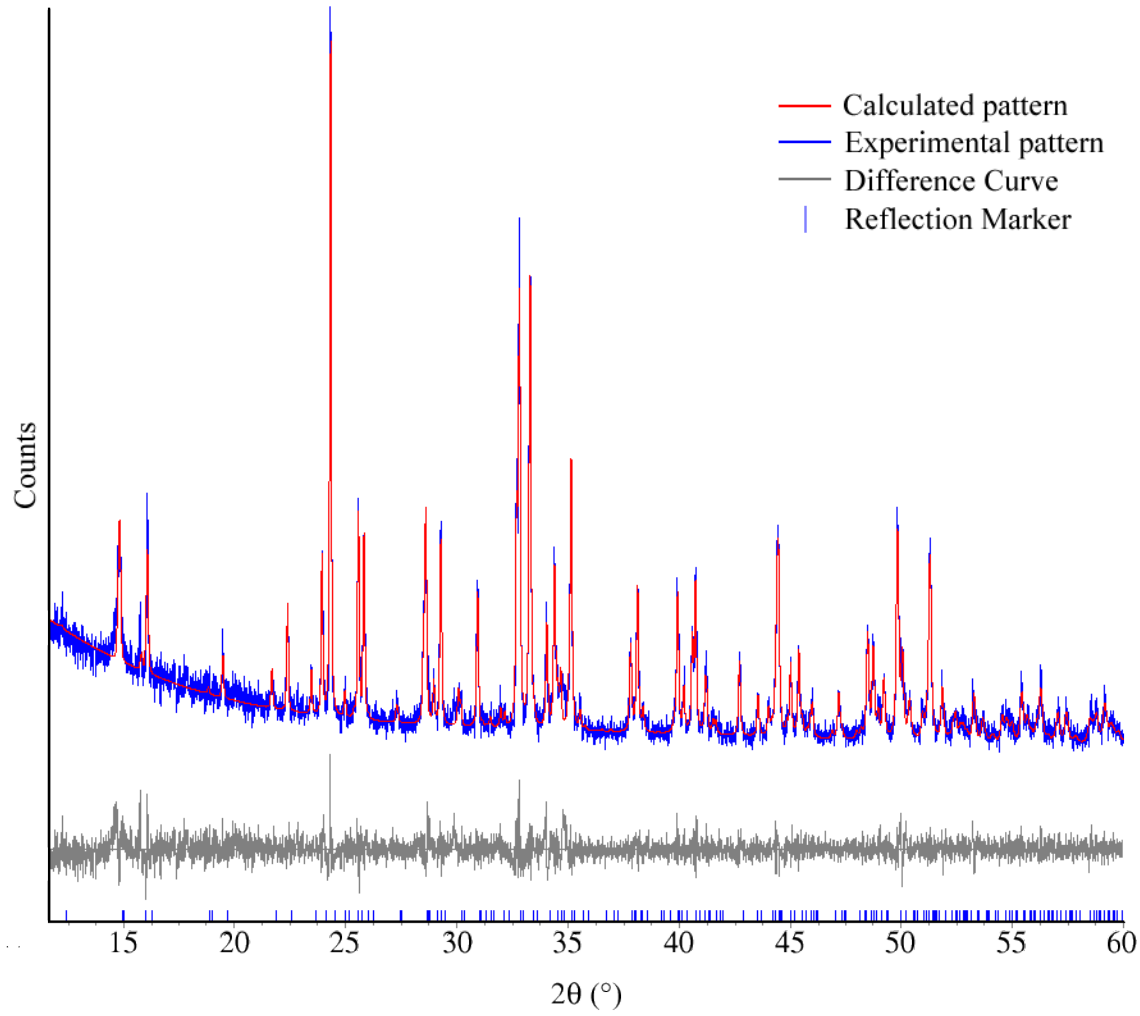

Figure 5.21: Refinement of lattice parameters and allowed peaks for $Cr_2Sn_3S_7$.

5.4.2 $Cr_2Sn_5Se_{11}$

While attempting to synthesise single phase $Cr_2Sn_3Se_7$, it was noted that the reaction mixture in the literature stated a 2:4:9 ratio of Cr:Sn:Se was used. The effect of additional tin and selenium in the reaction mixture was investigated. A reaction mixture of stoichiometry $Cr_2Sn_5Se_{11}$ produced an unidentified phase along with some binary products. The phase was also observed in the reaction with the stoichiometry $Cr_2Sn_5Se_{10}$, however this latter sample contained a high percentage of $Cr_2Sn_3Se_7$. This suggests that the actual stoichiometry of the new ternary chromium tin selenide is closer to the $Cr_2Sn_5Se_{11}$ reaction stoichiometry than $Cr_2Sn_5Se_{10}$.

Attempts to grow single crystals of the new phase proved unsuccessful. The sample was sealed in an evacuated silica tube. The tube was placed in a three-zone furnace. A 50 °C temperature gradient was created inside the furnace. The temperature on the hot side

was increased to 800 °C and 750 °C at the cool side. The sample was positioned in the hot side with the empty section of the reaction vessel in the cool side. At best, weak streaky marks that could not be indexed were observed in the diffraction pattern when potential crystals were investigated using single crystal X-ray diffraction. The powder pattern was indexed using the Topas3[68] software package. After eliminating peaks due to minor impurities of $Cr_2Sn_3Se_7$ and SnSe, indexing suggested a space group of $P3_1$ and lattice parameters of $a = 3.7884(2)$ and $c = 38.086(2)$. The Le Bail fitted X-ray diffraction pattern of the new chromium tin selenide material is shown in Figure 5.22. Further work on the synthesis and characterisation of this material is required to confirm the stoichiometry and determine the structure of this new phase.

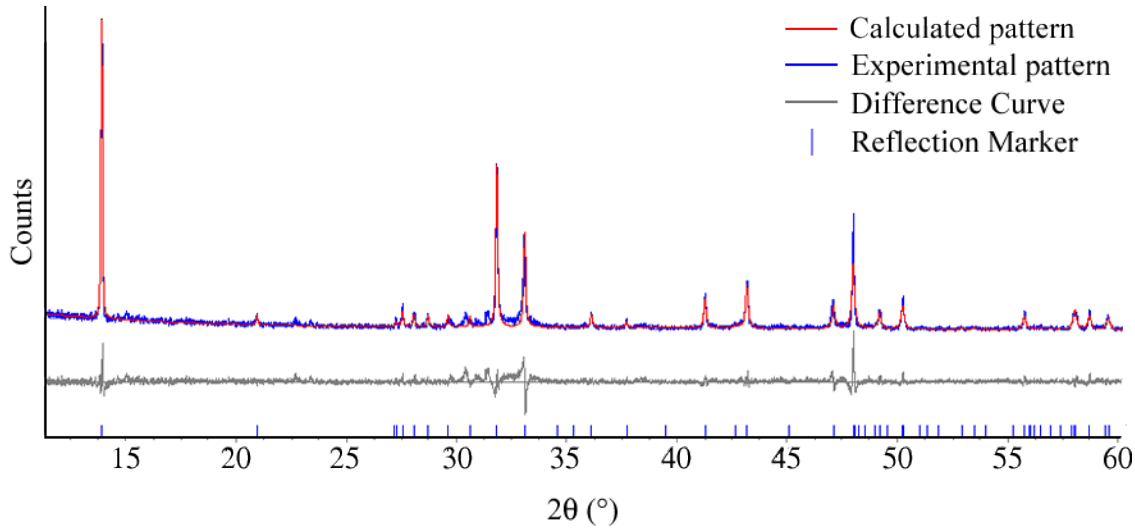

Figure 5.22: Le Bail fitted powder X-ray diffraction data of the unknown phase from the $Cr_2Sn_5Se_{11}$ reaction.

5.5 Conclusions

The synthesis of a bulk polycrystalline powdered sample of $In_2Sn_3S_7$ was successful with only a very minor impurity observed in the X-ray diffraction pattern. Neutron diffraction experiments at the synthesis temperature indicated $In_2Sn_3S_7$ is molten while the suspected In_2S_3 impurity is still a solid. High temperature DSC measurements could be performed to determine the melting point of $In_2Sn_3S_7$ more accurately. This could help tune the synthesis temperature to just below or above the melting point. This will allow the effects of the sample melting during synthesis to be studied. The issues encountered with the Goodness of Fit parameters during the Rietveld refinements of the structural model against the powder neutron diffraction data can be explained by the

poor signal to background ratio. These non-ideal statistics do not affect the validity of the refinement, as visually the structural model fits the experimental data well. Indium is an absorber of neutrons, which leads to the low peak intensities observed and part of the high background. Other contributors to the high background could be removed by repeating the experiment with the sample contained in a vanadium can outside of the furnace and no Suprasil tube. However, this would not improve high temperature measurements, where the Suprasil tube and furnace were essential for the heating and containment of the sample. Measuring the sample for longer periods of time would improve the signal to noise ratio, but since the room temperature data were already collected over a 16 hour time span, it would be impractical to produce better quality data due to the substantially increased collection times needed to achieve this. The neutron diffraction experiments themselves, allowed the cation ordering of the octahedral sites to be investigated. Refinements suggest that around two thirds of the sites are occupied by indium and one third by tin.

The refinement of $Cr_2Sn_3S_7$ also produced results where the Goodness of Fit statistics were not ideal. On this occasion, the unknown impurity phase was the cause of this. The overlapping impurity peaks with those of the main phase made refinements of the site occupancy factors unreliable and the literature values were used and not refined.

Previously unreported physical property measurements indicate that $In_2Sn_3S_7$ is a p-type semiconductor. The electrical resistivity is in the MΩcm range at low temperatures. Seebeck coefficient measurements practically zero below 197 K, which suggests that the resistivity becomes high enough that charge carriers are localised. Thermal conductivity measurements yield results around 0.5 W m^{-1} K^{-1} with the main contribution to this from the lattice thermal conductivity. This is a low value and can be attributed to the negligible electronic contribution to the thermal conductivity and the phonon scattering caused by the low-dimensional structural motifs in the structure.

Electrical resistivity measurements of the hot-pressed $Cr_2Sn_3Se_7$ ingot resulted in semiconducting behaviour being observed and values in the Ωcm range. This is in contrast to measurements performed on a single crystal, which reportedly measured above 100 kΩ.[64] Measurements of the electrical resistivity for a single crystal would be anisotropic and the difference in the values suggests that the resistivity was measured along the axis of layer stacking. Seebeck measurements indicated that both holes and

electrons are responsible for conduction, with electrons the dominant charge carrier between 100 and 415 K and holes between 415 and 623 K. The thermal conductivity is similar to the indium tin sulphide analogue. Again the electrical contribution is small and the major contribution to phonon scattering is from the low-dimensional structure.

Further work on the previously unreported phase, $Cr_2Sn_3S_7$ would give insight into the materials structural and physical properties, and how they compare to the measurements performed on the previously reported phases. The lattice parameters of $Cr_2Sn_3S_7$, $In_2Sn_3S_7$ and $Cr_2Sn_3Se_7$ where layers stack along the *a* axis are shown in Table 5.6.

Table 5.6: Refined lattice parameters of three isostructural analogues with the space group $P2_1/m$ and general formula $M_2Sn_3X_7$ (M = In, Cr, Sn; X = S, Se).

Sample	*a (Å)*	*b (Å)*	*c (Å)*	*β (°)*
$In_2Sn_3S_7$	11.6690(3)	3.78854(6)	12.6424(2)	105.814(2)
$Cr_2Sn_3S_7$	11.2945(6)	3.6456(2)	12.2473(7)	105.352(2)
$Cr_2Sn_3Se_7$	11.7656(4)	3.8171(1)	12.7424(4)	105.309(3)

M = Cr, In; X = S, Se.

Substitution of indium in $In_2Sn_3S_7$ for chromium caused a contraction in all directions and the angle β in the unit cell. This is due to the smaller effective ionic radii of Cr^{3+} (0.615 Å[77]) when compared to In^{3+} (0.62 Å[77]). Replacing sulphur for selenium in $Cr_2Sn_3X_7$ (X = S, Se) causes an expansion along the *a*, *b* and *c* axis and a contraction in the β angle. The expansion of the unit cell can again be explained by the increase in ionic radii from sulphur (1.84 Å[77]) to selenium (1.98 Å[77]).

The monoclinic and orthorhombic phases of $Cr_2Sn_3Se_7$ are the only two reported ternary chromium tin selenides in the literature. The unknown phase synthesised with proposed stoichiometry $Cr_2Sn_5Se_{11}$ will increase the known literature of these ternary compounds by 50%. Although further work is required before the structure can be confirmed, it shows that there is more diversity in these ternary compounds than previously thought. This could potentially open up a whole range of materials with new low-dimensional structures to investigate.

Conclusions

In this thesis, work based around three families of low-dimensional chalcogenides has been undertaken. The synthesis and physical property measurements of polycrystalline samples has allowed the structure-physical property relationships of these low-dimensional materials to be investigated. The effect of chemical substitution has also been studied.

The focus on low-dimensional chalcogenides was to investigate and exploit quantum confinement effects on various physical properties. Each series of materials investigated has low-dimensional characteristics in the structure. The Jamesonite family of materials, $Fe_{1-x}Mn_xPb_4Sb_6S_{14}$ ($0 \leq x \leq 1$), has a highly anisotropic structure consisting of MS_6 (M = Fe, Mn) one-dimensional chains and $Pb_4Sb_6S_{14}$ rods. Cobalt Shandite phases consist of low-dimensional kagome sheets and $In_2Sn_3S_7$ related solids consist of a bridged-layered structure, containing two different layer types.

The magnetism of the cobalt Shandites and the Jamesonite-Benavidesite series has been investigated. In both cases, the magnetic atoms are located within low-dimensional structural motifs. The cobalt atoms are located in the kagome sheets of the Shandite structure. While the iron and manganese atoms are situated in the one-dimensional octahedral chains in the Jamesonite structure. Magnetic property measurements for both $Fe_{1-x}Mn_xPb_4Sb_6S_{14}$ ($0 \leq x \leq 0.75$) and $Co_3Sn_{2-x}In_xS_2$ ($0.6 \leq x \leq 2$) demonstrate localised magnetic order occurs within the low-dimensional motifs without full magnetic order being observed. The separation between the low-dimensional motifs means that intra-chain and intra-layer ordering dominates the magnetic properties. Samples of $MnPb_4Sb_6S_{14}$ show long-range magnetic order. Magnetic reflections in the powder neutron diffraction pattern associated with antiferromagnetic behaviour were observed for $MnPb_4Sb_6S_{14}$. The refined magnetic structural model showed that the moments have a collinear antiferromagnetic alignment along the b axis. However the non-zero saturation magnetisation indicated that the moments are probably slightly canted. Samples of $Co_3Sn_{2-x}In_xS_2$ ($0 \leq x \leq 0.4$) show ferromagnetic behaviour on cooling below the ordering temperature. The low saturation magnetisation of less than 1 μ_B suggests these materials are type 1_A half metallic ferromagnets. No other Shandite phases of any known composition show long-range magnetic ordering.

Recent developments in thermoelectric materials have led to materials with large complex unit cells and low symmetry.[14] Materials such as clathrates and skutterudites have shown that complex unit cells can reduce the thermal conductivity of materials.[95] In the cases of $Cr_2Sn_3Se_7$, $In_2Sn_3S_7$ and $Fe_{1-x}Mn_xPb_4Sb_6S_{14}$ ($0 \leq x \leq 1$), the complex low-dimensional structure resulted in thermal conductivities of between 0.4 – 0.6 W m^{-1} K^{-1}). These are significantly lower than those found in filled skutterudites[96] (3 to 5.5 W m^{-1} K^{-1}) and clathrates[96-97] (1 to 2 W m^{-1} K^{-1}). However, the electronic contribution for $Cr_2Sn_3Se_7$, $In_2Sn_3S_7$ and $Fe_{1-x}Mn_xPb_4Sb_6S_{14}$ ($0 \leq x \leq 1$) is vanishingly low due to the high electrical resistivity. This highlights the difficulties faced when attempting to optimise contrasting properties. The cobalt Shandite series has a thermal conductivity between 2.5 and 5.5 W m^{-1} K^{-1}. The broad minima around 2.5 W m^{-1} K^{-1} in the thermal conductivity near the stoichiometric Co_3SnInS_2 phases is not as low as those measured for materials discussed in Chapters 3 and 5. However, the electrical resistivities measured were in the mΩ cm range, which indicates their potential as thermoelectric candidate materials. The electrical resistivity of thermoelectric candidates β-Zn_3Sb_4[20] (2 mΩ cm to 3.5 mΩ cm) and $Yb_{14}MnSb_{11}$[27] (2 mΩ cm to 5.5 mΩ cm) are both in the mΩ cm range. The electrical resistivity of phases in the Jamesonite-Benavidesite series, In_2Sn3S_7 and $Cr_2Sn_3Se_7$ are all too large for thermoelectric applications. The Seebeck coefficients measured in this work range from -155 μV K^{-1} to 539 μV K^{-1} for $Co_3Sn_{1.05}In_{0.95}S_2$ and $MnPb_4Sb_6S_{14}$ respectively. Information obtained from the Seebeck coefficient includes the dominant charge carrier and the sharpness of band at the Fermi level in the density of state. The sharp cobalt d-bands in the density of states of the cobalt Shandites is the reason for the large Seebeck coefficient in a material with metal-like conduction. The sharp bands are a result of the low-dimensional kagome sheet in which the cobalt atoms are located.

The effects of chemical substitution have been investigated in this work. The double metal-to-semiconductor-to-metal transition in $Co_3Sn_{2-x}In_xS_2$ is a unique result. By tuning the number of valence electrons in the system and therefore the electron population of the conduction band, a marked difference in physical properties was observed. This shows the importance of band structure and filling of the bands in relation to the physical properties of the material. There are several reported metal-to-semiconductor transitions that occur through chemical substitution. The layered oxychalcogenides $La_{1-n}Sr_nOCuSe$ show a semiconducting-to-metal transition. Samples with a small strontium content ($n \leq 0.05$) exhibit semiconducting behaviour, while

samples with n > 0.05 show a metallic temperature dependence.[98] Materials in the family $CoTi_{1-z}M_zSb$ (*M* = Sc, V, Cr, Mn, Fe) show a compositional dependence to the conduction behaviour. CoTiSb exhibits a semiconducting temperature dependence, however a 5 mol % substitution of titanium by iron ($CoTi_{0.95}Fe_{0.05}Sb$) leads to a metallic temperature dependence of the electrical resistivity.[99] Some samples in the series $Co_3Sn_{2-x}In_xS_2$ ($0.7 \leq x \leq 1.6$) show a metal-to-semiconductor transition on heating. The same trend is observed in $CoTi_{0.95}Cr_{0.05}Sb$ which is semiconducting at room temperature. However, a semiconductor-to-metal transition is observed on cooling below 210 K.[99] The substitution of titanium by chromium and iron increases the number of d electrons available for conduction. A 5% substitution by vanadium and the phase $CoTi_{0.95}V_{0.05}Sb$, exhibits a semiconducting temperature dependence. Substitution of titanium by the more electron rich chromium results in a phase where a transition in conduction behaviour was observed. While the phase with titanium being substituted by the even more electron rich iron shows a metal-like temperature dependence. Systems with a double metal-to-semiconductor-to-metal transition through compositional variance appear to be limited to the $Co_3Sn_{2-x}In_xS_2$ ($0 \leq x \leq 2$) described in this work. Across the cobalt Shandite series, there is a two valence electron difference between the fully substituted tin and indium end-members. In other systems that exhibit metal-to-semiconductor transitions through substitution, the difference in valence electron count between the end-member phases is one. It is possible that the extended range of valence electron count found in $Co_3Sn_{2-x}In_xS_2$ ($0 \leq x \leq 2$) is the reason for the unique electrical properties.

There are several possible areas of further work in relation to materials discussed in this thesis. Physical property measurements should be performed on the previously unreported $Cr_2Sn_3S_7$ phase. It is likely the thermal conductivity will be similar to the $In_2Sn_3S_7$ and $Cr_2Sn_3Se_7$ analogues measured in this work. However, predicting the electrical transport properties is not quite so simple. Phases where partial substitution of indium by chromium, and sulphur by selenium should be prepared to investigate the effects of chemical substitution. Additional work on the synthesis and structural determination of the new phase with the stoichiometry close to $Cr_2Sn_5Se_{11}$ would lead to the discovery of a whole new set of low-dimensional materials. The Co_2TlS_2 phase was prepared after unsuccessful attempts to synthesise $Co_3Tl_2S_2$. Chemical substitution could be used to improve the Seebeck coefficient and reduce the thermal conductivity. Partial substitution of thallium for a lighter element could lead to alloy scattering of

phonons, which would reduce the lattice contribution to the thermal conductivity. As has been discussed in Chapter 4, $Co_3Sn_{1.2}In_{0.8}S_2$ and $Co_3Sn_{1.15}In_{0.85}S_2$ have the highest reported thermoelectric figure of merit (0.28) for a sulphide around 425 K. Initial investigations into substitution at the transition-metal site of $Co_3Sn_{1.2}In_{0.8}S_2$ were promising. Samples with small quantities of nickel substitution showed an improvement in Seebeck coefficient could be obtained while retaining the electrical resistivity and thermal conductivity of a fully-cobalt substituted phase. Further investigations surrounding transition-metal substitution could therefore increase the thermoelectric figure of merit for Shandite phases. The figure of merit for cobalt Shandite is a promising step towards sulphides being used for power generation from low-grade waste heat sources.

References

[1] W. Shi, R. W. Hughes, S. J. Denholme and D. H. Gregory, *Cryst. Eng. Comm.* **2010**, *12*, 641.

[2] R. Agarwal and C. M. Lieber, *Appl. Phys. A* **2006**, *85*, 209.

[3] H. Imai, Y. Shimakawa and Y. Kubo, *Phys. Rev. B* **2001**, *64*, 241104.

[4] W. Tremel and R. Hoffmann, *Inorg. Chem.* **1987**, *26*, 118.

[5] J. Schmidt, A. Sagua and A. Robledo, *Mater. Chem. Phys.* **1998**, *55*, 84.

[6] P. Atkins, *Atkins' Physical Chemistry*, **2002**.

[7] P. A. Cox, *The Electronic Structure and Chemistry of Solids*, **1987**.

[8] C. N. R. Rao and J. Gopalakrishnan, *New Directions in Solid State Chemistry*, Cambridge University Press, Cambridge, **1997**.

[9] J. T. Devreese "*Polarons"* in Encyclopedia of Applied Physics, (Ed. G. L. Trigg), Wiley, **1996**.

[10] M. Ross and T. W. Barbee "*Pressure-induced Metallization"* in Metal-Insulator Transitions Revisited, (Eds.: P. P. Edwards and C. N. R. Rao), Taylor & Francis, London, **1995**.

[11] J. M. D. Coey, M. Venkatesan and M. A. Bari "*Half-Metallic Ferromagnets"* in High Magnetic Fields, (Eds.: C. Berthier, L. P. Lévy and G. Martinez), Springer Berlin Heidelberg, **2001**.

[12] M. S. Dresselhaus, G. Chen, M. Y. Tang, R. Yang, H. Lee, D. Wang, Z. Ren, J.-P. Fleurial and P. Gogna, *Adv. Mater.* **2007**, *19*, 1043.

[13] G. Chen, *Phys. Rev. B* **1998**, *57*, 14958.

[14] G. J. Snyder and E. S. Toberer, *Nat. Mater.* **2008**, *7*, 105.

[15] E. A. Skrabek and D. S. Trimmer, *CRC Handbook of Thermoelectrics*, CRC, Boca Raton, **1995**.

[16] O. Yamashita and N. Sadatomi, *J. Appl. Phys.* **2000**, *88*, 245.

[17] B. Chen, C. Uher, L. Iordanidis and M. G. Kanatzidis, *Chem. Mater.* **1997**, *9*, 1655.

[18] M. F. Reznichenko, B. M. Kuchumov, T. P. Koretskaya, A. Alexeyev and S. A. Gromilov, *J. Phys. Chem. Solids* **2008**, *69*, 680.

[19] E. Guilmeau, Y. Bréard and A. Maignan, *Appl. Phys. Lett.* **2011**, *99*, 052107.

[20] T. Caillat, J. P. Fleurial and A. Borshchevsky, *J. Phys. Chem. Solids* **1997**, *58*, 1119.

[21] K. Biswas, L. Zhao and M. G. Kanatzidis, *Adv. Energy Mater.* **2012**, *2*, 634.

[22] K. F. Hsu, S. Loo, F. Guo, W. Chen, J. S. Dyck, C. Uher, T. Hogan, E. K. Polychroniadis and M. G. Kanatzidis, *Science* **2004**, *303*, 818.

[23] W. Cao, Y. Yan, X. Tang and S. Deng, **2008**, *41*, 215105.

[24] M. Ohta and S. Hirai, *J. Electron. Mater.* **2009**, *38*, 1287.

[25] M. Ohta, H. Obara and A. Yamamoto, *Mater. Trans.* **2009**, *50*, 2129.

[26] M. Ohtaki, *18th Int. Conf. Thermoelectrics* (Baltimore) **1999**, 565.

[27] S. Brown, S. Kauzlarich, F. Gascoin and G. Snyder, *Chem. Mater.* **2006**, *18*, 1873.

[28] M. Ohtaki, T. Tsubota, K. Eguchi and H. Arai, *J. Appl. Phys.* **1996**, *79*, 1816.

[29] O. Ben-Yehuda, R. Shuker, Y. Gelbstein, Z. Dashevsky and M. P. Dariel, *J. Appl. Phys.* **2007**, *101*, 113707.

[30] A. Adam, *Mater Res Bull* **2007**, *42*, 1986.

[31] D. Bachan, *Radiat. Eff. Defect S.* **2010**, *165*, 211.

[32] Y. Q. Cao, T. J. Zhu and X. B. Zhao, *J. Alloy Compd.* **2008**, *449*, 109.

[33] R. Venkatasubramanian, E. Siivola, T. Colpitts and B. O'Quinn, *Nature* **2001**, *413*, 597.

[34] K. Lukaszewicz, Y. Stepen' Damm, A. Pietraszko, A. Kajokas and J. Grigas, *Pol. J. Chem.* **1999**, *73*, 541.

[35] H. Mizoguchi, H. Hosono, N. Ueda and H. Kawazoe, *J. Appl. Phys.* **1995**, *78*, 1376.

[36] L. Zhao, J. He, C. Wu, T. P. Hogan, X. Zhou, C. Uher, V. P. Dravid and M. G. Kanatzidis, *J. Am. Chem. Soc.* **2012**, *134*, 7902.

[37] S. Hébert, W. Kobayashi, H. Muguerra, Y. Bréard, N. Raghavendra, F. Gascoin, E. Guilmeau and A. Maignan, *Phys. Status Solidi A* **2012**, *210*, 69.

[38] C. Wan, Y. Wang, N. Wang and K. Koumoto, *Materials* **2010**, *3*, 2606.

[39] Y. E. Putri, C. Wan, Y. Wang, W. Norimatsu, M. Kusunoki and K. Koumoto, *Scripta Mater.* **2012**, *66*, 895.

[40] M. Ohta, S. Hirai and T. Kuzuya, *J. Electron. Mater.* **2011**, *40*, 537.

[41] M. R. Geller, *Quantum Phenomena in Low-Dimensional Systems*, **2004**.

[42] A. Barnes, T. Baikie, V. Hardy and M. B. Lepetit, *J. Mater. Chem.* **2006**, 3489.

[43] M. A. Zwijnenburg, R. G. Bell and F. Corà, *J. Solid State Chem.* **2008**, *181*, 2480.

[44] B. Liu, J. Yang, Y. Han, T. Hu, W. Ren, C. Liu, Y. Ma and C. Gao, *J. Appl. Phys.* **2011**, *109*, 053717.

[45] Z. J. Chen, X. T. Zu, Y. X. Wang and S. W. Xue, *J. Appl. Phys.* **2009**, *105*, 063532.

[46] A. Shakouri and M. Zebarjadi, *Thermal Nanosystems and Nanomaterials*, Springer, Heidelberg, **2009**.

[47] L. L. Y. Chang, X. L. Li and C. S. Zheng, *Can. Mineral.* **1987**, *25*, 667.

[48] S. Derakhshan, A. Assoud, N. Soheilnia and H. Kleinke, *J. Alloy. Compd.* **2005**, *390*, 51.

[49] P. Leone, G. Andre, C. Doussier and Y. Moelo, *J. Magn. Magn. Mater.* **2004**, *284*, 92.

[50] P. Leone, C. Doussier-Brochard, G. Andre and Y. Moelo, *Phys. Chem. Miner.* **2008**, *35*, 201.

[51] K. Range, F. Rau, M. Zabel and H. Paulus, *Z. Kristallogr.* **1997**, *212*, 50.

[52] R. Weihrich, S. F. Matar, V. Eyert, F. Rau, M. Zabel, M. Andratschke, I. Anusca and T. Bernert, *Prog. Solid State Chem.* **2007**, *35*, 309.

[53] A. Michelet, G. Collin and O. Gorochov, *J. Less-Common Met.* **1984**, *97*, 73.

[54] R. Weihrich, I. Anusca and M. Zabel, *Z. Anorg. Allg. Chem.* **2005**, *631*, 1463.

[55] F. Bachhubera, I. Anuscaa, J. Rothballera, F. Pielnhofera, P. Petera and R. Weihrich, *Solid State Sci.* **2011**, *13*, 337.

[56] I. Anusca in *Neue Shandite und Parkerite Darstellung und röntgenographische Charakterisierung*, *Vol.* Universität Regensburg, Regensburg, **2008**.

[57] P. Vaqueiro and G. G. Sobany, *Solid State Sci.* **2009**, *11*, 513.

[58] S. Natarajan, G. V. S. Rao, R. Baskaran and T. S. Radhakrishnan, *J. Less-Common Met.* **1988**, *138*, 215.

[59] Y. S. Dedkov, M. Holder, S. L. Molodtsov and H. Rosner, *J. Phys. Conf. Ser.* **2008**, *100*, 072011.

[60] R. Weihrich and I. Anusca, *Z. Anorg. Allg. Chem.* **2006**, *632*, 1531.

[61] A. I. Baranov, A. V. Olenev and B. A. Popovkin, *Russ. Chem. Bull.* **2001**, *50*, 353.

[62] C. Adenis, J. Olivier-Fourcade, J. Jumas and E. Philippot, *J. Solid State Chem.* **1986**, *65*, 251.

[63] C. Adenis, J. Olivier-Fourcade, E. Philippot and J. Jumas, *Rev. Chim. Miner.* **1986**, *23*, 735.

[64] S. Jobic, P. Leboterf, R. Brec and G. Ouvrard, *J. Alloy. Compd.* **1994**, *205*, 139.

[65] F. Bodenan, V. Cajipe, M. Danot and G. Ouvrard, *J. Solid State Chem.* **1998**, *137*, 249.

[66] S. Jobic, F. Bodenan and G. Ouvrard, *J. Solid State Chem.* **1995**, *115*, 165.

[67] Bruker AXS GmbH, "EVA", Karlsruhe, Germany, **2007**.

[68] Bruker AXS GmbH, "Topas3", Karlsruhe, Germany, **2005**.

[69] A. C. Larson and R. B. von Dreele"General Structure Analysis System (GSAS)", Los Alamos National Laboratory Report LAUR 86-748, **2004**.

[70] R. I. Smith and S. Hull, User Guide for the Polaris Powder Diffractometer at ISIS, [online], available from: http://www.isis.stfc.ac.uk/instruments/polaris/,

[71] A. C. Hannon, GEM Homepage [online], available from: http://wwwisis2.isis.rl.ac.uk/disordered/gem/gem_home.htm.

[72] A. C. Hannon, *Nucl. Instrum. Meth. A* **2005**, *551*, 88.

[73] K. Knight, HRPD User Manual, [online], available from: http://www.isis.stfc.ac.uk/instruments/hrpd/documents/,

[74] R. A. Young, *The Rietveld Method*, Oxford University Press, Oxford, **1996**.

[75] D. Briggs and M. P. Seah, ed. Practical Surface Analysis: Volume 1 - Auger and X-ray Photoelectron Spectroscopy, Wiley, Chichester, **1990**.

[76] P. Gütlich, E. Bill and A. X. Trautwein, Mössbauer Spectroscopy and Transition Metal Chemistry, Springer [online], available from: http://link.springer.com/book/10.1007/978-3-540-88428-6/page/1, **2011**.

[77] R. D. Shannon, *Acta Cryst. A* **1976**, *32*, 751.

[78] M. S. Jagadeesh and M. S. Seehra, *Phys. Lett. A* **1980**, *80*, 59.

[79] S. A. Al'fer and V. F. Skums, *Inorg. Mater.* **2001**, *37*, 1216.

[80] H. J. Goldsmid, *Proc. Phys. Soc. B 69*, 203.

[81] A. Ishida, Y. Sugiyama, H. Tatsuoka, A. Ito and K. Isobe, *AIP Conf. Proc.* **2012**, *1449*, 147.

[82] A. K. Larsson, M. Haeberlein, S. Lidin and U. Schwarz, *J. Alloy. Compd.* **1996**, *240*, 79.

[83] J. Rothballer, F. Bachhuber, F. Pielnhofer, F. M. Schappacher, R. Pöttgen and R. Weihrich, *Eur. J. Inorg. Chem.* **2013**, *2013*, 248.

[84] F. S. Varley, *Neutron News* **1992**, *3*, 26.

[85] H. Eschrig and W. E. Pickett, *Solid State Commun.* **2001**, *118*, 123.

[86] P. Gutlich, K. J. Range, C. Felser, C. Schultz-Munzenberg, W. Tremel, D. Walcher and M. Waldeck, *Angew. Chem. Int. Edit.* **1999**, *38*, 2381.

[87] NIST XPS Database, available from: http://srdata.nist.gov/xps/

[88] K. T. Ramakrishna Reddy, P. Purandar Reddy, R. W. Miles and P. K. Datta, *Opt. Mater.* **2001**, *17*, 295.

[89] P. M. R. Kumar, T. T. John, C. S. Kartha, K. P. Vijayakumar, T. Abe and Y. Kashiwaba, *J. Mater. Sci.* **2006**, *41*, 5519.

[90] C. Battistoni, G. Gastaldi, G. Mattogno, M. G. Simeone and S. Viticoli, *Solid State Commun.* **1987**, *61*, 43.

[91] H. Peisert, T. Chassé, P. Streubel, A. Meisel and R. Szargan, *J. Electron Spectrosc.* **1994**, *68*, 321.

[92] P. E. Lippens, *Phys. Rev. B* **1999**, *60*, 4576.

[93] G. Huan, M. Greenblatt and K. V. Ramanujachary, *Solid State Commun.* **1989**, *71*, 221.

[94] L. D. Hicks and M. S. Dresselhaus, *Phys. Rev. B* **1993**, *47*, 12727.

[95] G. S. Nolas, J. Poon and M. Kanatzidis, *MRS Bull.* **2011**, *31*, 199.

[96] H. Kleinke, *Chem. Mater.* **2010**, *22*, 604.

[97] A. Saramat, G. Svensson, A. E. C. Palmqvist, C. Stiewe, E. Mueller, D. Platzek, S. G. K. Williams, D. M. Rowe, J. D. Bryan and G. D. Stucky, *J. Appl. Phys.* **2006**, *99*, 023708.

[98] K. Horigane and J. Akimitsu, *Sci. Technol. Adv. Mat.* **2006**, *7*, 6.

[99] B. Balke, G. Fecher, A. Gloskovskii, J. Barth, K. Kroth, C. Felser, R. Robert and A. Weidenkaff, *Phys. Rev. B.* **2008**, *77*, 045209.

Appendix A – D Spacing Equations

Crystal geometry equations for X-ray diffraction d-spacing calculations.

Orthorhombic:
$$\frac{1}{d_{hkl}^{\,2}} = \frac{h^2}{a^2} + \frac{k^2}{b^2} + \frac{l^2}{c^2} \tag{A.1}$$

Tetragonal:
$$\frac{1}{d_{hkl}^{\,2}} = \frac{h^2 + k^2}{a^2} + \frac{l^2}{c^2} \tag{A.2}$$

Cubic:
$$\frac{1}{d_{hkl}^{\,2}} = \frac{h^2 + k^2 + l^2}{a^2} \tag{A.3}$$

Hexagonal:
$$\frac{1}{d_{hkl}^{\,2}} = \frac{4}{3}\left(\frac{h^2 + hk + k^2}{a^2}\right) + \frac{l^2}{c^2} \tag{A.4}$$

Monoclinic:
$$\frac{1}{d_{hkl}^{\,2}} = \frac{1}{\sin^2\beta}\left(\frac{h^2}{a^2} + \frac{k^2\sin^2\beta}{b^2} + \frac{l^2}{c^2} - \frac{2hl\cos\beta}{ac}\right) \tag{A.5}$$

Rhombohedral:
$$\frac{1}{d_{hkl}^{\,2}} = \frac{\left(h^2 + k^2 + l^2\right)\sin^2\alpha + 2\left(hk + kl + hl\right)\left(\cos^2\alpha - \cos\alpha\right)}{a^2\left(1 - 3\cos^2\alpha + 2\cos^3\alpha\right)} \tag{A.6}$$

Triclinic:
$$\frac{1}{d_{hkl}^{\,2}} = \frac{1}{V^2}\left(S_{11}h^2 + S_{22}k^2 + S_{33}l^2 + 2S_{12}hk + 2S_{23}kl + 2S_{13}hl\right) \tag{A.7}$$

where

$$S_{11} = b^2c^2\sin^2\alpha$$
$$S_{22} = a^2c^2\sin^2\beta$$
$$S_{33} = a^2b^2\sin^2\gamma$$
$$S_{12} = abc^2\left(\cos\alpha\cos\beta - \cos\gamma\right)$$
$$S_{23} = a^2bc\left(\cos\beta\cos\gamma - \cos\alpha\right)$$
$$S_{13} = ab^2c\left(\cos\alpha\cos\gamma - \cos\beta\right)$$
$$V = abc\sqrt{1 - \cos^2\alpha - \cos^2\beta - \cos^2\gamma + 2\cos\alpha\cos\beta\cos\gamma}$$

Appendix B – Neutron Diffraction Data.

Table B.1: Powder neutron diffraction experiments for $Fe_{1-x}Mn_xPb_4Sb_6S_{14}$ performed on the Polaris diffractometer.

Run Number	*Sample*	*Temperature (K)*	*Counts (μA)*
55615	$MnPb_4Sb_6S_{14}$	RT	516
55622	$MnPb_4Sb_6S_{14}$	4.2	600
55623	$MnPb_4Sb_6S_{14}$	2	580
55624	$Fe_{0.25}Mn_{0.75}Pb_4Sb_6S_{14}$	1.8	478
55626	$Fe_{0.75}Mn_{0.25}$ $Pb_4Sb_6S_{14}$	1.8	529
55627	$Fe_{0.75}Mn_{0.25}$ $Pb_4Sb_6S_{14}$	10	519
55629	$Fe_{0.25}Mn_{0.75}Pb_4Sb_6S_{14}$	10	430
56746	$Fe_{0.75}Mn_{0.25}$ $Pb_4Sb_6S_{14}$	RT	600
56747	$Fe_{0.25}Mn_{0.75}Pb_4Sb_6S_{14}$	RT	600

Table B.2: Powder neutron diffraction experiments for $Fe_{1-x}Mn_xPb_4Sb_6S_{14}$ performed on the GEM diffractometer.

Run Number	*Sample*	*Temperature (K)*	*Counts (μA)*
53868	$FePb_4Sb_6S_{14}$	1.5	600
53869	$FePb_4Sb_6S_{14}$	10	600
53870	$FePb_4Sb_6S_{14}$	150	496
53871	$Fe_{0.5}Mn_{0.5}Pb_4Sb_6S_{14}$	1.5	509
53877	$FePb_4Sb_6S_{14}$	RT	300
53878	$Fe_{0.5}Mn_{0.5}Pb_4Sb_6S_{14}$	RT	300

Table B.3: Powder neutron diffraction experiments for $Co_3Sn_{2-x}In_xS_2$ performed on the GEM diffractometer.

Run Number	*Sample*	*Temperature (K)*	*Counts (μA)*
53265	Co_3SnInS_2	RT	450
53266	$Co_3Sn_{0.2}In_{1.8}S_2$	RT	403

53267	$Co_3Sn_{1.8}In_{0.2}S_2$	RT	300
53268	$Co_3Sn_{0.6}In_{1.4}S_2$	RT	400
53269	$Co_3Sn_{1.4}In_{0.6}S_2$	RT	300
53270	$Co_3In_2S_2$	RT	400
53271	$Co_3Sn_2S_2$	RT	300
53272	$Co_3Sn_{1.6}In_{0.4}S_2$	RT	300
53861	$Co_3Sn_{1.2}In_{0.8}S_2$	RT	409
53862	$Co_3Sn_{1.6}In_{0.4}S_2$	RT	355
53876	$Co_3Sn_{0.4}In_{1.6}S_2$	RT	409
53879	$Co_3Sn_2S_2$	5	450
53880	$Co_3Sn_2S_2$	165	450
53881	$Co_3Sn_2S_2$	190	476
53882	Empty Cryostat	RT	211

Table B.4: Powder neutron diffraction experiments for $In_2Sn_3S_7$ and $Cr_2Sn_3Se_7$ performed on the HRPD diffractometer.

Run Number	*Sample*	*Temperature (K)*	*Counts (μA)*
52401	$Cr_2Sn_3Se_7$	RT	150
52402	$In_2Sn_3S_7$	RT	616
52403	$In_2Sn_3S_7$	400	350
52404	$In_2Sn_3S_7$	500	350
52405	$In_2Sn_3S_7$	600	238
52406	$In_2Sn_3S_7$	650	175
52407	$In_2Sn_3S_7$	700	175
52408	$In_2Sn_3S_7$	750	175

Appendix C – Powder Neutron Diffraction Data and the Fit of the Structural Model for $FePb_4Sb_6S_{14}$.

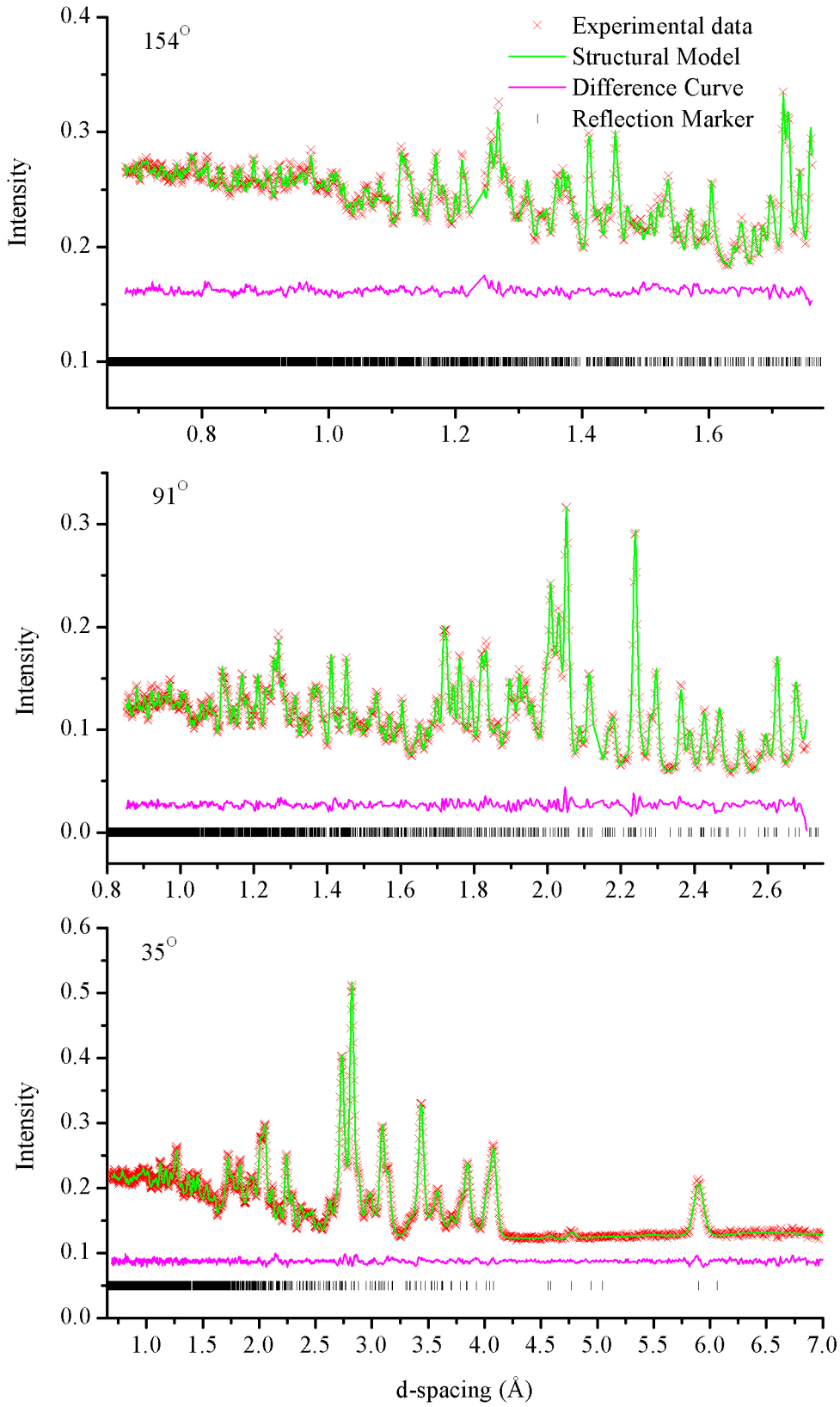

Figure C.1: Powder neutron diffraction data from the 154°, 91° and 35° detector banks on the GEM diffractometer and the fit of the structural model for $FePb_4Sb_6S_{14}$ at 150 K.

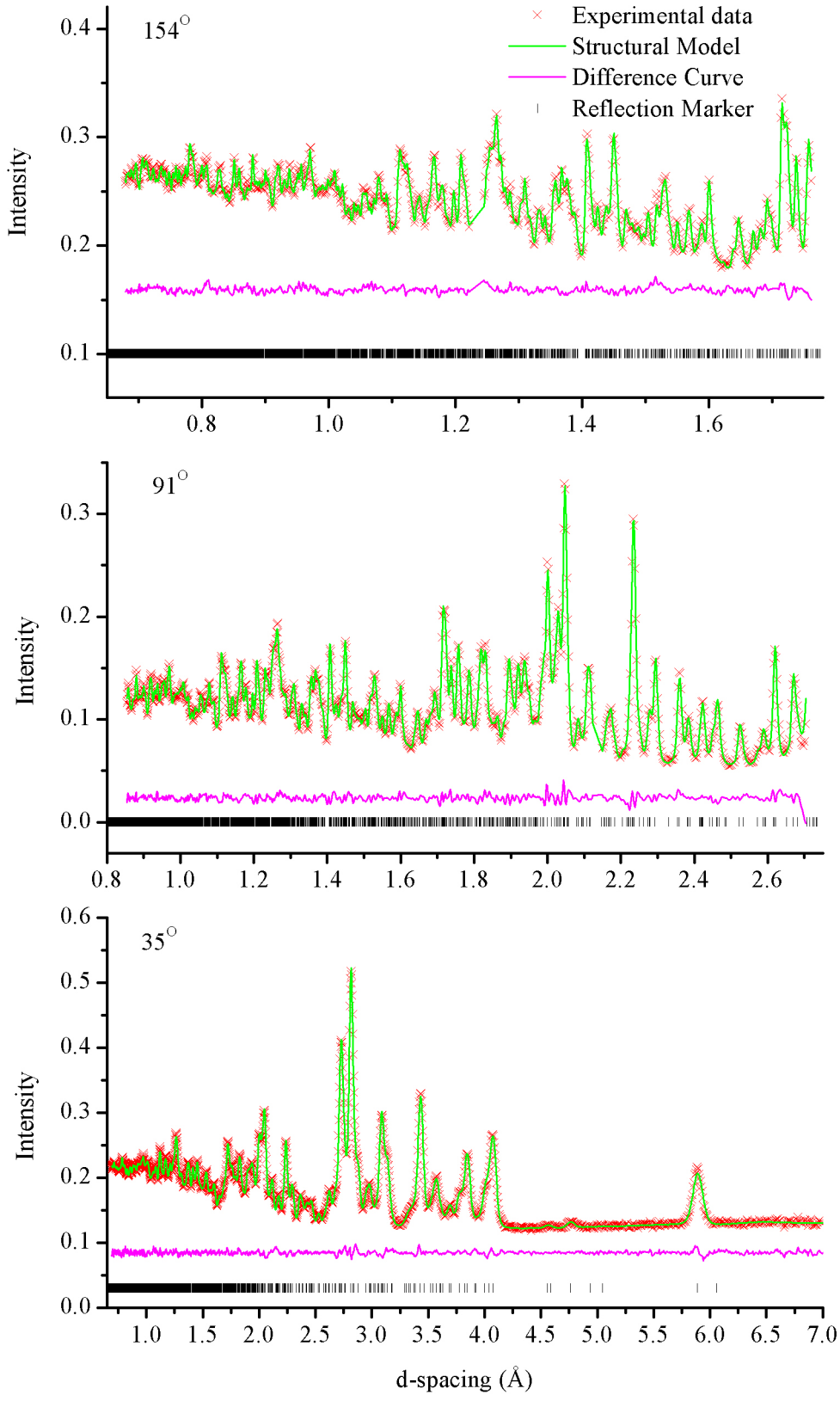

Figure C.2: Powder neutron diffraction data from the 154°, 91° and 35° detector banks on the GEM diffractometer and the fit of the structural model for $FePb_4Sb_6S_{14}$ at 10 K.

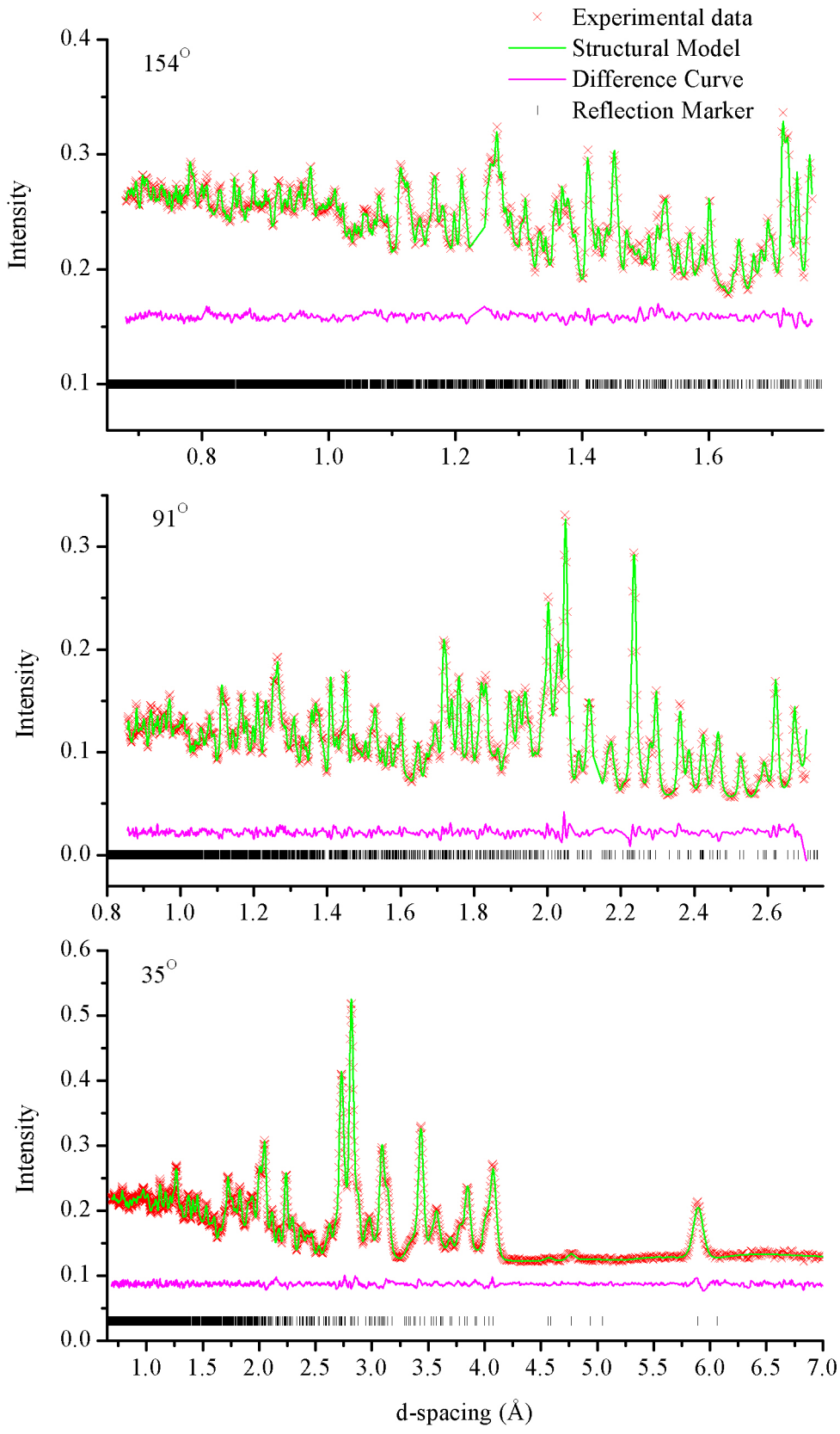

Figure C.3: Powder neutron diffraction data from the 154°, 91° and 35° detector banks on the GEM diffractometer and the fit of the structural model for $FePb_4Sb_6S_{14}$ at 2 K.

Appendix D - Powder Neutron Diffraction Data and the Fit of the Structural Model for $Fe_{0.75}Mn_{0.25}Pb_4Sb_6S_{14}$.

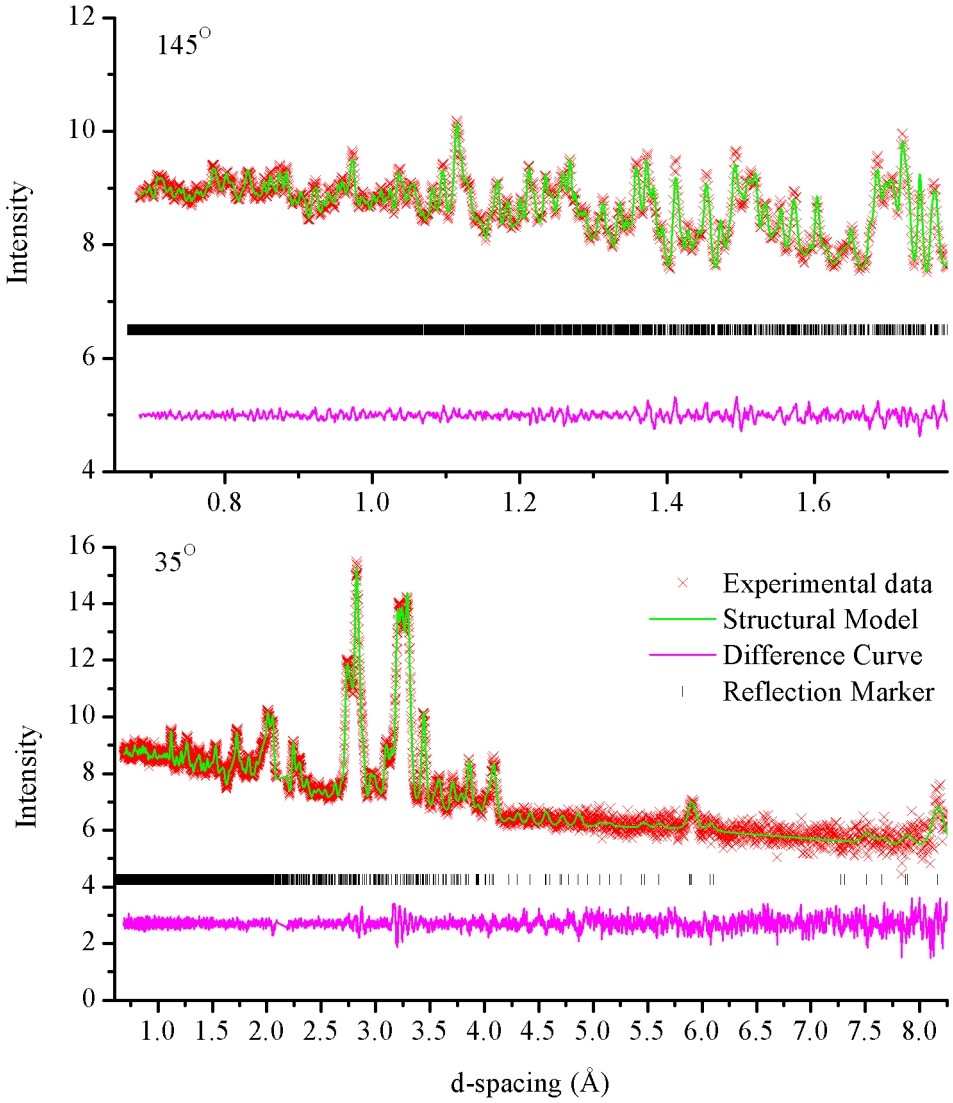

Figure D.1: Powder neutron diffraction data from the 145° and 35° detector banks on the Polaris diffractometer and the fit of the $Fe_{0.75}Mn_{0.25}Pb_4Sb_6S_{14}$ structural model at 2 K.

Appendix E- Powder Neutron Diffraction Data and the Fit of the Structural Model for $Fe_{0.5}Mn_{0.5}Pb_4Sb_6S_{14}$.

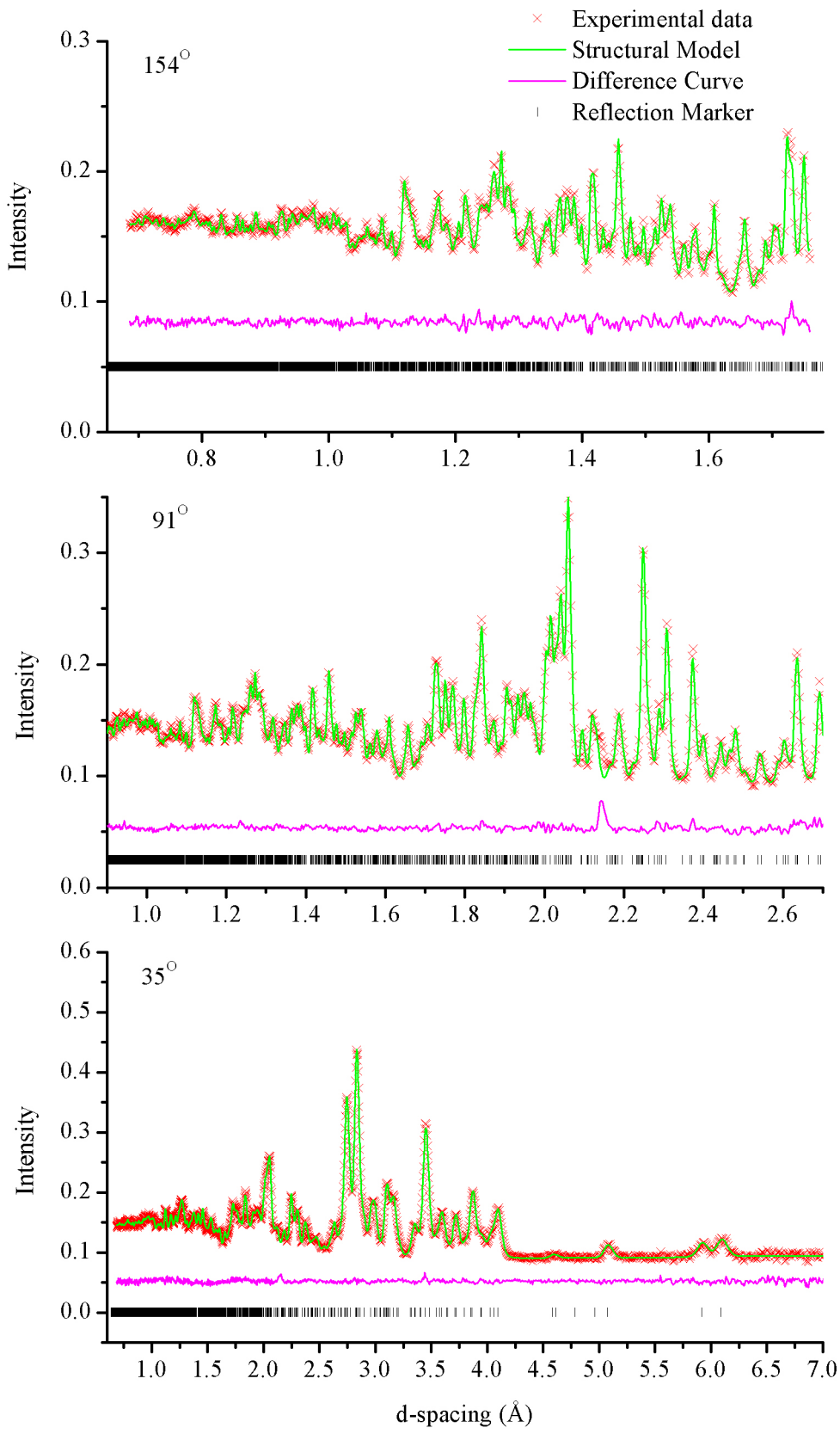

Figure E.1: Powder neutron diffraction data from the 154°, 91° and 35° detector banks on GEM and the fit of the $Fe_{0.5}Mn_{0.5}Pb_4Sb_6S_{14}$ structural model at 298 K.

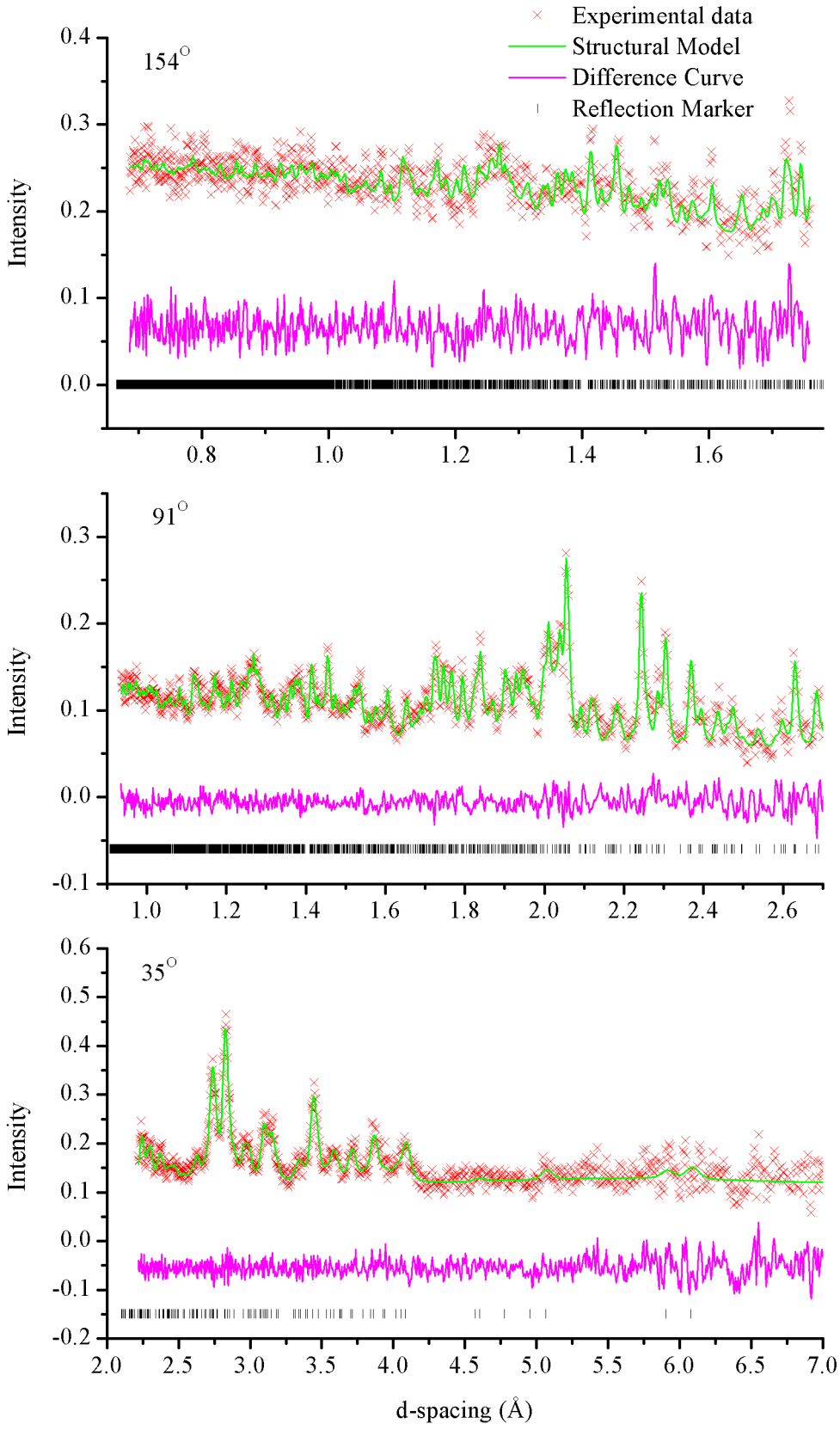

Figure E.2: Powder neutron diffraction data from the 154°, 91° and 35° detector banks on GEM and the fit of the Fe0.5Mn0.5Pb4Sb6S14 structural model at 2 K.

Appendix F- Powder Neutron Diffraction Data and the Fit of the Structural Model for $Fe_{0.25}Mn_{0.75}Pb_4Sb_6S_{14}$.

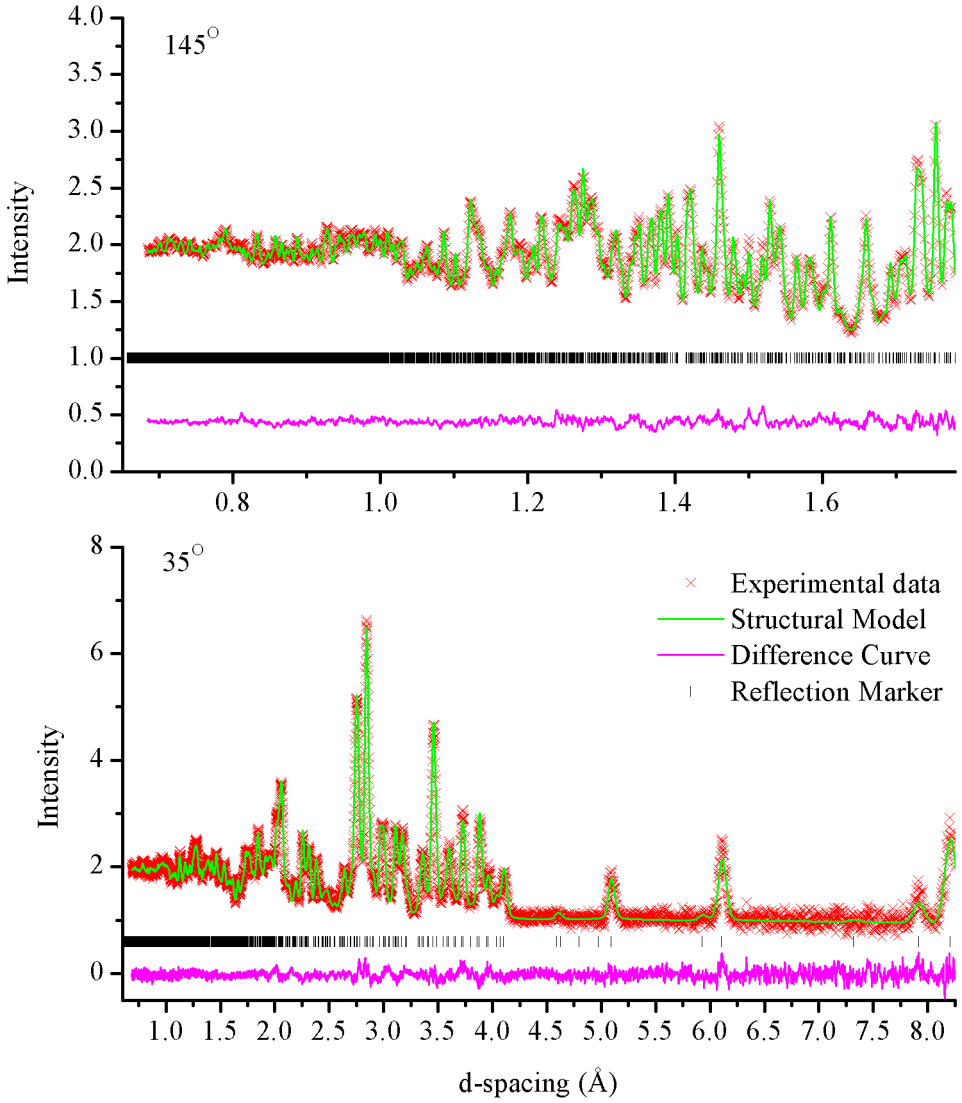

Figure F.1: Powder neutron diffraction data from the 145° and 35° detector banks on the Polaris diffractometer and the fit of the $Fe_{0.25}Mn_{0.75}Pb_4Sb_6S_{14}$ structural model at 298 K.

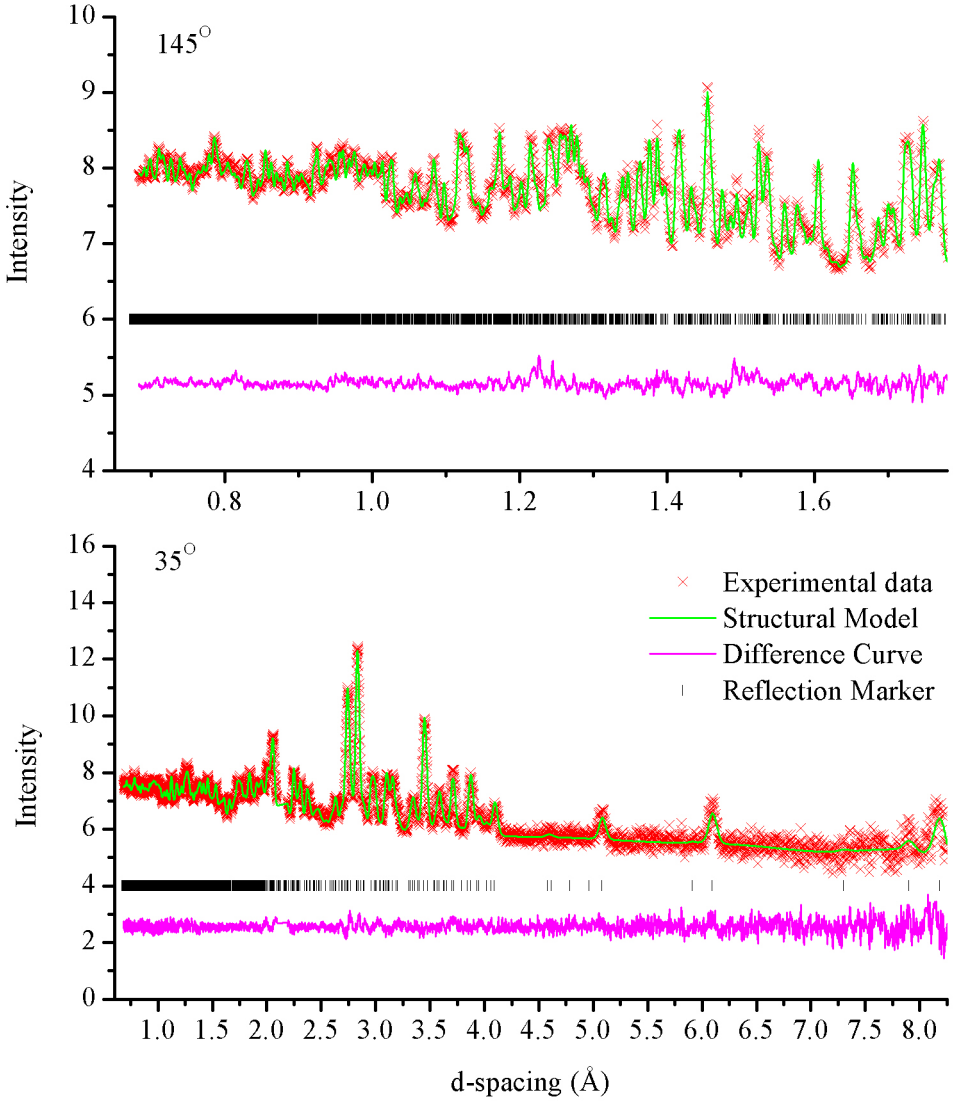

Figure F.2: Powder neutron diffraction data from the 145° and 35° detector banks on the Polaris diffractometer and the fit of the $Fe_{0.25}Mn_{0.75}Pb_4Sb_6S_{14}$ structural model at 2 K.

Appendix G - Powder Neutron Diffraction Data and the Fit of the Structural Model for $MnPb_4Sb_6S_{14}$.

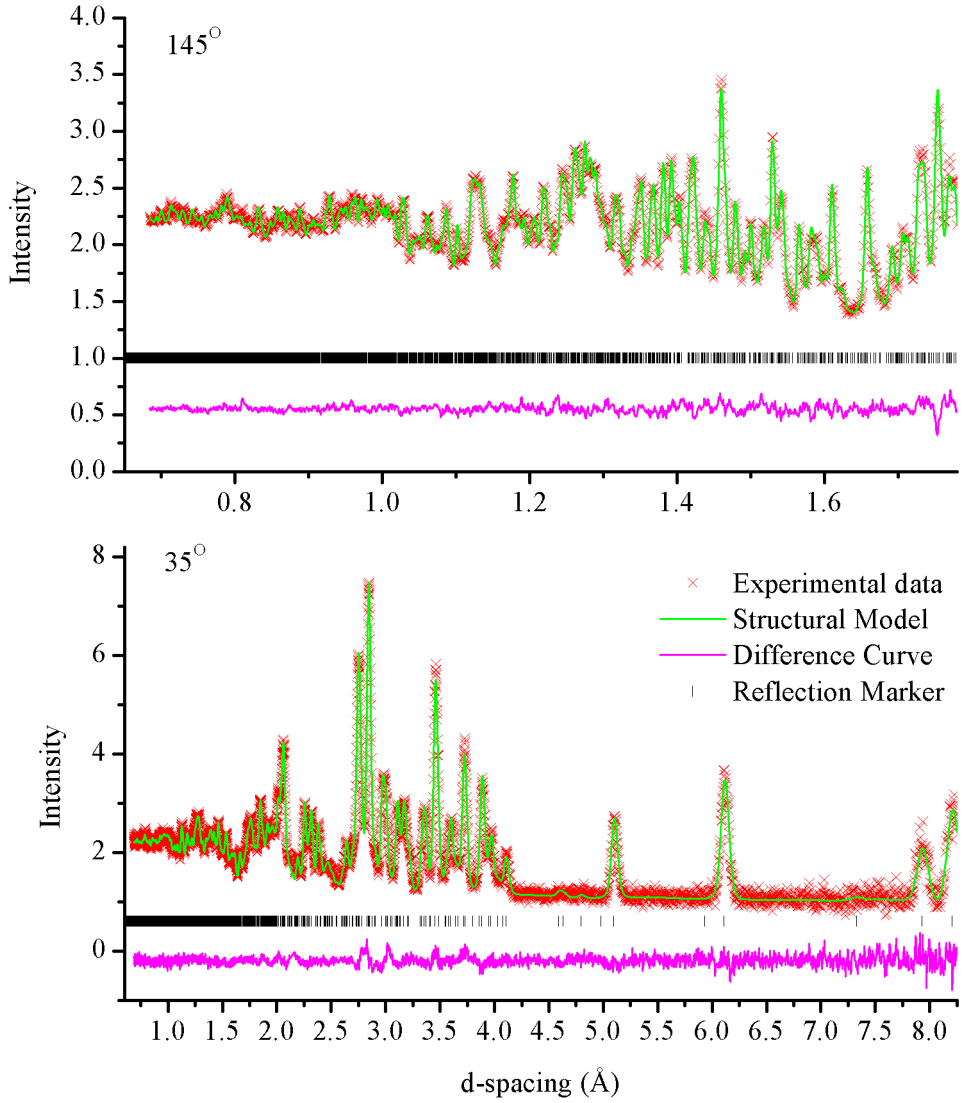

Figure G.1: Powder neutron diffraction data from the 145° and 35° detector banks on the Polaris diffractometer and the fit of the $MnPb_4Sb_6S_{14}$ structural model at 298 K.

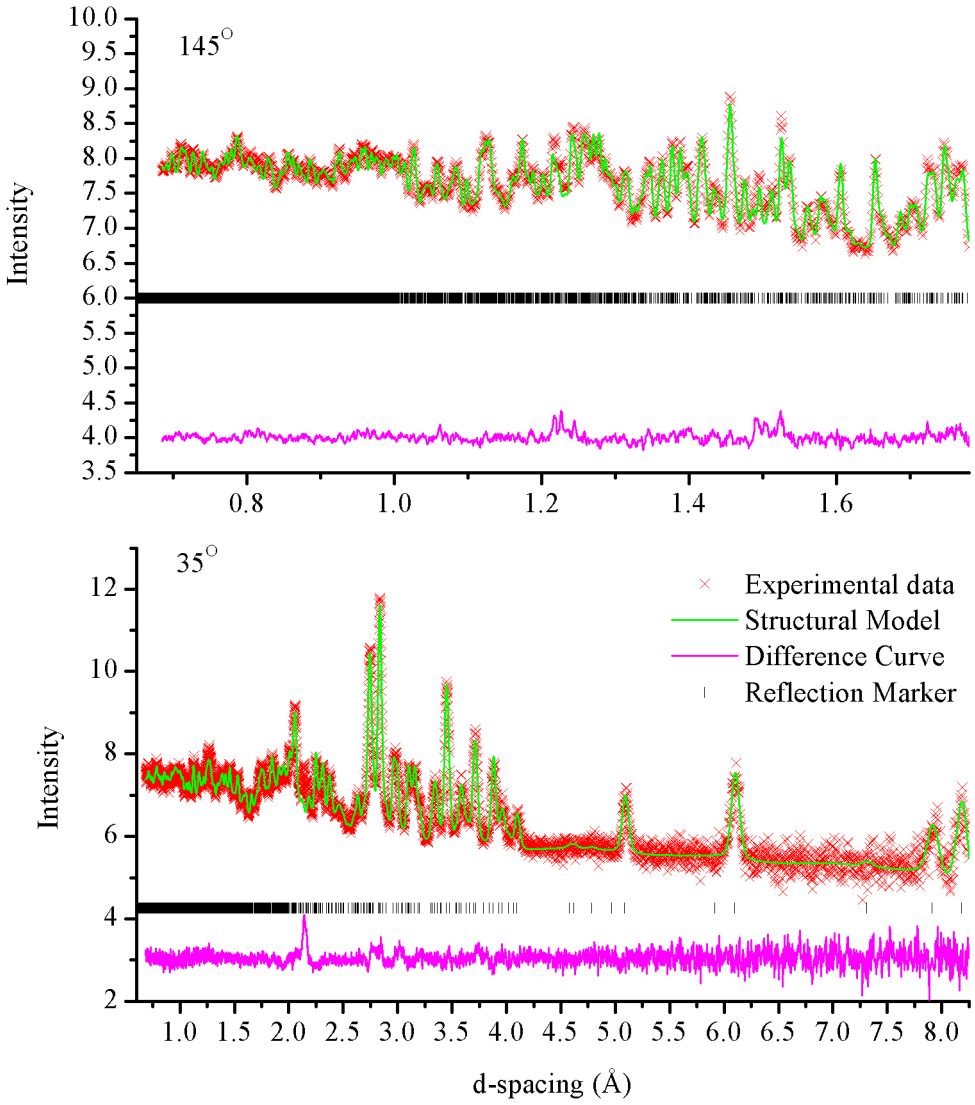

Figure G.2: Powder neutron diffraction data from the 145° and 35° detector banks on the Polaris diffractometer and the fit of the structural model for $MnPb_4Sb_6S_{14}$ at 4 K.

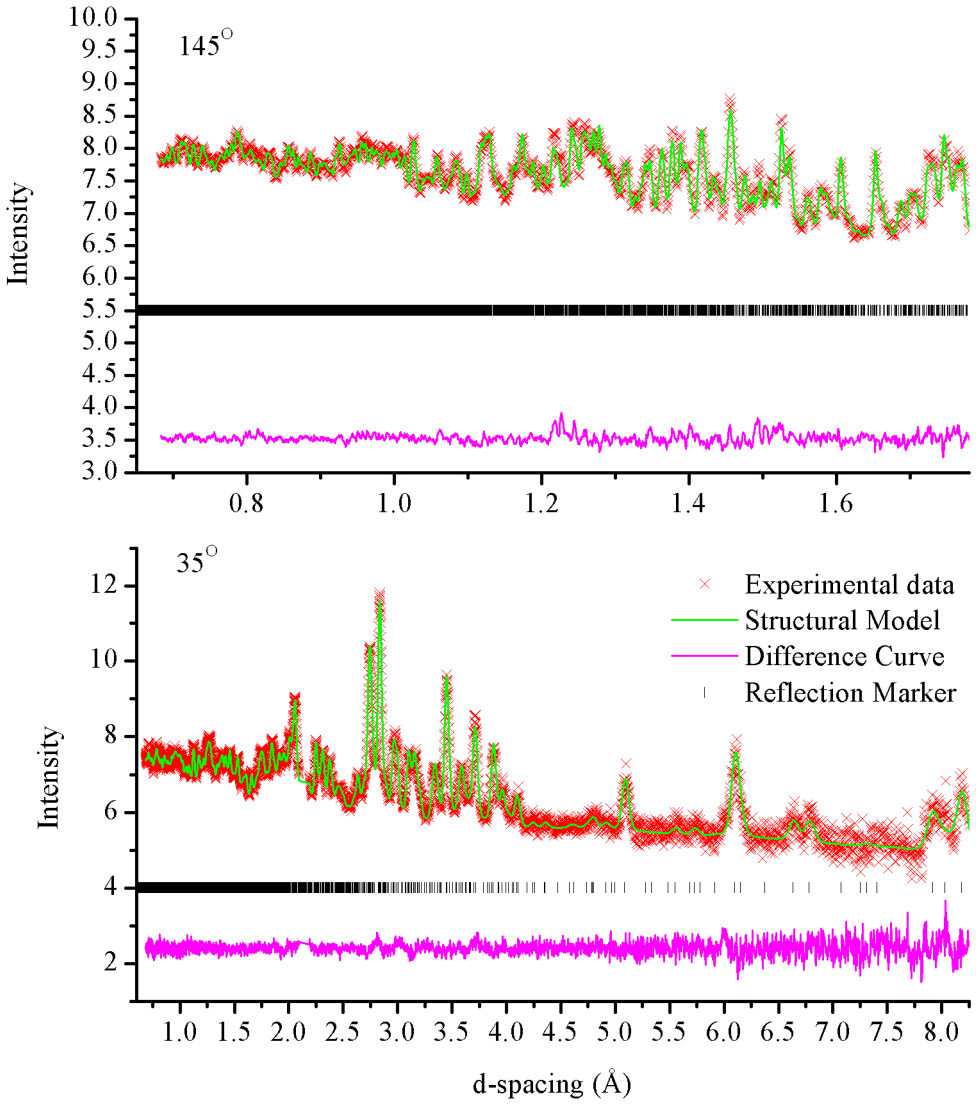

Figure G.3: Powder neutron diffraction data from the 145° and 35° detector banks on the Polaris diffractometer and the fit of the structural model for $MnPb_4Sb_6S_{14}$ at 2 K.

Appendix H - Final Refinement Parameters using Powder Neutron Diffraction Data for $Fe_{1-x}Mn_xPb_4Sb_6S_{14}$.

Table H.1: Atomic coordinates of $Fe_{0.5}Mn_{0.5}Pb_4Sb_6S_{14}$ obtained from Rietveld refinements of powder neutron diffraction experiments collected on the GEM diffractometer. Space Group: $P2_1/a$.

atom		*298 K*	*2 K*
Fe / Mn[a]	Uiso (Å^2)	0.0203(6)	0.013(5)
Pb(1)	x	-0.0750(1)	-0.0725(6)
	y	0.2605(1)	0.2610(5)
	z	0.0638(6)	0.055(3)
Pb(2)	x	-0.3140(1)	-0.3133(7)
	y	0.3594(1)	0.3614(5)
	z	0.0387(5)	0.035(3)
Pb	Uiso (Å^2)	0.0203(6)	0.013(5)
Sb(1)	x	0.1302(2)	0.1311(9)
	y	0.3402(2)	0.3380(9)
	z	-0.3807(9)	-0.383(5)
Sb(2)	x	-0.1031(2)	-0.102(1)
	y	0.4520(2)	0.458(1)
	z	-0.3805(8)	-0.388(4)
Sb(3)	x	-0.1797(2)	-0.177(1)
	y	0.0638(2)	0.0646(9)
	z	0.4034(9)	0.402(5)
Sb	Uiso (Å^2)	0.0203(6)	0.013(5)
S(1)	x	-0.2139(4)	-0.215(2)
	y	0.4963(3)	0.499(2)
	z	0.0312(16)	0.037(8)
S(2)	x	-0.0804(4)	-0.076(2)
	y	0.1068(3)	0.106(2)
	z	-0.0167(16)	-0.016(8)
S(3)	x	0.0954(4)	0.096(2)
	y	0.0428(3)	0.042(2)

	z	-0.474(2)	-0.472(9)
S(4)	x	0.0519(4)	0.054(2)
	y	0.2325(3)	0.234(2)
	z	-0.416(2)	-0.435(9)
S(5)	x	-0.1813(4)	-0.185(2)
	y	0.3390(4)	0.341(2)
	z	-0.451(2)	-0.454(8)
S(6)	x	0.0002(4)	0.002(2)
	y	0.3975(4)	0.400(2)
	z	0.054(2)	0.057(8)
S(7)	x	-0.2751(4)	-0.274(2)
	y	0.2041(4)	0.202(2)
	z	0.078(2)	0.06(1)
S	Uiso ($Å^2$)	0.0203(6)	0.013(5)
	a ($Å^2$)	15.7919(4)	15.768(2)
	b ($Å^2$)	19.1437(4)	19.105(2)
	c ($Å^2$)	4.02987(9)	4.0182(5)
	β (°)	91.834(2)	91.77(1)
	R_{wp} 35° (%)	1.9	9.0
	R_{wp} 91° (%)	1.6	7.0
	R_{wp} 154° (%)	1.6	6.8
	χ^2	1.1	1.5

Fe / Mn site occupancy factors 0.5 / 0.5 on (a) 0 0 0.

Table H.2: Atomic coordinates of $Fe_{0.75}Mn_{0.25}Pb_4Sb_6S_{14}$ obtained from Rietveld refinements of powder neutron diffraction data collected on the original Polaris diffractometer. Space Group: $P2_1/a$.

atom		*298 K*	*2 K*
Fe / Mn[a]	Uiso ($Å^2$)	0.010(1)	0.0036(8)
Pb(1)	x	-0.0739(2)	-0.0708(2)
	y	0.2611(1)	0.2637(2)
	z	0.0602(6)	0.0617(7)
Pb(2)	x	-0.3146(2)	-0.3167(2)
	y	0.3584(1)	0.3589(1)
	z	0.0428(6)	0.0351(7)
Pb	Uiso ($Å^2$)	0.0164(3)	0.0146(4)
Sb(1)	x	0.1308(2)	0.130(2)
	y	0.3408(2)	0.3399(2)
	z	-0.380(1)	-0.3887(9)
Sb(2)	x	-0.1053(3)	-0.1009(3)
	y	0.4526(2)	0.4569(2)
	z	-0.388(1)	-0.396(1)
Sb(3)	x	-0.1779(3)	-0.1775(3)
	y	0.0640(2)	0.0651(2)
	z	0.403(1)	0.4214(9)
Sb	Uiso ($Å^2$)	0.0151(5)	0.0044(3)
S(1)	x	-0.2164(4)	-0.2216(5)
	y	0.4982(4)	0.5117(4)
	z	0.039(2)	-0.006(2)
S(2)	x	-0.0732(5)	-0.0808(6)
	y	0.1082(4)	0.1091(4)
	z	-0.004(2)	-0.008(2)
S(3)	x	0.0949(4)	0.0838(5)
	y	0.0448(3)	0.0665(5)
	z	-0.478(2)	-0.420(2)
S(4)	x	0.0522(4)	0.0598(5)
	y	0.2329(4)	0.2403(4)

	z	-0.420(2)	-0.437(2)
S(5)	x	-0.1860(5)	-0.1833(6)
	y	0.3397(4)	0.3502(4)
	z	-0.439(2)	-0.481(2)
S(6)	x	-0.0002(5)	-0.0103(5)
	y	0.4001(4)	0.3849(4)
	z	0.057(2)	0.058(2)
S(7)	x	-0.2712(4)	-0.2689(5)
	y	0.2026(4)	0.2044(4)
	z	0.077(2)	0.062(2)
S	Uiso ($Å^2$)	0.0122(5)	0.0171(7)
	a ($Å^2$)	15.7807(3)	15.7496(4)
	b ($Å^2$)	19.1424(4)	19.0871(5)
	c ($Å^2$)	4.02802(7)	4.01066(9)
	β (°)	91.732(2)	91.718(2)
	R_{wp} 35° (%)	3.4	1.6
	R_{wp} 145° (%)	1.7	0.8
	χ^2	1.5	1.1

Fe / Mn site occupancy factors 0.75 / 0.25 on (a) 0 0 0.

Table H.3: Atomic coordinates of $MnPb_4Sb_6S_{14}$ obtained from Rietveld refinements of powder neutron diffraction data collected on the original Polaris diffractometer. Space Group: $P2_1/a$.

atom		*298 K*	*5 K*	*2 K*
Mn[a]	Uiso (Å^2)	0.024(2)	0.003(2)	0.011(2)
Pb(1)	x	-0.0735(1)	-0.7440(2)	-0.0731(1)
	y	0.26096(9)	0.2608(1)	0.2607(1)
	z	0.0651(5)	0.0575(7)	0.0599(6)
Pb(2)	x	-0.3129(1)	-0.3109(2)	-0.3121(1)
	y	0.35883(8)	0.3601(1)	0.3605(1)
	z	0.0417(4)	0.0347(7)	0.0326(6)
Pb	Uiso (Å^2)	0.0188(4)	0.0014(4)	0.0018(3)
Sb(1)	x	0.1302(2)	0.1317(2)	0.1320(1)
	y	0.3404(2)	0.3397(2)	0.3399(2)
	z	-0.3773(7)	-0.382(1)	-0.384(1)
Sb(2)	x	-0.1027(2)	-0.1019(3)	-0.1027(3)
	y	0.4520(2)	0.4546(3)	0.4541(2)
	z	-0.3845(7)	-0.393(1)	-0.393(1)
Sb(3)	x	-0.1803(2)	-0.1797(3)	-0.1797(3)
	y	0.0636(2)	0.0647(3)	0.0639(2)
	z	0.4047(7)	0.398(1)	0.400(1)
Sb	Uiso (Å^2)	0.0157(5)	0.0038(6)	0.0048(5)
S(1)	x	-0.2123(4)	-0.2100(6)	-0.2111(5)
	y	0.4964(3)	0.4964(4)	0.4958(4)
	z	0.031(2)	0.023(2)	0.013(2)
S(2)	x	-0.0809(3)	-0.818(6)	-0.0808(5)
	y	0.1082(3)	0.1090(5)	0.1079(4)
	z	-0.006(1)	-0.009(2)	0.003(2)
S(3)	x	0.0983(3)	0.0951(5)	0.0962(4)
	y	0.0451(3)	0.0469(5)	0.0468(4)
	z	-0.473(1)	-0.486(2)	-0.485(2)
S(4)	x	0.0530(4)	0.0518(6)	0.0503(5)
	y	0.2316(3)	0.2290(5)	0.2281(4)

	z	-0.414(1)	-0.423(2)	-0.435(2)
S(5)	x	-0.1794(3)	-0.1796(6)	-1.825(4)
	y	0.3410(3)	0.3436(5)	0.3438(4)
	z	-0.439(1)	-0.447(2)	-0.434(2)
S(6)	x	0.0034(4)	-0.0001(6)	0.0026(5)
	y	0.3999(3)	0.4024(5)	0.4026(4)
	z	0.061(1)	0.051(2)	0.058(2)
S(7)	x	-0.2758(4)	-0.2731(6)	-0.2738(5)
	y	0.2054(3)	0.2063(5)	0.2054(4)
	z	0.096(2)	0.072(3)	0.068(2)
S	Uiso ($Å^2$)	0.0178(5)	0.0041(6)	0.0036(5)
	a ($Å^2$)	15.8656(4)	15.8322(5)	15.8347(4)
	b ($Å^2$)	19.1781(4)	19.1213(5)	19.1202(4)
	c ($Å^2$)	4.0323(1)	4.0167(1)	4.0170(1)
	β (°)	91.905(1)	91.834(2)	91.799(1)
	R_{wp} 35° (%)	3.4	2.1	1.6
	R_{wp} 145° (%)	1.5	0.9	0.9
	χ^2	1.1	1.6	1.1

Mn on (a) 0 0 0.

Appendix I - Powder Neutron Diffraction Data and the Fit of the Structural Model for $Co_3Sn_{2-x}In_xS_2$ ($0 \leq x \leq 2$).

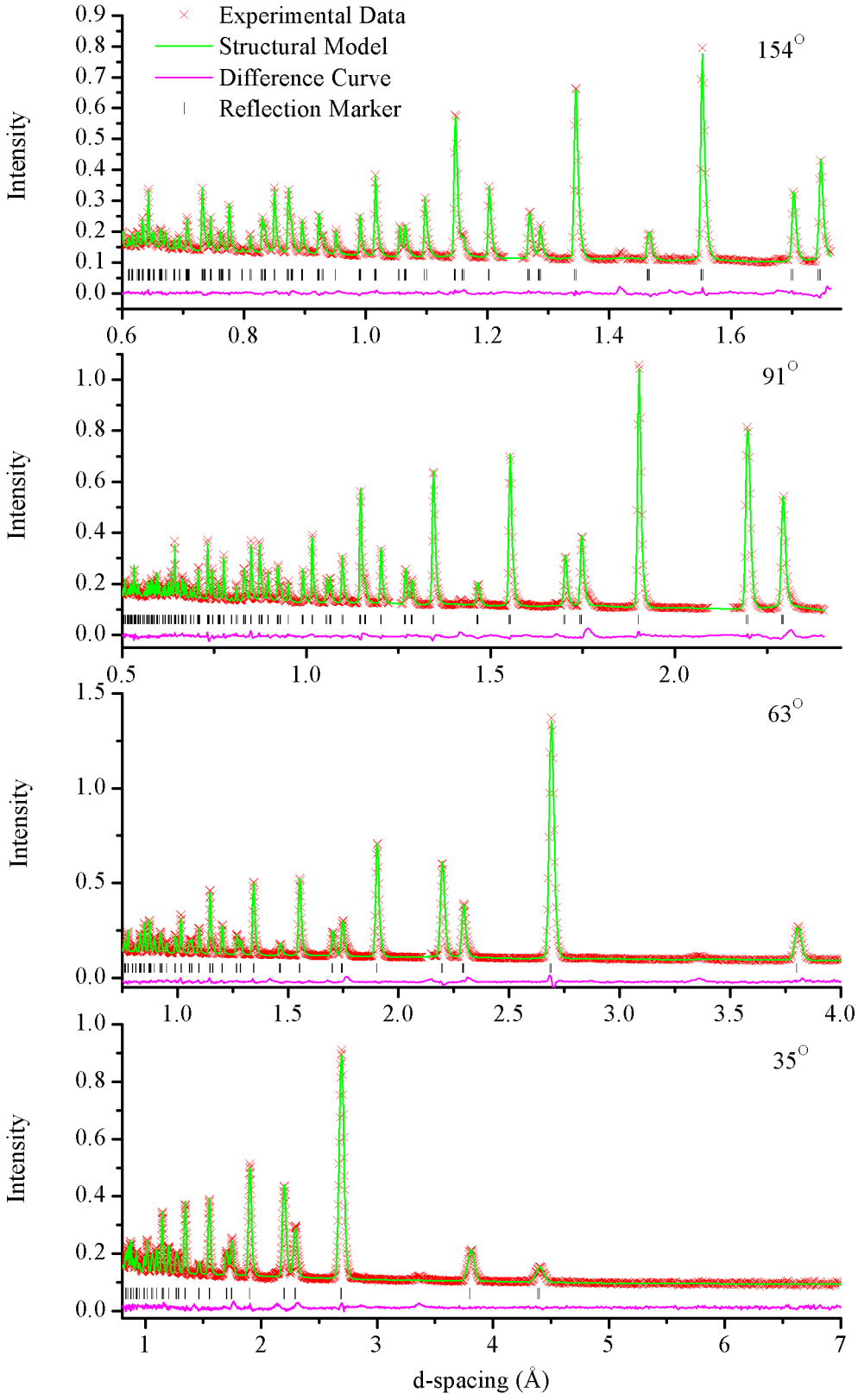

Figure I.1: Powder neutron diffraction data collected from four banks of the GEM diffractometer and structural refinements of $Co_3Sn_2S_2$.

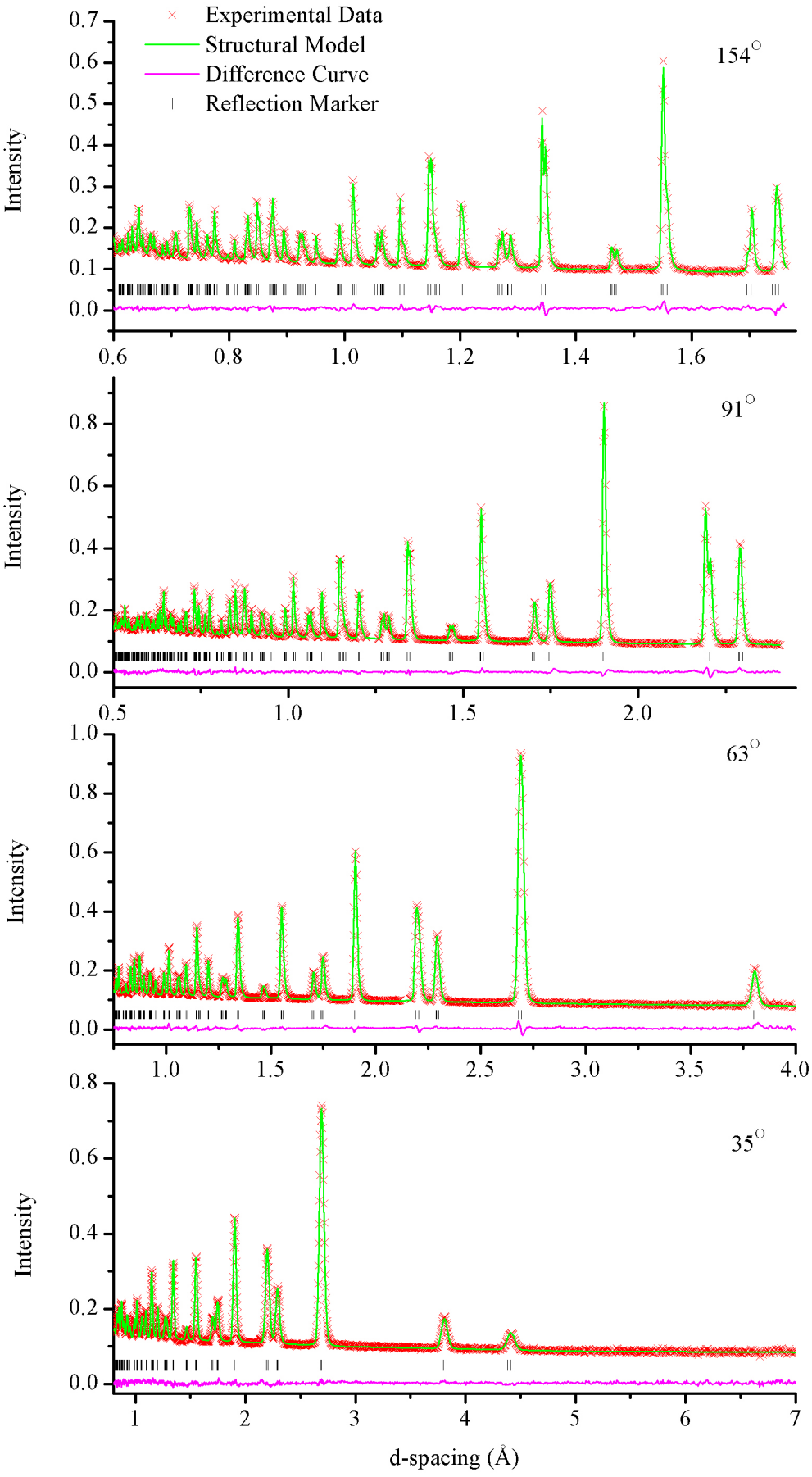

Figure I.2: Powder neutron diffraction data collected from four banks of the GEM diffractometer and structural refinements of $Co_3Sn_{1.8}In_{0.2}S_2$.

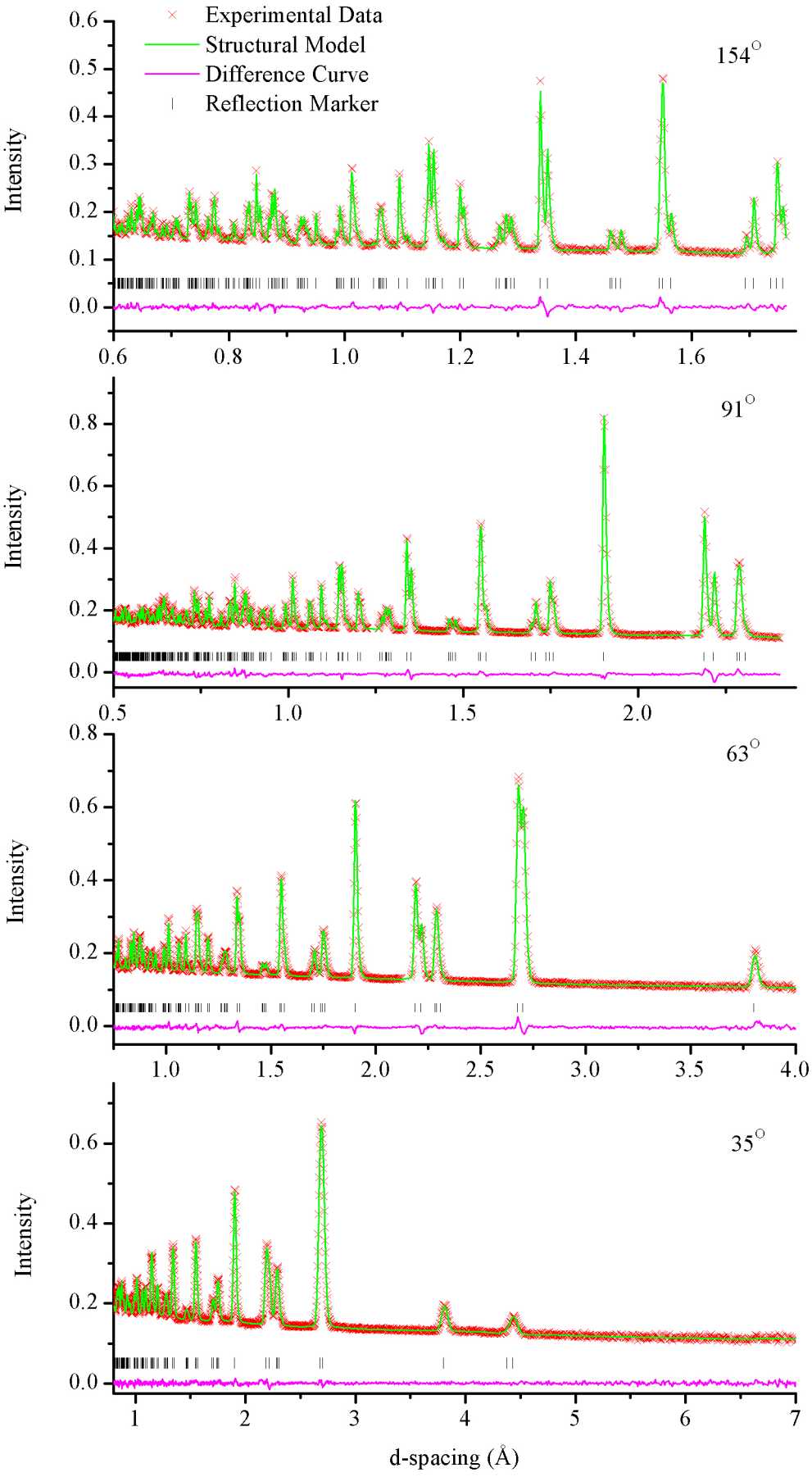

Figure I.3: Powder neutron diffraction data collected from four banks of the GEM diffractometer and structural refinements of $Co_3Sn_{1.6}In_{0.4}S_2$.

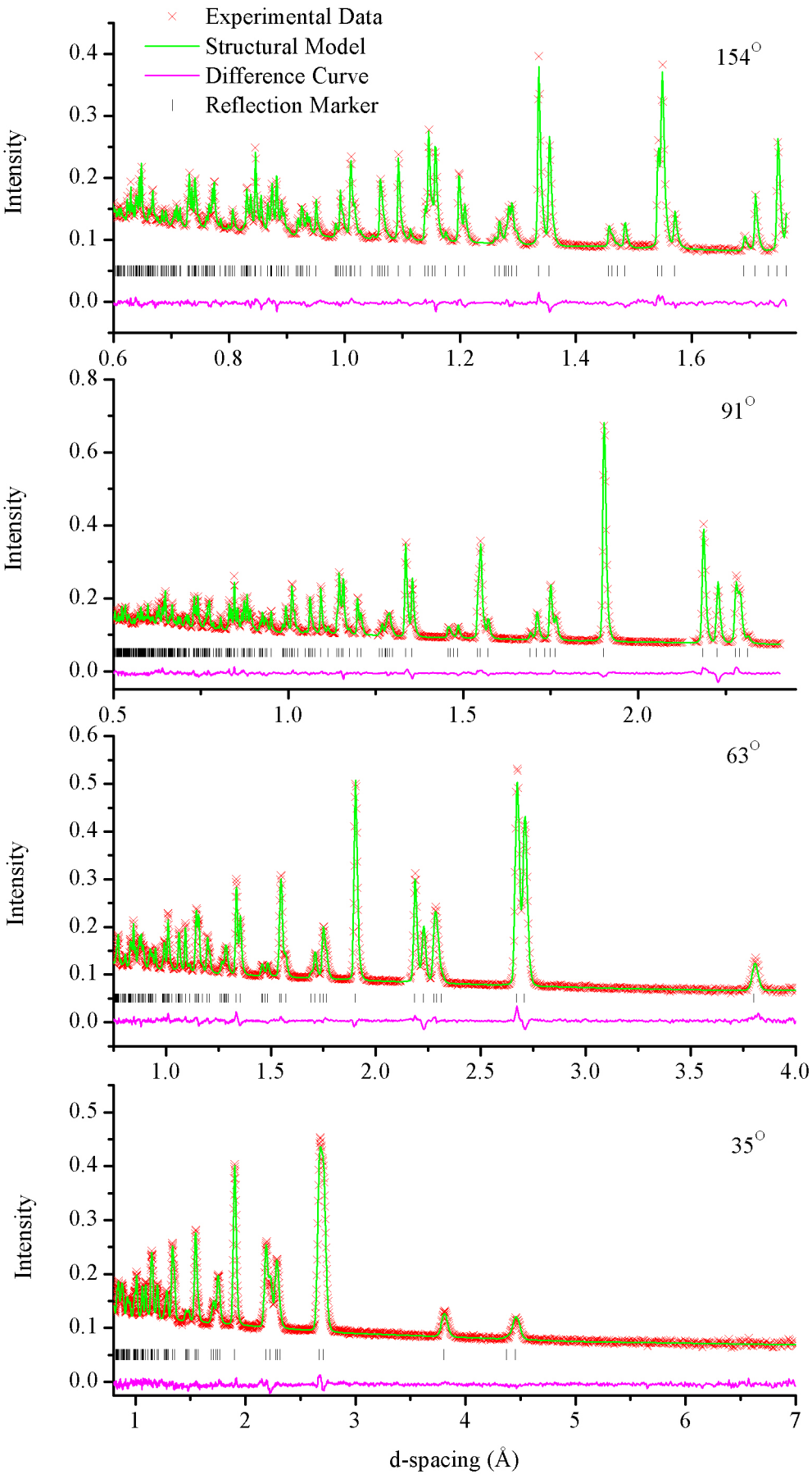

Figure I.4: Powder neutron diffraction data collected from four banks of the GEM diffractometer and structural refinements of $Co_3Sn_{1.4}In_{0.6}S_2$.

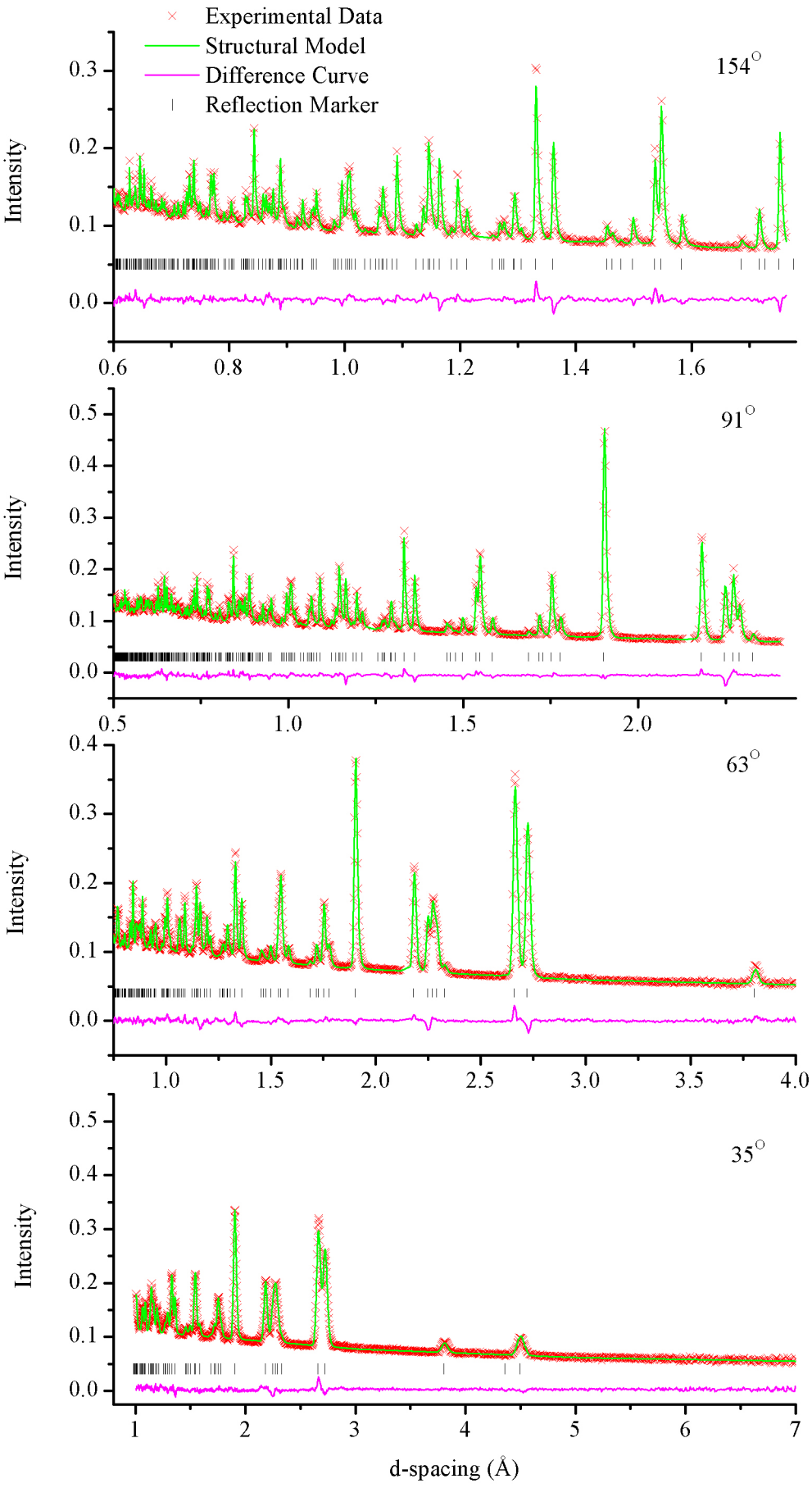

Figure I.5: Powder neutron diffraction data collected from four banks of the GEM diffractometer and structural refinements of Co_3SnInS_2.

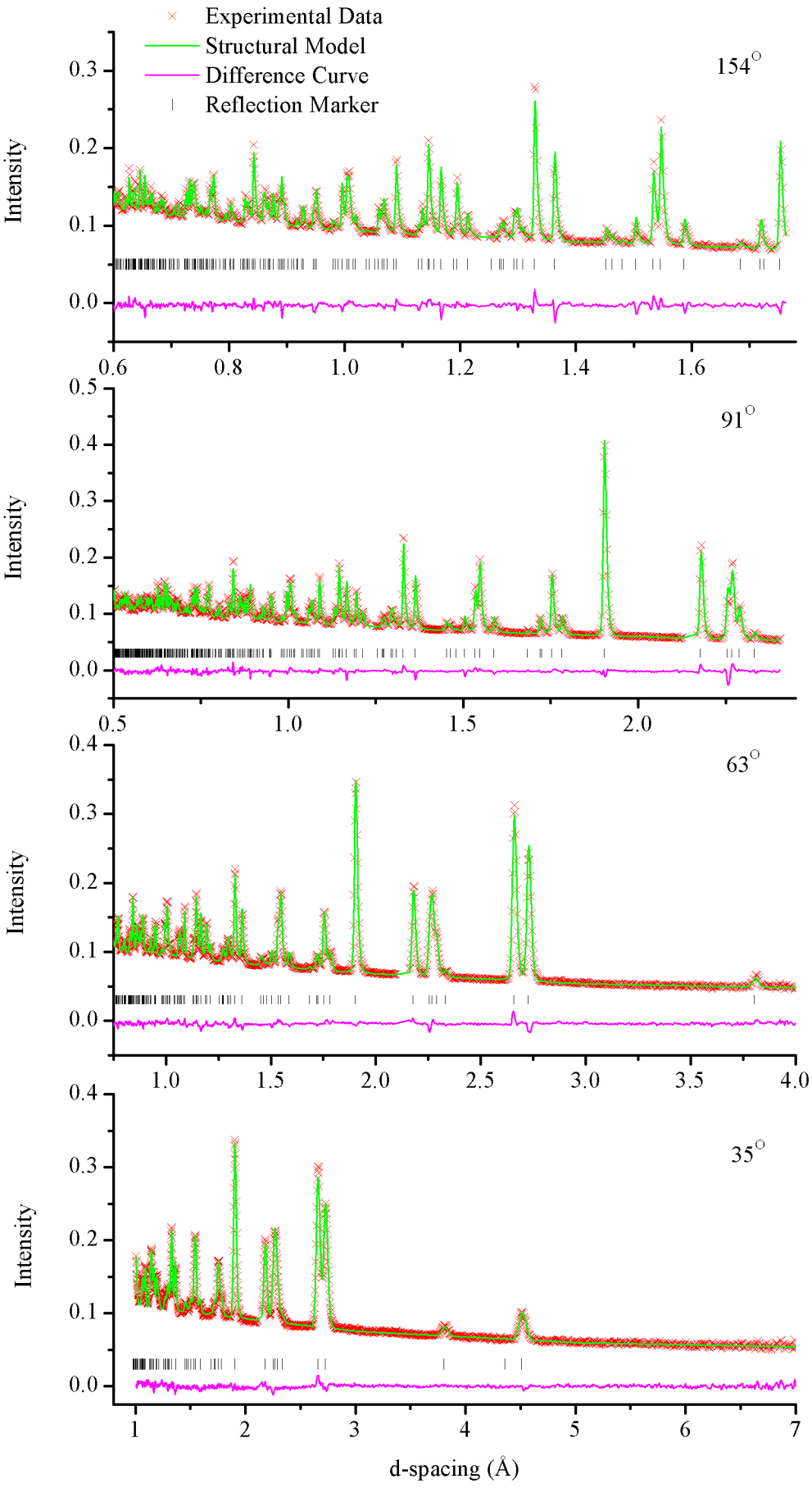

Figure I.6: Powder neutron diffraction data collected from four banks of the GEM diffractometer and structural refinements of $Co_3Sn_{0.8}In_{1.2}S_2$.

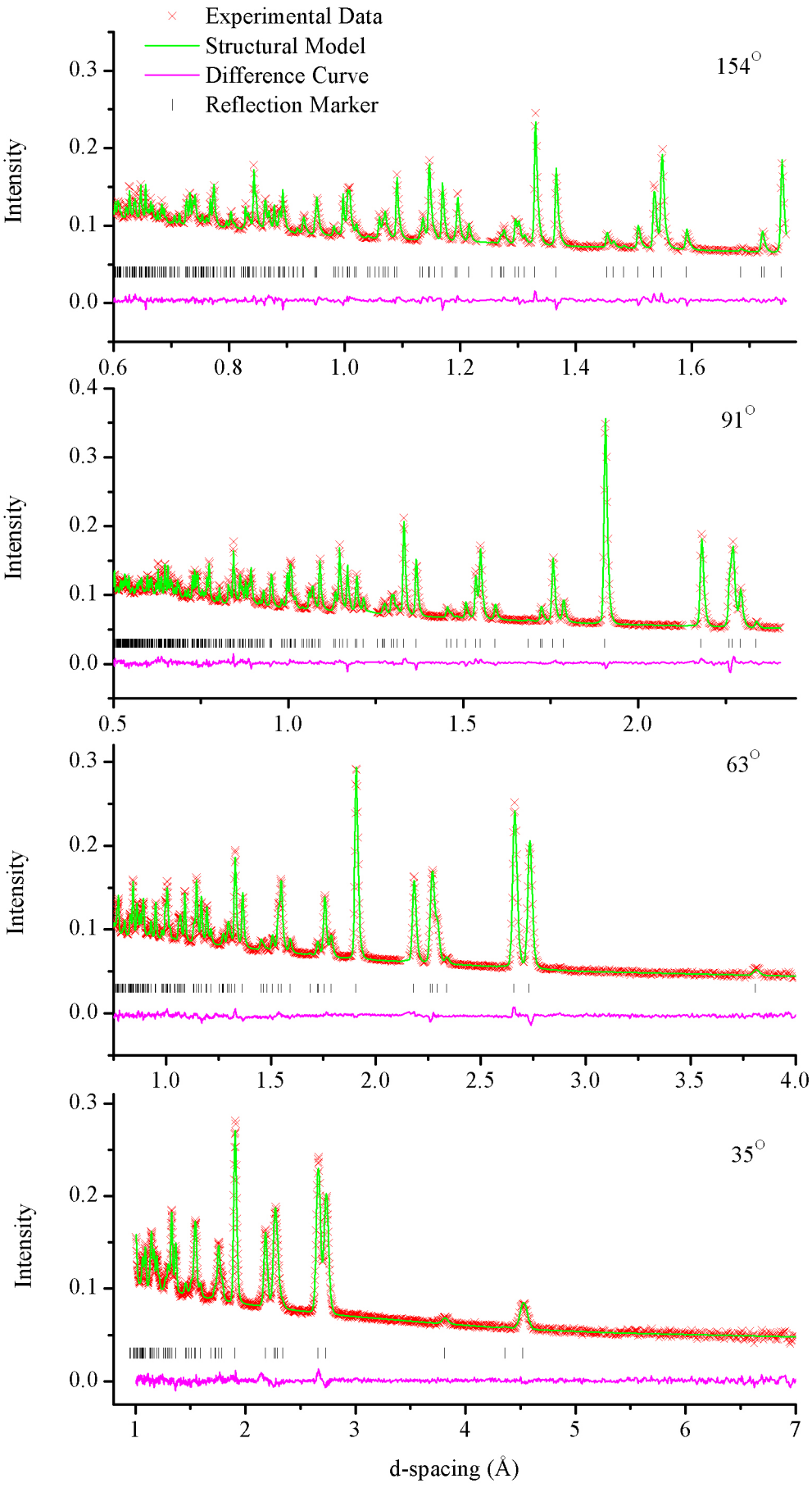

Figure I.7: Powder neutron diffraction data collected from four banks of the GEM diffractometer and structural refinements of $Co_3Sn_{0.6}In_{1.4}S_2$.

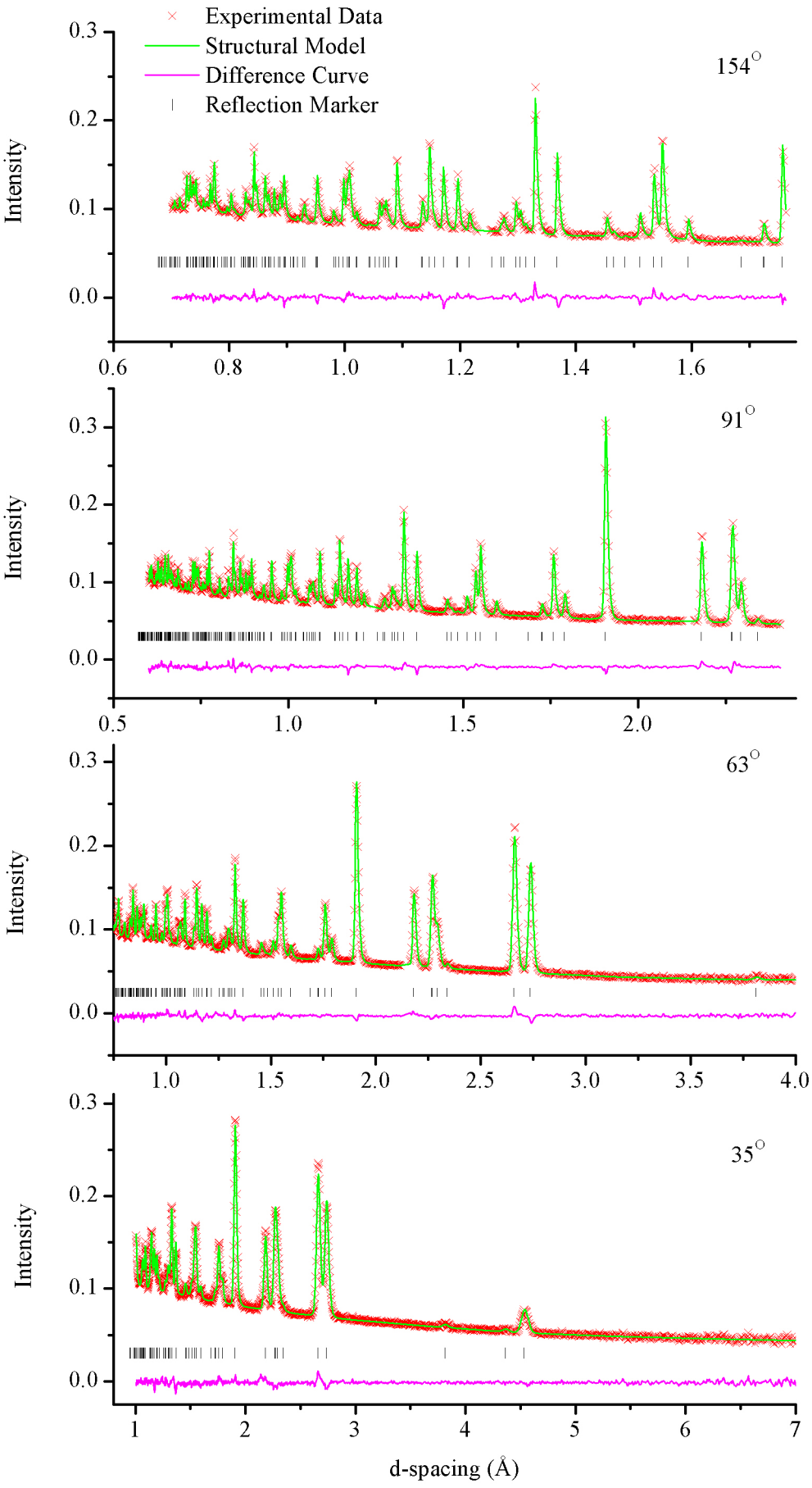

Figure I.8: Powder neutron diffraction data collected from four banks of the GEM diffractometer and structural refinements of $Co_3Sn_{0.4}In_{1.6}S_2$.

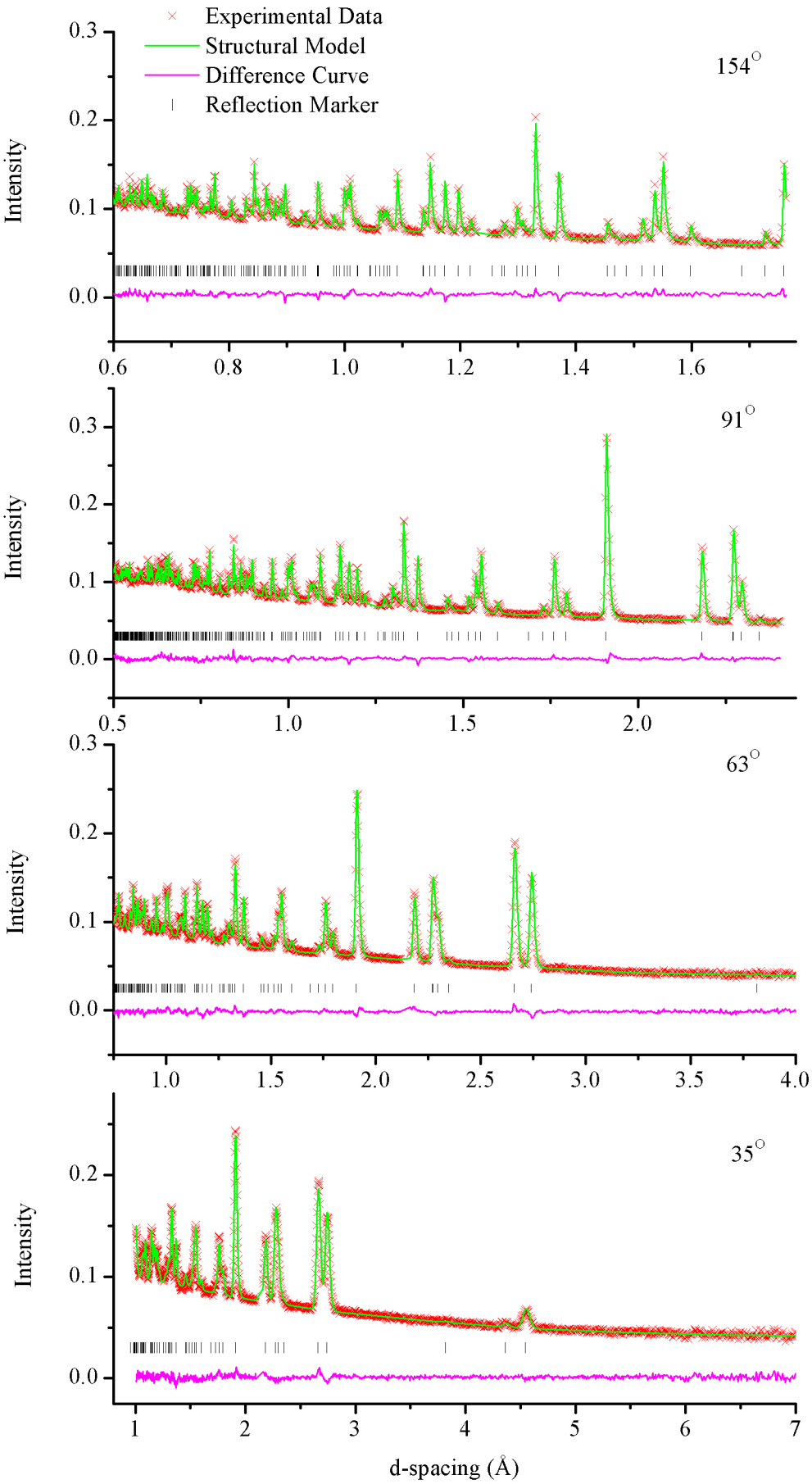

Figure I.9: Powder neutron diffraction data collected from four banks of the GEM diffractometer and structural refinements of $Co_3Sn_{0.2}In_{1.8}S_2$.

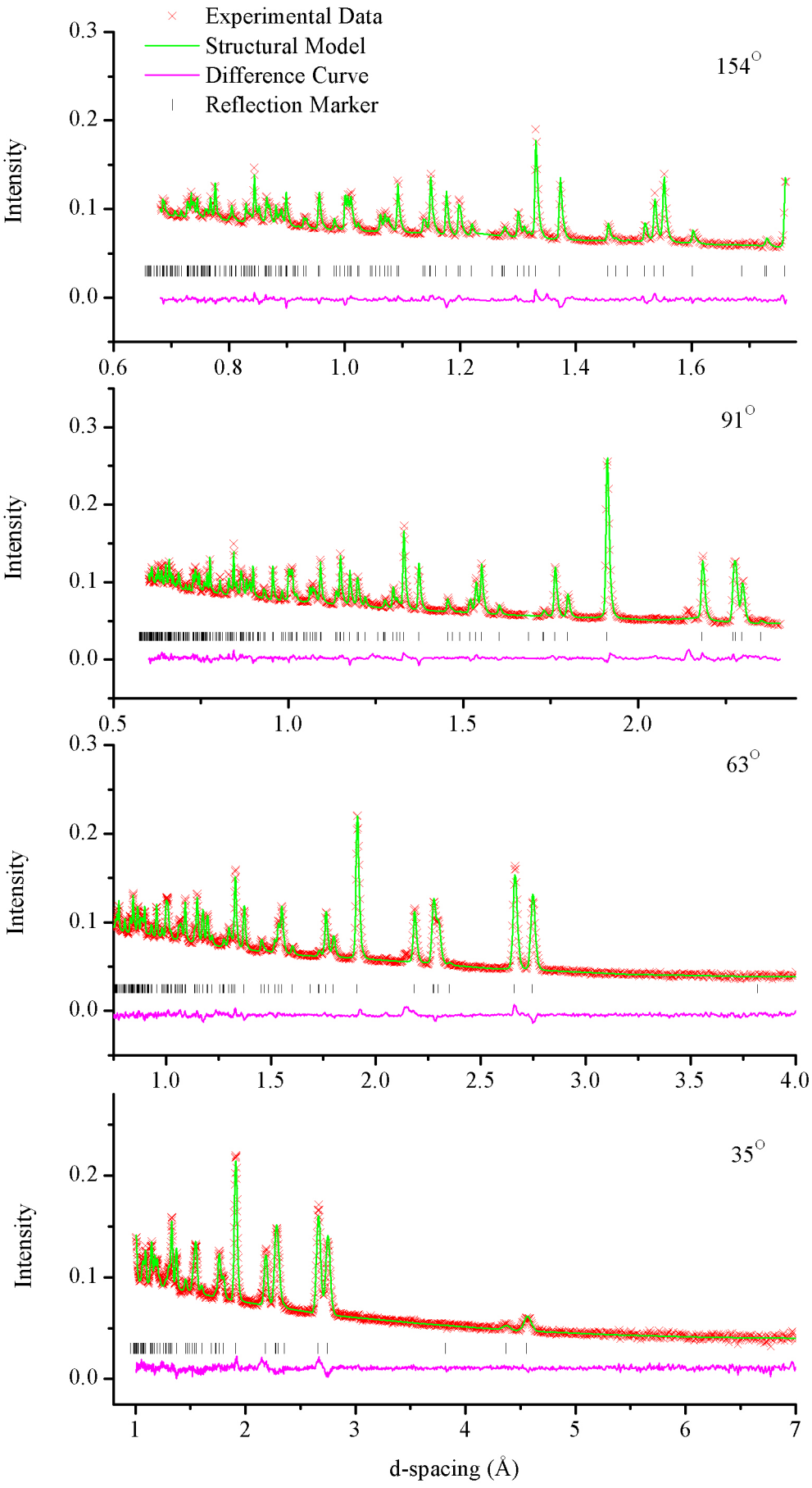

Figure I.10: Powder neutron diffraction data collected from four banks of the GEM diffractometer and structural refinements of $Co_3In_2S_2$.

Appendix J – XPS Spectra of $Co_3Sn_{2-x}In_xS_2$ ($0 \leq x \leq 2$)

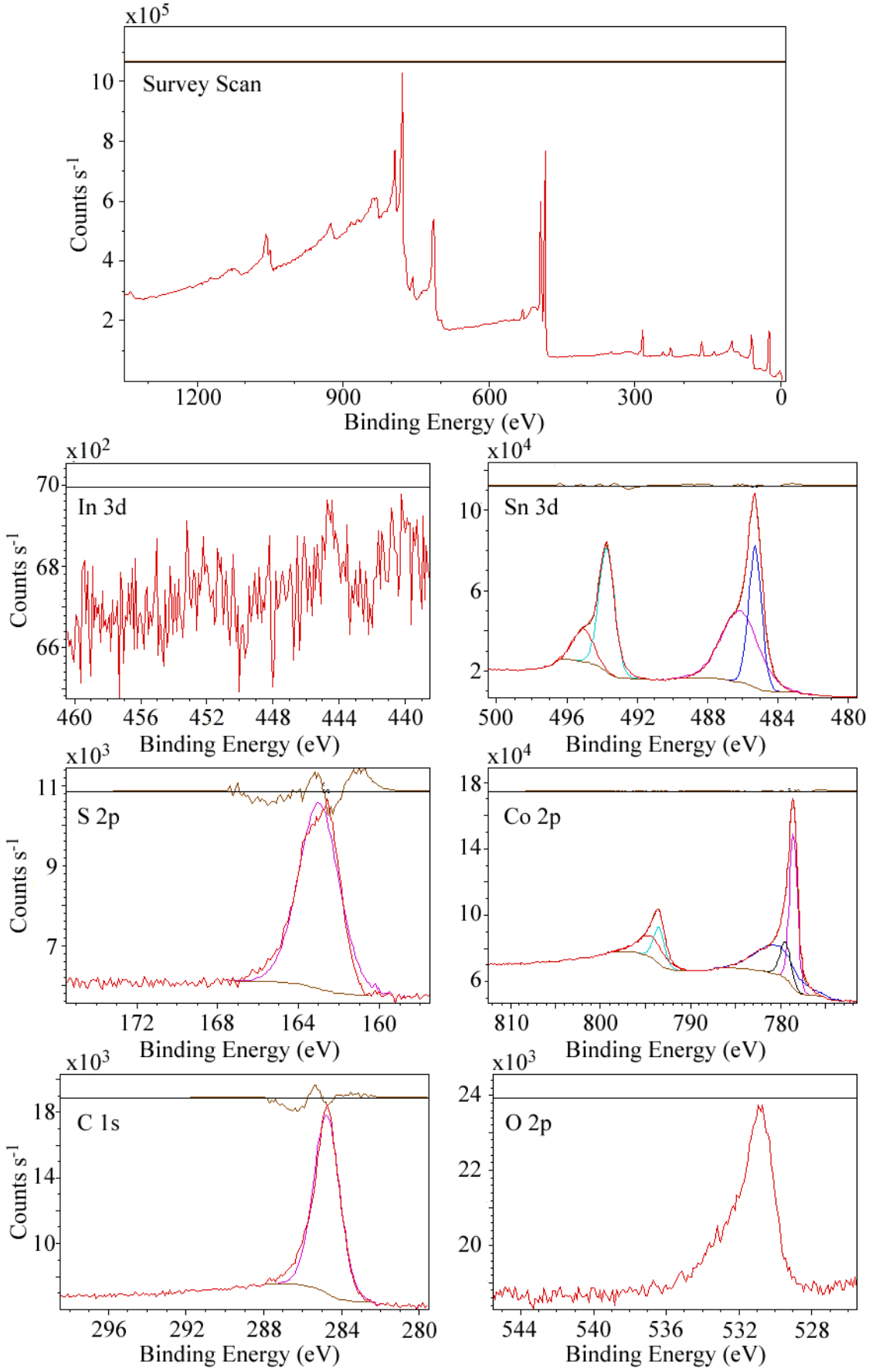

Figure J.1: XPS spectra of $Co_3Sn_2S_2$ showing peak fitting and difference curve.

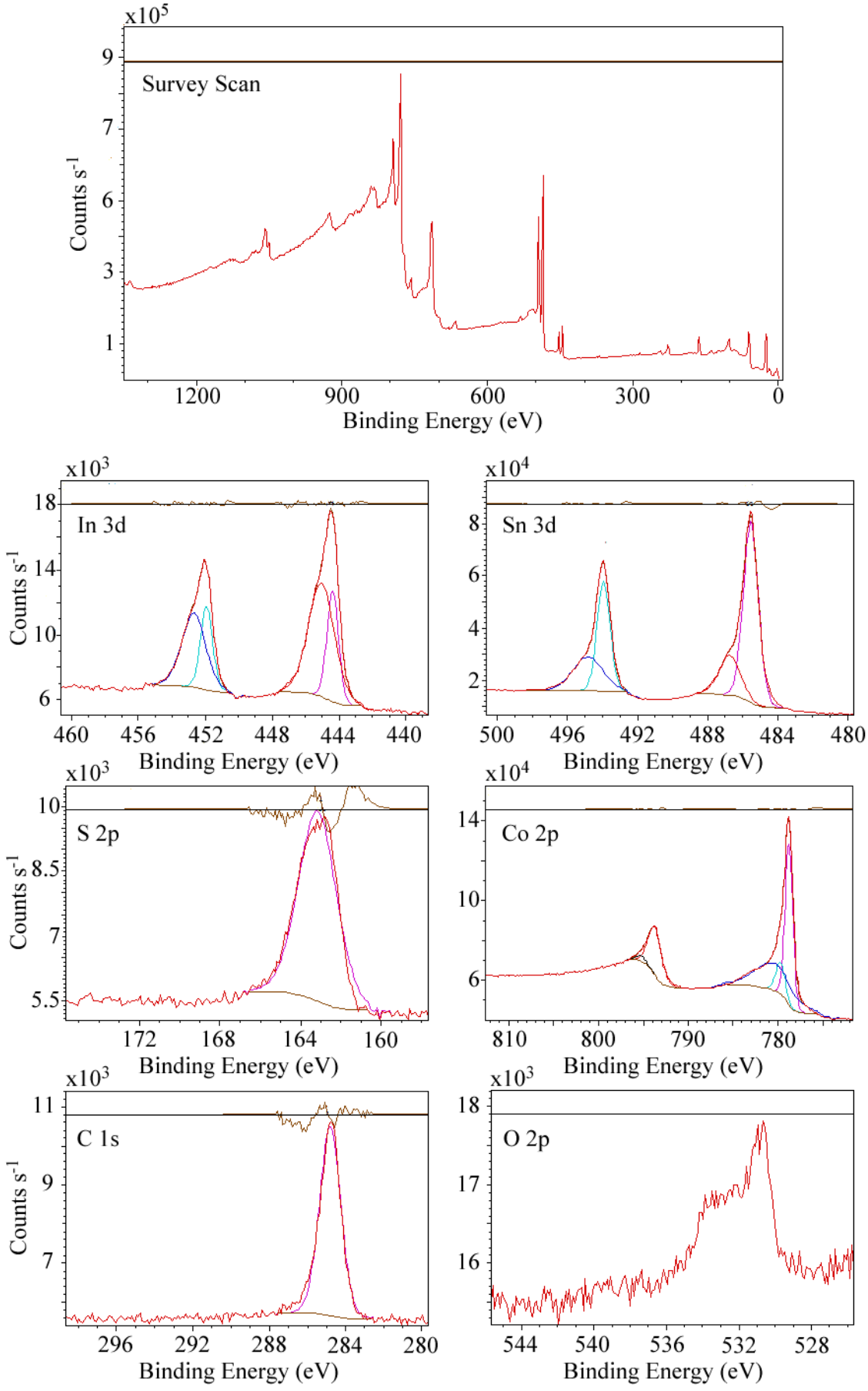

Figure J.2: XPS spectra of $Co_3Sn_{1.6}In_{0.4}S_2$ showing peak fitting and difference curve.

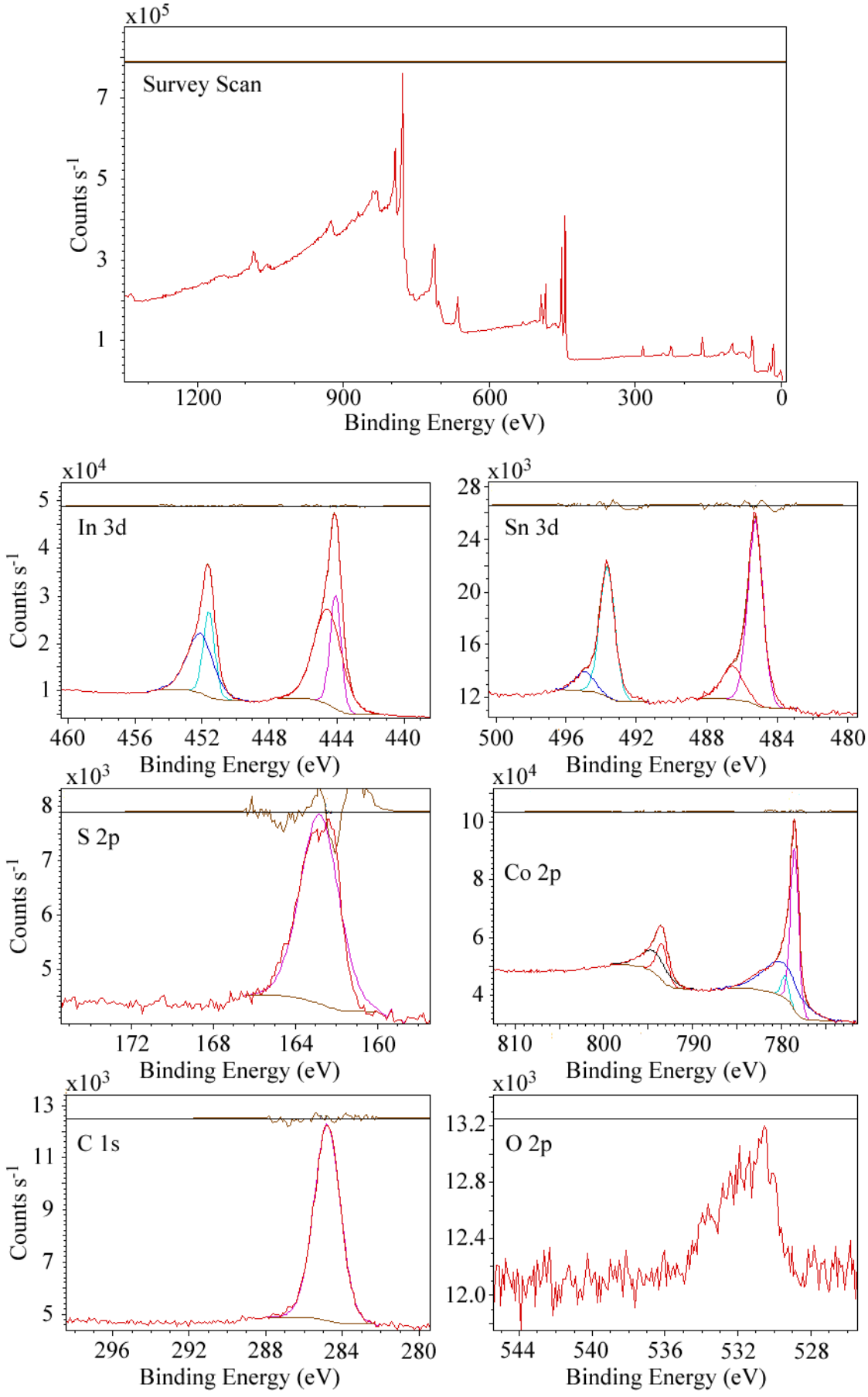

Figure J.3: XPS spectra of $Co_3Sn_{0.4}In_{1.6}S_2$ showing peak fitting and difference curve.

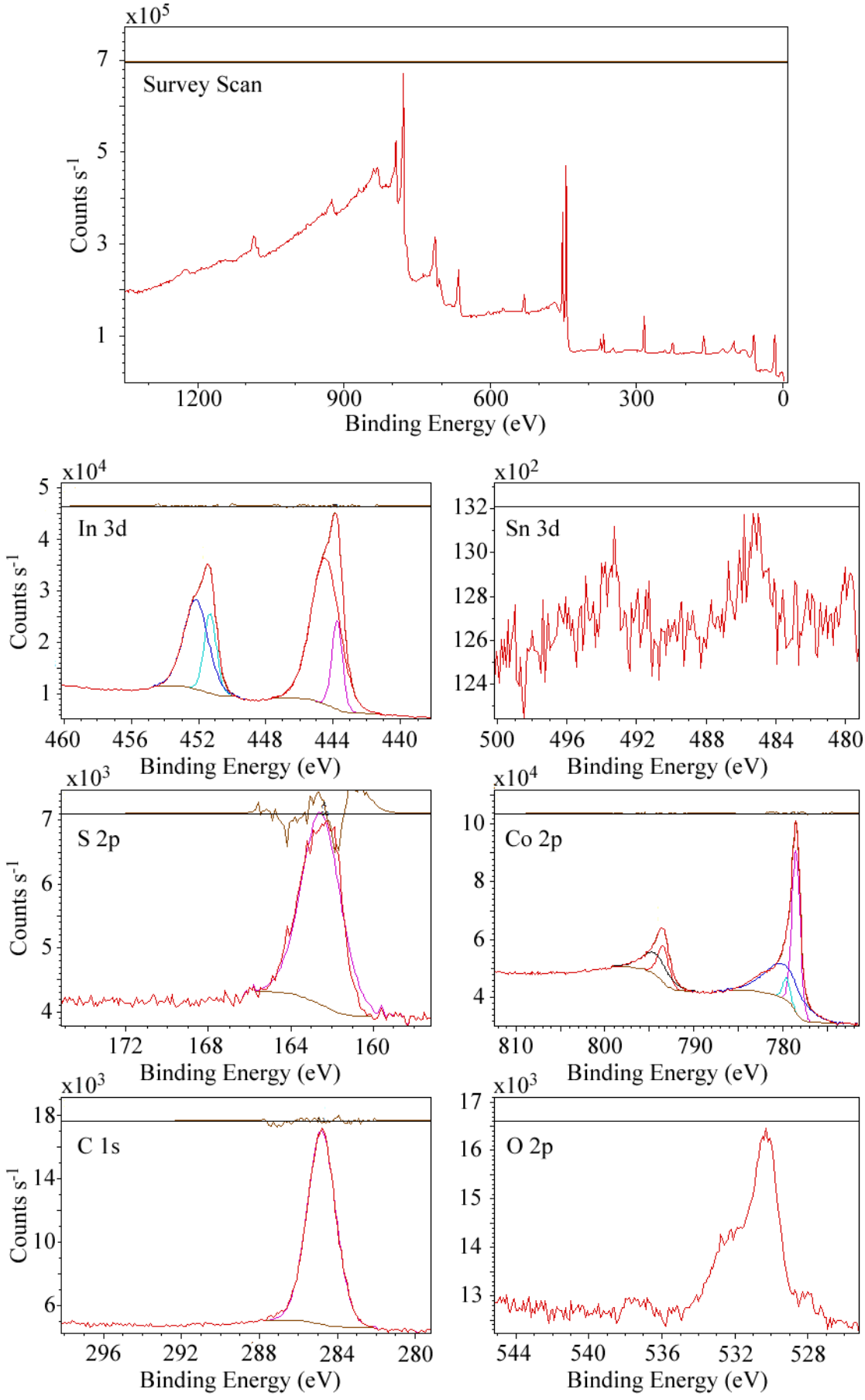

Figure J.4: XPS spectra of $Co_3In_2S_2$ showing peak fitting and difference curve.

Appendix K – ^{119}Sn Mössbauer Spectroscopy for Samples of $Co_3Sn_{2-x}In_xS_2$ ($0 \leq x \leq 2$).

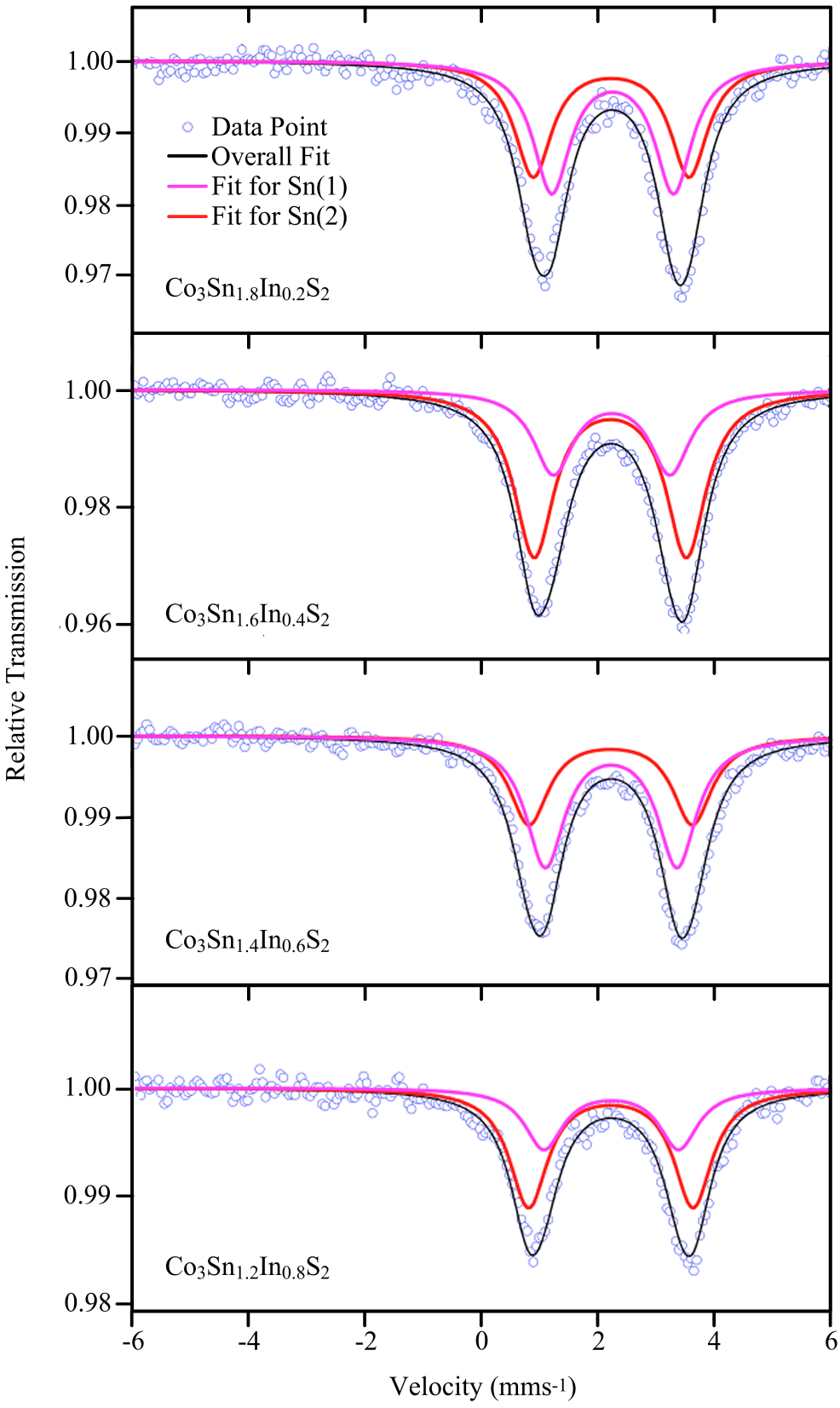

Figure K.1: ^{119}Sn Mössbauer spectra of $Co_3Sn_{2-x}In_xS_2$ ($0.2 \leq x \leq 0.8$).

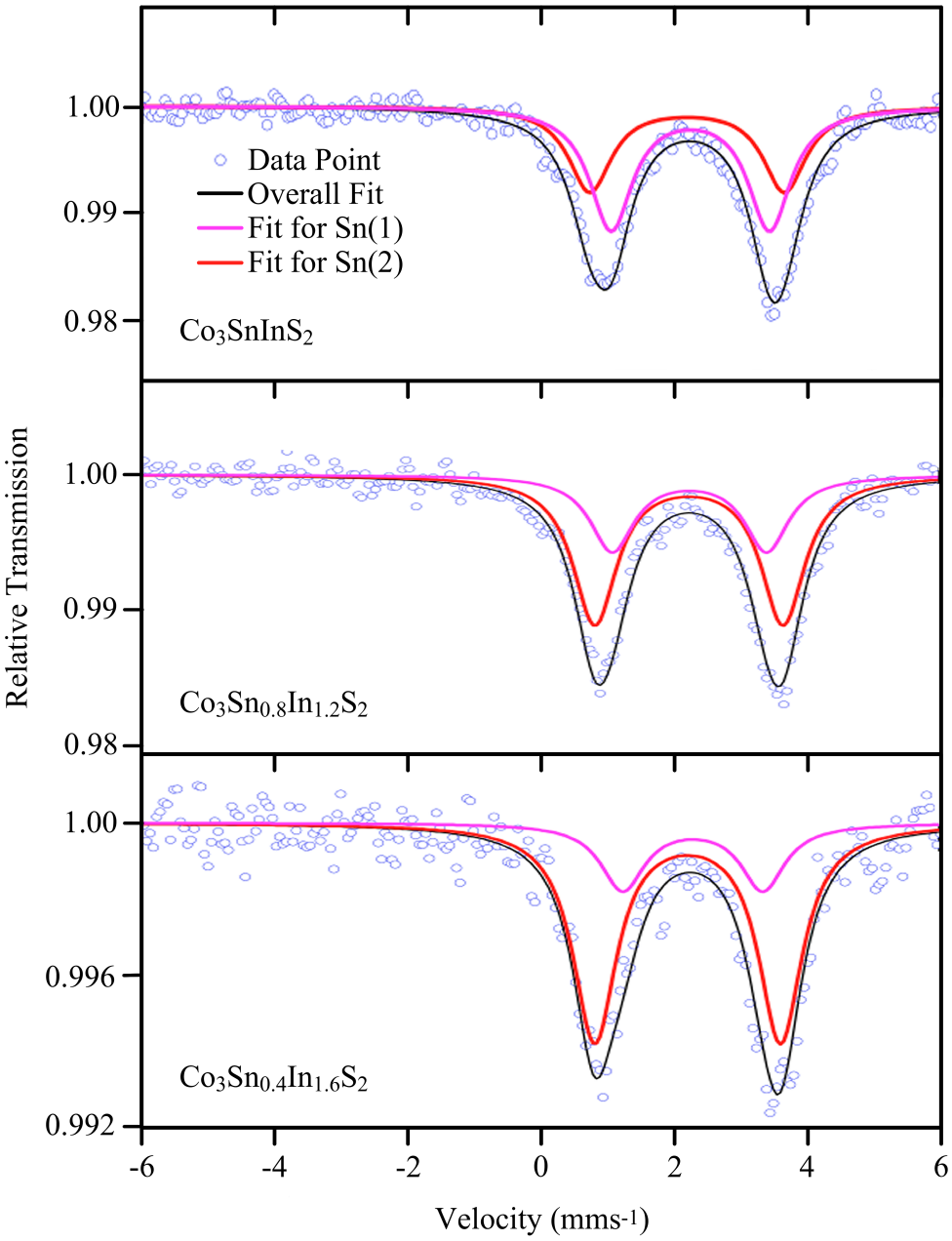

Figure K.2: ^{119}Sn Mössbauer spectra of $Co_3Sn_{2-x}In_xS_2$ ($1 \leq x \leq 1.6$).

Appendix L - Atomic Coordinates of $In_2Sn_3S_7$ From Powder Neutron Diffraction Experiments.

Table L.1: Atomic coordinates of $In_2Sn_3S_7$ obtained from Rietveld refinements of a structural model against powder neutron diffraction data collected on the HRPD diffractometer at 400 °C. Space group: *$P2_1/m$*, *$a = 11.76725(34)$ Å*, *$b = 3.80319(7)$ Å*, *$c = 12.72150(27)$ Å*, *$\beta = 105.726(2)$ °*.

atom	*x*	*y*	*z*	*Uiso (Å^2)*	*SOF In*	*SOF Sn*
M(1)	0.525(1)	0.25	0.379(2)	0.047(2)	0.68(-)	0.32(-)
M(2)	0.495(2)	0.25	0.873(2)	0.047(2)	0.68(-)	0.32(-)
M(3)	0.112(2)	0.25	0.612(2)	0.047(2)	0.68(-)	0.32(-)
Sn(4)	0.145(2)	0.25	0.277(2)	0.112(4)	0(-)	1(-)
Sn(5)	0.146(1)	0.25	0.967(2)	0.112(4)	0(-)	1(-)
S(1)	0.639(2)	0.25	0.073(3)	0.055(2)		
S(2)	0.394(2)	0.25	0.188(3)	0.055(2)		
S(3)	0.359(3)	0.25	0.675(3)	0.055(2)		
S(4)	0.624(2)	0.25	0.568(3)	0.055(2)		
S(5)	0.922(2)	0.25	0.225(3)	0.055(2)		
S(6)	0.884(2)	0.25	0.525(2)	0.055(2)		
S(7)	0.888(2)	0.25	0.875(2)	0.055(2)		

M = In, Sn.

Table L.2: Atomic coordinates of $In_2Sn_3S_7$ obtained from Rietveld refinements of a structural model against powder neutron diffraction data collected on the HRPD diffractometer at 500 °C. Space group: *$P2_1/m$*, *a = 11.78759(30) Å*, *b = 3.80810(7) Å*, *c = 12.75403(26) Å*, *β = 105.698(3)* °.

atom	*x*	*y*	*z*	*Uiso (Å^2)*	*SOF In*	*SOF Sn*
M(1)	0.526(2)	0.25	0.380(2)	0.063(3)	0.68(-)	0.32(-)
M(2)	0.489(2)	0.25	0.873(2)	0.063(3)	0.68(-)	0.32(-)
M(3)	0.115(2)	0.25	0.614(2)	0.063(3)	0.68(-)	0.32(-)
Sn(4)	0.148(2)	0.25	0.276(2)	0.132(5)	0(-)	1(-)
Sn(5)	0.151(2)	0.25	0.970(2)	0.132(5)	0(-)	1(-)
S(1)	0.630(2)	0.25	0.072(3)	0.064(3)		
S(2)	0.391(2)	0.25	0.199(3)	0.064(3)		
S(3)	0.351(3)	0.25	0.674(3)	0.064(3)		
S(4)	0.617(2)	0.25	0.576(2)	0.064(3)		
S(5)	0.920(2)	0.25	0.237(2)	0.064(3)		
S(6)	0.878(2)	0.25	0.521(2)	0.064(3)		
S(7)	0.881(3)	0.25	0.871(2)	0.064(3)		

M = In, Sn.

Table L.3: Atomic coordinates of $In_2Sn_3S_7$ obtained from Rietveld refinements of a structural model against powder neutron diffraction data collected on the HRPD diffractometer at 600 °C. Space group: *$P2_1/m$*, *a = 11.81384(27) Å*, *b = 3.81062(6) Å*, *c = 12.78680(22) Å*, *β = 105.644(2)* °.

atom	*x*	*y*	*z*	*Uiso ($Å^2$)*	*SOF In*	*SOF Sn*
M(1)	0.529(2)	0.25	0.380(2)	0.061(3)	0.68(-)	0.32(-)
M(2)	0.494(2)	0.25	0.872(2)	0.061(3)	0.68(-)	0.32(-)
M(3)	0.110(2)	0.25	0.616(2)	0.061(3)	0.68(-)	0.32(-)
Sn(4)	0.155(2)	0.25	0.278(2)	0.150(6)	0(-)	1(-)
Sn(5)	0.156(2)	0.25	0.963(2)	0.150(6)	0(-)	1(-)
S(1)	0.626(2)	0.25	0.062(3)	0.062(3)		
S(2)	0.401(2)	0.25	0.195(3)	0.062(3)		
S(3)	0.346(3)	0.25	0.673(3)	0.062(3)		
S(4)	0.617(2)	0.25	0.568(3)	0.062(3)		
S(5)	0.911(2)	0.25	0.247(2)	0.062(3)		
S(6)	0.874(2)	0.25	0.520(2)	0.062(3)		
S(7)	0.892(2)	0.25	0.877(3)	0.062(3)		

M = In, Sn.

Table L.4: Atomic coordinates of $In_2Sn_3S_7$ obtained from Rietveld refinements of a structural model against powder neutron diffraction data collected on the HRPD diffractometer at 700 °C. Space group: *$P2_1/m$*, *a = 11.84895(35) Å*, *b = 3.813098(64) Å*, *c = 12.82237(26) Å*, *β = 105.613(2)* °.

atom	*x*	*y*	*z*	*Uiso (Å^2)*	*SOF In*	*SOF Sn*
M(1)	0.520(2)	0.25	0.385(2)	0.081(4)	0.68(-)	0.32(-)
M(2)	0.485(2)	0.25	0.874(2)	0.081(4)	0.68(-)	0.32(-)
M(3)	0.122(2)	0.25	0.609(2)	0.081(4)	0.68(-)	0.32(-)
Sn(4)	0.162(2)	0.25	0.290(2)	0.153(7)	0(-)	1(-)
Sn(5)	0.148(2)	0.25	0.952(2)	0.153(7)	0(-)	1(-)
S(1)	0.624(3)	0.25	0.072(3)	0.058(3)		
S(2)	0.393(3)	0.25	0.196(3)	0.058(3)		
S(3)	0.338(3)	0.25	0.670(3)	0.058(3)		
S(4)	0.614(3)	0.25	0.575(3)	0.058(3)		
S(5)	0.904(2)	0.25	0.244(2)	0.058(3)		
S(6)	0.869(2)	0.25	0.510(2)	0.058(3)		
S(7)	0.906(3)	0.25	0.903(3)	0.058(3)		

M = In, Sn.

Appendix M - Selected Bond Lengths and Angle from Final Rietveld Refinement.

Table M.1: Selected bond lengths and angles from Rietveld refinements of the structural model for $M_3Sn_2S_7$ (M = In, Sn) against powder neutron diffraction data at various temperatures. Atoms numbered as in Figure 5.9.

Compound	*$In_2Sn_3S_7$*				
Temperature (°C)	*25*	*400*	*500*	*600*	*700*
M(1)-S(1) (Å)	2.44(2)	2.38(4)	2.44(3)	2.35(3)	2.39(4)
M(1)-S(2) (Å) × 2	2.63(2)	2.79(2)	2.70(3)	2.77(3)	2.61(3)
M(1)-S(4) (Å) × 2	2.66(2)	2.54(3)	2.60(3)	2.61(3)	2.76(3)
M(1)-S(6) (Å)	2.60(3)	2.50(4)	2.42(4)	2.44(4)	2.48(5)
∠S(1)-*M*(1)-S(2) (°) × 2	86.7(6)	85.5(9)	85.2(9)	83.5(9)	86.5(9)
∠S(1)-*M*(1)-S(4) (°) × 2	97.9(6)	96.7(9)	98.4(9)	97.9(9)	96.2(9)
∠S(2)-*M*(1)-S(3) (°)	92.1(7)	86.0(9)	89.8(9)	86.9(9)	93.7(9)
∠S(2)-*M*(1)-S(4) (°) × 2	88.3(4)	88.4(6)	87.9(6)	89.6(6)	89.3(7)
∠S(2)-*M*(1)-S(6) (°) × 2	87.5(6)	88.6(9)	84.9(9)	88.4(9)	87.4(9)
∠S(4)-*M*(1)-S(5) (°)	91.0(8)	97.0(9)	94.2(9)	93.9(9)	87.5(9)
∠S(4)-*M*(1)-S(6) (°) × 2	87.9(6)	96.7(9)	91.1(9)	89.7(9)	90.2(9)
M(2)-S(5) (Å)	2.60(2)	2.60(4)	2.62(4)	2.67(4)	2.73(4)
M(2)-S(6) (Å) × 2	2.62(2)	2.55(3)	2.68(3)	2.55(3)	2.69(4)
M(2)-S(8) (Å) × 2	2.56(2)	2.67(3)	2.58(3)	2.65(3)	2.50(3)
M(2)-S(10) (Å)	2.57(2)	2.65(4)	2.63(4)	2.51(4)	2.62(4)
∠S(5)-*M*(2)-S(6) (°) × 2	88.9(6)	86.4(9)	85.2(9)	86.1(9)	86.5(9)
∠S(5)-*M*(2)-S(8) (°) × 2	89.5(7)	90.0(9)	91.5(9)	92.0(9)	91.3(9)
∠S(6)-*M*(2)-S(7) (°)	92.7(8)	96.5(9)	90.5(9)	96.9(9)	90.1(9)
∠S(6)-*M*(2)-S(8) (°) × 2	85.9(4)	86.2(6)	87.0(6)	85.4(6)	85.3(7)
∠S(6)-*M*(2)-S(10) (°) × 2	89.9(7)	92.3(9)	94.2(9)	95.4(9)	93.9(9)
∠S(8)-*M*(2)-S(9) (°)	95.4(8)	90.7(9)	95.3(9)	92.2(9)	99.2(9)
∠S(8)-*M*(2)-S(10) (°) × 2	91.7(5)	91.3(9)	89.0(9)	86.5(9)	88.3(9)
M(3)-S(5) (Å)	2.72(2)	2.80(4)	2.68(4)	2.69(4)	2.47(4)
M(3)-S(11) (Å) × 2	2.52(1)	2.60(2)	2.59(2)	2.62(2)	2.46(2)

M(3)-S(13) (Å) × 2	2.72(2)	2.92(3)	2.80(3)	2.64(3)	2.77(3)
M(3)-S(15) (Å)	2.59(2)	2.61(3)	2.72(3)	2.73(3)	2.92(4)
∠S(5)-*M*(3)-S(11) (°) × 2	89.6(5)	89.0(8)	88.2(8)	85.6(8)	88.9(9)
∠S(5)-*M*(3)-S(13) (°) × 2	91.4(5)	97.5(8)	98.0(8)	95.7(8)	94.5(9)
∠S(11)-*M*(3)-S(12) (°)	97.5(6)	94.5(6)	94.7(9)	93.2(9)	101.5(9)
∠S(11)-*M*(3)-S(13) (°) × 2	87.2(3)	91.8(6)	89.4(5)	87.3(5)	90.4(9)
∠S(11)-*M*(3)-S(15) (°) × 2	86.6(5)	85.4(7)	85.8(8)	87.1(7)	86.7(8)
∠S(13)-*M*(3)-S(14) (°)	88.1(7)	81.3(9)	85.9(9)	92.2(9)	87.4(9)
∠S(13)-*M*(3)-S(15) (°) × 2	92.7(5)	88.7(8)	88.5(8)	91.6(7)	90.4(9)
S(16)-Sn(4) (Å) × 2	2.81(2)	2.66(3)	2.63(3)	2.70(3)	3.06(3)
S(16)-Sn(6) (Å) × 2	2.86(2)	2.88(3)	2.89(3)	2.96(3)	2.85(4)
S16)-Sn(8) (Å)	2.83(2)	2.94(3)	3.09(3)	3.01(3)	2.77(4)
∠Sn(4)-*X*(16)-Sn(5) (°)	84.8(7)	91.3(9)	92.9(9)	89.8(9)	77.2(9)
∠Sn(4)-S(16)-Sn(6) (°) × 2	92.5(3)	90.9(4)	90.5(5)	90.7(8)	93.1(9)
∠Sn(4)-S(16)-Sn(8) (°) × 2	105.6(5)	102.7(6)	102.0(7)	104.9(8)	102.4(9)
∠Sn(6)-S(16)-Sn(7) (°)	82.8(7)	82.6(9)	82.5(9)	80.2(9)	83.9(9)
∠Sn(6)-S(16)-Sn(8) (°) × 2	94.8(5)	92.5(6)	91.7(9)	96.9(13)	104.5(9)

Table M.2: Selected bond lengths and angles from Rietveld refinements of the structural model for $Cr_2Sn_3Se_7$ and $In_2Sn_3S_7$ at 25 °C against powder neutron diffraction data at various temperatures. *M* = In, Cr, Sn; *X* = S, Se. Atoms numbered as in Figure 5.9.

Bond Length / Angle	*$Cr_2Sn_3Se_7$*	*$In_2Sn_3S_7$*
M(1)-*X*(1) (Å)	2.56(1)	2.44(2)
M(1)-*X*(2) (Å) × 2	2.60(1)	2.63(2)
M(1)-*X*(4) (Å) × 2	2.59(9)	2.66(2)
M(1)-*X*(6) (Å)	2.60(2)	2.60(3)
∠*X*(1)-*M*(1)-*X*(2) (°) × 2	85.4(4)	86.7(6)
∠*X*(1)-*M*(1)-*X*(4) (°) × 2	101.0(3)	97.9(6)
∠*X*(2)-*M*(1)-*X*(3) (°)	94.5(5)	92.1(7)
∠*X*(2)-*M*(1)-*X*(4) (°) × 2	84.9(2)	88.3(4)
∠*X*(2)-*M*(1)-*X*(6) (°) × 2	84.9(4)	87.5(6)

∠*X*(4)-*M*(1)-*X*(5) (°)	95.0(5)	91.0(8)
∠*X*(4)-*M*(1)-*X*(6) (°) × 2	88.5(8)	87.9(6)
M(2)-*X*(5) (Å)	2.63(3)	2.60(2)
M(2)-*X*(6) (Å) × 2	2.64(2)	2.62(2)
M(2)-*X*(8) (Å) × 2	2.52(1)	2.56(2)
M(2)-*X*(10) (Å)	2.46(2)	2.57(2)
∠*X*(5)-*M*(2)-*X*(6) (°) × 2	86.8(4)	88.9(6)
∠*X*(5)-*M*(2)-*X*(8) (°) × 2	95.8(4)	89.5(7)
∠*X*(6)-*M*(2)-*X*(7) (°)	92.6(6)	92.7(8)
∠*X*(6)-*M*(2)-*X*(8) (°) × 2	84.5(2)	85.9(4)
∠*X*(6)-*M*(2)-*X*(10) (°) × 2	89.4(4)	89.9(7)
∠*X*(8)-*M*(2)-*X*(9) (°)	98.3(6)	95.4(8)
∠*X*(8)-*M*(2)-*X*(10) (°) × 2	87.8(4)	91.7(5)
M(3)-*X*(5) (Å)	2.90(1)	2.72(2)
M(3)-*X*(11) (Å) × 2	2.63(1)	2.52(1)
M(3)-*X*(13) (Å) × 2	2.62(1)	2.72(2)
M(3)-*X*(15) (Å)	2.35(1)	2.59(2)
∠*X*(5)-*M*(3)-*X*(11) (°) × 2	88.3(6)	89.6(5)
∠*X*(5)-*M*(3)-*X*(13) (°) × 2	90.1(4)	91.4(5)
∠*X*(11)-*M*(3)-*X*(12) (°)	93.1(5)	97.5(6)
∠*X*(11)-*M*(3)-*X*(13) (°) × 2	86.6(1)	87.2(3)
∠*X*(11)-*M*(3)-*X*(15) (°) × 2	86.9(4)	86.6(5)
∠*X*(13)-*M*(3)-*X*(14) (°)	93.7(5)	88.1(7)
∠*X*(13)-*M*(3)-*X*(15) (°) × 2	94.6(4)	92.7(5)
X(16)-Sn(4) (Å) × 2	2.810(8)	2.81(2)
X(16)-Sn(6) (Å) × 2	2.918(9)	2.86 (2)
X(16)-Sn(8) (Å)	2.87(1)	2.83(2)
∠Sn(4)-*X*(16)-Sn(5) (°)	85.6(3)	84.8(7)
∠Sn(4)-*X*(16)-Sn(6) (°) × 2	89.3(2)	92.5(3)
∠Sn(4)-*X*(16)-Sn(8) (°) × 2	107.1(3)	105.6(5)
∠Sn(6)-*X*(16)-Sn(7) (°)	81.7(3)	82.8(7)
∠Sn(6)-*X*(16)-Sn(8) (°) × 2	101.6(3)	94.8(5)